

Development of a Wide Bandwidth Array Acousto-Optical Spectrometer for the Herschel Satellite Mission

Inaugural-Dissertation

zur

Erlangung des Doktorgrades

der Mathematisch-Naturwissenschaftlichen Fakultät

der Universität zu Köln



vorgelegt von

Csaba Gál

aus **Bonyhád (Ungarn)**

Köln 2005

Berichterstatter: Prof. Dr. R. Schieder
Prof. Dr. A. Eckart

Tag der letzten mündlichen Prüfung: 20.07.2005

In memory of my father József Gál (1945-1999)

“I’m here. I’m overwhelmed with my desire
to be allowed to see into the works of nature,
to understand, to have the satisfaction
of that superior knowledge which commands
the world of matter and the realm of spirits.”

Imre Madách: The Tragedy of Man (1861)



 **esa**



HERSCHEL

Space Observatory

Exploring the formation of galaxies and stars
Découvrir la formation des galaxies et des étoiles

Astronomers' website: <http://www.rssd.esa.int/herschel>

Contents

| | |
|---|-----------|
| Zusammenfassung | 1 |
| Abstract | 3 |
| Introduction | 5 |
| 1 The Herschel satellite project | 7 |
| 1.1 Science aims of HIFI..... | 8 |
| 1.2 Orbit properties | 9 |
| 2 The Herschel satellite | 13 |
| 2.1 Launcher..... | 13 |
| 2.2 Herschel structural construction..... | 14 |
| 2.2.1 The Herschel Payload Module | 14 |
| 2.2.1.1 The telescope..... | 14 |
| 2.2.1.2 The helium cryostat..... | 15 |
| 2.2.2 The Herschel Service Module | 16 |
| 2.3 Heterodyne receiving and the HIFI instrument..... | 17 |
| 3 Spectrometer requirements | 19 |
| 3.1 Different spectrometer types used for submm astronomy | 21 |
| 4 Acousto-optical signal processing | 25 |
| 4.1 Diffraction angles..... | 28 |
| 4.2 Diffraction efficiency | 29 |
| 4.3 Time-bandwidth product..... | 31 |
| 4.4 Intermodulation and dynamic range..... | 33 |
| 5 The Wide Bandwidth Spectrometer design | 35 |
| 5.1 WBE IF part design description..... | 36 |
| 5.2 WBE Electronics sub-unit design description..... | 36 |
| 5.3 WBO design principle..... | 37 |
| 6 Optical design of the Wide Bandwidth Spectrometer | 39 |
| 6.1 Design concept | 39 |
| 6.2 Optical description of the Bragg cell illuminating optics | 40 |

| | | |
|----------|--|-----------|
| 6.3 | Imaging of the deflected light | 44 |
| 6.3.1 | Optimisation of the cylindrical lens | 46 |
| 6.3.2 | Position of the slit aperture..... | 48 |
| 6.4 | Image size on the CCD..... | 49 |
| 7 | Opto-mechanical design of the Wide Bandwidth Spectrometer | 51 |
| 7.1 | The Laser Source Unit..... | 51 |
| 7.1.1 | Collimating optics | 52 |
| 7.1.2 | Cylindrical lens | 53 |
| 7.1.3 | Mounting precision of the laser diode, collimation requirement | 55 |
| 7.1.4 | Measurement of the collimation quality and wavefront distortion | 58 |
| 7.1.5 | Centring of the laser | 63 |
| 7.1.6 | Collimation procedure..... | 63 |
| 7.2 | Beam splitter | 67 |
| 7.3 | Opto-mechanical design of the laser source unit | 71 |
| 7.4 | Performance results of the source unit | 73 |
| 7.5 | Bragg cell | 76 |
| 7.5.1 | IF frequency coupling | 76 |
| 7.5.2 | Bandpass performance | 77 |
| 7.5.3 | Acousto-optical cross talk | 78 |
| 7.6 | Illumination of the Bragg cell | 79 |
| 7.7 | Diffraction on the Bragg cell - Theoretical resolution of the WBS | 80 |
| 7.7.1 | Diffraction limit of the focal spot..... | 85 |
| 7.7.2 | Focal spot quality influenced by lens aberrations | 87 |
| 7.7.3 | Simulation of alignment errors..... | 88 |
| 7.7.4 | Simulation of positioning accuracy of the laser diode on the optical axis..... | 91 |
| 7.8 | Scan optics..... | 92 |
| 7.9 | CCD detector..... | 93 |
| 8 | Mechanical investigations of the WBO Housing | 97 |
| 8.1 | WBO Housing Deformation Analysis..... | 97 |
| 8.1.1 | Results of the WBO deformation analysis | 98 |
| 8.2 | Impact of the WBO optical bench deformation on the WBO performance..... | 99 |
| 8.3 | Resonance analysis of the WBO | 101 |
| 8.3.1 | Vibration measurement system | 101 |

| | | |
|-----------|---|------------|
| 8.3.2 | Resonance search of the WBO housing assembled with dummy loads..... | 102 |
| 9 | Laser tests..... | 105 |
| 9.1 | Laser power stability attained with constant current supply | 106 |
| 9.2 | Laser power stability attained with constant voltage supply..... | 106 |
| 9.3 | Mode hop characteristics of the laser diode | 109 |
| 9.4 | Investigation of the wavelength hysteresis..... | 111 |
| 9.5 | Output power and wavelength stability of the laser at stabilized temperature..... | 112 |
| 9.6 | Lifetime statistics | 113 |
| 9.7 | Laser light feedback from the collimating optics..... | 114 |
| 10 | Performance tests of the WBO..... | 117 |
| 10.1 | Zero level of the detector | 117 |
| 10.2 | Light scatter..... | 118 |
| 10.3 | IF zero level..... | 119 |
| 10.4 | Bandpass of the WBO | 119 |
| 10.5 | Power linearity | 121 |
| 10.6 | Frequency non-linearity | 122 |
| 10.7 | Frequency calibration..... | 122 |
| 10.8 | Frequency resolution | 123 |
| 10.9 | Noise performance | 125 |
| 10.9.1 | Stability | 125 |
| 10.9.2 | Noise fluctuation bandwidth – noise dynamic range | 128 |
| 10.10 | Thermal vacuum performance | 129 |
| 10.11 | Vacuum correction | 131 |
| 10.12 | Vacuum-air performance..... | 132 |
| 10.13 | Bragg cell heating effect | 135 |
| 10.14 | Resolution performance verification calculation | 136 |
| | Conclusions and Outlook..... | 139 |
| | Appendix A | 143 |
| | Acousto-optic materials..... | 143 |
| | Appendix B..... | 144 |
| | Normalization of Gaussian beams in cylindrical coordinate system. | 144 |
| | Normalization of Gaussian beams in Descartes coordinate system. | 144 |

| | |
|--|------------|
| Appendix C | 145 |
| Dimensions of Gaussian beams..... | 145 |
| Appendix D | 147 |
| Lens prescription data of the laser source unit..... | 147 |
| Appendix E..... | 148 |
| Laser light feedback calculation..... | 148 |
| References | 155 |
| Acknowledgement | 161 |

Zusammenfassung

Der Satellit *Herschel* soll das Universum im Ferninfraroten, Sub-Millimeter und Millimeter Wellenlängenbereich untersuchen. Dieser Bereich des elektromagnetischen Spektrums ist wenig erforscht, da der in der Erdatmosphäre vorhandene Wasserdampf die Signale der meisten astronomischen Quellen fast vollständig absorbiert. Durch das größte, jemals für einen Satelliten gebaute, Teleskop mit 3.5m Durchmesser, wird es möglich sein eine Vielzahl von atomaren und molekularen Linien des stellaren und interstellaren Mediums mit außerordentlich hoher räumlicher Auflösung zu beobachten. Das Empfangssystem basiert auf der *Heterodyn-Technik*, während die spektrale Information mit Echtzeit-Spektrometern gewonnen wird. Diese Arbeit beschäftigt sich mit den Anforderungen, Spezifikationen, Design-Konzepten und der Entwicklung eines breitbandigen akusto-optischen Array-Spektrometers, dem sogenannten *WBS (Wide Bandwidth Spectrometer)*.

Langjährige Erfahrungen während der Entwicklung und dem Betrieb von akusto-optischen Spektrometern (*AOS*) bei bodengebundenen und Raumfahrt-Anwendungen haben die hohe Zuverlässigkeit dieses Spektrometertyps belegt. Die hohen Anforderungen des *Herschel*-Projekts an Bandbreite und Auflösung konnten nur mit einer Hybrid-Lösung realisiert werden. Dabei wird das Signal in Sub-Bänder aufgeteilt und mithilfe einer 4-Kanal Bragg-Zelle analysiert. Die einzelnen Spektren der vier unabhängigen Kanäle werden per Software wieder zusammengesetzt, um das komplette Spektrum des Eingangssignals zu erhalten. Alle Kanäle der Bragg-Zelle werden dabei mit einem einzelnen Halbleiterlaser betrieben. Um eine hohe Effizienz des Spektrometers zu gewährleisten ist eine Optimierung des optischen Aufbaus erforderlich. Im Vergleich zu früheren akusto-optischen Spektrometern wurde beim *WBS* eine enorme Steigerung der optischen Effizienz erreicht. Das neuentwickelte Laser-Modul beinhaltet die notwendige Optik zur Ausleuchtung der Bragg-Zelle. Es besteht aus zwei Lasern - aus Sicherheitsgründen wurde ein Ersatzlaser integriert - mit zugehörigen Kollimations- und Zylinderoptiken und einem Strahlteiler. Die Verwendung von Prismen als Strahlteiler ermöglicht die Erzeugung von vier parallelen Laserstrahlen bei gleichzeitiger verlustfreier Einkopplung des redundanten Lasers. Dies ist ein wesentlicher Aspekt zur Gewährleistung der hohen optischen Effizienz. Der zweite Teil der Optik bildet das durch die Bragg-Zelle gebeugte Licht auf einen linearen 4-zeiligen CCD-Detektor ab. Dabei stellt das neue Design der beugungslimitierten Optik eine hohe Auflösung und Lichtausbeute sicher.

Die Optimierung der optischen Effizienz bewirkt gleichzeitig eine Steigerung der mechanischen Empfindlichkeit des gesamten Spektrometers. Eine hohe mechanische Stabilität ist allerdings von besonderer Bedeutung bei der Erfüllung der spektroskopischen Stabilitätsanforderungen. Dies erzwingt den Einsatz von stabilen Materialien mit geringen thermischen Ausdehnungskoeffizienten. Insbesondere die Laserdioden-Montierung verlangte den Einsatz von Titan, um die thermischen Deformationen möglichst gering zu halten. Erschwerend ist bei einem Satellitenprojekt die geforderte hohe mechanische Stabilität bei gleichzeitig geringem Gewicht.

Das Design des optischen Systems sollte eine beugungsbegrenzte Abbildung ermöglichen. Limitiert wird die Auflösung des WBS durch die begrenzte Apertur und die vergleichsweise schlechte optische Qualität der Bragg-Zelle. In dieser Arbeit wurden zum ersten Mal detaillierte theoretische Untersuchungen über das Auflösungsvermögen eines akusto-optischen Array-Spektrometers durchgeführt. Die Beugung an der akustischen Apertur der Bragg-Zelle wurde mithilfe der Fraunhofer-Beugungstheorie berechnet. Das präzise Modell des Deflektors berücksichtigt neben der frequenzabhängigen Größe der akustischen Zone auch die Abschwächung der Schallwelle durch das Deflektor-Material. Des Weiteren wurde die Auswirkung der Laserstrahl-Position auf das Auflösungsvermögen des Spektrometers untersucht. Dies ist besonders wichtig bei der Bestimmung des Einflusses der Justage-Toleranzen. Das theoretische Modell bietet zusätzlich die Möglichkeit durch Linsen- und Kristallfehler bedingte Wellenfrontstörungen und deren Auswirkung auf die Auflösung zu untersuchen.

Als wichtiger Bestandteil der Qualifizierung wurden eingehende Untersuchungen der mechanischen Stabilität bei thermischen, Vibrations- und Montagebelastungen gemacht. Die frühen Thermaltests während der Entwicklungsphase gaben entscheidende Informationen, um eine weitere Optimierung des mechanischen und optischen Aufbaus zu erreichen. Die Resonanztests dienten zur Verifizierung der mechanischen Steifigkeit und Stabilität des Spektrometers.

Die Laserdiode und deren Spannungsversorgung haben wesentlichen Einfluss auf die Frequenz- und Leistungsstabilität des Spektrometers. Besonders entscheidend sind dabei Modenstabilität, Modensprungverhalten und Wellenlängenstabilität. Um eine Vergleichbarkeit sicherzustellen, wurden Dioden aus dem selben Fertigungsprozess, aus dem auch die Flugdioden ausgewählt wurden, bezüglich dieser Eigenschaften untersucht. Auch Laser-Feedback von der Kollimationsoptik kann zu gravierenden Leistungsinstabilitäten führen. Eine Minimierung dieser Problematik wurde durch ein spezielles Design der Optik erreicht. Von besonderer Bedeutung sind die Ergebnisse des beschleunigten Lebensdauertests. Diese belegen, dass die Zuverlässigkeit des Spektrometers während der Missionsdauer gewährleistet ist.

Die Qualifikationstests simulieren die extremen Bedingungen, unter denen das WBS ausgesetzt wird. Durch eine Vergleichsmessung vor und nach jedem Test wird verifiziert, dass die Performanz des Geräts auch unter extremen Bedingungen und Belastungen erhalten bleibt. Das gute Ergebnis dieser Tests ist ein Beleg für die hohe Qualität des mechanischen und optischen Aufbaus, aber auch der außerordentlichen Präzision der Justierung. Innerhalb des Betriebstemperaturbereichs wurden vor allem die Änderung der Effizienz, des Bandpass und der Auflösung charakterisiert. Zusätzlich wurde das Rauschverhalten eingehend untersucht. Bei astronomischen Beobachtungen mit langen Integrationszeiten ist dies besonders bedeutsam, damit sichergestellt ist, dass vom Spektrometer keine zusätzlichen Beiträge zum radiometrischen Rauschen erzeugt werden. Aufgrund des soliden Aufbaus des WBS werden Integrationszeiten von mehreren 100 Sekunden ohne deutliche Effizienzverschlechterung erreicht. Alle durchgeführten Tests haben gezeigt, dass das Spektrometer die Anforderungen des Herschel Satelliten-Projekts erfolgreich erfüllen wird.

Abstract

The Herschel satellite observatory will explore the universe at far-infrared, submillimetre, and millimetre wavelengths. This regime of the electromagnetic spectrum is difficult to observe, because water vapour in the Earth's atmosphere absorbs the signals of almost all the astronomical sources. With the 3.5m telescope (the largest ever placed aboard a spacecraft), it will be possible to observe various atomic and molecular lines with exceptionally high spatial resolution. The receiver system employs the heterodyne technique, and the spectral information is obtained by means of real-time spectrometers. Within this thesis, the requirements, specifications, design concept, and development of a wide bandwidth array acousto-optical spectrometer (*WBS*) is discussed.

Both ground-based and satellite applications have demonstrated that acousto-optical spectrometers (*AOS*) utilize a reliable signal-processing technique. For the Herschel mission, the spectrometers demand a large frequency bandwidth and high resolution. These are achieved by means of hybrid technology. This means that the signal is split into four sub-bands and analyzed by using a four-channel array Bragg cell. The spectra of the four individual channels are co-added by software to create the complete wide bandwidth spectrum of the input signal. Since the channels of the deflector are illuminated by a semi-conductor laser that provides relatively low optical power, the imaging optical system requires careful design to make the instrument efficient. In comparison with earlier *AOSs*, the Herschel *WBS* has outstanding optical efficiency due to its diffraction-limited and efficiency-optimized optical design. The first part of the optics that illuminates the Bragg cell (*Laser Source Module*) comprises two laser diodes (the second laser is needed for redundancy reasons), the collimation and imaging optics, and the specially-designed beam splitter. The great advantage of the prism-based beam splitter design is that it generates the four beams necessary for the illumination of the deflector and makes it possible to couple the light of the redundant laser without applying an additional beam splitter, which would significantly reduce the efficiency of the instrument. The second part of optics images the deflected light of the Bragg cell onto a four-line linear CCD detector. The design of the diffraction limited lens system makes it possible to achieve the required high resolution and high efficiency.

At the same time, the optimization of the optical efficiency affects the mechanical and thermal sensitivity of the spectrometer. Since the high mechanical stability is an important concern for the spectroscopic stability performance of the instrument, it is essential to use materials that have high stiffness and low thermal expansion. Specifically, the mounting of the laser diode requires a thermally compensated design to reduce the deformations caused by thermal changes. In addition to the high stiffness, the weight of satellite-borne instruments must be minimized. Thus, most of the components are light weighted and made of a special aluminium alloy.

The imaging optical system of the spectrometer is designed to be diffraction limited. However, the deflector considerably reduces the resolution, since it has a small aperture, and the acousto-optical material has poor optical quality. For the first time, theoretical investigations of the resolution involving the Bragg cell were carried out. The diffraction phenomenon of the acoustic aperture of the Bragg cell is studied by using the Fraunhofer diffraction theory. The model of the deflector includes the frequency-dependent dimension of the acoustic zone and the attenuation of the acousto-optical material. Furthermore, the model makes it possible to explore the impact of the illuminating laser beam position change relative to the active zone of the Bragg cell on the resolution of the spectrometer. For investigations of alignment errors, this is of particular importance. An additional highlight of this theoretical investigation is that lens aberration errors and crystal imperfections that adversely affect the wavefront aberration, i.e. the resolution, can be also examined by diffraction analysis.

As part of the qualification procedure, thorough thermal, deformation, and resonance investigations are made with the spectrometer assembled with dummy loads. During the development phase, the early tests of mechanical deformations caused by thermal variations show the mechanical stability and thermal sensitivity of the instrument and therefore provide detailed information for further optical and mechanical development phases. Further resonance search tests are conducted to measure the mechanical stability of the unit.

The power and frequency stability of the spectrometer is partly dependent on the performance of the laser diode and the stability of its power supply. Thus, the laser diodes selected from the batch of the flight lasers were investigated to determine their single mode behaviour, mode jump characteristics, wavelength hysteresis, and wavelength stability. Because the laser light feedback from the surfaces of the collimating optics might also appreciably reduce the power stability of the instrument, investigations are performed with the special collimator design of the WBS. In order to determine the reliability of the lasers, accelerated lifetime tests are performed, and conclusions are drawn relating to lifetime statistics.

The WBS must meet strict performance standards before it can be flown on Herschel. The space-qualification procedure comprises diverse tests that simulate the extreme environment of the spectrometer in orbit. The results of these tests indicate the quality of the mechanical and optical design and confirm the adjustment precision of the instrument. Within the operating temperature range of the spectrometer, the efficiency, bandpass, and resolution variations are characterized. Moreover, the noise performance is investigated in detail. For prolonged astronomical measurements it is of crucial importance that the backend system does not significantly contribute to the radiometric noise. Due to the meticulous design of the WBS, the outstanding noise performance makes it possible to efficiently perform integrations of hundreds of seconds. All these tests indicate that the array acousto-optical spectrometer designed for the Herschel satellite will operate successfully.

Introduction

The discovery of more than 130 molecules in interstellar space through their rotational transitions observed in millimetre and submillimetre wavelengths has demonstrated that the enormous space between the stars in our and other galaxies is filled with a great multitude of atomic, molecular and ionized matter. The observation of the composition of stellar and interstellar matter, as well as the detailed information about the kinematics of these regions through their highly resolved spectra is the key to understanding the evolution of the universe. The enormously rapid development of instrumentation in radio astronomy and the ever-increasing spatial and spectral resolution provides detailed data that are used for astronomical models of stars, galaxies or molecular clouds for example. It has become clear on account of the latest achievements of modern astrophysics, that the dense parts of extensive molecular cloud complexes (*Giant Molecular Clouds*) play an important role in star forming processes, thus it is essential to explore these regions in more detail.

The great importance of studying the interstellar clouds was recognized first through Sir F. W. Herschel's¹ activities in the 18th century. He observed all astrophysically interesting phenomena like stars, nebulae, and star clusters. In the infinite "heaven" of stars, he discovered about 3000 clusters and nebulae, which are nowadays often called "dark dust clouds". In his paper "*Account of some Observations tending to investigate the construction of Heaven*" in 1784, as the result of years of his profound research, he discussed the evolution of matter from the nebulous material to the final planetary state by means of gravitation. In this paper, he explicitly notes "*the spaces preceding them were generally quite deprived of their stars, so as often to afford many fields without a single star in it*". This is of equivalence of regions in the sky, where the number and the brightness of the stars "*on nebulous ground*" is drastically reduced relative to the neighbouring areas. Especially beautiful examples of these obvious dust clouds are the dark dust clouds in Taurus region, like the sources TMC 1 (*Taurus Molecular Cloud*), TMC 2, etc [15]. Herschel was an unflagging astronomer. For many years, he conducted night by night systematic observations of the sky, examined planets, stars, star clusters, and nebulae. By daytime, he worked over his results or led the construction of his telescopes. Herschel observed sunspots, approved the gaseous nature of the sun, rediscovered the Martian polar ice caps, and believed in possible life on Mars. He announced the trade-wind theory of Jupiter's belts and explored two of Jupiter's and two of Uranus's moons. His main intent, he said, was a "*knowledge of the construction of the heavens*". His principal work was on stars, and in this field he made two discoveries of principal importance: the movement of the solar system through space, and the substantiation that binary stars move around their common centre of gravity. This evidence validated the

¹ Sir William Herschel (1738-1822), British astronomer, was born Friedrich Wilhelm in Hannover, Germany, Nov. 15, 1738. He was musician in the Hanoverian Guards but in 1757, he went to England and worked as a music teacher and organist. From private interests he observed the stars and during his nocturnal survey of the heavens on Mar. 13, 1781, Herschel discovered the planet Uranus. For his discovery, he immediately became famous, and George III made him King's Astronomer. He created many telescopes, including a 20-foot and a 40-foot reflector. These enormous instruments were assembled at his home in Slough and made him world-famous. He became one of the greatest astronomers of his time. Herschel died in Slough, England, August 25, 1822.

universality of Newton's gravitation theory. Herschel explored nearly 1.000 double stars. In 1785, he introduced the disc theory of the stellar system, stating that all nebulae are clusters of stars, which he called "*island universes*". He abandoned the idea of the Milky Way as a collection of uniformly distributed stars and came to believe that it was composed of local groups and clusters. The nebulae, he thought, were all clusters not yet resolved into stars. However, a profound investigation of the "cold" interstellar matter at that time was impossible through observations exclusively performed at optical wavelengths.

The technical achievements of the last century opened a new branch in the science of astronomy. In 1932 Karl Jansky, who worked for the famous Bell Laboratories, became the assignment to explore the extraordinary noise in short wavelengths that gave rise to problems during intercontinental radio-telecommunications. With his "*Sterba curtain array*" antennae he received interesting noise phenomena at 20.5MHz. Jansky presumed that these signals might not originate from the Earth, but possibly from the Milky Way. Nevertheless, more precise investigation of these radio waves was not possible with his curtain array, because of the pure angle resolution (30°) of the aerial, and Bell Laboratories did not supported further costly experiments. However, the young radio engineer Grote Reber was fascinated as he red the study about Jansky's theory of electromagnetic waves coming from the space. He considered if the radiation had purely thermal origin the intensity should increase with decreasing wavelength. He decided on a frequency of 3300MHz and in 1938 constructed the first radio telescope in the world in the garden of his parents in Wheaton, Illinois, USA. It is astonishing if one bears in mind that in the late 1930s, the highest frequency available through commercial technology was about 100MHz. After the first attempts it was apparent that the intensity of radio signals did not rise with increasing frequency. However, the long-awaited success did not fail to come, at 160MHz he measured the first the radio waves of the Milky Way [51].

After the World War II, the "One man" radio astronomy was over and a swift development of the new science began. By now, at millimetre and submillimetre wavelengths the universe is well explored, yet the mid- and far-infrared regime (300-20 μm) is still purely observed. The main reason for that is the opacity of the Earth atmosphere. The huge quantity of water vapour in the atmosphere restricts exploration of all but a restricted frequency regime. Even high-altitude observatories like CSO², IRAM³, JCMT⁴, ALMA⁵, or air-borne missions like KAO⁶, SOFIA⁷ will never completely resolve the transmission problems of the atmosphere. In the far-infrared and submillimetre regions there are only a few scientific data observed by the precursor air-borne and satellite missions of ISO⁸, SWAS⁹, ODIN¹⁰, SIRTIF¹¹ and IRAS¹². In addition, the main advantage of sub-mm spectroscopy is that at higher frequencies (THz) the electromagnetic waves are less absorbed by the "*nebulous background*" i.e. the dark interstellar clouds. Herschel must have made great use of the excellent technology of our age in his researches and understanding of the construction of the heavens. In this sense, the sub-mm explorer satellite presented below is worthy of bearing the name of Herschel.

² Caltech Submillimeter Observatory

³ Institute für Radioastronomie im Millimeterbereich

⁴ James Clerk Maxwell Telescope

⁵ Atacama Large Millimeter Array

⁶ Kuiper Airborne Observatory

⁷ Stratospheric Observatory For Infrared Astronomy

⁸ Infrared Space Observatory

⁹ Submillimeter Wave Astronomy Satellite

¹⁰ Swedish Small Satellite Project for Astronomical and Atmospheric Research

¹¹ Spitzer Space Telescope (formerly, the Space Infrared Telescope Facility)

¹² Infrared Astronomical Satellite

1 The Herschel satellite project

The *Herschel & Planck* satellite missions are cornerstone projects of the *European Space Agency (ESA)* within the *ESA Horizon 2000 Science Programme*. The *Herschel & Planck* satellites were established to explore the far-infrared, submillimetre and millimetre frequency range. Onboard of the *Herschel Space Observatory (HSO)* there are three instruments: *HIFI*, *PACS* and *SPIRE*. *HIFI*, the *Heterodyne Instrument for the Far Infrared Space Telescope* (formerly *FIRST*), is designed to study the universe in one of the last unexplored regions of a wide electromagnetic spectrum. *HIFI* is an observatory-type satellite telescope that is going to be operated with an unusually high spectral resolution and sensitivity with wide frequency coverage, and high stability providing spectra for the versatile science themes of modern astrophysics. The *Photodetector Array Camera and Spectrometer (PACS)* employs two photoconductor arrays, and two bolometer arrays to perform imaging line spectroscopy and imaging photometry of galaxies and star forming regions in the $60\text{-}210\mu\text{m}$ wavelength band. The *Spectral and Photometric Imaging Receiver (SPIRE)* was established to explore the statistics and physics of galaxies and star formations at far-infrared and submillimetre wavelengths ($200\text{-}700\mu\text{m}$).

The *Planck* satellite is intended to perform astronomical observations in the submillimetre and millimetre regime. On the board of *Planck* there are two astronomical instruments *HFI (High Frequency Instrument)* and *LFI (Low Frequency Instrument)*.

HIFI is a unique instrument, because it provides spectra with high spectral resolution and high sensitivity at frequencies, which are mostly unexplored. It has a large spectral coverage ($480\text{GHz}\text{-}1910\text{GHz}$), the high calibration accuracy guaranties a high measurement precision, and since the instrument uses the heterodyne measurement technique, the observed lines are directly velocity resolved, therefore the results are adequate for studying the kinematics and energetics of star forming regions, for instance. These capabilities of the instrument make it possible to contribute significantly to the science of modern astrophysics. The major science aims of *HIFI* are to study the following themes [88]:

- water trail in the universe,
- molecular universe,
- CII and OI in star forming regions,
- interstellar medium and star forming in galaxies,
- diffuse interstellar medium in the Milky Way, and
- comets.

The following section briefly describes these science topics and the required instrument capabilities.

1.1 Science aims of HIFI

The *HIFI* instrument is intended to help answer questions like water trail in the universe, especially in star forming regions. Although, missions like SWAS and ODIN have already gathered some information from water, details are still unavailable. From the existing scientific data, it is known that water is a key element in interstellar chemistry and serves as a reservoir of elementary oxygen. In addition, water plays a significant role in the energy balance of the interstellar and circumstellar regions as well as star and planet formation regions, hot cores, in winds from dying stars, around active galactic nuclei, comets, and planetary atmospheres.

HIFI is going to explore the composition of the interstellar medium in star forming regions. The millimetre and submillimetre astronomy is required mainly to understand the physical and chemical properties of the interstellar mediums (*ISM*) of galaxies. An important aspect is the cyclic interrelation of stars and dense molecular clouds. The molecules of the *ISM* will be excited and ionized by stars producing a high complexity of atomic- and molecular spectral lines at the millimetre and submillimetre wavelength. The composition of the *ISM* can be also changed through supernova explosions of dying stars resulting in heavy elements in the cloud that initially consisted of mainly light atoms, like hydrogen and helium. The rotational spectra of these heavy elements are purely explored, especially at *THz* frequencies. The other important theme for *HIFI* is that stars and planetary systems as well, are formed through gravitational collapse of interstellar molecular clouds, therefore it is essential to deepen our knowledge in this field. The complex interaction between stars and the *ISM* drives the evolution of galaxies like the *Milky Way* and others.

HIFI will make studies of complex organic molecules, which can help to understand the evolution of life on the Earth and possibly on other planets in the universe. Furthermore, the instrument is going to contribute to the redshifted [CII] line survey researches at $158\mu\text{m}$, which is a direct probe of star formation. The [CII] 158 micron line is the most dominant one for gas cooling in star forming regions, and because of the high luminosity of the line, conclusions can be drawn to the evolution of the early universe.

HIFI is going to make studies about the pressure of the interstellar gas in our galaxy, the *Milky Way*, and may answer the dynamics of diffuse interstellar mediums. The satellite instrument is going to observe dying stars, hot cores, comets, and planets with their atmospheres, trying to clear up their origin. To make these observations possible it was decided to establish six frequency bands that cover the required frequency range needed for the science themes of the *HIFI* project. In Table 1-1 the proposed band coverage is listed against the main science drivers [88]:

| | HIFI Bands | | | | | |
|-----------------------|------------|---------|---------|----------|-----------|-----------|
| Number of band | 1 | 2 | 3 | 4 | 5 | 6 |
| Frequency range [GHz] | 480-640 | 640-800 | 800-960 | 960-1120 | 1120-1250 | 1410-1910 |
| Water trail | • | | | • | • | • |
| Molecular Universe | • | • | • | • | • | • |
| ISM in galaxies | • | • | • | • | • | • |
| [CII] lines | • | • | • | • | • | |
| Star formation | • | • | • | • | • | • |
| Diffuse ISM | • | | • | • | | • |
| Comets | • | | • | • | | |
| Planets | • | • | | • | • | • |

Table 1-1 Demanding frequency coverage of the HIFI science drivers

The technical demands of the satellite observatory must comply with the science topics listed above. These requirements are:

- high sensitivity (for [CII] survey it is approx. 4 Jy km/s or $7 \times 10^{-17} \text{ erg cm}^{-2} \text{ s}^{-1}$ at 500GHz and 70 Jy km/s or $3 \times 10^{-15} \text{ erg cm}^{-2} \text{ s}^{-1}$ at 1.25THz),
- high spectral resolution (0.1 -0.5 km/s),
- large bandwidth (4GHz),
- high spectroscopic stability,
- good pointing, tracking,
- high calibration accuracy (10% absolute or 3% as a goal), and
- flexible observing strategies like beam switch, frequency switch, raster mapping, on-the-fly (OTF), dual beam switch, chop, line scanning, etc.

1.2 Orbit properties

The Herschel spacecrafts will be put into large amplitude Lissajous orbits around the second Lagrangian point L_2 in the Earth/Moon - Sun system, as shown in Figure 1-1, [35], [36]. Such a collinear libration point (L_1) has already been considered and used for other space missions like SOHO¹³ and ISEE-3¹⁴ [12]. The advantages of orbits around the L_2 and L_1 points are that eclipses will not interrupt the observation, because the Earth and the Sun remain relatively together as seen from the spacecraft, and the radiation and thermal environment is favourably stable. The disadvantages of these orbits are that the transfer of the satellite takes a long time, the communication must travel large distances, 1.5million km (1%AU) and there must be small orbit corrections taken place frequently to guarantee the stabile Lagrange orbit.

¹³ Solar and Heliospheric Observatory

¹⁴ International Sun-Earth Explorer 3

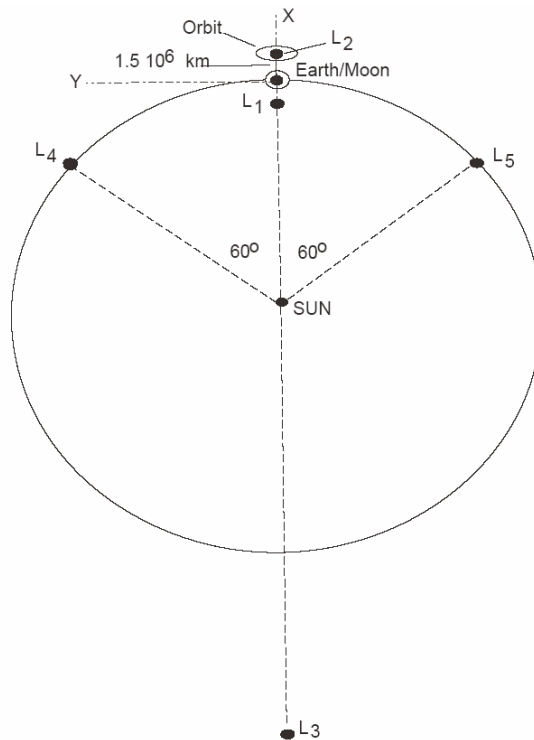


Figure 1-1 Libration points in the Sun-Earth/Moon system. The L_2 point, used for Herschel, lies approximately 1.5 million km from the Earth in the opposite direction of the Sun. The satellite moves on a quasi-periodical orbit, which is at the gravitational equilibrium of the Sun-Earth/Moon system

The Lissajous orbits are harmonics oscillations with small phase changes. Choosing the initial phase angle and applying small manoeuvres it can set an orbit where the satellite will not be eclipse during the mission. There are additional manoeuvres necessary to keep the spacecraft on orbit because of gravitational perturbation of other planets in our solar system and the Sun, and because of the solar radiation pressure [37]. Note, that the large mass of Herschel is responsible for the large amplitude of the Lissajous orbit. The launch is proposed to take place in 2007/2/15 near the equator at Kourou, which results in the consequence that the orbits around the L_2 libration point lie near the ecliptic plane. The transfer and the Lissajous orbits of Herschel can be seen from two projection planes in Figure 1-2 [16].

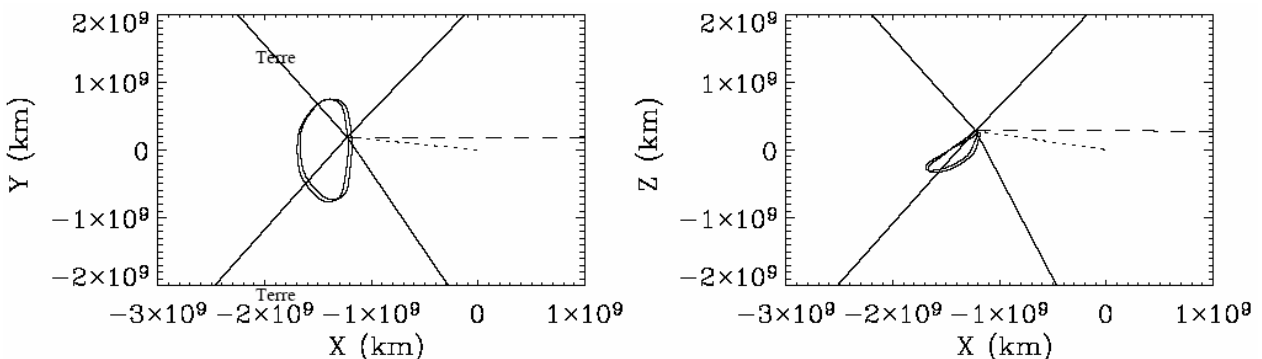


Figure 1-2 Lissajous orbits of Herschel in the first two weeks period. In the picture the direction of the Earth and the Sun are marked with dashed and dotted lines respectively.

The Planck satellite will have slightly different orbit with smaller amplitude than Herschel because of its sky scanning strategy and the constraints on the Sun to Earth viewing angle. Therefore, the two spacecrafts will separate approximately 133 minutes after launch [34].

The estimated lifetime of Herschel is 3.5 years from launch, which will be mainly limited by the finite quantity of the cooling material of liquid helium. Calculating that the transfer to orbit will take half a year, the useful lifetime is reduced to 3 years. The telecommunication between the satellite and ground station, which will be in Perth, will produce an additional observation time reduction. The downlink of the scientific data packages will take up to 3 hours daily, and during these periods the instrument computer will be not able to observe or may conduct only limited observations. Additional observation time losses will be caused by the not immediate intervention into the system operation in case of a failure when the telescope collects unusable data.

2 The Herschel satellite

2.1 Launcher

Within the ESA cornerstone mission the Herschel and Planck satellites will be launched with a single ARIANE5 ESV-type launcher in stacked configuration, as shown in Figure 2-1 [40].

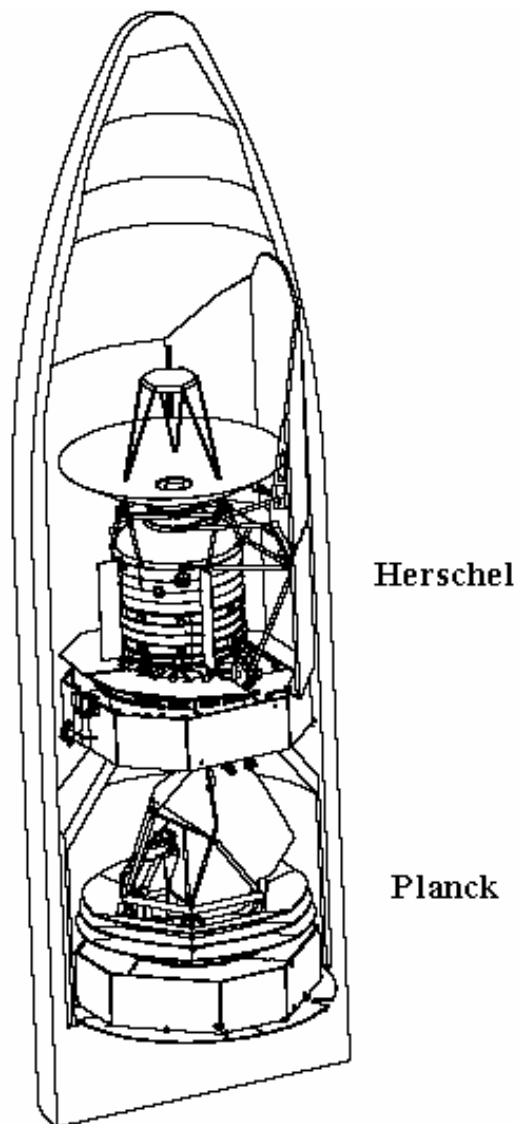


Figure 2-1 The Herschel/Planck satellites in stacked arrangement

The rocket is designed to be able to inject the large payloads of the two satellites; it allows for a maximum in-orbit mass of 5310kg.

2.2 Herschel structural construction

Structurally the Herschel satellite can be divided into two components:

- the Herschel Payload Module (HPLM) and
- the Herschel Service Module (HSVM).

2.2.1 The Herschel Payload Module

2.2.1.1 The telescope

The Herschel Payload Module comprises a 3.5m diameter axial-symmetric Cassegrain telescope, shown in Figure 2-2, and the helium cryostat. The telescope consists of a parabolic primary and a hyperbolic secondary mirror, the mirror support structures, baffles and the contamination release system.

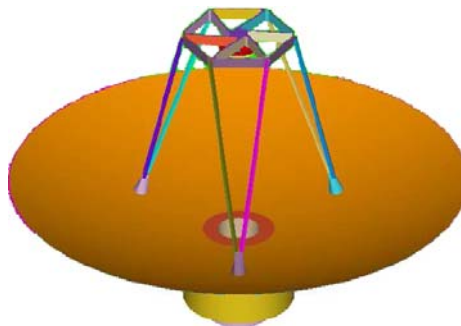


Figure 2-2 Model of the 3.5m diameter axial-symmetric Cassegrain telescope and the secondary mirror supporting structure [52]. The telescope is designed for the operating wavelength range of 60-670 μ m.

The useful aperture of the primary mirror is less than its total mechanical diameter. On one hand, the 308.1mm secondary mirror is undersized relative to the primary mirror. This results in an effective diameter of 3.28m of the primary mirror. On the other hand, there is a 560mm hole in the primary mirror, where the beam is coupled out to the focal plane unit, and there is an obscuration caused by the hexapod supporting structure of the secondary mirror. The overall geometrical blockage caused by the sub-reflector and its supporting structure shows up twice in the beam path. Once when the sky beam enters the primary mirror, second when the beam is reflected from the primary mirror. The geometrical blockage, which is 7.7% of the full aperture of the primary mirror [53], reduces the beam efficiency of the telescope.

The expected total surface error of the primary mirror, taking cool down distortions also into account, is less than 3 μ m rms [3]. Compared to the perfect mirror, this results in antennae efficiency degradation, especially at the highest frequency band (5.5% at 1.9THz [52]). The effective focal length of the mirror is 28500mm at the operating wavelength range of 60-670 μ m [40].

2.2.1.2 The helium cryostat

The cryostat, shown in Figure 2-3, provides a thermal- and optical interface between the telescope and the focal plane units. Inside the cryostat is the Focal Plane Unit (FPU) of the three astronomical instruments HIFI, PACS and SPIRE mounted on the common Herschel Optical Bench (HOB). Moreover, the cryostat accommodates the Local Oscillator Unit (LOU), the beam folding optics and waveguides towards the Herschel Service Module.

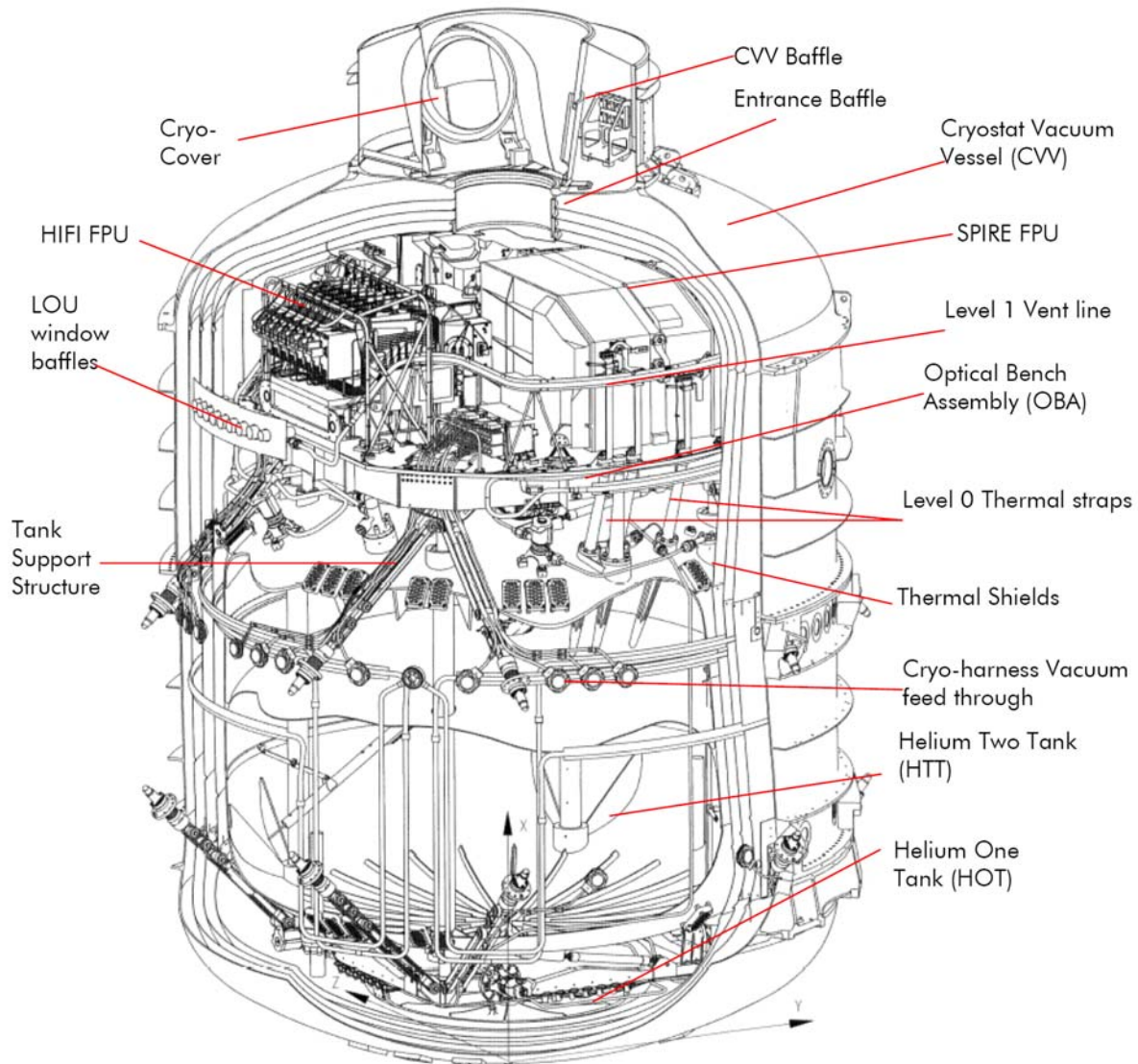


Figure 2-3 The Herschel Cryostat [40]

The FPU contains the relay optics assembled with the SIS and HEB mixers, the optical combiners, preamps, IF amplifiers, power combiners, chopping mechanisms and the calibration sources. The mixers are cooled down to 1.7K, which guarantees the low noise and high sensitivity performance. The first IF amplifier chain and the receiver optics work at 20K in order to keep the additional noise level low. In the next 120-150K stage the second IF amplifier chain and the local oscillators operate. The last IF power amplifiers, the correlators (HRS), the acousto-optical spectrometers (AOS) and the control electronics operate at ambient temperature, outside the cryostat (c.f. next Section).

2.2.2 The Herschel Service Module

On the Herschel Service Module, seen in Figure 2-4, are placed the following spacecraft subsystems [40]:

- the Structure Subsystem,
- the warm units of HIFI, PACS, and SPIRE,
- the Thermal Control System (TCS),
- the Attitude Control and Measurement Subsystem (ACMS),
- the Propulsion System,
- the Telemetry, Tracking and Command Subsystem,
- the Command and Data Management Subsystem,
- the Power Control Subsystem,
- the Solar Cell Array, and
- the Harness.

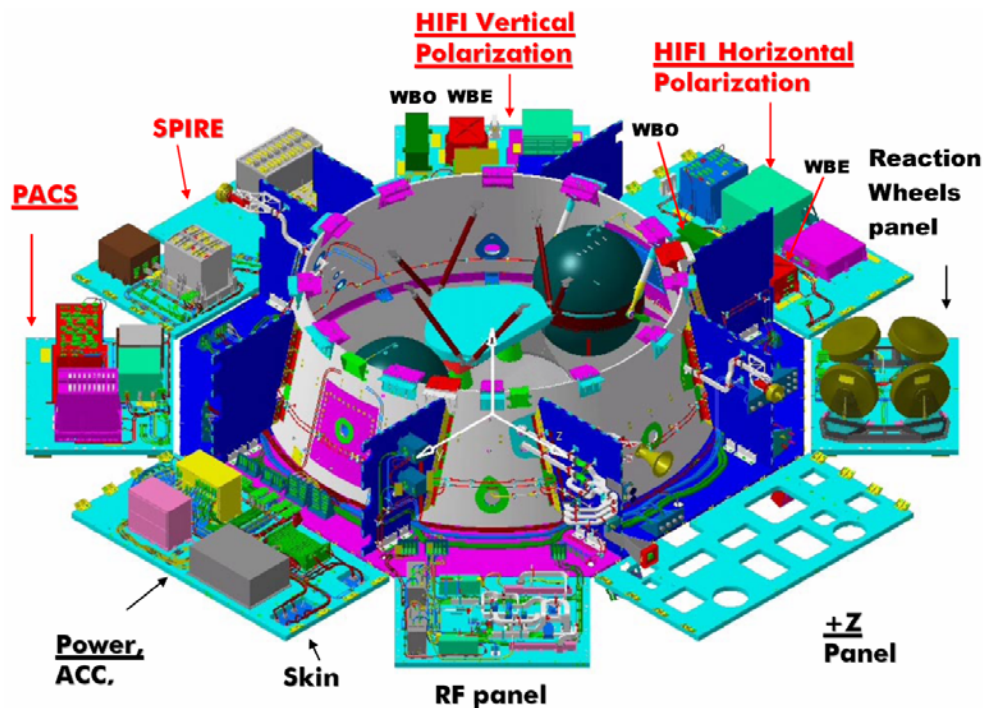


Figure 2-4 The Herschel Service Module consisting of the spacecraft subsystems. The eight panels of the HSVM will be turned up during the launch and transfer to the orbit.

The *Structure Subsystem* of the HSVM, seen in Figure 2-4, carries all the warm units of the three instruments (HIFI, PACS and SPIRE), the avionics, and the sunshield, which protects the telescope from the direct radiation of the Sun and minimize the thermal fluctuations of the primary and secondary mirrors. On two panels of the HSVM structure are mounted the two *Wide Bandwidth Array Acousto-Optical Spectrometers*, which comprises the WBO optical units and the WBE electrical units developed by KOSMA¹⁵.

The *Thermal Control System* regulates the temperature of the interface plates required for the proper operation of the subunits. For instance, the operation temperature range of the WBO is

¹⁵ Kölner Observatorium für Submillimeter Astronomie

2.3 Heterodyne receiving and the HIFI instrument

between $+5^{\circ}\text{C}$ and $+15^{\circ}\text{C}$ with a maximum gradient of $0.3\text{mK}/\text{sec}$. If the thermal I/F does not maintain this range the instrument would work with reduced resolution and stability.

The *Attitude Control and Measurement Subsystem* is a composition of altitude sensors, actuators and electronics with its onboard software that controls the altitude of the satellite during the whole mission.

In order to keep the satellite in the right position and to be able to realize small orbit corrections modifications and navigations, a *Propulsion System* is equipped on board. To the system belong the propellant storage tanks, valves, pipes and pressure thrusters. All of this equipment is driven by the Attitude Control System.

The communication between the Earth station and the spacecraft is managed by the *Telemetry, Tracking and Command Subsystem*. Here there are radio frequency signals transmitted and received up to 3 hours a day carrying the scientific and housekeeping data packages.

Before the scientific and housekeeping data are transceived, the *Command and Data Management Subsystem* collects, validates, decodes, and encodes them. After processing, the unit distributes the commands for the other instruments.

The *Power Control Subsystem* monitors, and distributes the electrical power produced by the solar cells. The unit consists of safety circuits, which prevents the consumers from receiving higher current and voltage than permitted.

The *Solar Cell Array*, which is assembled together with the sunshield on the side of the spacecraft, supplies all the electrical equipments on the satellite.

2.3 Heterodyne receiving and the HIFI instrument

The *HIFI* instrument uses the heterodyne signal processing technology. This allows astronomical observations at high frequencies, where low noise amplification is impossible. The principal of the heterodyne receiving is that the high frequency electromagnetic radiation is down converted to lower frequencies, where the signal processing is easier [33]. The down conversion is attained by using a very stable, monochromatic signal, the local oscillator (LO) signal, and a mixer. The mixer multiplies the astronomical signal with the LO signal, producing an output having the difference frequency of the two input signals. The output signal or Intermediate Frequency (IF) contains the same spectral information as the astronomical signal itself, but at much lower frequency:

$$A_S \cos(\omega_S t) A_{LO} \cos(\omega_{LO} t) = \frac{A_S A_{LO}}{2} \{ \cos(\omega_S + \omega_{LO}) \cdot t + \cos(\omega_S - \omega_{LO}) \cdot t \} \quad (1.1)$$

Further advantage of the heterodyne detection is that the local oscillator (low noise) amplifies the intensity of the weak astronomical signals. A major drawback is that the down conversion process results in the same IF frequency band if the input signal was mirrored to the LO signal. The mirrored frequency band is also called the image sideband. The IF band is therefore a combination of the signal and image sidebands. This has consequences for science planning, because the desired line in the signal sideband may be blended with unwanted lines from the image sideband. Thus, the frequency deconvolution of the observed line must be

performed in software. Other disadvantages of the system are that the receiver needs mixers working at very high frequencies, the mixers themselves contribute to the noise level of the astronomical signal, there is a considerable signal loss during the mixing process, and the system requires extremely stable high frequency local oscillators.

The functional diagram of the HIFI instrument is shown in Figure 2-5 [95].

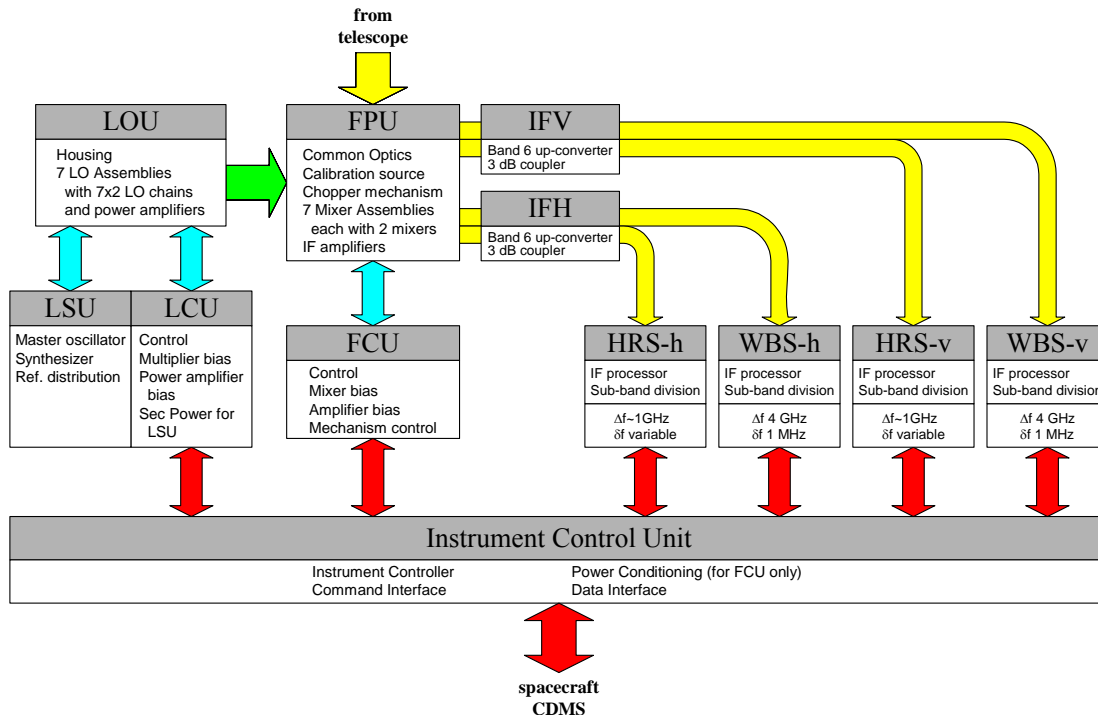


Figure 2-5 Functional diagram of the HIFI instrument

The local oscillator signal is generated in LO sub-bands consisting of a chain of frequency doublers or triplers and power amplifiers. The master signal of the local oscillator is produced in the Local oscillator Source Unit (LSU), and the Local oscillator Control Unit (LCU) regulates the components of the LOU. In the Focal Plane Unit (FPU), the signal from the sky is combined with the LO signal and fed into the mixers, where the mixing process is performed for the horizontal and vertical polarizations. At the low frequency (below 1250GHz) bands of the HIFI instrument, SIS tunnel junction mixers are used. They consume very little LO power and their sensitivity is very high. On the high and low sections of band 6, hot-electron bolometers (HEB) are used, providing the required high working frequency and sensitivity.

The HIFI instrument is capable of observing horizontally and vertically polarized signals in parallel. Thus, the backend system consists of two IF signal processors, where the IF signals coming from the mixers are amplified and converted to the input frequency bands of the spectrometers. Onboard Herschel are two different spectrometers: two *Wide Band Spectrometers* (WBS) [76] and two *High Resolution Spectrometers* (HRS), according to the two polarization directions. The WBS has 4GHz bandwidth, and spectral resolution of 1MHz , while the HRS has 2GHz bandwidth, and its spectral resolution is adjustable: 135 , 270 , 539 and 1078kHz , in varying bandwidths. The Instrument Control Unit (ICU) controls the individual units of the receiver system.

3 Spectrometer requirements

Bandwidth

The spectrometers, considered as backends for submm heterodyne receivers, must deal with various technical and instrumental performance requirements. The exploration at submm and far-infrared wavelengths creates a great demand for spectrometers with large bandwidth. For instance, observations of Doppler-broadened atomic or molecular transitions in galactic sources require a velocity coverage of 600km/s , which corresponds to approximately 4GHz bandwidth at 2THz . Similarly, for pressure broadened line observations in the Earth or other planetary atmospheres, wideband spectrometers are indispensable.

Frequency resolution

In general, with increasing frequency of the observed line the required frequency resolution decreases (the ratio of the resolution and observed frequency is practically constant). Taking into account that on HIFI the observations are going to be performed from 480GHz up to nearly 2THz frequencies, 1MHz resolution will be appropriate in almost all cases.

Efficiency

Since the costs of the observing time of satellite missions are enormous, it is important to conduct fast and efficient observations. This requires real time spectrometers with maximum efficiency.

Signal-to-Noise ratio

Generally, the observed signals of radio astronomical sources are very weak; their intensities are small compared to the background noise. The only possibility to increase the Signal-to-Noise ratio is to perform long integration on the source. The signal itself is proportional to the integration time, while the noise background, which is characterized as white noise, increases only with the square root of the integration time. So long as the statistical behaviour of the background noise is white noise dominated, the S/N ratio can be improved by integration time. For heterodyne receivers the S/N ratio is generally given by the radiometer equation [54]

$$\frac{S}{N} = \frac{T_{\text{Signal}}}{T_{\text{Sys}}} \sqrt{B_{fl} \cdot t_{\text{int}}} , \quad (3.1)$$

T_{Signal} – signal temperature (equivalent temperature of a black body),
 T_{Sys} – system temperature,

- B_{fl} – fluctuation bandwidth of the spectrometer (c.f. Section 7.9),
 t_{int} – integration time.

Depending on the fluctuation bandwidth of the spectrometer and the system temperature, the radiometer formula expresses the necessary integration time within which a required S/N ratio is reached. During an observation, the upper limit of the achievable maximum S/N ratio is determined by the noise contribution of the system. This can be affected by instabilities of the receiver system (e.g. through thermal drifts) or by the Earth atmosphere (at ground-based observations). From the radiometer formula it also follows that increasing the resolution of the spectrometer results in a S/N ratio reduction. Thus, the resolution should be adapted to the line widths of the observed lines.

Spectroscopic stability

In case of white noise and idealized operation of the spectrometer, the radiometric noise decreases according to the radiometer equation with the square root of the integration time. Instabilities in the instrument can occur due to thermal fluctuations, electrical drifts or mechanical influences that degrade the ideal functioning of the spectrometer. The spectroscopic stability of the device is characterized by the maximum integration time, over which the background noise decreases, i.e. the S/N ratio increases. Further integration on the source results in increased noise of the observed signal. The standard method to determine the stability performance of an instrument is the Allan variance measurement, which is discussed in Section 10.9.1. So long as the system noise behaves as white noise, the spectroscopic Allan plot shows a decrease of noise with the slope of -1. Due to system drifts, the slope of the curve increases and finally becomes positive. The minimum of the Allan plot (Allan minimum time) indicates the maximum integration time when system drifts become equal to the background noise, and therefore it is a measure of the stability.

The allocated mass of the HIFI instrument is 189kg, and the whole Herschel satellite is rather heavy, weighing around 3.25 tonnes. To move such a big mass during an observation is time consuming, therefore it has a direct consequence for the required stability of the instrument and its components. In case of observations of galaxies, for instance, the telescope is needed to move to an off position, because of calibration reasons. In this case, the slewing time is approximately 3 minutes within which the instruments of the satellite must be stable. Thus, the required stability for the instruments of HIFI is a few hundred seconds. Such a long time stability can only be attained with a careful mechanical, optical, and electrical design of the instrument, moreover a very stable thermal environment is required.

Total power stability

For absorption line studies, for instance, accurate continuum levels are required, thus the total power stability of the instrument is important. The total power stability requirement at instrument level is 2 seconds.

Noise dynamic range

From the noise performance point of view, it is essential that the spectrometer does not increase the system noise significantly. Since the detection efficiency of the spectrometer depends on the additional noise added by the final detector (CCD in an AOS), its noise contribution is crucial. Thus, this noise contribution, which is also function of the detector efficiency, determines the usable intensity range of the input signal. The dynamic range where

the system noise contribution to the radiometric noise remains below 1dB defines the noise dynamic range of a spectrometer. This value determines the minimum input signal intensity where a measurement can be accomplished. Therefore, it is also important that spectrometers have as large noise dynamic range and high efficiency as possible.

Power linearity

In case of sources with continuum signals or during measurements like position switching where large offsets are present in the observed signals, good linearity of the instrument is required in order to prevent the introduction of baseline distortions in the measured data and to achieve good calibration accuracy.

Physical properties

For satellite missions the physical aspects of the instruments are of special interests: these are the *small size, low weight, but high mechanical stiffness, low power consumption and high reliability* of the components.

3.1 Different spectrometer types used for submm astronomy

The science demand of the HIFI project for high resolution is fulfilled by digital auto-correlators (HRS) working at moderate bandwidths ($<1\text{GHz}$, variable), while the large bandwidth is covered by applying wide bandwidth (4GHz) hybrid acousto-optical spectrometers (WBS). In the following sections, the commonly used spectrometer types are briefly discussed and their advantages and disadvantages are compared.

Filterbanks

A classical spectrometer type is the widely used filterbank. It consists of a large number of narrow bandpass filters; their shape and bandwidth can be designed to any desired form. The single frequency detectors square the input amplitude, so the output signal is proportional to the signal intensity. The filters can be constructed by using passive electrical components, but applying integrated circuits is also feasible. Filterbanks are working successfully at many ground base observatories, like the IRAM 30m telescope ($2\times 1\text{GHz}$ bandwidth, 4MHz resolution) [61], SMTO¹⁶ near Tucson, AZ or even on satellite missions, like the MLS¹⁷ instrument on UARS¹⁸. However, a major drawback is the enormous complexity of the filter system if a bandwidth of several GHz with a few MHz resolution is desired. Moreover, such instruments have large size and weight, and relatively high electrical power consumption. The stability of the system could be adequate, but needs a very good temperature control system. Thus, for satellite applications where large number of frequency pixels is required, filterbanks are not an appropriate choice.

Digital auto-correlators

In auto-correlator spectrometers the input signal is digitized, then delayed in a sequence of discrete steps. The delayed samples are multiplied with the undelayed input signal and the products are integrated separately for each of the delay lines. The resulting auto-correlation

¹⁶ Submillimeter Telescope Observatory

¹⁷ Microwave Limb Sounder

¹⁸ Upper Atmosphere Research Satellite

function is Fourier transformed to get the power spectrum. Since the main part of the signal processing is done in the time domain, the input signal can be digitized with few quantisation levels (usually with 1.5 or 2 bit samplers) [17], therefore high-speed digital electronics must be used. The bandwidth of a correlator is proportional to the sampling frequency

$$B = \frac{1}{2\delta t}, \quad (3.2)$$

where δt is the sampling time of the A/D converter. The number of the delays (lags) determines the bandwidth δf of a single frequency channel

$$\delta f = \frac{1}{2N\delta t}. \quad (3.3)$$

The real resolution of the instrument depends also on the weighting function used for the deconvolution. Due to the rapid development of high-speed samplers it seems possible to fabricate auto-correlators with large bandwidths (2GHz or even higher) with a resolution of 250kHz, but they are still only available as hybrid systems [23]. Despite their promising large and variable bandwidth, high resolution, good stability and high reliability; the relative high power consumption, due to the fast samplers and the complexity of the system, is still a problem to be solved. Further drawbacks are that the software is rather complex and the instrument has a relatively low efficiency (80% at 1.5 bit) compared, for instance, to an acousto-optical spectrometer. Nevertheless, auto-correlators are widely used at many ground-based observatories like JCMT¹⁹, SMA²⁰, EVLA²¹, GBT²², IRAM, APEX²³ and one hybrid instrument with moderate total bandwidth of 800MHz is flying onboard Odin.

Chirp transform spectrometer

In a Chirp Transform Spectrometer (CTS) the input HF signal of the heterodyne receiver is mixed with a swept (chirp waveform) local oscillator signal. After mixing, one of the resulting sidebands is fed into a compressor chirp filter (surface acoustic wave filter) that has the inverse slope of the multiplier chirp signal (dispersion). The process effectively causes a compression of the input signal with frequency dependent delay. Thus, the various frequency components of the input signal leave the system as series of consecutive pulses. After separation of the frequency components of the local oscillator, the output signal of the dispersive filter is square law detected and finally digitized. Since the output signal has the same bandwidth as the input signal, the sampling rate must be very high to achieve the maximum bandwidth of the instrument ($\delta t=1/(2B)$). Actually, the CTS is the fastest of all spectrometers, because only one “detector” is used for all frequency channels, there is no read out time, and it does not require integration before the detection. The resolution of the device is determined by the chirp time $\delta f=1/T$. The latest improvements with applying the fastest samplers allow a frequency bandwidth of 205MHz and a resolution of 50kHz [32]. A further advantage of the instrument is that it has large dynamic range, small weight and compact design. Nevertheless, large bandwidths have not been attained so far.

¹⁹ James Clerk Maxwell Submillimetre Telescope

²⁰ Submillimetre Array, Manua Kea, Hawaii

²¹ Expanded Very Large Array

²² Green Bank Telescope

²³ Atacama Pathfinder Experiment

Digital FFT spectrometers

In a digital Fast Fourier transform spectrometer the input signal amplitude is digitized with a high speed A/D sampler, then the fast Fourier transformation of the signal is performed in real time by using FPGA²⁴. Main advantages of the spectrometer are the relatively large bandwidth, high resolution, high efficiency, large dynamic range, low weight, small size and the absence of optical or mechanical components. Achieving large bandwidths with FFTs is still a challenge, but the rapid development of the digital technology gives hope for their applications. FFTs are in operation at the Effelsberg Radio Observatory and ETH Zürich, and will be operated at KOSMA. The latest achievements at ETH Zürich with the ARGOS²⁵ instrument are 1GHz frequency bandwidth, 61kHz resolution (16384 channels) and 50dB dynamic range [45].

Acousto-optical spectrometers

The principle of the acousto-optical signal processing is based on the deflection of light on an ultrasonic wave in an acousto-optical material [89]. The high frequency (*HF*) input signal is coupled into the acoustic crystal by using piezoelectric transducers. Through the photo-elastic effect, the ultrasonic wave produces a periodic variation of the refractive index, which can be considered as a thick phase grating. Illuminating the phase grating with a monochromatic light source, a portion of the light beam is deflected. Since the grating constant is proportional to the input frequency, the deflection angle is dependent on the input frequency. The deflected laser beam is then imaged onto a CCD line detector, where each pixel represents a single frequency component of the input signal. The resulting analogue signal of the CCD is read out and digitally converted in the electronics unit. The bandwidth of the instrument depends on the material constants of the deflector (c.f. Section 4.3, Eq. 4.28), but it varies typically between 40MHz and 3GHz. With special zoom optics, there have even been variable resolution devices constructed [79]. The achievable resolution of an AOS lies between 30kHz and a few MHz depending on the bandwidth (30MHz – 3GHz) and the number of resolvable spots (usually around 1000). The small number of components allows a compact design with small weight and high reliability, and, due to the slow readout time, the power consumption of the instrument is very low. The stability of the device depends on its thermal environment, but a few 100 seconds of integration time is realizable. The fabrication of hybrid deflectors makes it possible to build very compact hybrid spectrometers that can be used either for array receiver systems providing 4x1GHz bandwidth or as wide bandwidth spectrometers by combining the single channels into one 4GHz band. In comparison with 4 single 1GHz AOSs the advantages of an array AOS are the less complexity, smaller weight, smaller size, higher reliability, lower power consumption, and lower costs. Furthermore, since the thermal, mechanical and optical conditions are the same for all bands, the frequency response of the four 1GHz bands is identical, thus, identical frequency calibration is guaranteed. The stability of the bands is very similar and in case of relative short integration times; there is no platforming effect recognizable. The disadvantage of the hybrid solution is that rather complicated IF frequency processing is needed to split the 4GHz bandwidth into the input frequency range of the four 1GHz bands. Acousto-optical spectrometers are widely used at many ground-based telescopes (KOSMA, CSO, SEST²⁶, MARS²⁷, AST/RO²⁸), a 1.4GHz bandwidth AOS has been successfully operating aboard the SWAS mission since December

²⁴ Field Programmable Gate Arrays

²⁵ Astronomical Receiver for Gazing Outer Space

²⁶ Swedish-ESO Submillimetre Telescope

²⁷ Mérida Atmospheric Research Station, Venezuela

²⁸ Antarctic Submillimeter Telescope and Remote Observatory

1998 [50], [86], and several 4GHz bandwidth array-AOSs are going to be operated on the airborne SOFIA²⁹ observatory.

²⁹ Stratospheric Observatory For Infrared Astronomy

4 Acousto-optical signal processing

For phase- and amplitude modulation of light, there is a wide variety of possibilities. Among the electro-optical, magneto-optical or liquid crystal modulators, devices based on the acousto-optical effect are the most commonly used instruments for spectral analysis. The principals of these modulators are based on the acousto-optical interaction that was discovered first theoretically by Brillouin in the 1920s and later experimentally by Debye et al. [20].

The principle of the acousto-optical effect is that in an optically transparent material the light propagating through the medium interacts with the excited ultrasonic wave. The sound wave mechanically deforms the crystal lattice: at the nodal points of the acoustic wave the crystal lattice is at standstill, whereas it is vibrating with the acoustic frequency. These kinds of density oscillations give rise to periodic changes in the dielectric constant, and hence in the refractive index. This phenomenon is known as the elasto-optical Pockles-effect. The structure of the periodically changing refractive index acts as a phase diffraction grating on which the incident beam of light is diffracted and modulated. Depending on the diffraction regime, two special cases are distinguished: the Raman-Nath diffraction, which can be observed in case of normally incident light to the ultrasonic wave, small interaction lengths and low acoustic frequencies. The diffraction pattern can be compared with a usual phase grating; the angular positions of the diffraction orders are given by

$$\sin \vartheta_n = \frac{n\lambda}{\Lambda}, \quad n=0, \pm 1, \pm 2, \dots, \quad (4.1)$$

where λ is the wavelength of the incident light and Λ is that of the ultrasonic wave. The frequencies of the diffracted orders are Doppler-shifted by $\omega_i = \omega + n\Omega$.

The other regime of the acousto-optical diffraction is the Bragg diffraction. It occurs at higher sound wave frequencies, for not normal incidence of light and large interaction length. In this case, only one diffraction order can be observed, either the first positive or negative order. Physically the interaction zone can not be considered as a simple phase grating because both the phase and the amplitude will be modulated by the acoustic wave. The interaction in the active zone becomes three-dimensional and acts as a thick phase grating. With destructive interferences, there is a selective diffraction of the incident beam and therefore only one diffraction order exists. The effect can only be observed at one particular angle, the Bragg angle. The two types of diffraction can be characterized by the Debye-Sears ratio [20]

$$Q = \frac{2\pi\lambda L}{n\Lambda^2}, \quad (4.2)$$

where

λ – wavelength of the incident beam in vacuum

$\Lambda = v/f$ – wavelength of the acoustic beam

v – acoustic velocity

f – acoustic frequency

L – interaction length in the crystal

n – refractive index of the crystal

It has been established experimentally that for $Q \leq 0.3$ Raman-Nath diffraction is observed, whereas for $Q \geq 4\pi$ Bragg diffraction is visible [57].

Theoretically, the acousto-optic interaction in anisotropic media can be described by the Maxwell equations in the absence of currents and free charges

$$\text{rot}\mathbf{E} = -\partial\mathbf{B}/\partial t \quad (4.3)$$

$$\text{rot}\mathbf{H} = \partial\mathbf{D}/\partial t \quad (4.4)$$

$$\text{div}\mathbf{D} = 0 \quad (4.5)$$

$$\text{div}\mathbf{B} = 0 \quad (4.6)$$

$$\mathbf{D} = \varepsilon\mathbf{E}. \quad (4.7)$$

The sound wave causes perturbations in the dielectric constant of the medium

$$\varepsilon = \varepsilon_0 + \Delta\varepsilon \sin(\Omega t - Kx) \quad (4.8)$$

and in the polarization of the incident light

$$\mathbf{P} = \mathbf{P}_0 + \Delta\mathbf{P}, \quad (4.9)$$

where Ω , K and x denote the angular acoustic frequency, the acoustic wave number vector and the propagation direction of the ultrasonic wave, respectively. The perturbation of the polarization $\Delta\mathbf{P}$ can be expressed by [19]

$$\Delta P_i = \Delta\varepsilon_{ij}E_j = -1/2\varepsilon_{im}\varepsilon_{in}p_{mnkl}s_{kl}E_j, \quad (4.10)$$

where p_{mnkl} is the photo-elastic tensor, s_{kl} is the acoustic strain in different directions and the Einstein summation convention is used. Using these relations, the system of equations simplifies to the so called polarisation dependent wave equation in perturbed medium

$$\nabla^2\mathbf{E} = n(x,t)\partial^2\mathbf{E}/\partial t^2 + \mu\partial^2(\Delta\mathbf{P})/\partial t^2, \quad (4.11)$$

where we applied the relation between the refractive index and the dielectric constant

$$n(x,t) = \sqrt{\varepsilon(x,t)}. \quad (4.12)$$

The solution of the wave equation yields the coupled, phase matched periodic functions in terms of the electric field and polarization components, respectively. Since the refractive

indices in eq. (4.12) are functions of the incident wave directions, an explicit general solution of (4.11) can be found only in particular cases.

From the momentum conservation law it follows that the sum of the diffracted (k_d) and acoustic (K) wave number vectors are equal to the incident (k_i) wave vector

$$k_i = k_d + K . \quad (4.13)$$

In other words, at a certain incidence angle of the light wave the triangle consisting of these three vectors must be complete. The special condition of the wave vectors is known as the Bragg condition and the angle of incidence the Bragg angle. Figure 4-1 shows the general anisotropic case of the Bragg diffraction for LiNbO_3 . The ultrasonic wave is always divergent due to the finite dimension of the transducer. Therefore, the momentum conservation is always fulfilled within the relatively wide range of divergence of the acoustic wave and corresponds to a large bandwidth of the Bragg cell. By choosing materials that offer low acoustic attenuation and by applying the tangential phase matching technique - where the acoustic wave vector is nearly orthogonal to the diffracted light vector - bandwidths of 2-3GHz can be obtained [13].

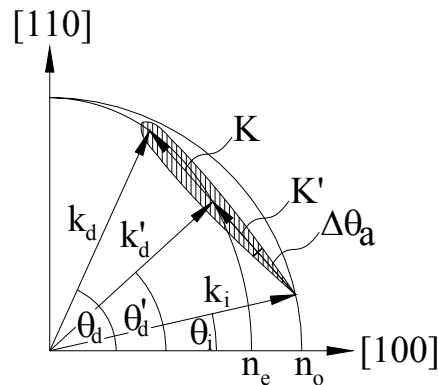


Figure 4-1 Interaction geometry of the anisotropic Bragg diffraction for LiNbO_3 . The case of an ultrasonic wave perpendicular to the optical axis is of particular interest. There the relative small divergence of the acoustic wave vector results in a significant large range of the diffraction angle and therefore in a high bandwidth of the device.

The diffracted light has maximum intensity when the phase matching is exactly fulfilled. In birefringent crystals, this occurs at two different acoustic frequencies (\mathbf{K} and \mathbf{K}' wave vectors in Figure 4-1). Near these frequencies (quasi-conservation of momentum) the efficiency is smaller, resulting in the typical bandpass shape of an anisotropic Bragg deflector, as shown in Figure 4-2.

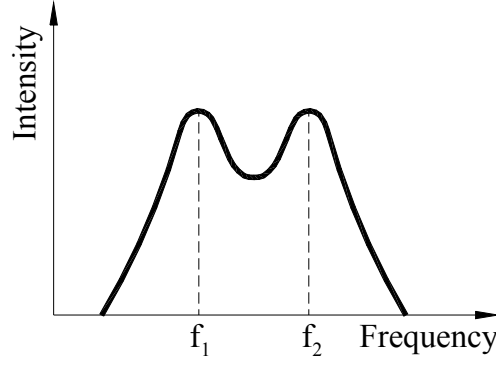


Figure 4-2 Frequency bandpass function of an anisotropic acousto-optical deflector. The exact phase matching occurs at two acoustic frequencies resulting in the double-peaked frequency response.

4.1 Diffraction angles

In case of the Bragg condition, when eq. (4.13) is valid, the incidence and diffraction angles can be expressed as functions of the acoustic frequency [72]:

$$\sin \vartheta_i = \frac{\lambda f}{2n_o v} \left[1 + \frac{v^2}{f^2 \lambda^2} (n_o^2 - n_e^2) \right], \quad (4.14)$$

$$\sin \vartheta_d = \frac{\lambda f}{2n_e v} \left[1 + \frac{v^2}{f^2 \lambda^2} (n_e^2 - n_o^2) \right], \quad (4.15)$$

where the refractive indices n_o and n_e are generally functions of the light wave directions, $n_o = n_o(\vartheta_i)$ and $n_e = n_e(\vartheta_d)$; ϑ_i and ϑ_d are the angles of the incidence and diffracted light waves relative to the straight line orthogonal to the [100] crystal lattice vector (see Figure 4-1).

Theoretically, from equations (4.14) and (4.15) it follows that Bragg diffraction can occur at rather low and high frequencies. Depending on the laser wavelength and the acoustic material, the lower and upper limit of the operating frequency is at the order of a few 100MHz and 20GHz, respectively [44]. Nevertheless, the bandpass range of the device strongly depends on the working point, i.e. the incidence angle of light. Figure 4-3 shows a theoretical plot of the incident and diffracted beam angles versus the acoustic frequency in anisotropic crystals for the Bragg condition.

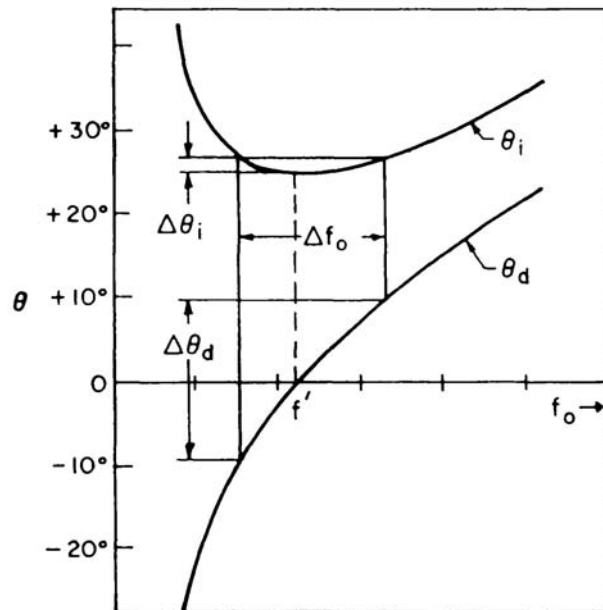


Figure 4-3 Incident and diffracted beam angles of the Bragg diffraction vs. acoustic frequency.

An optimal operation of the acousto-optic deflector can be achieved in the region where $\frac{d\theta_i}{df} = 0$, because with small angular dispersion of the incident beam large deflection angular range, θ_d i.e. large bandwidths can be obtained. Moreover, the small dispersion of the incident beam improves the angular power density of the acoustic field, and consequently, the acousto-optical efficiency.

4.2 Diffraction efficiency

For applications of acousto-optical devices, it is important to have high diffraction efficiency. The greater the efficiency, the less the required incident light intensity and acoustic power. If the required laser light intensity is small, semiconductor light sources can be applied. The small ultrasound power, i.e. the HF frequency intensity makes it possible to process weak signals. Keeping the power levels low has consequences on the overall power and mass budget, both being important concerns for space applications.

The expression of the diffraction efficiency can be derived from the ratio of the intensities of the diffracted and incident light [19]

$$\eta = \frac{I_d}{I_0} = \sin^2 \sqrt{\frac{\pi^2 LP_{tot} M_2}{2H\lambda^2}}, \quad (4.16)$$

H – ultrasonic beam height

M_2 – acousto-optic figure of merit

$P_{tot} = LHP_a$ – total acoustic power

P_a – acoustic power

High diffracted light intensity can be achieved by using an incident light beam with short wavelength and high power (recently there are frequency doubled laser diodes of 488nm wavelength with 200mW power applicable). Furthermore, choosing materials with small acoustic attenuation keeps the interaction zone long. The large figure of merit and the small acoustic transducer height increase the diffraction efficiency as well. The figure of merit, a material parameter introduced by Smith and Korpel [85], can be used for comparing the efficiency properties of different acousto-optical materials

$$M_2 = \frac{p^2 n_0^6}{\rho v^3}, \quad (4.17)$$

p – photo-elastic coefficient

n_0 – refractive index of the crystal in the direction of the acoustic propagation

ρ – density of the medium

v – acoustic velocity

If we consider the effect of the acoustic bandwidth and match the height of the optical beam to the acoustic transducer, a considerably different expression of the diffraction efficiency results [19]

$$\eta = \frac{I_d}{I_0} = \frac{1.8\pi^2 P_{tot} M_2'}{2\Delta f_a f_c \cos \mathcal{G}_B} \frac{1}{\lambda^3}, \quad (4.18)$$

f_c – centre frequency of the acoustic beam

Δf_a – bandwidth of the acousto-optic deflector

\mathcal{G}_B – Bragg angle

M_2' – acousto-optic figure of merit, with a slightly different definition

$$M_2' = \frac{p^2 n_0^7}{\rho v^2}. \quad (4.19)$$

Expression (4.18) reflects that using laser light of short wavelength rapidly increases the diffraction efficiency. Furthermore, applying optical materials with large figure of merit, i.e., crystals with high refractive index, is also favourable. On the other hand, the velocity of the ultrasonic wave should be kept low. In practice, to improve the performance of a deflector, detailed calculations are needed on the crystal cut, and compromises must be made concerning centre frequency, bandwidth, resolution and optical quality. A comparison of the characteristics of commonly used acousto-optical materials can be found in Appendix A. In addition to the widely used Lithium-niobate (LiNbO₃), there are other promising optical materials, like TeO₂ or rutile (TiO₂) which have high density, high refractive index, wide optical transmission, small acoustic wave velocity, and therefore a large figure of merit. Due to the high density of the crystal, the sound wave attenuation is also rather high. This is undesirable, because it results in limitations in centre frequency, bandwidth, and resolution and in certain cases produce a heat effect that leads to spectroscopic stability problems of the instrument (see Section 10.13). An investigation of rutile is currently being done at KOSMA within the project of an ultra-large bandwidth (3-4GHz) spectrometer [64].

4.3 Time-bandwidth product

The *spectral resolution* of the device is determined by the *time-bandwidth product*. It expresses the maximal amount of resolvable angles, N , and is defined as the ratio of deflection angular range to the angular resolution

$$N = \frac{\Delta\mathcal{G}}{\delta\mathcal{G}}. \quad (4.20)$$

For ultrasonic waves, the product of wavelength and frequency is the acoustic velocity

$$\lambda_a f_a = v_a. \quad (4.21)$$

As mentioned before, the acoustic frequency represents a phase grating with the spatial frequency of ν defined by

$$\nu = \frac{1}{\lambda_a}. \quad (4.22)$$

The diffraction angle of a phase grating is proportional to the incident light wavelength and inversely proportional to the spatial frequency of the grating

$$\mathcal{G} = \frac{\lambda}{\nu}. \quad (4.23)$$

The substitution of (4.21) and (4.22) into (4.23) yields

$$\mathcal{G} = \frac{\lambda f_a}{v_a}. \quad (4.24)$$

From this simple consideration it can be seen the diffraction angle is a linear function of the acoustic i.e. signal frequency. However, that is a first order approximation. The real diffraction is slightly nonlinear due to the nonlinear interaction geometry of the acousto-optical interaction, the nonlinear refraction of the diffracted beam at the crystal surface, and the nonlinear angle dependence of the extraordinary component of the refractive index. For small variations of the acoustic frequency, (4.24) yields the diffraction angular range of

$$\Delta\mathcal{G} = \Delta f_a \frac{\lambda}{v_a}. \quad (4.25)$$

The optical angular resolution, $\delta\mathcal{G}$, can be expressed by using the definition of the effective aperture, A_{eff} , of the deflector (see Section 7.6):

$$\delta\mathcal{G} = \frac{\lambda}{A_{eff}}. \quad (4.26)$$

The time-bandwidth product now can be derived by inserting (4.25) and (4.26) into (4.20) [19]:

$$N = \frac{\Delta \mathcal{G}}{\delta \mathcal{G}} = \frac{\Delta f_a A_{eff} \lambda}{v_a \lambda} = \Delta f_a \frac{A_{eff}}{v_a} = \Delta f_a \tau. \quad (4.27)$$

The quotient of the effective aperture and acoustic velocity is the *aperture time* (τ). This is the time (also called *access time* or *time delay*) that the acoustic wave needs to cross the interaction zone of the acousto-optical medium. The maximal number of resolvable spots (N) can be calculated by multiplying the aperture time and the bandwidth of the deflector.

The *frequency bandpass* of an acousto-optical deflector is defined by the frequencies where the deflected intensity falls $3dB$ relative to the maximal intensity. For the bandwidth of the Bragg cell built using an optically anisotropic material for the case of the tangential phase matching interaction geometry, the following approximation can be used by rearranging the expression used by [14]

$$\Delta f_a = \sqrt{\frac{2 \cdot 3.6 n v_a^2 \cos \mathcal{G}}{\lambda L}}, \quad (4.28)$$

\mathcal{G} – is the internal Bragg angle within the crystal.

The large bandwidth requires acousto-optical materials that allows for high acoustic velocities and small interaction lengths. Thus, the high diffraction efficiency and large bandwidth are always a trade-off of the design.

The *frequency resolution* of the deflector is given by the frequency bandwidth of the device over the number of resolvable spots. This is the inverse of the aperture time. Thus, the resolution of the device in frequency improves as the acoustic velocity falls and the overall optical aperture is increased. The resolution can be measured by feeding two frequency signals into the Bragg cell and imaging the diffracted light carefully onto a detector array. The imaging optics should be diffraction limited in order not to decrease the resolution of the device. The output video signal of the detector is monitored (for instance on an oscilloscope screen) and the separation of the signals is changed until the resolution criterion is achieved. For the resolution various definitions exist. The classical definition in optics is given by the Rayleigh criterion, according to which two signals can be resolved if the dip between the signal peaks is at least $1 - \frac{8}{\pi^2} = 0.19$ ($\approx 1dB$) of the maximum intensity [9]. The performed resolution for the lithium niobate Bragg cell at the design wavelength of $785nm$ has been determined to be $0.98MHz$.

For the *Herschel WBS LiNbO₃* is chosen as acousto-optical material of the Bragg cell. The performance parameters achieved with the deflector device are listed in Table 4-1 [10]

| | |
|--|---|
| acoustic velocity (v) | 3445m/s |
| aperture time (τ) | 1 μ s |
| figure of merit (M_2) | 14 \cdot 10 ⁻¹⁸ s ³ / g |
| acoustic attenuation ³⁰ (at 2.1GHz) | 4.87dB/ μ s |
| centre frequency (f_c) | 2.1GHz |
| bandwidth (Δf_a) | 1GHz |
| frequency resolution (δf) | 1MHz |
| number of channels | 4 |

Table 4-1 Performance data of the Herschel Bragg cell

4.4 Intermodulation and dynamic range

Since the acousto-optical interaction is a nonlinear effect, there are harmonic distortions and spurious frequency components in the detected spectra limiting the dynamic range of the deflector. Other limiting factors of the dynamic range are the crystal lattice errors and imperfections in the polished optical surfaces of the Bragg cell producing light scatter. Moreover, diffracted light from the aperture of the imaging optics could also increase the light scatter level. The first effect mentioned above is manifested by the two tone test feeding two signals with frequencies of f_1 and f_2 in a distance of approximately one octave into the Bragg cell and measuring the third order intermodulation product at the frequency of $2f_1 - f_2$. The intermodulation effect may be caused by multiphonon scattering or by acoustic mixing effects. In the case of low acoustic power densities, the multiphonon scattering process (which is a multiple scattering of the incident light by the acoustic beam) is dominant. The intensity of the third order intermodulated signal is given by [38]

$$I(2f_1 - f_2) = \frac{I_1^2 I_2}{36}, \quad (4.29)$$

where I_1 and I_2 are the diffracted light intensities at the signal frequencies f_1 and f_2 , respectively. The ratio of the intensities of the intermodulation products to one of the input signal intensities defines the *spur-free dynamic range*. The dynamic range limited by the two-tone third order intermodulation product is determined by [5]

$$D_f = -10 \lg \left(\frac{I_1 I_2}{36} \right). \quad (4.30)$$

A typical value of the dynamic range for an input signal level of -20dBm and 10% diffraction efficiency is 135dB, independent of the illumination position of the Bragg cell.

In case of devices with large bandwidth (1-2GHz) and higher acoustic power densities the measured dynamic range is smaller than the values predicted theoretically by [38]. This is due to the dominant acoustic mixing process generating intermodulation products. The effect is nonlinear, thus the spur free dynamic range in this case is determined by

³⁰ The empirically observed acoustic attenuation scales as $1.31f^{1.77}$ where f is the frequency in GHz [5].

$$D_f = -10 \lg \left(\frac{P_a}{LH} \right)^2 + K, \quad (4.31)$$

where the constant K is the nonlinear coupling parameter incorporates the acoustic dispersion, frequency, path length and attenuation [5].

The dynamic range is increasing if the acoustic zone is illuminated near to the transducer. There the acoustic mixing effect is not dominant and only multi-phonon scattering contributes substantially to the generation of intermodulation products. Increasing the illumination distance from the transducer, the deflected light intensity will decrease due to the acoustic attenuation, yet the acoustic mixing effect shows up, resulting in a reduced dynamic range. At the optimized illumination of a 1GHz bandwidth Bragg cell (see also Section 7.6) the typical spur free dynamic range is of the order of 45dB , while in case of a 2GHz device it is only 22dB .

As mentioned above, the optical scattering also contributes to the limitation of the dynamic range. However, with high optical quality and coatings of the surfaces of the Bragg cell and carefully aligned optics a scattered light intensity of -90dB has already been achieved. Using the polarisation rotation property between the diffracted and undiffracted light of an anisotropic acousto-optic device the dynamic range can be improved by using polarisation filtering. This removes an additional $10\text{-}15\text{dB}$ scattered light from the diffracted signal level.

5 The Wide Bandwidth Spectrometer design

The WBS is devoted to analysing the intermediate frequency coming from the receiver using the acousto-optical signal processing technique. The spectrometer consists of two separate units

- the Electronics unit (WBE) and
- the Optics unit (WBO).

The WBE unit includes the IF processing sub-unit, which converts the 4-8GHz bandwidth IF input signals to the four input frequency bands of the WBO (4 x 1.55-2.65GHz), and the electronics sub-unit, which controls the WBS system and data acquisition, and conducts the communication with the on-board computer. The WBO optical unit analyses the split IF signals by means of a four channel array acousto-optical Bragg deflector. The block diagram of the WBS design is shown in Figure 5-1, [80].

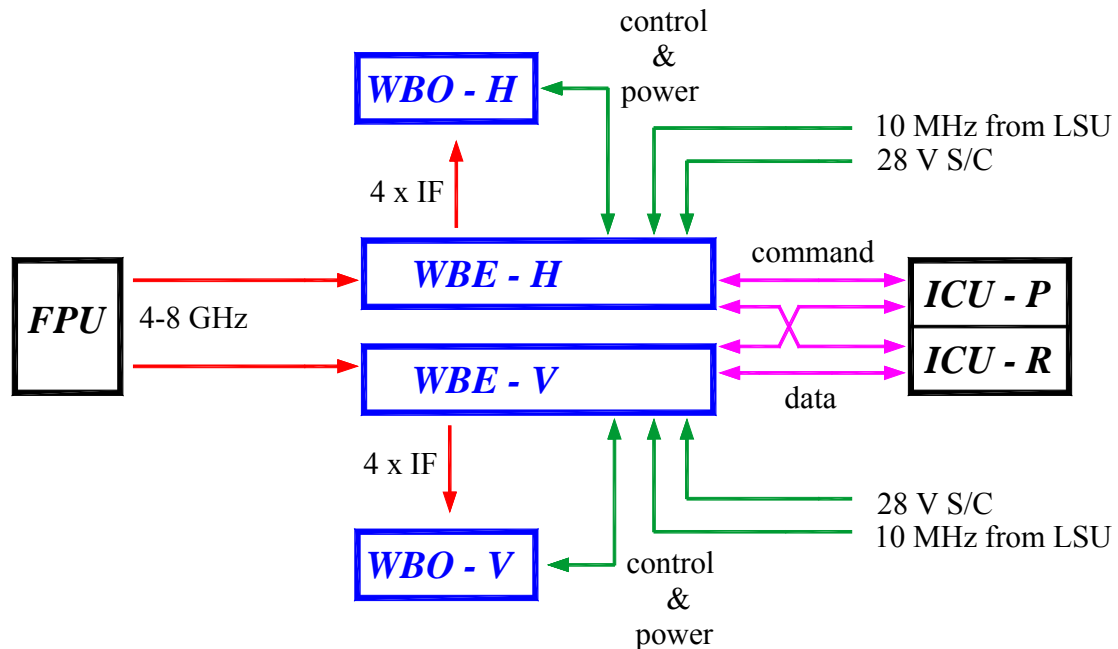


Figure 5-1 Principle scheme of the WBS unit. The 4-8GHz bandwidth IF signals, correspond to the horizontal and vertical polarization, are fed into the WBS IF processing unit then analysed by the WBS optical unit.

The receiver system makes it possible to process the signals of the observed radio astronomical sources in two polarization directions. Thus, the IF signal coming from the

Focal Plane Unit (FPU) is processed by two completely independent spectrometers, one for the horizontal, the other for the vertical polarization.

5.1 WBE IF part design description

The working principle of the IF part of the WBE unit for one polarization is depicted in Figure 5-2, [80]. The IF signal coming from the FPU is pre-amplified then fed into a four-channel power splitter. Each channel is filtered by bandfilters having 1.1GHz bandwidth so that the channels cover the total IF frequency range of 4-8GHz. Then, the single channels are converted down to the 1.55-2.65GHz input bands of the optics unit. After further amplification the output signals of the mixers are equalized in order to correct the gain variations of WBO. At the output of the equalizers, variable attenuators make it possible to correct the different power levels of the WBO sub-bands. Finally, the signals are amplified to the input power level of the WBO unit by means of power amplifiers.

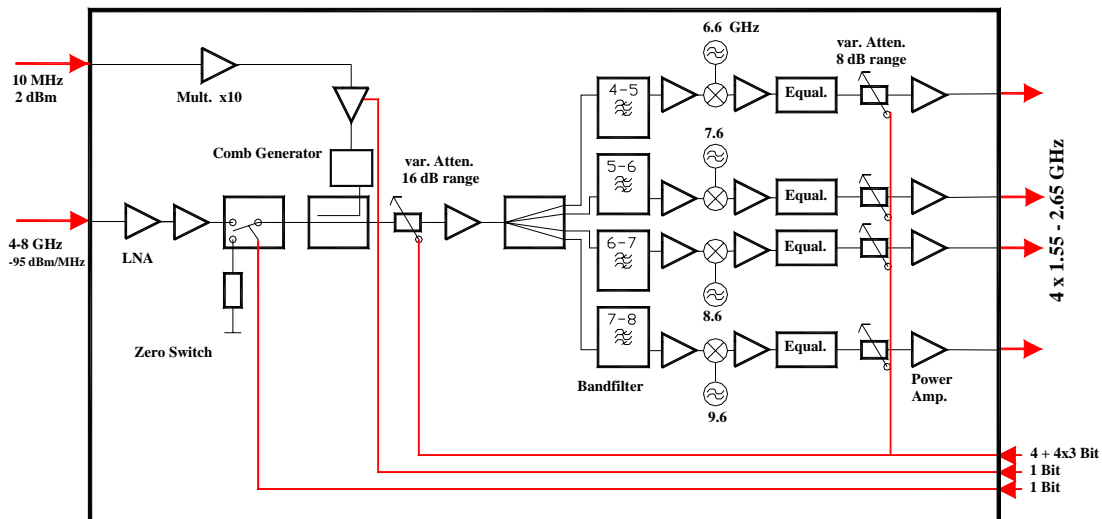


Figure 5-2 Operation scheme of the WBE IF section.

To be able to frequency calibrate the instrument, the signal of a comb generator with 100MHz line spacing can be applied. In addition, for calibration purposes, the system zero level can be determined by means of a zero switch. With a variable attenuator (4bit, 1dB step) in front of the power splitter the overall power level at the WBO input can be adjusted.

5.2 WBE Electronics sub-unit design description

The electronics sub-unit controls the WBS optical and IF unit. Furthermore, it accommodates the digital signal processing and power supply circuits. The read-out of the CCD (WBO unit) is controlled by a small digital electronics board using an FPGA. It generates the pixel clocks and the 10ms transfer impulses needed for the appropriate clocking of the CCD. The four analogue output signals of the CCD are digitized by means of 14bit analogue-digital converters, which efficiently reduce differential nonlinearity effects of ADCs [79]. Then the

5.3 WBO design principle

output data are co-added to 32bit by using ASICs³¹. After a CCD read-out, the signals of each CCD line can be stored in two separate memory banks (RAM), which allow for continuous integration also during the data transfer to the HIFI ICU³². The output data of WBE and the housekeeping data of the instrument are transmitted to ICU through a 24bit serial interface. A second serial interface is used as the command line for the WBS.

5.3 WBO design principle

The principle design of the array acousto-optical spectrometer is shown in Figure 5-3 [75].

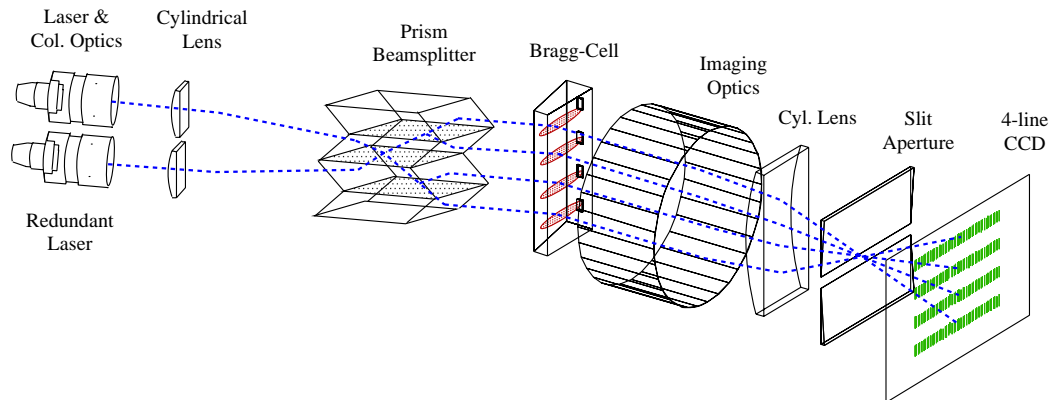


Figure 5-3 Optical setup of the Herschel WBO unit. A second laser is implemented for redundancy reasons. The light of the two lasers is coupled together by using a prism beam splitter

The emitted light of a laser diode is collimated and vertically focused onto the acousto-optical deflector. In case of the WBO, the deflector is a four-channel array Bragg cell (4x1GHz) that covers the 4GHz bandwidth of the IF signal. The four beams needed for the illumination of the array Bragg cell are produced by means of a prism beam splitter. The unique design of the beam splitter makes it possible to couple a redundant laser without applying an additional beam splitter, which would significantly reduce (by at least 50%) the laser light intensity and therefore the total optical efficiency of the instrument. The only way to compensate the efficiency loss is to increase the laser power, but it is undesired due to laser lifetime concerns. The optical system behind the Bragg cell images the deflected laser light onto a four line linear CCD array. The individual pixels of the detector correspond to frequency channels, and the detected intensity scales with the input signal intensity. The slit aperture between the cylindrical lens and the CCD significantly reduces the scattered light level and therefore improves the stability of the instrument.

The overall design of the wideband spectrometer must comply with the demands of a space-qualified instrument. In Chapter 7, the individual components of the instrument are investigated in more detail.

³¹ Application-Specific Integrated Circuit

³² Instrument Control Unit

6 Optical design of the Wide Bandwidth Spectrometer

6.1 Design concept

The four channel acousto-optical spectrometer operates with only one laser light source, consequently the available laser power per channel is reduced compared to a single channel AOS. Furthermore, for space applications the reliability and lifetime of the laser is an important concern thus, its operating power level is reduced by approximately 30% of the maximum power. Nevertheless, these efficiency losses are compensated for by optimizing the design of the optical imaging system for maximum efficiency. This is done by focusing the laser light onto the acoustic zone of the Bragg cell as well as the deflected light onto the detector area. The imaging system of the WBO from the top (horizontal direction in the WBO) and from the side view (horizontal direction) is shown in Figure 6-1.

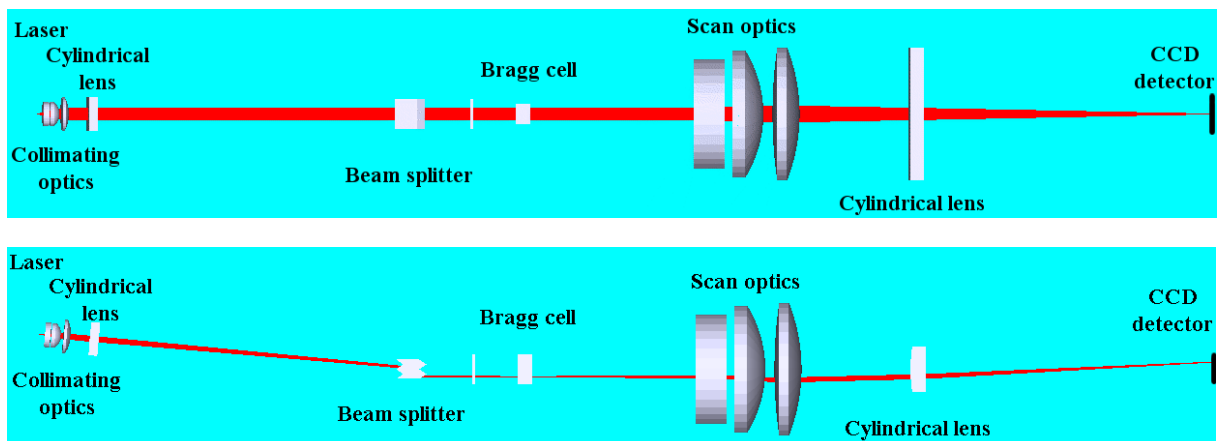


Figure 6-1 Optical system design of the WBO. In the horizontal direction (above), the collimated laser light illuminates the Bragg cell, and then the deflected beam is focused onto the detector using a scan lens. In the vertical direction (below), the laser light is focused onto the Bragg cell (only one channel is displayed) by applying a cylindrical lens and a beam splitter. The scan optics images the deflected light onto the CCD. An additional cylindrical lens is needed to match the light beams to the lines of the detector array.

The good optical efficiency is important to keep the power level of the IF signal as low as possible, which simultaneously reduces heating effects in the Bragg deflector (c.f. Section 10.13), and therefore improves the stability of the instrument. Besides the high optical efficiency, the spectrometer must be optimized for the maximum resolution as well. This requires diffraction limited imaging optics. The price to pay for the high optical efficiency and resolution is a high mechanical, thermal and alignment sensitivity of the instrument. For this reason, the mechanical stability of the housing and the supporting structures of the

components are of crucial importance. At the same time, not only high stiffness, but also low weight and small size of the housing are essential. The low power consumption is also an important concern for instruments used for space applications, therefore the only considerable light source is a laser diode. In order to attain the good spectroscopic stability of the spectrometer, thermal stability i.e. thermal isolation must be guaranteed, and the selection of low noise CCD detectors is essential to provide the good dynamic range, linearity and efficiency needed for the backend system.

6.2 Optical description of the Bragg cell illuminating optics

The proper illumination of the active zone of the acousto-optical Bragg cell is provided by the optics of the source module. The dimension of the ultrasonic wave is about $3.5\text{mm} \times 0.08\text{mm}$, on which the laser light has to be imaged.

In the array acousto-optical spectrometers, which have already been built by KOSMA, the acoustic zone of the Bragg cell is always over-illuminated [43]. This means the waist size of the laser beam at the Bragg cell is relatively large ($\sim 150\mu\text{m}$) compared to the “vertical” dimension of the acoustic zone, which gives an appropriate margin on the beam height positioning, and the accuracy of the mechanical support of the light pen is less critical.

In case of the Herschel WBS the design is optimized for maximum optical efficiency, therefore the Bragg cell is placed into the focus of the illuminating optics, as shown in Figure 6-3. The advantage of this arrangement is that the imaging optics system behind the Bragg cell is independent of any beam angle errors of the source module caused by mechanical deformations. The disadvantage of the system is that the illumination of the Bragg cell is rather sensitive to beam height changes due to mechanical and thermal effects.

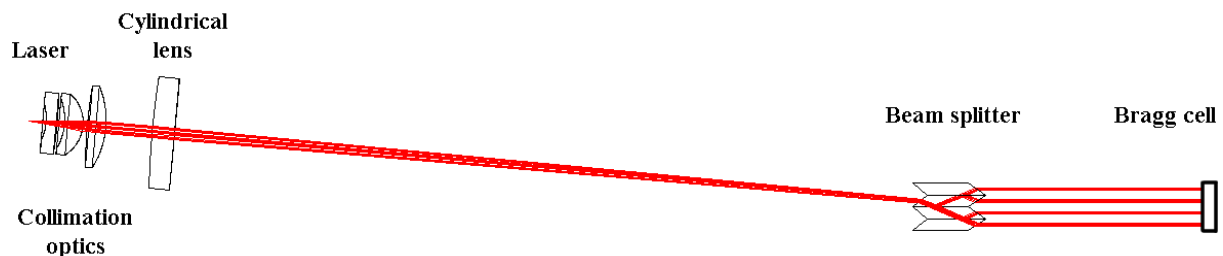


Figure 6-2 Components of the source module

The simple imaging optics used for the Bragg cell illumination consists of the laser collimation optics, the cylindrical lens and the beam splitter, as is shown in Figure 6-2. From the imaging point of view, the beam splitter changes only the focus position of the cylindrical lens; therefore it is not involved in the optical description. As a first approximation, the collimation optics and the cylindrical lens are described as thin lenses, but the results are compared with the thick lens simulation of the lens system as well.

The emitted light of the laser diode has some astigmatism, therefore the calculation has to be done differently for the two dimensions, vertical and horizontal. In the “vertical” direction (divergence perpendicular to the laser diode junction), the simplified optical layout of the laser source unit is depicted in Figure 6-3.

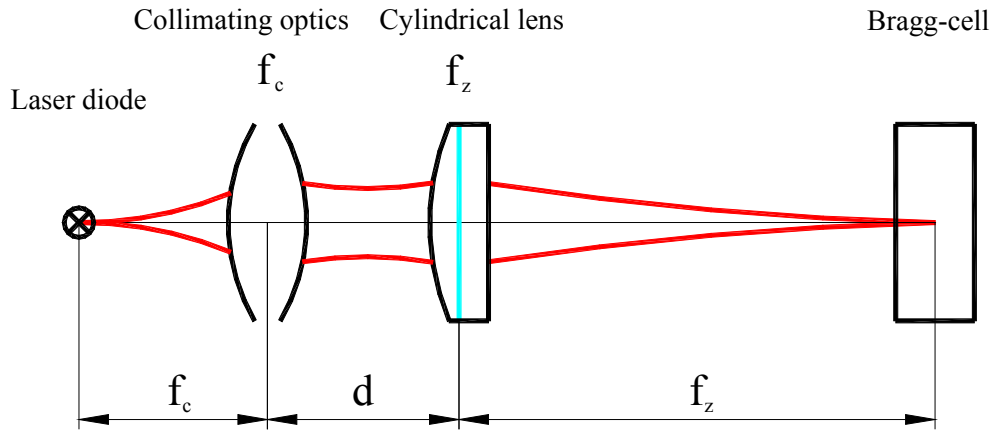


Figure 6-3 Illumination of the Bragg cell. The deflector is placed into the focus of the cylindrical lens for maximum diffracted light intensity. At the same time the angular sensitivity of the imaging optics behind the Bragg cell is eliminated.

The evaluation of the optical system is done by using the quasi-optical Gaussian beam propagation theory with its $ABCD$ ray matrix formalism. This gives us a satisfying description of the imaging without involving any diffraction effects on any aperture³³. The transformation matrix of the optical system can be written by using the following matrix multiplication [30]

$$\mathbf{T} = \begin{pmatrix} 1 & f_z \\ 0 & 1 \end{pmatrix} \begin{pmatrix} 1 & 0 \\ -\frac{1}{f_z} & 1 \end{pmatrix} \begin{pmatrix} 1 & d \\ 0 & 1 \end{pmatrix} \begin{pmatrix} 1 & 0 \\ -\frac{1}{f_c} & 1 \end{pmatrix} \begin{pmatrix} 1 & f_c \\ 0 & 1 \end{pmatrix} = \begin{pmatrix} -\frac{f_z}{f_c} & 0 \\ -\frac{f_c + f_z - d}{f_z f_c} & -\frac{f_c}{f_z} \end{pmatrix}, \quad (6.1)$$

where f_c and f_z are the focal lengths of the collimation optics and the cylindrical lens respectively, and d is the distance between the two lenses. From the transformation matrix the resultant focus f_r of the lens system can be identified

$$f_r = \frac{f_z f_c}{f_c + f_z - d}. \quad (6.2)$$

The beam propagation is described by the Gaussian beam parameter [71]

$$\tilde{q}(z) = z - iz_R, \quad (6.3)$$

where z_R is the Rayleigh range [71]

$$z_R = \frac{k}{2} w_0^2 = \frac{\pi w_0^2}{\lambda}, \quad (6.4)$$

and w_0 is the waist of the Gaussian beam. At the plane of the Rayleigh range the intensity becomes the half of the peak intensity and the radius of curvature of the wavefront is the smallest ($R = 2z_R$). The Rayleigh range, as the cardinal point of the Gaussian beam, is often called the confocal parameter or depth of focus.

³³ A procedure of calculating Fresnel- and Fraunhofer diffractions of Gaussian beams is discussed in [39].

The beam parameter transformed by an optical element obeys the *ABCD*-law

$$\tilde{q}'(z) = \frac{A\tilde{q}(z) + B}{C\tilde{q}(z) + D}. \quad (6.5)$$

Substituting the components of the transformation matrix \mathbf{T} into the expression of (6.5) and considering only the waist transformation ($z=0$), we obtain

$$\mathbf{q}'(z=0) = \frac{-\frac{f_z}{f_c} i z_R}{\frac{d - f_c - f_z}{f_z f_c} i z_R - \frac{f_c}{f_z}}. \quad (6.6)$$

The imaginer part of the transformed beam parameter expresses the transformed Rayleigh range

$$z_R' = \frac{z_R}{\left(\frac{f_c}{f_z}\right)^2 + \left(\frac{z_R}{f_r}\right)^2}. \quad (6.7)$$

Since $z_R \ll f_r$, the image beam waist results in

$$w_0' \approx w_0 \frac{f_z}{f_c}. \quad (6.8)$$

The ratio of the focal lengths of the cylindrical lens and the collimation optics describes the imaging of the laser beam waist in the vertical direction.

The waist dimension of the laser diode can be determined from the beam divergence angle. In the WBO Hitachi HL-7851G laser diodes are implemented. Their typical divergence angles of the FWHM intensity, in the direction of parallel- and perpendicular to the junction are $2\vartheta_y = 9.5$ and $2\vartheta_x = 23$ degrees [42], respectively. In the far field, if $z \gg z_R$, the $1/e$ radius of the electric field of the laser can be defined in terms of the asymptotic beam growth angle, from which the waist can be calculated

$$\operatorname{tg} \vartheta = \lim_{z \gg z_R} \left(\frac{w(z)}{z} \right) = \frac{\lambda}{\pi w_0}. \quad (6.9)$$

The divergence angles then correspond to the following waist sizes

$$w_{x0,y0} = \frac{\sqrt{2 \ln 2}}{2} \frac{\lambda}{\pi \operatorname{tg} \vartheta_{x,y}}, \quad (6.10)$$

where we used a scaling factor between the half width at half maximum (HWHM) intensity and the waist (see Appendix C). The resulting waists in the “horizontal” and “vertical”

directions are $0.723\mu\text{m}$ and $1.77\mu\text{m}$ respectively; and the corresponding confocal parameters are $2.092\mu\text{m}$ and $12.54\mu\text{m}$. Substituting the lens data ($f_c=8\text{mm}$, see Section 7.1.1 and $f_z=148\text{mm}$, see Section 7.1.2) into (6.8), the vertical waist size on the Bragg cell is calculated to be $32.7\mu\text{m}$.

In the horizontal direction, similar investigations are made in order to have a complete knowledge of the laser beam needed for further calculations. There the cylindrical lens acts only as a plan-parallel glass plate. Thus, the horizontal waist size is determined by the imaging of the collimation optics, as shown in Figure 6-4.

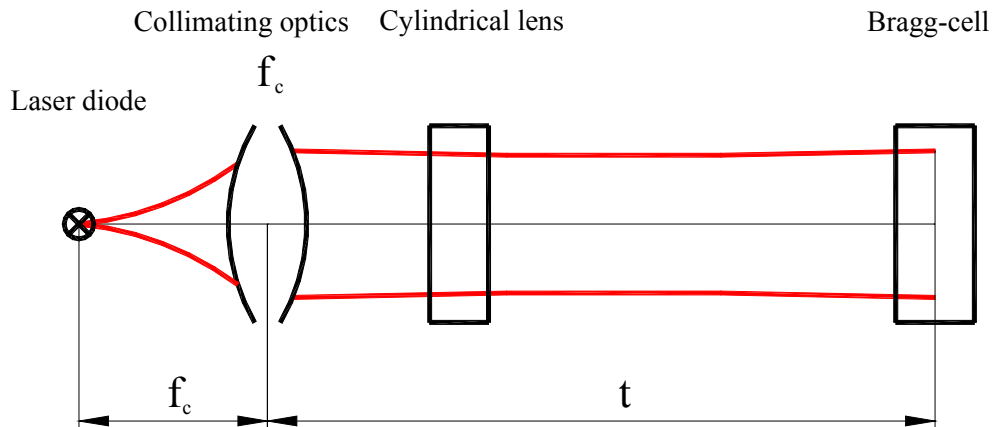


Figure 6-4 Top view of the Bragg cell illuminating optics (imaging in the horizontal direction).

The waist transformation of a simple lens is given by [30]

$$w'_0 = \frac{\lambda f_c}{\pi w_0} \quad (6.11)$$

Substituting the focal length of the collimation optics (8mm) and the “horizontal” waist size of the laser diode ($0.723\mu\text{m}$) into (6.11), the transformed waist size results in 2.765mm . The design of the Galileo collimating optics has a slightly different focal length ($f=8.0624\text{mm}$), therefore the horizontal waist dimension is 2.786mm .

The calculation of the Gaussian beam propagation is also done by using the thick lens approximation. The detailed information of the lens radii, distances and materials are summarized in Appendix D. During the evaluation the beam radii are determined at the surfaces of all the optical components to have a precise description of the beam propagation as needed for the opto-mechanical design of the laser source unit (cf. Chapter 7), and for the resolution and efficiency optimization of the WBO unit (see Section 6.3). The results of the laser beam propagation description are summarized in Table 6-1.

| Position | Horizontal waist size | Vertical waist size | Horizontal Rayleigh range | Vertical Rayleigh range |
|-------------|-----------------------|---------------------|---------------------------|-------------------------|
| Laser diode | $0.723\mu\text{m}$ | $1.77\mu\text{m}$ | $2.092\mu\text{m}$ | $12.54\mu\text{m}$ |
| Bragg cell | 2.786mm | $32.7\mu\text{m}$ | 31.06m | 4.28mm |

Table 6-1 Summary table of laser beam dimensions

6.3 Imaging of the deflected light

The optical setup of the acousto-optical spectrometer must guarantee perfect imaging to provide the excellent performance required for the Herschel satellite project. The high spectral resolution can only be achieved with a highly collimated laser beam and perfect optical surface qualities of all optical components including polarization filters and the acousto-optic crystal; moreover, the imaging optics must be designed for operation near the diffraction limit. Because of the diffraction on the small vertical aperture of the Bragg cell, the use of a simple spherical imaging optics would result in two different focus positions in the “vertical” and “horizontal” direction. Therefore, in one direction an additional focusing element, a cylindrical lens, is needed.

In the horizontal i.e. scanning direction, the laser light must be collimated to improve the bandwidth of the Bragg-cell [19]. The scan lens (f - θ lens) is responsible for the linear imaging in angle and for the horizontal spot size, thus for the optical resolution of the system as well. In the horizontal plane (scanning direction), the cylindrical lens acts as a plan parallel glass plate and only elongates the focal length of the scan optics, as illustrated in Figure 6-5.

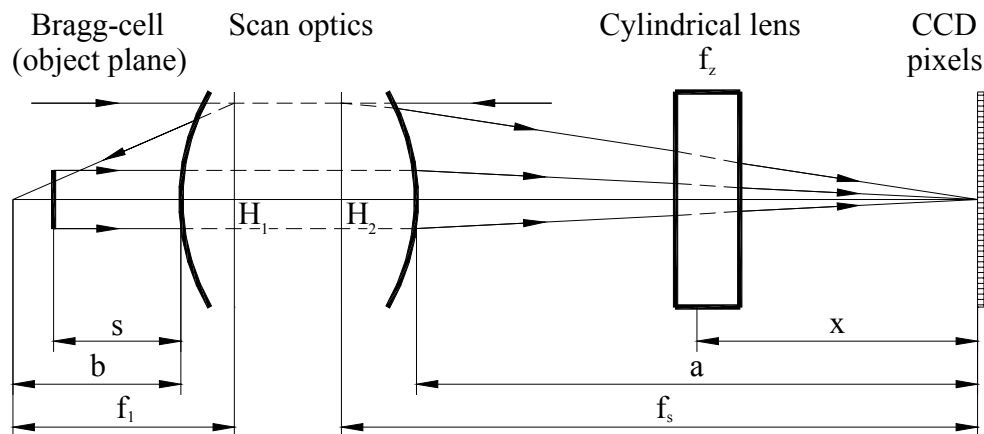


Figure 6-5 Top view of the imaging optical system. The corresponding distances used for the calculation are s – the object distance, b – the object space focal length, f_1 – the effective object space focal length, f_s – the effective image space focal length, and a – the image space focal distance.

In the vertical direction, the diffracted laser beam is divergent due to the small vertical aperture size of the Bragg-cell. Simple imaging only with the scan optics would result in a virtual focus, since the object is placed at the object plane focus. In other words, the vertical spot size in the horizontal focus position would be so large that the spots of the individual channels are overlapped, producing a crosstalk between the bands. Applying a cylindrical lens two problems can be solved; with the correct focal length the vertical and horizontal foci are in the same plane on one hand, and with the correct distance to the scan optics, the vertical spacing of the four beams can be adjusted to the rows of the CCD on the other. Figure 6-6 illustrates the side view (vertical imaging) of the optical system. In order to reach the maximum efficiency, the vertical focus has to be in the same plane as the horizontal focus. This leads to small vertical spot sizes requiring high mechanical stability (c.f. Section 8.1), therefore the WBO must have a rigid optical bench.

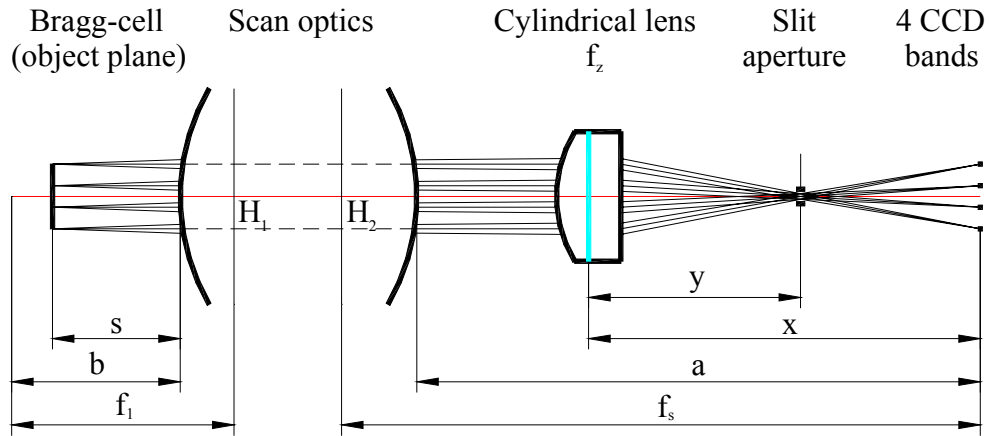


Figure 6-6 Side view of the optical system (vertical imaging). The necessary parameters used for the optimization are f_z – the focal length of the cylindrical lens, x – the distance of the cylinder lens to the CCD, and y – the position of cross point of the beams.

The scan lens is a three-lens system having different foci in the object and image space and different principal plains, therefore it can not be described as a simple thin lens. Its cardinal points are seen in Figure 6-7.

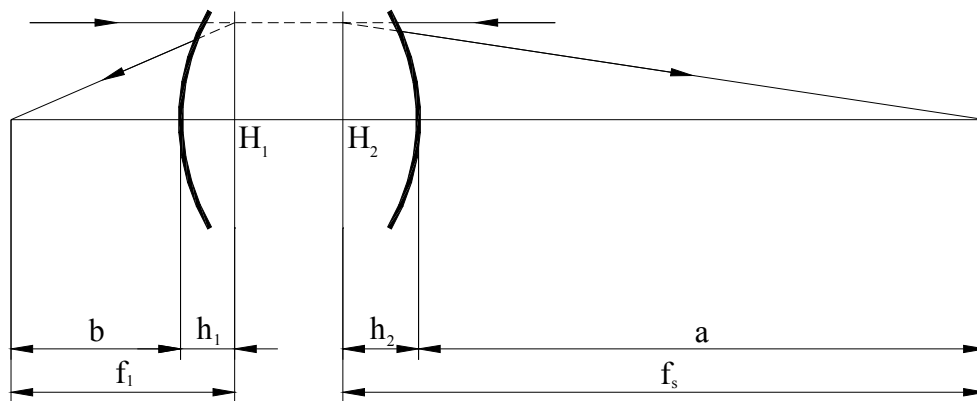


Figure 6-7 Cardinal points of an arbitrary optical system

In general, for an arbitray optical system the characterizing parameters can be expressed with the ABCD matrix elements [83]. The element “C” always shows the effective focal length in the image space

$$f_s = -\frac{1}{C}. \quad (6.12)$$

The position of the principal plane relative to the lens surface is given by [58]

$$h_2 = \frac{A-1}{C}, \quad (6.13)$$

from which the image space focal distance “a” can be calculated as

$$a = f_s - h_2 = -\frac{1}{C} - \frac{A-1}{C} = -\frac{A}{C}. \quad (6.14)$$

The first matrix element A can be expressed by dividing the equation (6.14) with (6.12)

$$A = \frac{-\frac{A}{C}}{-\frac{1}{C}} = \frac{a}{f_s}. \quad (6.15)$$

Similarly the matrix element D can be expressed by using the object space focal distance

$$D = \frac{-\frac{D}{C}}{-\frac{1}{C}} = \frac{b}{f_s}. \quad (6.16)$$

Applying that the determinant of the imaging matrix is unity ($\det \mathbf{M} = 1$) the matrix element B can be expressed from

$$AD - CB = 1 \quad (6.17)$$

$$\frac{a}{f_s} \frac{b}{f_s} + \frac{1}{f_s} B = 1 \quad (6.18)$$

$$B = \frac{1}{f_s} (f_s^2 - ab), \quad (6.19)$$

Thus, the transformation matrix of the scan optics \mathbf{M} takes the form of

$$\mathbf{M} = \begin{pmatrix} A & B \\ C & D \end{pmatrix} = \begin{pmatrix} \frac{a}{f_s} & \frac{1}{f_s} (f_s^2 - ab) \\ -\frac{1}{f_s} & \frac{b}{f_s} \end{pmatrix}. \quad (6.20)$$

6.3.1 Optimisation of the cylindrical lens

As stated before, the laser light deflected by the Bragg-cell has to be imaged onto the CCD in the vertical and horizontal directions, therefore the focal length and the position of the cylindrical lens is fully determined. Using the geometrical beam optics description for an arbitrary optical system the transformed ray position and the slope can be written as

$$\begin{pmatrix} x' \\ m' \end{pmatrix} = \begin{pmatrix} \alpha & \beta \\ \gamma & \delta \end{pmatrix} \begin{pmatrix} x \\ m \end{pmatrix}. \quad (6.21)$$

Substituting the Bragg-cell channel spacing (d_{Bragg}) and the CCD line distances (d_{CCD}), the matrix equation of (6.21) can be expressed with

$$\begin{pmatrix} -d_{CCD} \\ m' \end{pmatrix} = \begin{pmatrix} \alpha & \beta \\ \gamma & \delta \end{pmatrix} \begin{pmatrix} d_{Bragg} \\ m \end{pmatrix}. \quad (6.22)$$

From the boundary conditions that rays leaving the Bragg-cell parallel to the optical axis ($m=0$) must hit the CCD line at the focus, and rays origin from the object plane having arbitrary slope must be also imaged onto the CCD, we can determine the first matrix element of the transformation matrix by separating eq. (6.22).

$$\alpha = -\frac{d_{CCD}}{d_{Bragg}} = -\frac{1}{u} \quad \text{with } u = \frac{d_{Bragg}}{d_{CCD}}, \quad (6.23)$$

where u is the lateral magnification of the system. In case of the Bragg-cell and CCD used for the HIFI WBO the channel and line spacing, respectively is the same, 1.6mm, thus the object is imaged from “focus to focus” with the magnification of one.

The imaging of the system in the vertical direction (c.f. Figure 6-6) can be described with the matrix multiplication of

$$\mathbf{T} = \begin{pmatrix} 1 & s \\ 0 & 1 \end{pmatrix} \begin{pmatrix} 1 & x \\ 0 & 1 \end{pmatrix} \begin{pmatrix} -\frac{1}{f_z} & 0 \\ 1 & 1 \end{pmatrix} \begin{pmatrix} 1 & a-x \\ 0 & 1 \end{pmatrix} \begin{pmatrix} \frac{a}{f_s} & \frac{1}{f_s}(f_s^2 - ab) \\ -\frac{1}{f_s} & \frac{b}{f_s} \end{pmatrix}. \quad (6.24)$$

After multiplying and simplifying the expression of (6.24) it yields

$$\mathbf{T} = \begin{pmatrix} -\frac{x^2}{f_s f_z} & f_s - \frac{x}{f_z} \left(f_s - \frac{xb}{f_s} \right) - \frac{x^2}{f_s f_z} s \\ -\frac{x}{f_s f_z} - \frac{1}{f_s} & -\frac{sx}{f_s f_z} \frac{s}{f_s} + \frac{b}{f_s} \left(1 + \frac{x}{f_z} \right) - \frac{f_s}{f_z} \end{pmatrix}. \quad (6.25)$$

The distance between the cylindrical lens and the CCD can be directly seen from the first matrix element and the definition of (6.23), respectively

$$x = \sqrt{\frac{f_s f_z}{u}}. \quad (6.26)$$

Furthermore, for arbitrary rays leaving the object space focus the imaging is independent on the ray angles. That means that the image height x' is independent on the slope m

$$x' = \alpha x + \beta m. \quad (6.27)$$

This is only true for $\beta = 0$, from which the necessary focal length of the cylindrical lens can be determined by the following expression

$$f_s = \frac{x}{f_z} \left(f_s - \frac{xb}{f_s} + \frac{sx}{f_s} \right). \quad (6.28)$$

From eq. (6.26) and eq. (6.28) we can evaluate all the necessary parameters to describe the system. The distance between the cylindrical lens and the CCD and the effective focal length of the cylindrical lens are given by

$$x = \frac{f_s}{u + \frac{b-s}{f_s}}, \quad (6.29)$$

$$f_z = \frac{f_s u}{\left(u + \frac{b-s}{f_s}\right)^2}. \quad (6.30)$$

Placing the Bragg-cell exactly in the object space focus ($s=b$), the results of (6.29) and (6.30) can be simplified as

$$x = \frac{f_s}{u} \quad \text{and} \quad f_z = \frac{f_s}{u}. \quad (6.31)$$

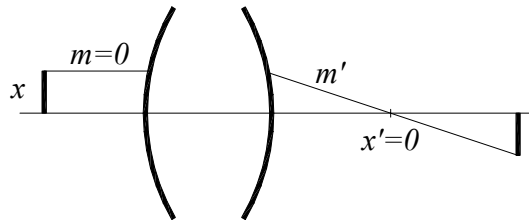
The focal length and the position of the cylindrical lens depend only on the image space focal distance of the scan lens and the required magnification of the optical system.

6.3.2 Position of the slit aperture

The position, where the four beams cross each other (see Figure 6-6) offers the opportunity to apply spatial filtering. This is realized by using a slit aperture, which reduces laser light scatter and laser spackles. To calculate the position of the slit aperture we use the following expression

$$\mathbf{T}' = \begin{pmatrix} \alpha' & \beta' \\ \gamma' & \delta' \end{pmatrix} = \begin{pmatrix} 1 & y-x \\ 0 & 1 \end{pmatrix} \begin{pmatrix} \alpha & \beta \\ \gamma & \delta \end{pmatrix}, \quad (6.32)$$

where $y-x$ represents the distance between the CCD and the cross point. Considering a ray that has a zero slope ($m=0$) in the object space and intersects the optical axis ($x'=0$)



and using the ray transformation equation

$$x' = \alpha' x + \beta' m = 0 \quad (6.33)$$

it can be directly seen that the first matrix element α' must be equal to zero

$$\alpha' = \frac{-x^2}{f_s f_z} + (x - y) \left(\frac{x}{f_s f_z} + \frac{1}{f_s} \right) = 0, \quad (6.34)$$

which can be simplified for y as

$$y = \frac{x}{1 + \frac{x}{f_z}}. \quad (6.35)$$

Substituting the results of eq. (6.29) and (6.30) into eq. (6.35), the position of the slit aperture can be expressed with the known parameters (f_s , u , b , s) of the optical system

$$y = \frac{f_s u}{\left(u + \frac{b-s}{f_s} \right) \left(2u + \frac{b-s}{f_s} \right)}. \quad (6.36)$$

If the Bragg-cell is exactly placed into the object space focus of the scan lens ($s=b$), the slit position is determined by

$$y = \frac{f_s}{2u}. \quad (6.37)$$

In the WBO the line spacing of the CCD detector is exactly the same as the channel spacing of the Bragg-cell ($u=l$), and the scan lens has of a focal length of $100mm$, which yields the following values for the cylindrical lens and the slit aperture position

focal length $f_z = f_s = 100mm$

position from the CCD $x = f_s = 100mm$

position of the slit aperture $y = \frac{f_s}{2} = 50mm$.

During the optimization of the imaging optics performed by Galileo Avionica, the scan lens and the cylindrical lens have been included in the aberration analysis.

6.4 Image size on the CCD

After having the detailed description of the optical system we can derive the waist size on the CCD in the horizontal and vertical direction neglecting any diffraction effects. For the horizontal direction, where the cylindrical lens acts as a plan parallel glass plate, the optical system can be modelled as a single lens having $100mm$ focal length. Using the results of the waist size achieved from the Bragg-cell illumination calculation (c.f. Section 6.2), the transformed horizontal waist size on the CCD is given by

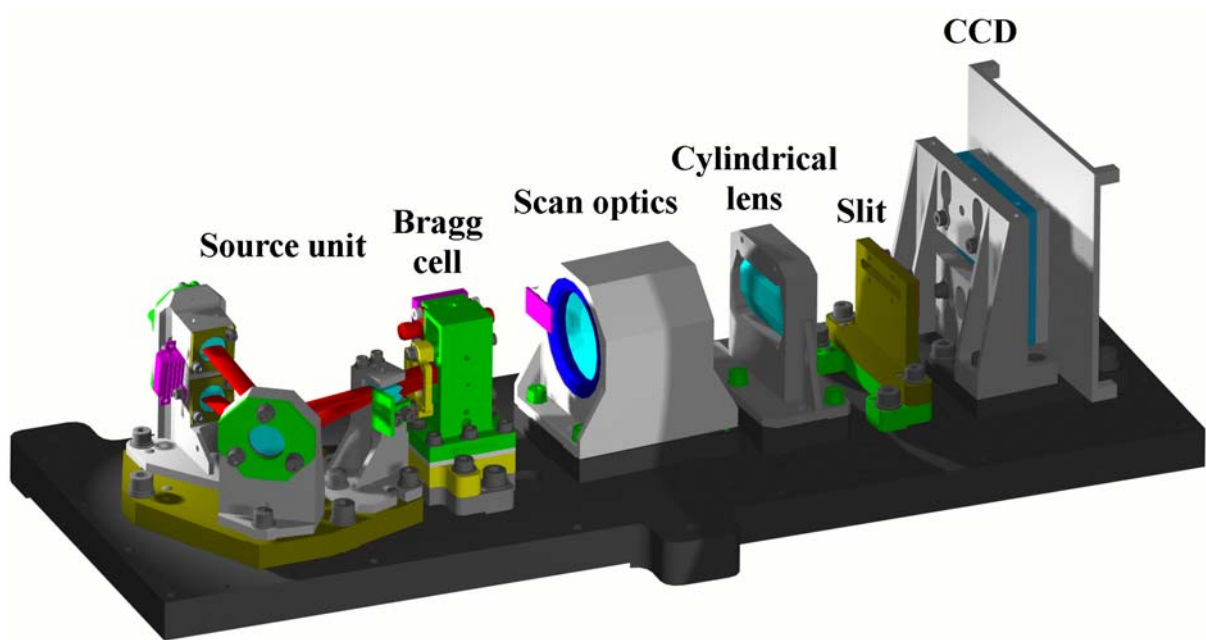
$$w_0' = w_0 \frac{f_s}{z_R} = \frac{\lambda}{\pi} \frac{f_s}{w_0} \approx 9 \mu m. \quad (6.38)$$

In the vertical direction, the waist size at the CCD can be calculated by substituting $f_z = f_s = x = 100mm$ into the transformation matrix of (6.25). Since it is a unity matrix, the lens system has a lateral magnification of $m=1$. This results in a transformed vertical waist size of

$$w'_0 = w_0. \quad (6.39)$$

The vertical waist size at the Bragg-cell is $w_0=32.7\mu m$ (c.f. eq. 6.8), which is equal to the vertical waist size at the CCD as well. Considering the $26\mu m$ vertical pixel dimension of the detector and the vertical beam diameter ($2w'_0$) of $66\mu m$ at the focus i.e. at the CCD, the mechanical vertical positioning must be better than $\pm 10\mu m$ over the operational thermal range of 10 degree. Otherwise, the optical efficiency of the instrument will be significantly decreased (c.f. Section 8.2).

7 Opto-mechanical design of the Wide Bandwidth Spectrometer



7.1 The Laser Source Unit

The experience gathered during the alignment of existing spectrometers shows how complicated and time consuming the adjustment procedure of an array spectrometer can be. The number of the alignment parameters is large, therefore it is fairly hard to attain the optimal performance of the instrument. In the WBO the most complex and critical part is the laser source unit, shown in Figure 7-1. Therefore it was decided to integrate its components onto one common interface plate, making a module that could be separately adjusted and tested before the final assembly of the spectrometer. This philosophy, as experienced from the SWAS AOS, significantly reduces the number of the adjustment parameters. This idea not only gives the possibility to control the performance of the module separately, but further tests could be also done without any effects from the other components of the instrument. These experiments like thermal environmental or deformation tests are useful to reduce risks of possible failures during the qualification program performed with the whole WBS. After getting the sub-unit to work properly, the final assembly and alignment of the WBO remains just a “simple” positioning and height fitting task for the pre-adjusted modules.

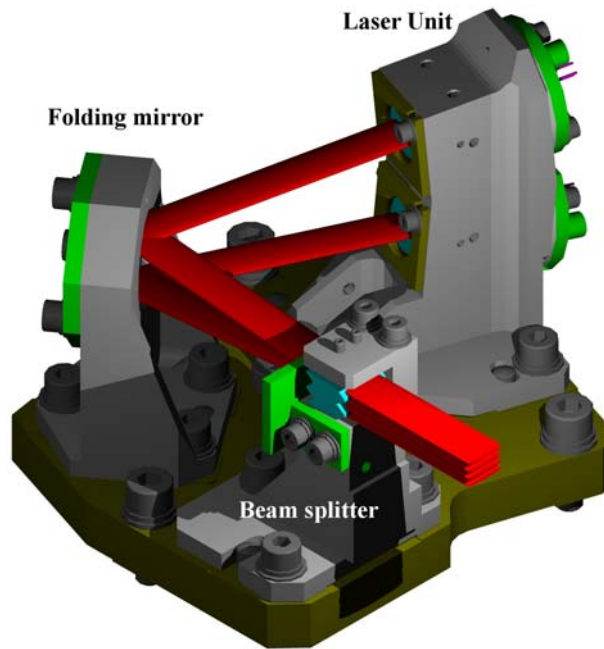


Figure 7-1 Laser source module of WBO

The illumination of the acoustic deflector is realized by means of the laser source module. The unit contains the two laser diodes, the collimation optics, the cylindrical lenses and the beam splitter. In addition, there is a folding mirror applied in order to reduce the mechanical dimension of the module.

7.1.1 Collimating optics

In order to exploit the maximum resolution of the Bragg cell, the laser light must be collimated. Moreover, the horizontal dimension of the collimated beam should be matched to the size of the useful aperture of the Bragg cell. This criterion defines the necessary focal length of the collimator. However, investigations have been shown that the resolution of the Bragg cell can be increased by using a decentred illumination. The acoustic intensity in the deflector decays exponentially, which can be partly compensated for by increasing the light intensity where the ultrasonic wave is weak. Thus, the laser beam has to be shifted away from the transducer, which results in an *effective illumination*. In relation with the effective illumination and resolution of the spectrometer it has been shown by [56] that the optimal resolution can be attained with a larger beam diameter than the aperture of the deflector itself. The optimum beam width of the laser is related to the horizontal dimension of the Bragg aperture [48]

$$A = \frac{w_x^{FWHM}}{0.673}, \quad (7.1)$$

A – useful aperture of the deflector (3.5mm given by [4])

w_x^{FWHM} – optimized horizontal beam diameter of the laser beam (FWHM).

From these parameters the required waist size can be calculated as

$$w_0' = \frac{0.673}{\sqrt{2 \ln 2}} A = 2.773 \text{ mm}, \quad (7.2)$$

where a scaling factor between the FWHM intensity and beam waist (see Appendix C) is used. The necessary focal length of the collimator is then given by using (6.10) and (6.11)

$$f = \frac{\pi}{\lambda} w_0 w_0' = 8.025 \text{ mm}. \quad (7.3)$$

In the WBO, the effective illumination is accomplished by using an 8mm focal length of the collimation optics.

7.1.2 Cylindrical lens

In order to achieve high diffracted light intensity from the Bragg cell, the intensity of the incident laser light should be as high a possible. The optical power of the laser cannot be arbitrarily increased, therefore an optimization of the optics is needed. In the “horizontal” direction, the collimation optics are responsible for the optimal width of the laser beam to achieve the maximum resolution. The short (8mm) focal length of the collimator guarantees that the beam width has the same dimension as the interaction length of the acoustic zone. In the “vertical” direction, the laser beam can be focused, but the following condition must be satisfied as well: the divergence of the focused laser beam should not be larger than the diffraction angle of the laser beam diffracted at the Bragg aperture, as is shown in Figure 7-2. Otherwise, additional aberration errors could be introduced by the three-dimensional phase matching condition of the Bragg deflection.

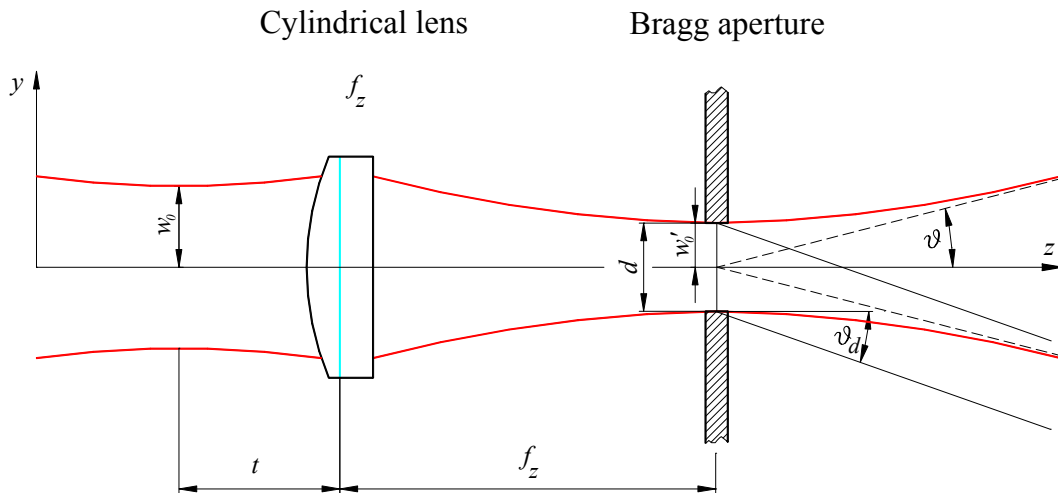


Figure 7-2 Minimal focal length of the cylindrical lens. The dimensions of the collimated and transformed beam waists determine the focal length of the lens.

In the first order approximation, the active zone of the Bragg cell is considered as a rectangular aperture having the height d , on which the laser beam is diffracted. The diffraction angle of the first diffraction order is given by [9]

$$\vartheta_d = \arcsin \frac{\lambda}{d}. \quad (7.4)$$

From the far field divergence angle of a Gaussian beam, the divergence condition of the laser beam can be calculated as

$$\frac{\lambda}{d} \geq \frac{\lambda}{\pi w'_0}, \quad (7.5)$$

where w' expresses the waist transformed by the cylindrical lens. This leads to

$$w'_0 \geq \frac{d}{\pi}. \quad (7.6)$$

With the knowledge of the collimated and transformed beam waists, we can determine the necessary focal length of the cylindrical length by using the Gaussian beam propagation description. The transformation matrix of the cylindrical lens is determined by

$$\mathbf{T} = \begin{pmatrix} 1 & f_z \\ 0 & 1 \end{pmatrix} \begin{pmatrix} 1 & 0 \\ -\frac{1}{f_z} & 1 \end{pmatrix} \begin{pmatrix} 1 & t \\ 0 & 1 \end{pmatrix} = \begin{pmatrix} 0 & f_z \\ -\frac{1}{f_z} & 1 - \frac{t}{f_z} \end{pmatrix}. \quad (7.7)$$

Using (6.3) and (6.4), the transformed waist can be written as

$$w_0'^2 = w_0^2 \frac{f_z^2}{(f_z - t)^2 + z_R^2}. \quad (7.8)$$

Since the Rayleigh range of a collimated beam is very large ($z_R = 5.173m$), the term $(f_z - t)^2$ can be neglected, and the expression of (7.8) yields

$$f_z = \frac{w_0'}{w_0} z_R = \frac{w_0' w_0 \pi}{\lambda}. \quad (7.9)$$

Substituting (7.6) into (7.9), we get the following inequality for the necessary focal length of the cylindrical lens

$$f_z \geq \frac{w_0 d}{\lambda}, \quad (7.10)$$

- $w_0=1.137mm$ $-1/e^2$ intensity contour of the collimated beam, which is also equal to the $1/e$ amplitude contour
- $d=80\mu m$ $-$ aperture height of the active zone considered as the height of the transducer
- $\lambda=785nm$ $-$ nominal laser wavelength.

The substitution into (7.10) results in a minimal focal length of $f_z \geq 116mm$. In the WBO, the actual focal length of the cylindrical lens is $148mm$ to satisfy the requirements of the opto-mechanical design.

7.1.3 Mounting precision of the laser diode, collimation requirement

The collimation requirement of the laser light in the horizontal direction is specified by the condition that the divergence of the collimated beam should be smaller than the divergence caused by the diffraction at the effective aperture of the Bragg cell. This is necessary to avoid producing additional wavefront distortion in the deflected laser beam. Figure 7-3 shows the geometry of a divergent laser beam illuminating the Bragg cell aperture, where the beam divergence is equal to the diffraction angle of the diffracted beam at the Bragg aperture.

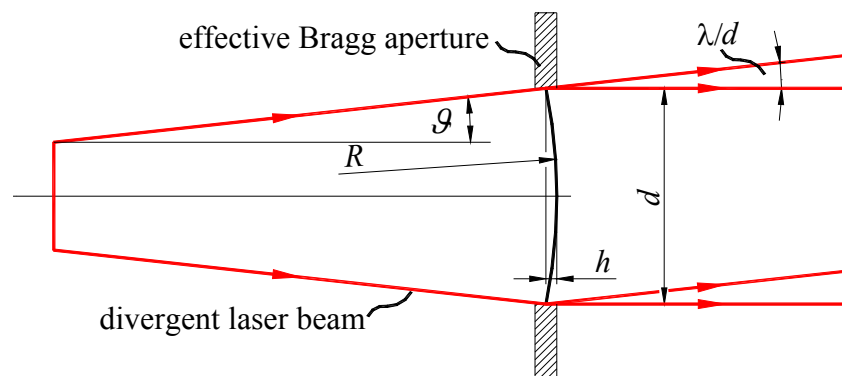


Figure 7-3 Collimation tolerance of the laser beam.

This criterion can be expressed by

$$\frac{\lambda}{d} > \vartheta, \quad (7.11)$$

d – horizontal aperture size of the Bragg-cell (5mm)

ϑ – beam divergence tolerance of the collimated laser light

Neglecting any lens aberration of the collimation optics, the wavefront of a divergent beam can be described as a spherical wavefront. The optical path difference between the plane wave and spherical wave (h) then can be expressed in terms of fractions of the wavelength. From the geometry in Figure 7-3 it can be written

$$\operatorname{tg}(\lambda/d) = \frac{d/2}{R-h}, \quad (7.12)$$

$$R^2 = \left(\frac{d}{2}\right)^2 + (R-h)^2. \quad (7.13)$$

The required collimation tolerance can be derived by solving the system of equation of (7.12) and (7.13) for h

$$h = \lambda \frac{-1 + \sqrt{1 + \left(\frac{\lambda}{d}\right)^2}}{2\left(\frac{\lambda}{d}\right)^2}. \quad (7.14)$$

Using the Taylor series of the $\sqrt{1+x^2}$ around $x \approx 0$ ($\frac{\lambda}{d}$ is very small besides 1)

$$\sqrt{1+x^2} = 1 + \frac{1}{2}x^2 - \frac{1}{8}x^4 + \dots, \quad (7.15)$$

the expression of (7.14) takes the simple form of $h \leq \frac{\lambda}{4}$.

In the most cases of acousto-optical spectrometers the $\lambda/4$ collimation quality is a sufficient requirement for the laser collimation. But, the HIFI WBO requires higher collimation accuracy if the redundant laser is involved. The images of the WBO optical system must be located exactly on the same plane, where the CCD is mounted. Otherwise, the resolution is degraded, at least for one laser. The requirement on the resolution difference attained by the main and redundant laser is specified to be $<10\%$. An equivalent definition with this requirement is that the two collimations have to agree within $\lambda/10$, as specified in [82]. To guarantee this, the mounting of the laser diodes must be very stable and the mechanical design must enable very high precision (see Section 7.3). The demand on the collimation means a certain positioning accuracy of the diode, which defines the tolerance of the distance between the collimator and laser diode. Figure 7-4 shows the collimation optics modelled as a thin lens, while the laser diode is to be placed in the focus of the lens with the tolerance of s . The positioning tolerance of the diode can be investigated by using the Gaussian beam transformation description.

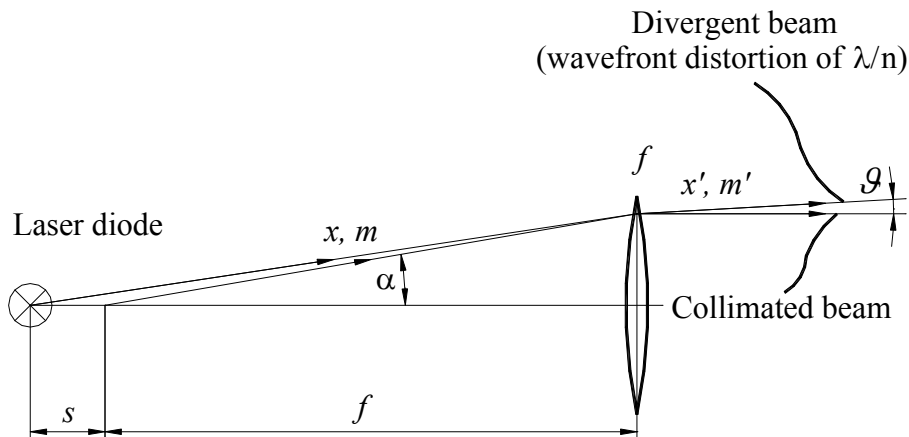


Figure 7-4 Mounting tolerance of the laser diode to achieve a wavefront distortion of λ/n , where $n \in \mathbb{N}$, $n > 4$. The symbols of x , x' , m , m' represent the beam heights and slopes, and f is the focal length of the collimation optics.

Similarly to (7.12) the divergence of the laser beam behind the collimator can be defined with

$$tg(\vartheta) = \frac{\frac{d}{2}}{R - \frac{\lambda}{n}}, \quad (7.16)$$

where the wavefront radius R corresponds to λ/n ($n=10$) wavefront distortion (relative to plane waves), as defined in (7.13). The linear relationship between the input and output beam positions and slopes are given by using the ray transformation matrix of the simple optical system

$$\begin{pmatrix} x' \\ m' \end{pmatrix} = \begin{pmatrix} 1 & f+s \\ -\frac{1}{f} & -\frac{f+s}{f} + 1 \end{pmatrix} \begin{pmatrix} x \\ m \end{pmatrix}. \quad (7.17)$$

Considering a ray, which comes from the laser diode ($x=0$) and propagates with a slope of m towards the lens, then hits the edge of the effective aperture of the Bragg cell, one has

$$x' = (f+s)m \quad (7.18)$$

$$m' = \left(-\frac{f+s}{f} + 1 \right) m. \quad (7.19)$$

Solving the system of equation of (7.18) and (7.19) for the alignment tolerance of the laser, s yields

$$s = -\frac{f}{1 + \frac{x'}{f} \frac{1}{tg \vartheta}}. \quad (7.20)$$

The term of $\frac{x'}{f}$ can be calculated from the Numerical Aperture of the collimation optics

$$tg \alpha = \frac{x'}{f}, \quad (7.21)$$

where

$$N.A. = n \sin \alpha = 0.5. \quad (7.22)$$

Thus, the equation of (7.20) takes the form of

$$s = -\frac{f}{1 + \frac{tg \alpha}{tg \vartheta}}. \quad (7.23)$$

The substitution of $\lambda/10$ wavefront distortion and $8mm$ focal length of the collimation optics yields $-0.87 \mu m$ for the mounting tolerance of the laser diode. The negative sign expresses to

which direction the laser is shifted from the position where the laser beam is perfectly collimated. In case of a shorter distance the beam is divergent, otherwise, if the $s > 0$, it is convergent.

It can be concluded that, in order to achieve the specified collimation accuracy, the distance between the laser diode and collimation optics must be aligned within a precision of $\leq \pm 1 \mu\text{m}$ for both lasers. Such an extremely high precision within the operating temperature range can only be attained with a thermally compensated design of the laser housing (c.f. Section 7.3).

7.1.4 Measurement of the collimation quality and wavefront distortion

With the AOSs built for ground applications (KOSMA Gornegrat AOSs, CSO, etc.), commercial collimating optics (made by Melles Griot [62]) are used. Their optical quality plays an important role in the spectral resolution of the instrument, because aberrations of the collimator contribute to the overall imaging errors of the whole optical system, resulting in a spot enlargement in the focal plane. Figure 7-5 shows a sample of collimations achieved with the Melles Griot collimators.

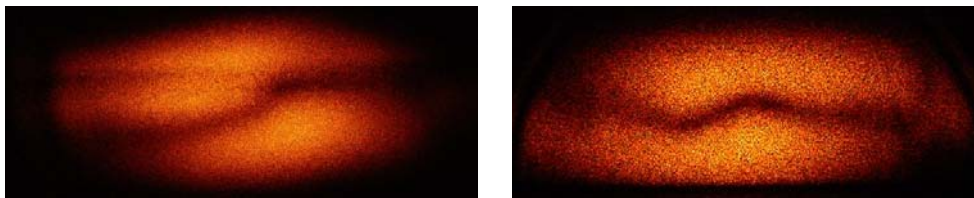


Figure 7-5 Collimation samples of laser beams achieved by the Melles Griot optics

The collimation quality is measured by means of a beam shear interferometer, which is able to reveal lens aberrations too. The measurement accuracy of the interferometer is approximately 35 arc seconds of beam divergence angle or at least $\lambda/4$ wavefront distortion [59].

Figure 7-5 verifies the good collimation quality of both samples (there are only two fringes observed), the beam divergence is of the order of the interferometer's resolution. However, the wavefront aberration is of the order of $\lambda/2$ to $\lambda/4$, which is rather large (in the pictures the ripple of the fringes have the same magnitude as the distance between two fringes, which is equal to the half of the laser wavelength). The fringes in the left hand picture correspond to a large spherical aberration combined with small astigmatism, in the right hand picture it is a combination of coma and spherical aberration [59].

Since the Melles Griot optics are not space qualified and their optical quality is also not very satisfying, a new design is chosen in collaboration with Galileo Avionica [27]. The new design of the collimating optics must satisfy the following requirements:

- the collimation quality must be $\lambda/10$ [82],
- the wavefront aberration should be below $\lambda/4$ maximum,
- no focused reflections from the lens surfaces back onto the lasers, and
- capability to cope the large horizontal divergence (23°) of the laser diode.

The small levels of collimation and wavefront aberration of the laser beams are necessary to attain the required spectral resolution of the spectrometer. For reasons of good power stability of the laser, the optical feed-back level must be kept as low as possible, which means that the

collimator should not permit focused reflections into the laser cavity (c.f. Section 9.7). The strongly divergent beam of the laser diode requires a fairly large numerical aperture (N.A.=0.5) for the collimation optics.

The design of the Galileo collimating optics is modelled with a ray tracing software (Zemax). The beam propagation is depicted in Figure 7-6.

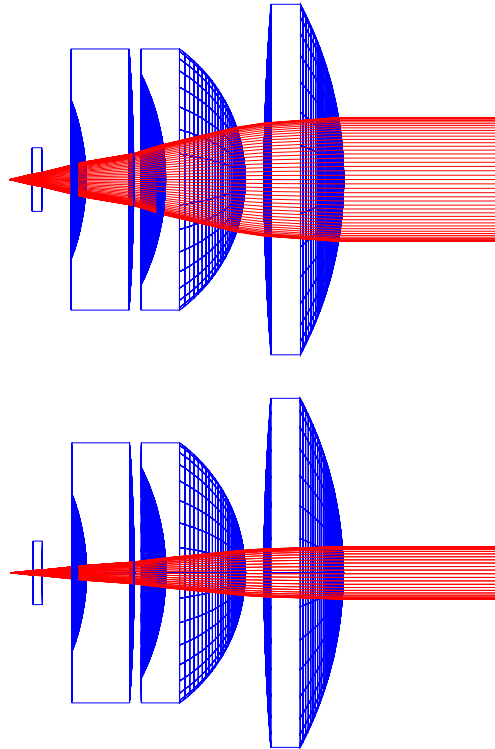


Figure 7-6 Optical design of the collimator made by Galileo. The ray tracing model performed with Zemax describes the beam propagation in the horizontal (upper) and vertical (lower) directions.

The elliptical shape of the collimated beam, shown in Figure 7-7, corresponds to the different divergence angles of the laser diode.

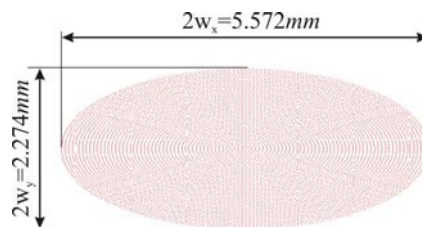


Figure 7-7 Elliptical shape of the collimated laser beam simulated with Zemax.

The dimensions of the collimated beam are calculated from the beam divergence data of the laser diode [42] (c.f. Section 6.2).

With ray tracing software, the theoretical wavefront distortion of designed collimator lens system can be analysed as well. Manufacturing tolerance and assembling error were not considered in the model, therefore the wavefront aberration describes a perfectly aligned lens

system. A three dimensional plot of the wavefront error 150mm behind the collimator is shown in Figure 7-8.

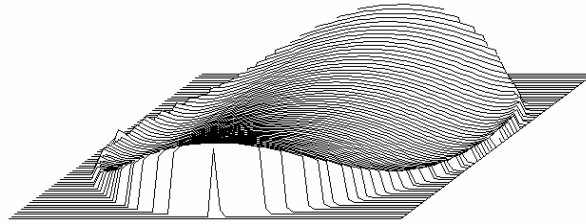


Figure 7-8 Wavefront aberration of the collimation optics. The $2\mu\text{m}$ astigmatism of the laser is taken into account.

The peak to valley distortion of the wavefront is 0.0409 waves at 785nm , which is an excellent achievement. The coloured map of the wavefront aberration in Figure 7-9 shows that the wavefront has a saddle shape, and in the horizontal direction (collimation direction in the WBO) the error is only 0.02λ .

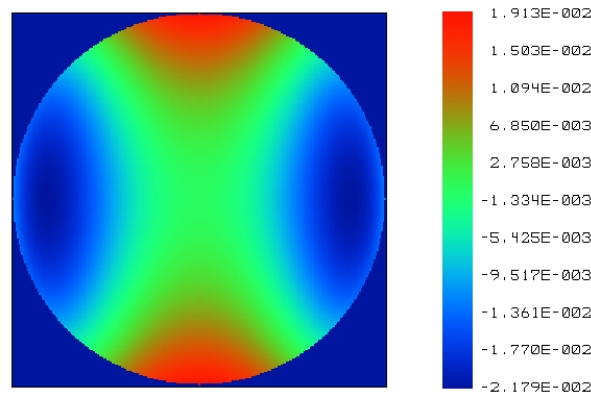


Figure 7-9 Two dimensional plot of the wavefront aberration of the collimation optics.

The performance of the manufactured collimator differs from the theoretically expected results. The lens design of the optics allows for small displacements of the single lenses without significant aberration degradation of the collimator. However, after mounting and aligning the collimator lenses it is necessary to verify the wavefront quality. Thus two measurements were carried out, one with a precise interferometer (Intomatik-N, resolution of 0.01λ) using a highly collimated beam of a HeNe laser ($\lambda = 632.8\text{nm}$). Note that at the wavelength of the laser diode, the aberrations are a factor of 1.24 smaller because of the different wavelengths. The second measurement was executed with a beam share interferometer, which has verified not only the performance of the collimation optics, but also the quality of the alignment done with the laser diode. Figure 7-10 shows an interferometric measurement of a flight model of the collimating optics taken with Intomatik-N.

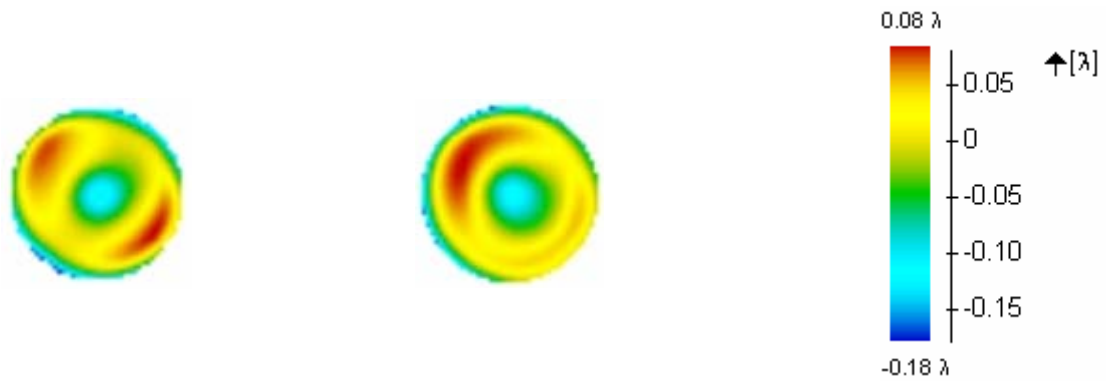


Figure 7-10 Wavefront distortion of a flight model of the collimation optics measured with the Intomatik-N interferometer at 632.8nm [27].

The interferogram of the collimator of the upper laser (left) corresponds to a wavefront error of 0.24λ (0.19λ @ 785nm) peak to valley or 0.05λ (0.04λ @ 785nm) RMS at 70% of the total aperture. The collimation optics of the lower laser (right) has a wavefront aberration of 0.26λ (0.21λ @ 785nm) P-V or 0.05λ (0.04λ @ 785nm) RMS. The results of the interferometric measurements show that the collimator lens design is adequate to achieve the required resolution of the WBO, even if the measured values are approximately a factor of 5 higher than the theoretical results.

The collimation and wavefront aberration of the Galileo collimator was verified by means of the beam share interferometer too, to be able to compare its performance with the Melles Griot optics. Figure 7-11 shows the fringes of the flight laser unit taken with the interferometer.

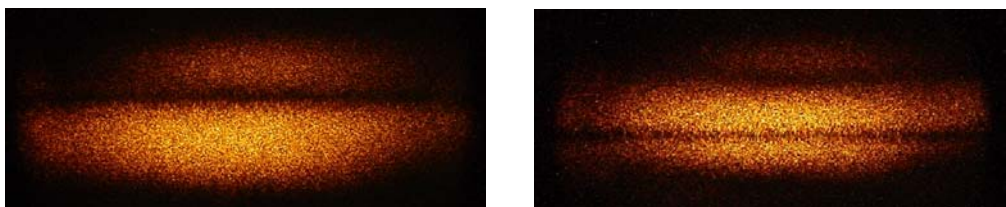


Figure 7-11 Collimation and wavefront distortion of the flight laser unit performed with the beam share interferometer.

In the interferometric pictures the small number of fringes represents a good collimation quality. The high parallelism of the fringes implies the Galileo collimator has smaller aberration errors than the beam share interferometer can resolve. This confirms not only the good lens design as well as manufacturing and assembly precision of the collimator, but reveals good positioning of the laser diode relative to the collimator.

The laser alignment accuracy, which corresponds to the collimation quality, has direct influence on the resolution of the spectrometer. If there is a positioning difference between the laser diodes, which can be an absolute deviation from the nominal positions of the lasers or a relative alignment error between the two lasers, the foci of the optical system established by the lasers are located in different planes. This results in resolution degradation, at least for one laser. To describe the imaging of a diffraction limited optical system correctly it is necessary to use a diffractive optical analysis. However, for a quantitative description of the spot size variation i.e. the resolution behaviour of the instrument as a function of the laser alignment accuracy, the quasi-optical Gaussian beam optics is used as first approximation analysis. The location and the dimension of the image waist can be calculated in terms of laser alignment

accuracy using the matrix representation of the whole optical system. Table 7-1 shows the waist shift versus laser alignment precision (relative to the nominal location of the image waist), the image waist size, and the beam radius at the nominal position of the CCD plane. These results are compared with the findings of a partly diffractive optical analysis, where the diffraction of light is considered only on the aperture of the Bragg cell, as discussed in Section 7.7.

| Laser alignment tolerance [μm] | Relative waist location [μm] | Image waist size [μm] | Gaussian analysis of the beam radius in the CCD plane ($1/e^2$ intensity contour) [μm] | | Diffractive analysis of the beam radius in the CCD plane ($1/e^2$ intensity contour) [μm] | |
|---|---|------------------------------------|--|-----------|---|----------|
| -5 | +744 | 8.772 | 22.932 | (+158.6%) | 20.58 | (+16.3%) |
| -2 | +299 | 8.829 | 12.236 | (+38.0%) | 18.19 | (+2.8%) |
| -1 | +150 | 8.848 | 9.81 | (+10.6%) | 17.82 | (+0.7%) |
| 0 | 0 | 8.867 | 8.867 | (0%) | 17.70 | (0%) |
| +1 | -151 | 8.887 | 9.848 | (+11%) | 17.82 | (+0.7%) |
| +2 | -302 | 8.891 | 12.30 | (+38.7%) | 18.21 | (+2.8%) |
| +5 | -761 | 8.965 | 23.015 | (+159.6%) | 20.70 | (+17.0%) |

Table 7-1 Transformed beam waist as a function of the laser alignment accuracy. The beam radius increase at the focus position is calculated by using the Gaussian beam propagation and partly diffractive analysis. The result of the diffractive analysis shows that the focal spot increase is in the order of 3% if there is $\pm 2\mu\text{m}$ alignment error at the laser diode.

Due to the Gaussian optical calculation $1\mu\text{m}$ relative (or absolute) positioning error of the lasers corresponds to a significant spot size enlargement at the CCD plane. This is caused by ignoring any diffraction effects on the apertures, consequently resulting in a very small horizontal spot size or short Rayleigh length.

The investigation of the focal spot size based on the diffraction calculation still does not exactly describe the beam propagation, although it rather precisely simulates the experimentally observed sensitivity of the CCD alignment. In the real optical system, the waist location is slightly different as those are calculated in Table 7-1, since the image waist size is also different. In Figure 7-12 the shapes of the transformed Gaussian beams are plotted if one laser is at its nominal position and the other is shifted by $2\mu\text{m}$ in the direction of the collimation optics.

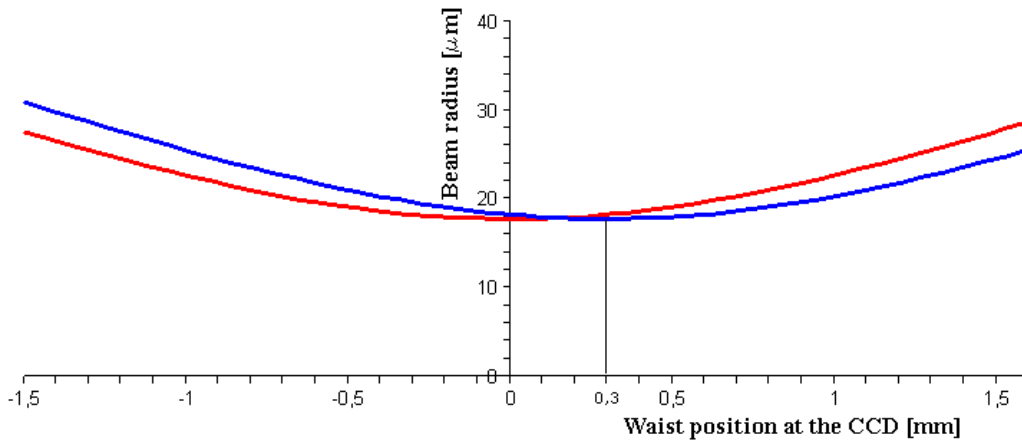


Figure 7-12 Gaussian beam transformed by the optical system of the WBO. The case of the perfectly aligned laser (red) is used as a reference position of the transformed beam waist. The $2\mu\text{m}$ alignment error of the second laser (blue) results in a focus shift of approximately $300\mu\text{m}$ and a waist enlargement of 2.8% at the CCD.

The model of the optical system used for the waist transformation of laser beams provides quite similar focal spot dimensions than measured during the performance check (c.f. Figure 7-16). Furthermore, it can be concluded that the specified maximum allowed decrease of resolution (10%) is expected at about $\pm 4\mu\text{m}$ positioning error of the laser diode.

7.1.5 Centring of the laser

Besides the adjustment of the right distance between the laser and the collimator, there is another important aspect for the collimation. Since the collimation optics have a very small field of view, the laser diode has to be placed precisely on the optical axis (*centring*), otherwise any off-axis error of the laser positioning would introduce an additional aberration. However, just this small field of view gives the possibility to centre the diode very accurately by observing the image quality in a large distance (8m).

The success of the centring procedure requires a precise production of the laser housing. Any angular errors directly affect the collimation quality and resolution, and can not be compensated for by the centring adjustment. A second effect of the machining precision is the nonparallel propagation of the main and redundant laser beams. For one frequency signal this results in a different deflection angle of the Bragg cell, therefore a different pixel number at the CCD. Even in case of small angle deviations it can happen that at the band edges the deflected light does not hit the CCD detector. The margin for such kind of angular error is specified to be <5 arc minutes [82] or an equivalent definition with this is <12 pixel.

7.1.6 Collimation procedure

The collimation of the laser light means an appropriate positioning of the laser diode relative to the collimation optics. The high precision of the alignment ($\pm 1\mu\text{m}$) is achieved by using high precision spacers between the laser flanges and the housing of the collimation optics. The optimum collimation is attained by lapping the spacer to the right thickness. The

polishing procedure also guarantees a high surface parallelism and good surface quality of the spacer, which are important to reduce additional angular errors during the assembly.

The quantitative description of the laser collimation is evaluated from the images taken with a CCD camera at two different positions. By measuring the “horizontal” beam radii at two different positions, and using the distance between the two images, the maximum beam radius change within the given distance can be evaluated. In case of a beam radius of 2.5mm , an image distance of 7.5m and the required $\lambda/10$ maximum wavefront error the maximum variation of the horizontal beam radius is 0.47mm . Such a beam radius enlargement can be easily detected by means of a CCD camera. Figure 7-13 shows the collimation images of the upper laser of a flight model taken with a CCD camera in 0.2m and 7.5m distance.

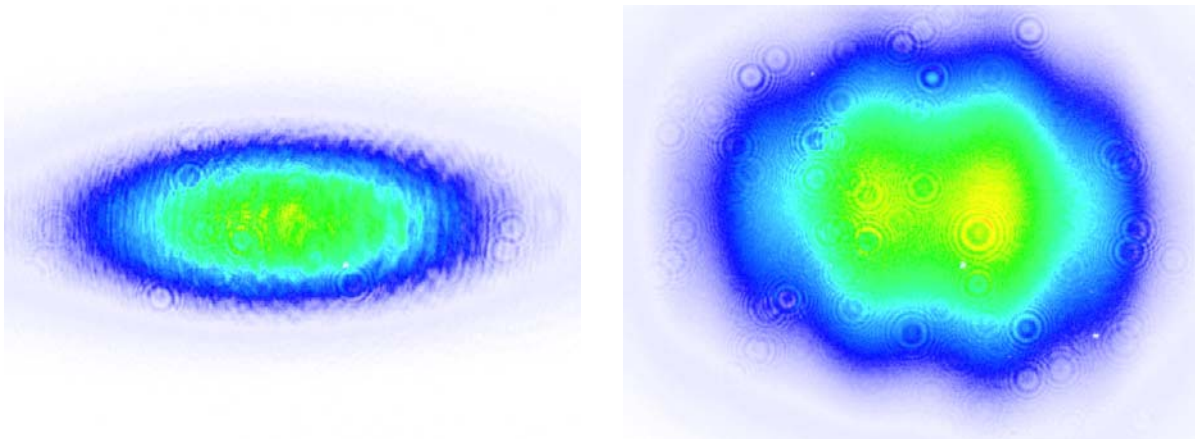


Figure 7-13 Beam profile of the upper laser unit after collimation [27]. In the picture taken at 0.2m distance (left) the beam has a Gaussian shape intensity distribution and a horizontal beam radius of 2.504mm (FWHM). In the picture taken at 7.5m distance (right) lens aberration errors can be recognised probably caused by the collimator itself and slight decentering of the laser. The horizontal beam radius corresponds to 2.550mm (FWHM).

The beam dimensions are determined by means of a fit to a Gaussian beam. From the evaluated beam radii it can be directly seen that the horizontal beam enlargement is well within the specified maximum value of 0.47mm . The beam divergence angle results in 2.65 arc seconds, which is also well in accordance with the required $\lambda/10$ maximum wavefront aberration. The vertical beam diameters behave differently due to the astigmatism of the laser. In the pictures of the collimated laser beam some interference fringes produced somewhere in the optics can be also seen. In the right picture of Figure 7-13, the two intensity maxima imply a large deviation from the Gaussian intensity distribution. This non-Gaussian beam profile is produced by the combination of adjustment errors of the laser (decentering, tilt) and aberration errors of the collimator. The collimation quality of the lower laser unit is investigated in the same way, the measured beam profiles are shown in Figure 7-14.

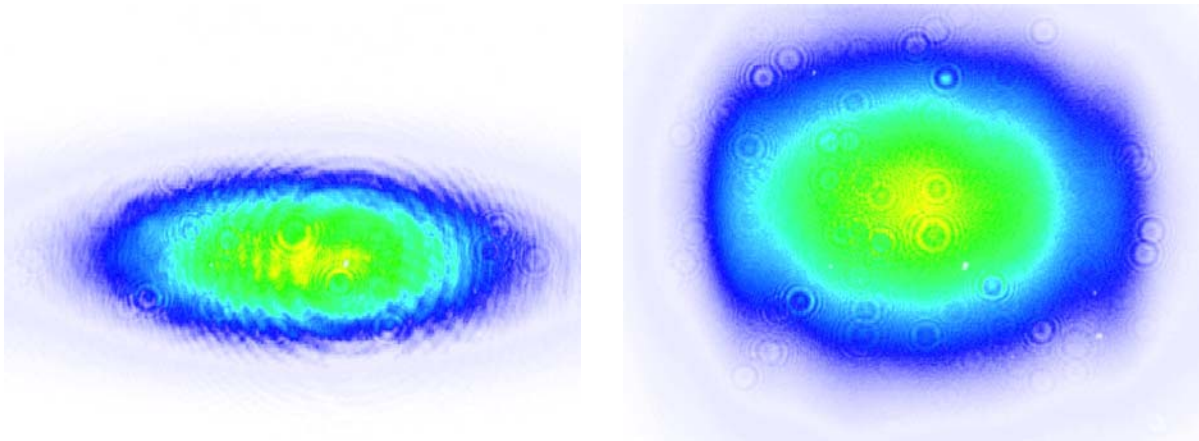


Figure 7-14 Beam profile of the upper laser unit after collimation [27]. In the picture taken at 0.2m (left) and 7.5m distance (right) the horizontal beam radius is 2.508mm (FWHM) and 2.538mm (FWHM), respectively.

From the measured beam radii, it can be directly seen that the beam divergence is less than that of the upper laser. The quite symmetric intensity profile at 7.5m reveals a good centring of the laser diode. Since the collimation procedure is iterative, the centring of the laser must be always performed after each polishing step of the spacer.

The result of the collimation procedure does not provide completely reliable information about the collimation, because the beams at 7.5m are influenced by interference effects, which may originate, for example, from a slight decentring of the laser. Thus, the Gaussian envelope of the beam could have the same width as the near field Gaussian beam width, but might still not be well collimated. If the same beam widths are found in the near and far fields, with constructive interference the laser beam could become convergent, or with destructive interference it could become divergent. The experience shows that applying the collimation procedure as described above, the accessible collimation accuracy, i.e. relative positioning tolerance of the lasers, is in the order of 2-3 μm . This precision is slightly larger than the required positioning tolerance of <1 μm , therefore the final collimation step might needed to be done after the laser unit is assembled into the spectrometer and the resolution is precisely measured for both lasers. The whole optical chain of the instrument is fairly sensitive to the collimation difference between the two lasers, because the resulting focal length of the system is very short (5.62mm attained from the optical system simulation). On the optical axis 1 μm relative position difference between the two laser diodes results in a focus position difference of 0.15mm [73], which is detectable in the resolution of the spectrometer. In principle, the imaging quality, i.e. the resolution of the optical system, can be analyzed without using the Bragg cell, because it makes only a horizontal deflection of the beam, and the additional wavefront distortion due to crystal errors and the finite aperture of the acoustic zone is irrelevant for the collimation procedure. Thus, a service optical bench was constructed, on which the imaging components of the spectrometer are aligned at their nominal positions; in the focal plane of the optical system a CCD camera is mounted on a translation stage, as illustrated in Figure 7-15.

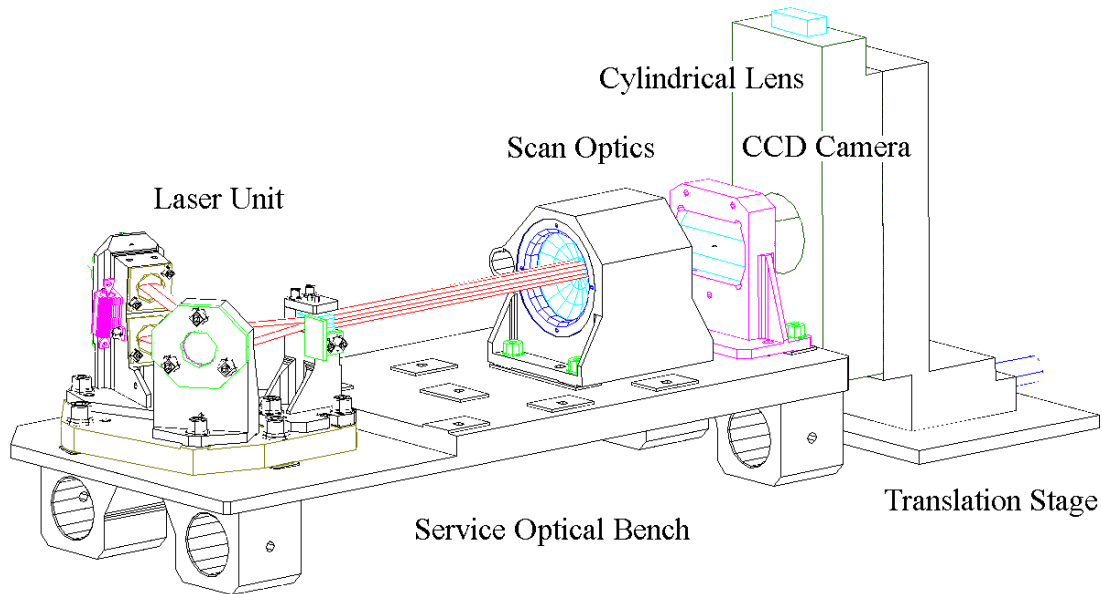


Figure 7-15 Service Optical Bench [27]. The setup is used for verifying the collimation quality of the lasers and the resolution of the optical system.

Moving the CCD camera through the focus and evaluating the actual beam dimensions, the foci of the lasers relative to each other can be found. If the collimation similarity of the lasers is high, the foci are nearly on the same plane, otherwise they are shifted by a few hundred microns on the optical axis. The measurement setup makes it possible to move the CCD camera very precisely by means of a micrometer screw. The results of the resolution performance measurement are illustrated in Figure 7-16, where the beam positions versus beam diameters (FWHM) are plotted for both lasers.

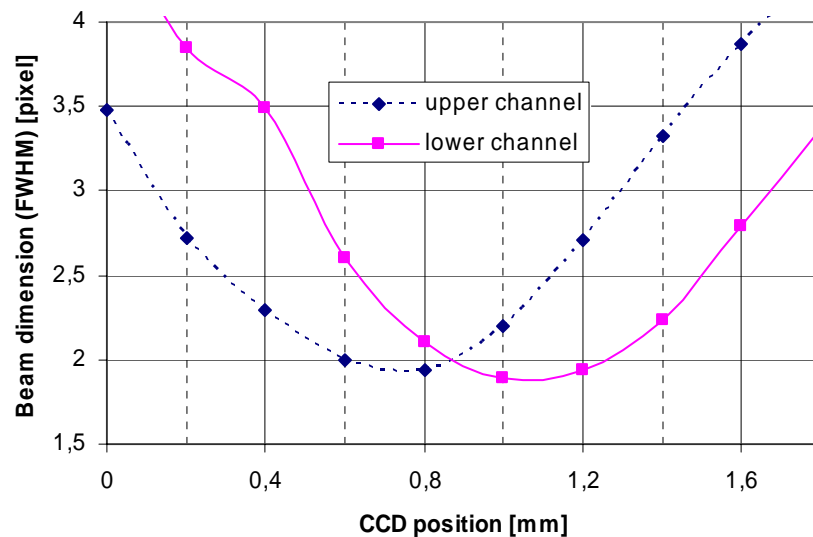


Figure 7-16 Comparison of the laser collimation. The pixel size of the CCD camera is $7.8\mu\text{m}$ [60]. The shape of the beam size versus position represents the propagation of a Gaussian beam.

Despite of the precise collimation adjustment done before, the focus analysis of the imaging system clearly shows a collimation difference between the lasers. The foci are approximately

300 μm apart, which corresponds to 2 μm relative positioning difference between the two laser diodes or a spot size difference of approximately 30% (c.f. Table 10-4). A compromise for the resolution would be position where the two curves cross. Here the spot size is 10% larger than at the focus, which is the upper limit for the resolution tolerance.

The measured minimum spot dimension (14 μm , FWHM) and the calculated spot size at the focal plane (10.4 μm , FWHM) are slightly different. This is because of manufacturing, lens assembling, and alignment errors, which degrade the imaging quality. Furthermore, diffraction effects originate from the Bragg cell becomes rather significant, since the deflector has the smallest aperture in the optical system. In addition, the optical quality of the acousto-optical material is only $\lambda/4$, which leads to further wavefront distortions. Consequently, the image size on the CCD becomes larger, and the positioning tolerance is less critical due to the increased focal depth of the imaging optics.

7.2 Beam splitter

In the WBO, the acousto-optical deflector is an array Bragg cell, which has four individual channels. For the illumination of the acoustic zones four equally-spaced parallel laser beams are needed. In the array-spectrometers that have been designed for ground-based applications so far, the deflector was illuminated by using optical phase gratings.

In case of the WBS, the arguments against its application are that the typical efficiency of such gratings is smaller than 80% [94]. The produced number of beams is usually odd (with special design it could be also even [78], but at higher losses into unwanted orders), therefore one diffraction order (+2 or -2) results in additional efficiency loss. Furthermore, in case of the WBO the coupling of a redundant laser beam with high accuracy would demand a 50-50% beam splitter, thus the remaining overall optical power of the laser, i.e. the optical efficiency of the spectrometer, is reduced by at least 4-5dB.

The large intensity loss of the grating and the coupling method of the redundant laser have made it attractive to design a unique prism beam splitter that produces four equally distanced parallel beams, and makes it possible to couple a second laser beam without introducing additional losses. Figure 7-17 shows the principal scheme of beam splitting using three commercial cube beam splitters.

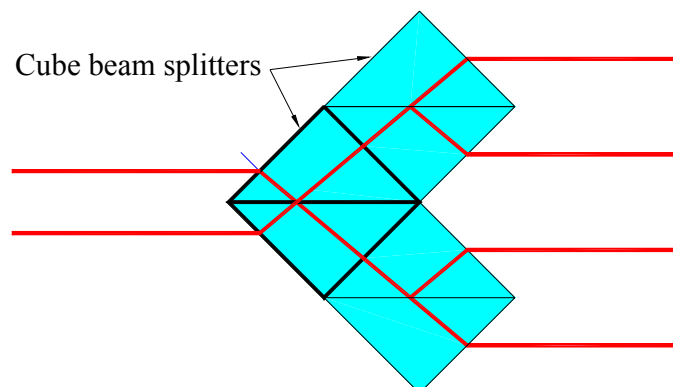


Figure 7-17 Assembly of three commercial cube beam splitters to produce four, equally distanced, parallel beams.

With the prism assembly it is possible to generate four beams. However, such a construction runs into difficulties, at least in the case of the WBO, because the $1.6\text{mm}\pm 10\mu\text{m}$ separation of the Bragg cell channels requires fairly small (2.26mm) cube beam splitters. Furthermore, the input beams must be parallel in order to produce four parallel output beams, and the separation of the input beams, which depends on the glass material as well, becomes very small. In this case, an accurate mounting of the lasers is also hardly feasible if we consider the diameter of the laser flange and of the collimation optics that are in the order of 10mm . For this reason, a custom design is approached that solves all the inconveniences of the cube prism assembly. The working principal of the beam splitter is depicted in Figure 7-18.

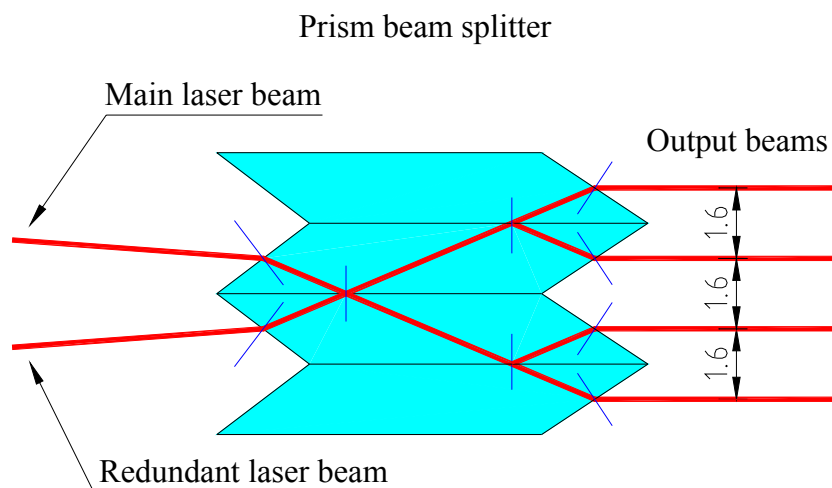


Figure 7-18 Scheme of the beam splitter. The two identical inner slabs provide the possibility to couple the redundant laser. With both lasers the beams are equally spaced.

The beam splitter consists of 4 identical glass prisms (made of BK7G18), which are coated on one surface for 50-50% beam splitting. Thus, at every connecting surface, the laser beam is refracted and reflected yielding the necessary four output beams. The input surface angles are chosen near to the Brewster angle in order to reduce reflection losses, and to guarantee adequate separation of the mechanical positions of the laser diodes. The output angles of the beam splitter are also cut under the Brewster angle. Therefore, no additional anti-reflection coating is needed. The requirements for the output beams are summarized in Table 7-2.

| | |
|--|---------------------------------|
| Beam spacing | $1.6\text{mm}\pm 10\mu\text{m}$ |
| Vertical beam parallelism | ± 10 arc minutes |
| Horizontal beam parallelism of the four output beams | 1.5 arc minutes |
| Maximum intensity variation between the four beams ($I_{\text{max}}/I_{\text{min}}$) | 20% (10% goal) |
| Horizontal parallelism between the main and redundant laser | 5 arc minutes |
| Beam orientation error between two output beams | ± 10 arc minutes |

Table 7-2 Requirements for the beams that illuminate the acoustic zone of the Bragg cell.

Beam spacing

To guarantee the adequate illumination of the Bragg cell, i.e. to achieve the maximum diffracted light intensity, the laser beams must precisely hit the acoustic zones of the deflector. Due to the small height of the acoustic zone ($80\mu\text{m}$ at the transducer side) and the small vertical dimension of the focused laser beam, the tolerance of the beam spacing is very tight ($\pm 10\mu\text{m}$). Furthermore, the beam spacing is also influenced by the “vertical” beam angles, as depicted in Figure 7-19. The alignment of the whole beam splitter must be done with the same precision, otherwise the instrument rapidly loses its optical efficiency (c.f. Section 7.7.3).

Vertical beam parallelism

The alignment of the source module relative to the Bragg cell is possible by over-dimensioning holes on the source unit baseplate. The adjustment range of the holes is $\pm 1\text{mm}$, within which the beam spacing may not significantly change, because any acoustic zone mismatching reduces the diffracted light intensity. The $\varphi = \pm 10$ arc minutes vertical beam parallelism, shown in Figure 7-19, corresponds to approximately $\pm 6\mu\text{m}$ beam spacing tolerance (over the 2mm adjustment range).

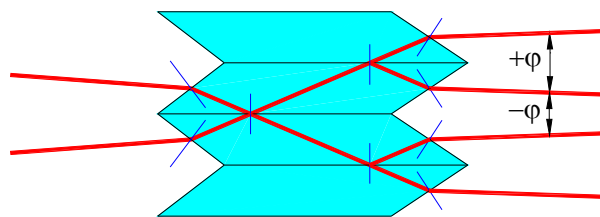


Figure 7-19 Vertical beam parallelism error. In the vertical plane parallel to the optical axis parallelism errors are introduced ($\pm\varphi$) by the angular errors of the input beams or the beam splitter slabs.

Horizontal beam parallelism of the four output beams

The relative horizontal angles of the laser beams have great importance for the frequency bandpass of the WBO. A small beam angle difference results in different focus position at the CCD in the horizontal plane. Since the number of the CCD pixels reserved for adjustment tolerances is very limited, the angular error of the beams cause that at the band edges the focal spot does not hit the detector.

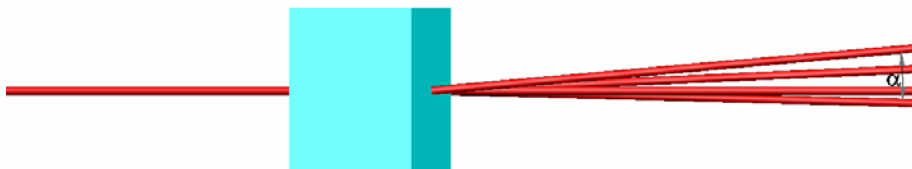


Figure 7-20 Horizontal angle error of the output beams. Only the propagation of the chief ray is depicted.

Intensity variation

The intensity variation of the four output beams of the beam splitter affects the strength of the four CCD signals. Since the dynamic range of the CCD and the IF attenuation range are

limited, there exists a tolerance on the intensity variation of the illuminating beams. This is specified to be 20% (I_{\max}/I_{\min}), which has consequences for the tolerance of the splitter coating. Assuming a transmission coefficient of $t=50\%$, a reflection coefficient of $r=50\%$, and their tolerance of $\Delta t = -\Delta r$, the intensity variation of the beams is given by

$$\frac{I_{\max}}{I_{\min}} = \frac{(r + \Delta r)^2}{(r - \Delta r)^2} = 1.2 \quad (7.24)$$

from which the allowed maximum deviation of the reflection, i.e. transmission coefficient, is $\Delta r=2.3\%$. The transmission curve of the splitting coating made by JENOPTIK Laser, Optik, Systeme GmbH [46] is depicted in Figure 7-21.

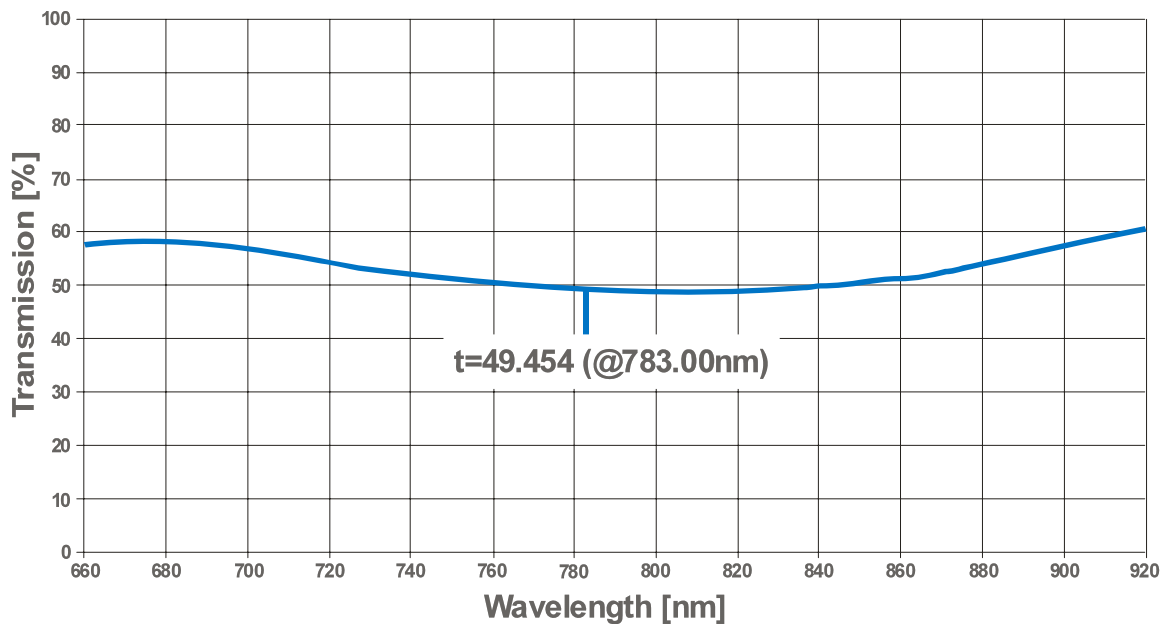


Figure 7-21 Transmission coefficient of the splitting coating versus wavelength in case of 61.7 degree angle of incidence (this is the angle of reflection within the prism) and p-polarization (“vertical”) of the laser beam [46].

At the operation wavelength of the laser (typically 783nm) the transmission coefficient is well within the required tolerance and the intensity variation is expected to be better than 10%.

Horizontal parallelism between the main and redundant lasers

The centring error of the laser diodes, the assembling precision of the collimator, and the mechanical tolerances of the housing produce parallelism error between the main and redundant laser in the “horizontal” plane. Similar to the horizontal angle errors of the output beams, this error results in a horizontally shifted focus position on the CCD for the two lasers if the same input IF frequency signal was applied. The limited number of the CCD pixels reserved for alignment errors represents a tight angle tolerance for the laser beams, because of the large distance between the deflector and the CCD. The maximum deviation between the spots of the main and redundant lasers is specified to be less than 10 CCD pixels (150 μm), which corresponds to a maximum horizontal parallelism error of <5 arc minutes.

On the other hand, the effect contributes to the vertical parallelism error of the four output beams. The input laser beam is reflected by an even and odd number within the beam splitter

7.3 Opto-mechanical design of the laser source unit

resulting in a different vertical propagation direction. The beams reflected twice undergo the largest propagation angle change. The vertical parallelism error scales with a factor of 0.56 of the horizontal angle between the input laser beams.

Beam orientation error between two output beams

The four elliptical spots of the laser unit must be parallel to the acoustic zones of the Bragg cell, as shown in Figure 7-22, to guarantee the optimal performance of the WBO. The angle error is introduced by the orientation error of the cylindrical lens and various angular errors of the beam splitter. The tolerance of ω is specified to be $<\pm 10$ arc minutes.

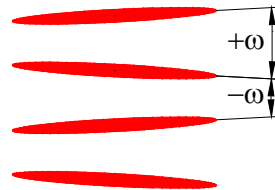


Figure 7-22 *Beam orientation at the focus of the laser unit*

In the focus of the laser unit, the angular errors of the beam splitter can be compensated for by rotating the cylindrical lens, yet in the focus of the whole optical system (CCD plane) the focal spots of the four channels are shifted horizontally relative to each other.

7.3 Opto-mechanical design of the laser source unit

During the opto-mechanical design of the source unit the following concepts are considered. The unit must have small size and low weight, but should provide maximum mechanical stability and remain insensitive against thermal changes. These criteria are applied during the development phase for all components of the source module components: laser unit, folding mirror, beam splitter holder and interface plate.

As has been already shown in Section 7.1.3, the relative position between the laser diode and the collimation optics must be stable within an accuracy of $\pm 1\mu m$. This can be attained by using materials with low thermal expansion, while keeping the length of the supporting parts as short as possible. Thus, the housing of the laser unit is made of titanium, the laser flange and the spacer ring out of stainless steel although it has a larger thermal expansion coefficient. But, stainless steel improves the heat conduction for the laser diode. The reference surfaces of the collimator lenses and the laser flange are chosen to have the shortest expanding length (4.2mm), as is shown in Figure 7-23. Note that the stability of the position of the collimator lens, which is placed near to the laser diode, is of particular importance.

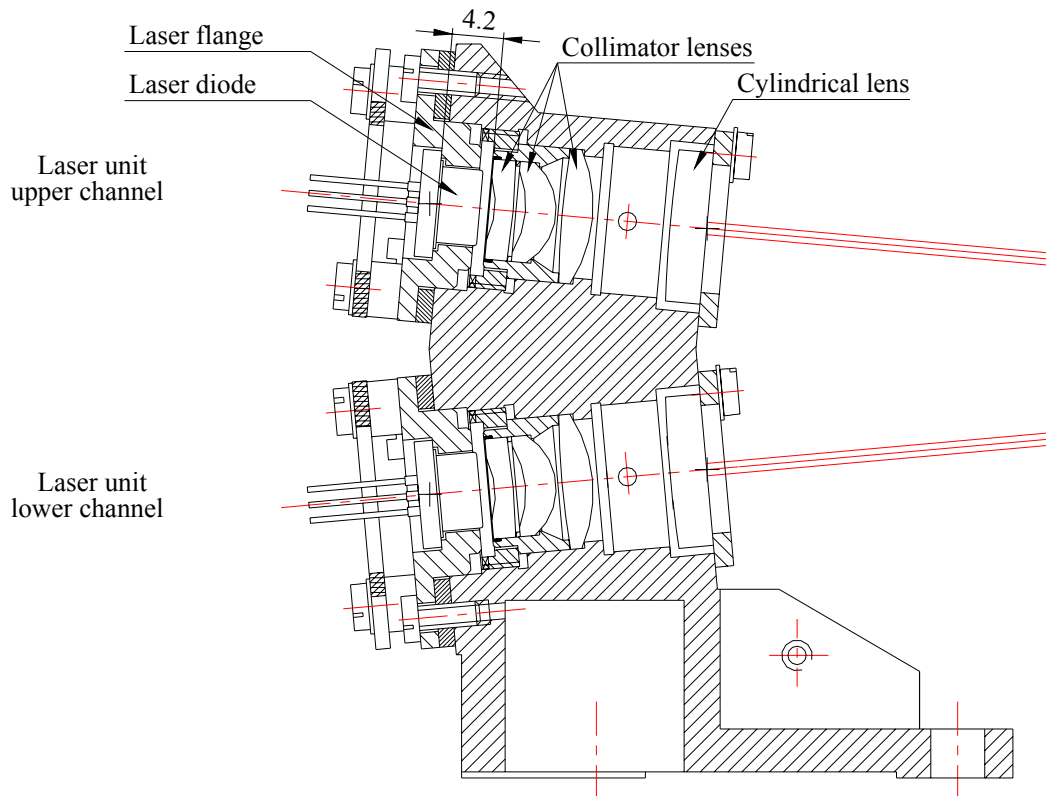


Figure 7-23 Mounting of the laser diode

Using the linear thermal expansion coefficient of titanium ($\alpha_0 = 10.8 \times 10^{-6}$) and stainless steel ($\alpha_0 = 16 \times 10^{-6}$), and applying the exact distances between the reference surfaces, the corresponding thermal expansion over the 10 degree operation temperature range yields approximately 0.65 micron.

Another important issue is that the laser lifetime strongly depends on its operating temperature. Since the thermal conductivity of stainless steel is fairly poor and the contact surface between the laser and the flange is very small, the diode is almost thermally isolated. In order to dissipate the heat of the laser and provide a larger contact surface, the mounting of the laser diode is done by means of a copper ring, as shown in Figure 7-24.

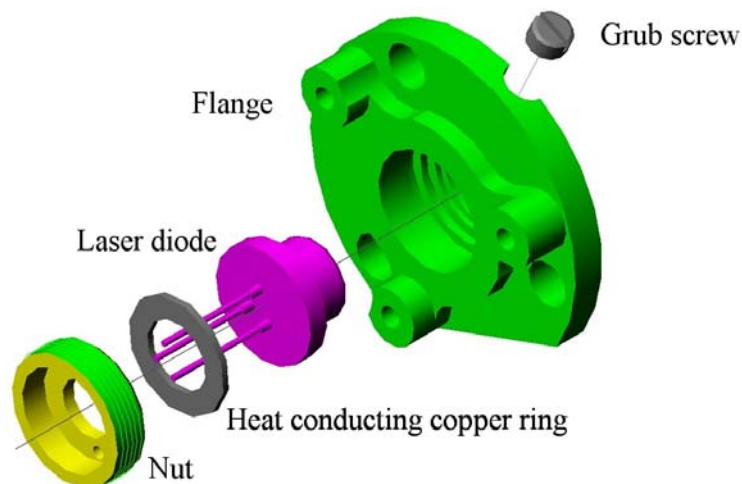


Figure 7-24 Close-up view of the laser mounting

To make the whole source module as compact as possible, a folding mirror is applied. The support of the mirror must guarantee that the optical path between the laser and the beam splitter does not change, and must provide a good angular stability for the mirror. By properly choosing of the supporting surfaces, the required positioning accuracy of the mirror is attained. The high stiffness is provided by the rigid supporting structure, and the low weight is achieved by using a space qualified aluminium alloy (AlMg4.5Mn0.7, AA 7075-T7351).

Due to the heat dissipation of the laser diode its temperature is actually a few degrees higher than that of the WBS baseplate. This means that the temperature of the spectrometer will always change when the laser is switched on and off, resulting in a spectroscopic stability problem and large warm up time of the instrument. In order to reduce such effects, a dummy resistor is mounted on the housing of the laser source unit. The resistor is switched on while the laser is off maintaining a quasi thermal equilibrium in the WBS.

7.4 Performance results of the source unit

In order to be able to measure the beam angles and distances with an accuracy of a few microns and arc minutes for all four beams simultaneously, it was necessary to develop a special test setup. The principle of the measurement technique is based on a linear CCD placed on an X-Y translation stage, which is controlled by a PC. The CCD line detector is mounted in the vertical plane (perpendicular to the optical axis) and moved across the beams of the source unit performing a beam scan, as shown in Figure 7-25.

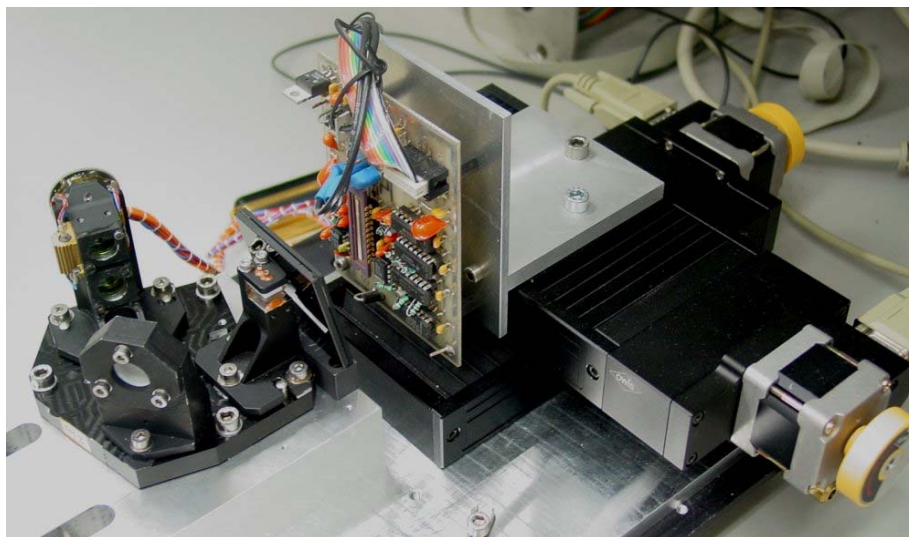


Figure 7-25 Test setup of the source unit. The CCD line detector is placed on the translation stages providing an accurate sampling of the laser beam in x and y direction.

The software tool (written for DADA [91]) allows nearly real time analysis of the laser beam parameters on a graphical surface. The number of scans is adjustable, but even a few tens of scans provide the necessary measurement accuracy. After each measurement a Gaussian fit is applied, then the maximum intensities and peak positions of the fitted data are plotted versus the horizontal beam position. The linear fit of these intensity maximums describes the orientation and beam interdistances of the output beams. Performing the beam scanning in two different planes (along the optical axis) the mutual parallelism of the beams can be also evaluated by the software. The precise movement of the translation stages ($0.6\mu\text{m}$ per step) guarantees a very good reproducibility and stability of the measurement. The achieved

precision is $2-3\mu\text{m}$ for the beam interdistances, and 2 arc minutes for the horizontal beam orientation and mutual beam parallelism. This high precision is accomplished with a CCD pixel size of $13\mu\text{m}$.

The performance of the four output beams measured by the measurement setup is summarized in Table 7-3.

Upper channel

| | |
|---------------------------------------|------------------|
| Focus position [mm] | 31/30/30/30 ±1 |
| Interdistances (1-2;2-3;3-4) [μm] | 1594/1592/1604 |
| Interdistances (1-3;2-4) | 3185; 3195 |
| Mutual parallelism [arc min] | -13.7/-0.1/+14.4 |
| Horizontal beam orientation [arc min] | ±0.55 |

Lower channel

| | |
|---------------------------------------|------------------|
| Focus position [mm] | 31/30/30/30 ±1 |
| Interdistances (1-2;2-3;3-4) [μm] | 1592/1595/1601 |
| Interdistances (1-3;2-4) [μm] | 3186; 3195 |
| Mutual parallelism [arc min] | -13.5/+0.1/+13.5 |
| Horizontal beam orientation [arc min] | ±0.55 |

| | |
|---|-----|
| Horizontal angle between the main and redundant laser [arc min] | 3.2 |
|---|-----|

Table 7-3 Source unit performance of a flight spare model.

The analysis of the intensity profile of the four beams and the intensity distribution verification in the focus of the cylindrical lens are part of the final performance analysis. The intensity profile could be distorted due to alignment errors of the collimator, therefore measurements were carried out with a CCD camera. The image of the four beams taken in the focus of the cylindrical lens is shown in Figure 7-26.

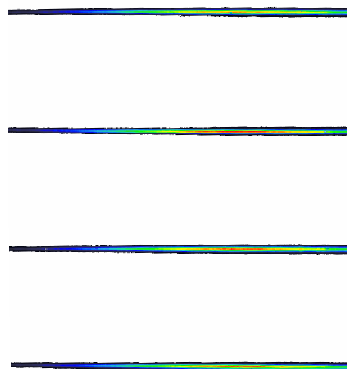


Figure 7-26 Beams of the flight laser model in the focus of the cylindrical lens (Bragg cell plane).

The intensity profile of one of the beams evaluated by software is depicted in Figure 7-27.

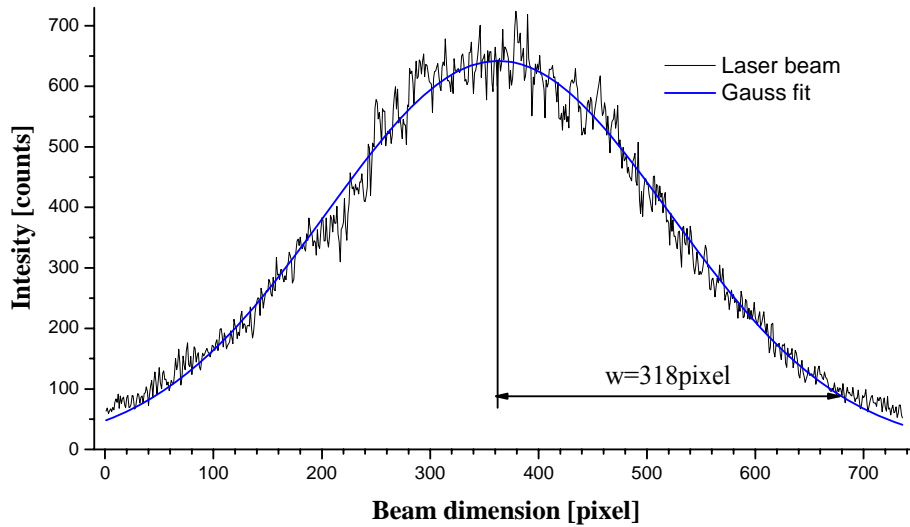


Figure 7-27 Intensity profile of one output beam of the source unit. The red line denotes the Gaussian fit of the beam, whose waist dimension corresponds to about $2.765 \pm 0.006 \text{ mm}$ (pixel size of the camera is $8.695 \times 9.917 \mu\text{m}$). The horizontal beam dimension is well in agreement with the theoretically calculated value of 2.786 mm .

The quality of the beam splitter coatings can be compared with the values measured by [46]. The peak intensities in the image vertical direction, as shown in Figure 7-28, indicate a very small difference between the beams, i.e. good performance of the beam splitter coating.

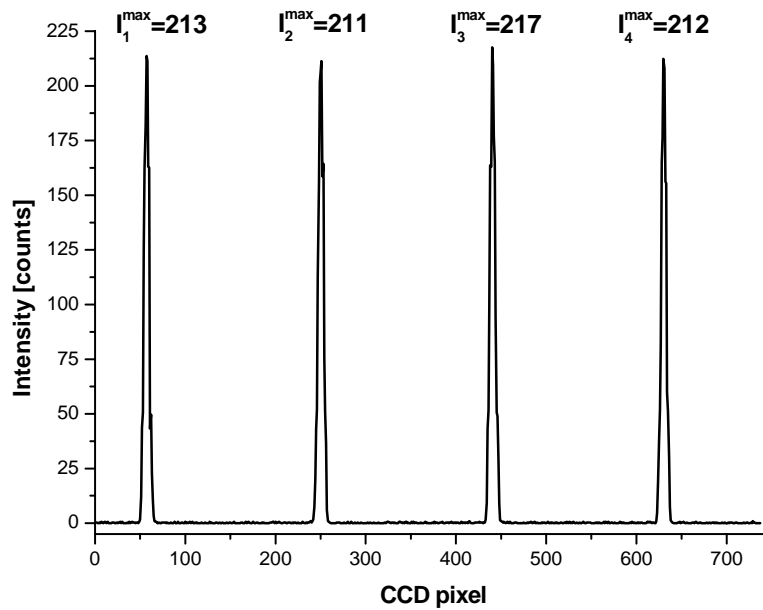


Figure 7-28 Intensity distribution of the four beams. The vertical waist size is in the order of $40 \pm 5 \mu\text{m}$ (theoretically expected value is $33 \mu\text{m}$).

The intensity variation is in the order of 3%, which is well within the specification (20%).

7.5 Bragg cell

The deflector applied in the WBO is a four-channel array Bragg cell provided by ASI³⁴ with collaboration of the institute of CAISMI³⁵. The special design of the Bragg cell (made by [4]) uses one large crystal to accommodate the four acoustic channels. The acousto-optical material of the deflector is anisotropic lithium-niobate. At the design wavelength of $785nm$ this material provides high diffraction efficiency ($>10\%/Watt$) due to the low acoustic velocity and low acoustic attenuation of the crystal. Actually, the array deflector provides two application possibilities: the hybrid mode, where the channels are merged into one large bandwidth by using additional IF processing electronics; and the array mode, where the individual channels of the Bragg cell process the signals of an array receiver, like STAR³⁶ or SMART³⁷. The bandwidth of one deflector channel is $1GHz$, but, using the array arrangement, $4GHz$ bandwidth is achieved. The design of the light weighted Bragg cell is shown in Figure 7-29.

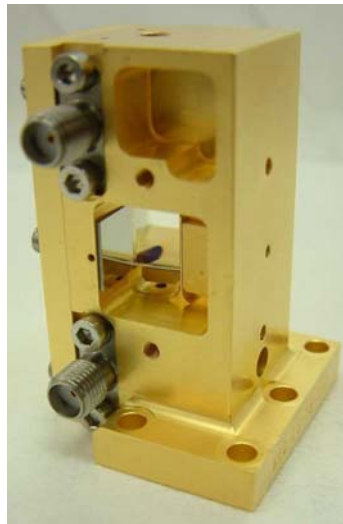


Figure 7-29 Photo of the flight model of the Herschel Bragg cell (MRQ-IS-FM001). The optical height of the deflector is 25mm. The mirror in front of the crystal is intended to reduce the light scatter coming from the package.

7.5.1 IF frequency coupling

To couple the IF frequency ($1.55-2.65GHz$) into the crystal there are four transducers attached to the crystal surface, as shown in Figure 7-30. A spacing of $1.6mm\pm 10\mu m$ was chosen for the four transducers, in order to guarantee a low level of acoustic cross talk.

³⁴ Agenzia Spaziale Italiana (Italian Space Agency)

³⁵ Centro per l'Astronomia Infrarossa e lo Studio del Mezzo Interstellare (National Research Council of Italy, Astronomical Institut for Interstellar Medium Exploration)

³⁶ German Receiver for Astronomy at Terahertz Frequencies

³⁷ SubMillimeter Array Receiver for Two Frequencies

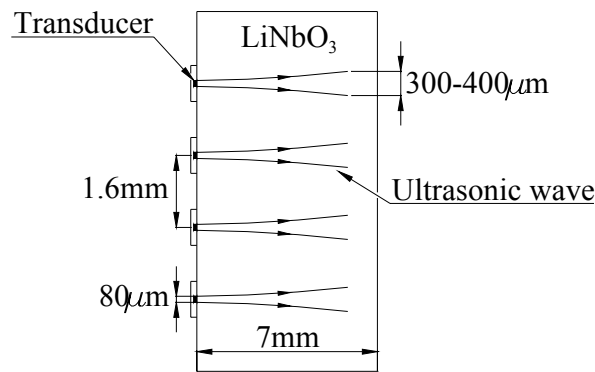


Figure 7-30 Arrangement of the ultrasonic waves

The output impedance of the IF unit is specified to 50Ω, which should be matched to the input of the deflector. The simplest solution for that is to use the bond-wires of the device's electrical interconnects as an impedance matching network, shown in Figure 7-31. By changing the length of the bond-wires, the resonance and the impedance can be adjusted [47].



Figure 7-31 Matching network of the bond-wires [47]. The IF signal is fed into the acousto-optical crystal by means of a transducer array, which provides a couple of bonding possibilities. In the picture, the micro-strip boards correspond to channel 1 and 2 of the deflector. With the length of the parallel bond-wire the inductance can be matched to become low SWR.

The result of the coupling quality can be examined by measuring the standing wave ratio (SWR). A typical VSWR attained with the flight hardware varies between 1:1.1 and 1:1.61 within the frequency range of 1.55-2.65GHz [47]. This implies that the reflected power from the transducer is less than 10%.

7.5.2 Bandpass performance

The bandpass shape of the deflector strongly depends on the crystal cut. In an optimized illumination configuration (with 1μs aperture time centred at 1.73mm from the transducer face) the frequency response of the deflector was measured. The results are plotted in Figure 7-32 [47].

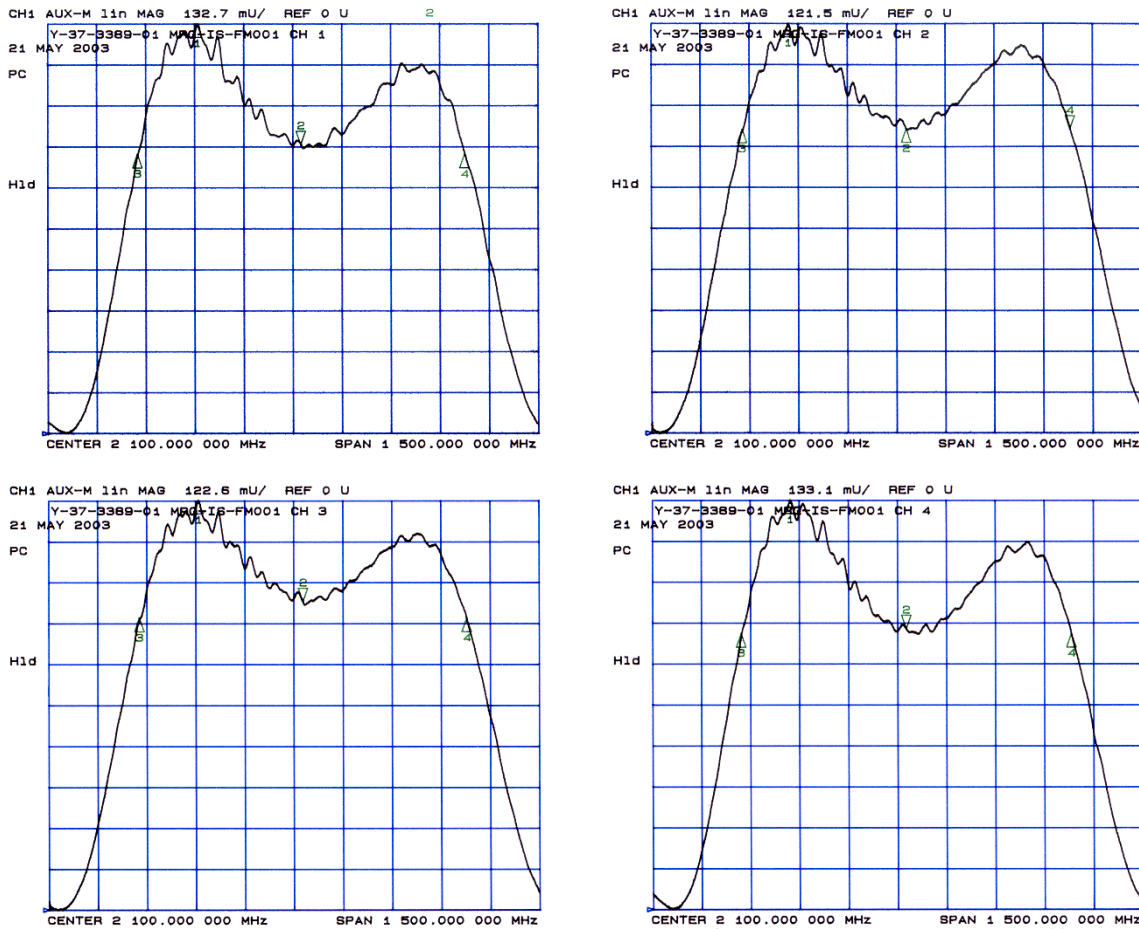


Figure 7-32 Bandpass of the four channels of the Bragg cell (flight model)

During the measurement, the centre frequency was optimized to have the smallest bandpass ripple over the 1GHz frequency span. Thus, the best achieved acousto-optical bandshape variation over a 1GHz bandwidth at the centre frequency of about 2.13GHz is between 1.3 and 1.7dB.

7.5.3 Acousto-optical cross talk

Interchannel crosstalk may originate from diffraction effects of the acoustic wave on the transducer and from an electrical coupling between the bond-wires. Since the vertical dimension of the acoustic wave within the useful interaction length is much smaller (about $400\mu\text{m}$ [63]) than the spacing of the acoustic channels (1.6mm), seen in Figure 7-33, the acoustic cross talk is extremely low.

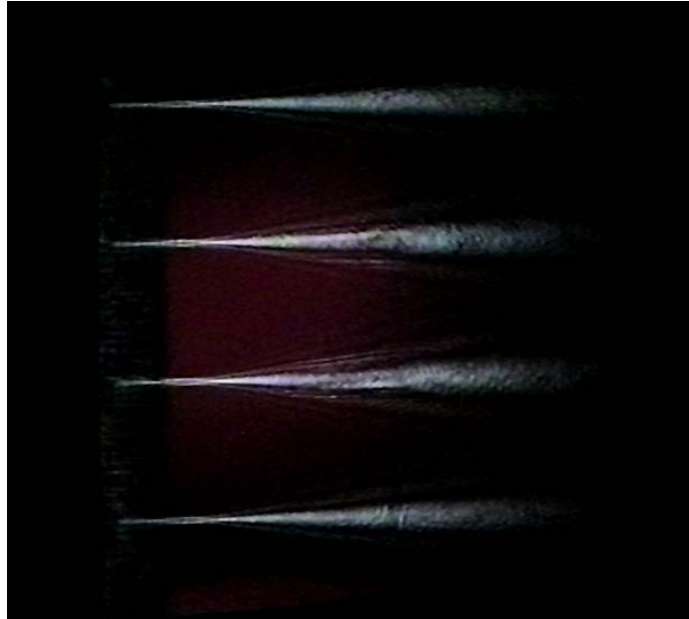


Figure 7-33 Ultrasonic waves in the Bragg cell. An adequate separation of the acoustic fields provides low level of acoustic crosstalk. In the picture, the ultrasonic wave propagates from the transducer side (left) to the right. The divergence of the acoustic waves and the higher diffraction orders are well recognizable.

The electrical coupling between the layout and bond-wires is more detectable but still a weak effect. The measured results are excellent: between adjacent channels the electrical cross-talk levels are typically around $-35dB$, and for non-adjacent channels around $-50dB$ [47].

7.6 Illumination of the Bragg cell

The intensity of the ultrasonic wave decreases with increasing distance from the transducer because of absorption and dispersion effects in the crystal and the diffraction on the transducer itself. This results in an effective acoustic interaction length, the so-called effective aperture of the deflector. The dimension of the effective aperture defines the spatial resolution of the deflector as follows (c.f. Section 4.3). The product of the aperture time and the bandpass of the Bragg deflector define the number of resolvable spots (4.28). From the aperture time (τ), which is the time required for the acoustic wave to pass through the acoustic zone, and from the velocity of the ultrasonic wave, the acoustic aperture length can be determined. This yields the following expression for the number of resolvable spots N

$$N = \frac{\Delta\mathcal{G}}{\delta\mathcal{G}} = \Delta f_a \tau = A_{eff} \sqrt{\frac{2 \cdot 3.6n \cos \mathcal{G}}{\lambda L}}. \quad (7.25)$$

To achieve high resolution with the deflector the acoustic materials must allow for large acoustic apertures (crystals with small attenuation), and applying large transducer width (small acoustic divergence) and short laser wavelength is preferable. Previous investigations have shown that the resolution can be increased by using a decentred illumination of the deflector, as shown in Figure 7-34 [56].

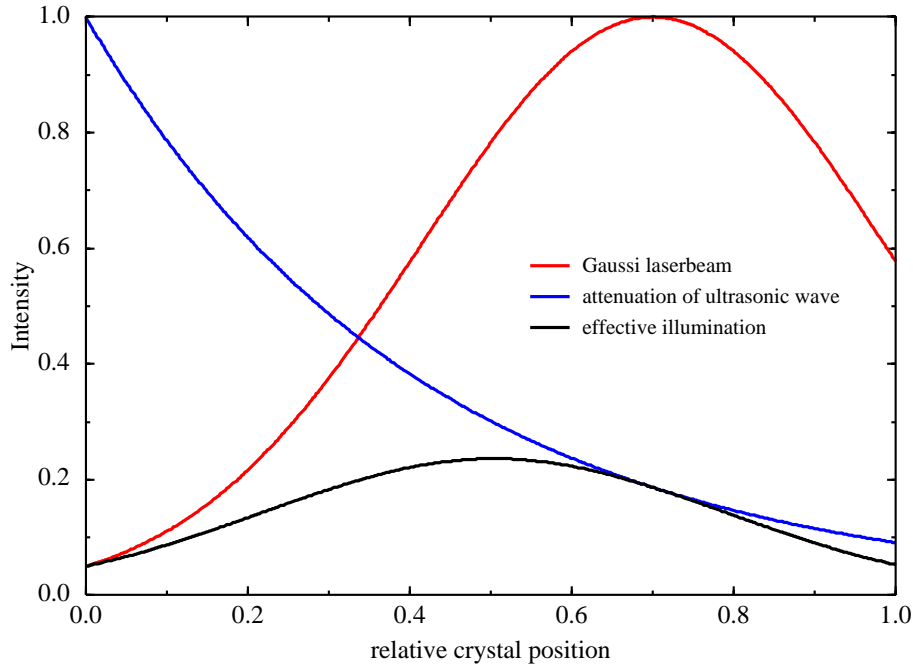


Figure 7-34 Optimized illumination of the Bragg deflector, supposing an exponential attenuation of the ultrasonic wave.

With this optimized illumination, absorption effects can be compensated further away from the transducer, which results in a larger effective aperture of the Bragg cell. Theoretically, the decentred illumination function can be expressed as the product of the amplitude profile of the Gaussian laser beam and the exponential attenuation function of the crystal

$$f(x) = E(x) \cdot S(x) = e^{-\frac{(x-x_0)^2}{w_0^2}} \cdot e^{-\frac{\Gamma_x}{2}x}, \quad (7.26)$$

where

- x_0 – is the position of the maximum amplitude of the laser light,
- w_0 – is the waist dimension of the laser light, and
- Γ_x – is the attenuation coefficient of the acoustic wave.

The product is also a Gaussian function having smaller amplitude, and is shifted in the “horizontal” direction. For a given useful aperture of the Bragg cell the achievable maximal resolution results in an optimum horizontal laser beam width of (see Eq. 7.1)

$$w_0^{FWHM} = 0.673 \cdot A. \quad (7.27)$$

7.7 Diffraction on the Bragg cell - Theoretical resolution of the WBS

During the optical system optimization, the spot size at the CCD is calculated neglecting any diffraction effects or lens aberrations. In the following, the laser light diffraction on the effective aperture of the Bragg cell is investigated in more detail, as it is the smallest aperture in the imaging optics and therefore limits the smallest reachable dimension of the focal spot, i.e. the achievable maximum resolution. The model used for the diffraction calculation is able to deal with lens aberration effects; thus, it provides an appropriate description of practically

achievable resolution bandwidths of the spectrometer (c.f. Section 10.8). Further important aim of the calculation is the simulation of various alignment errors and their impact on the filter function of a frequency channel.

In the Bragg cell the acoustic wave is diffracted on the rectangular shape transducer resulting in a diffraction pattern similar to from the optics known $\text{sinc}^2(x)$ function (see Figure 7-33). To keep the model as simple as possible, the three-dimensional acoustic field is approximated by a two-dimensional Gaussian beam that propagates in the vertical direction and has nearly the same dimension as the ultrasonic wave. The model of the Bragg aperture properly describes the frequency dependent dimension of the acoustic field, moreover comprises the frequency dependent acoustic attenuation.

The image plane of the optical system is located far away from the Bragg cell, thus the description of Fraunhofer diffraction is suitable for studying the diffraction phenomenon of aperture of the deflector. The electromagnetic field function at the image plane is given by [9]

$$E(x, y) = \iint G(\xi, \eta) e^{-ik(x\xi + y\eta)} d\xi d\eta, \quad (7.28)$$

where $G(\xi, \eta)$ is the normalized pupil function. In the case of the Bragg cell, the pupil function is a composition of the following functions:

- divergent acoustic wave due to the diffraction on the transducer,
- the acoustic attenuation function (in the direction of the ultrasonic wave propagation),
- the laser field distribution in the vertical direction, and
- the laser field distribution in the horizontal direction.

The amplitude of the divergent ultrasonic wave is described by the normalized Gaussian beam function

$$A_U(\xi, \eta) = \sqrt{\frac{2}{\pi w_S^2(\xi)}} e^{-\frac{\eta^2}{w_S^2(\xi)}}, \quad (7.29)$$

where

- ξ – is the horizontal coordinate at the Bragg cell,
- η – is the vertical coordinate at the Bragg cell, and
- $w_S(\xi)$ – is the waist function of the ultrasound defined by

$$w_S(\xi) = w_{S0} \sqrt{1 + \left(\frac{v_S \xi}{\pi f w_{S0}^2} \right)^2}, \quad (7.30)$$

where

- v_S – is the velocity of the ultrasound,
- f – is the frequency of the ultrasound, and
- w_{S0} – is the vertical waist of the ultrasound (or vertical dimension of the acoustic wave at the transducer).

The acoustic attenuation of the crystal can be approximated by an exponentially decaying function. Its amplitude as a function of acoustic frequency and position is expressed by

$$\Gamma(f, \xi) = \Gamma_0 e^{-\frac{\alpha(f)\xi}{2}}, \quad (7.31)$$

where Γ_0 is a normalizing factor and $\alpha(f)$ is the frequency dependent coefficient of acoustic attenuation per meter. In the crystallography the acoustic attenuation is given in the time domain in $dB/\mu s$ by the empirical formula of

$$\alpha^*(f) = 1.31f^{1.77}, \quad (7.32)$$

where the frequency f is meant in GHz , thus a correction factor $(\frac{\ln(10)}{10v_a t_A})$ must be considered

for the attenuation coefficient used in $[1/\text{length}]$ units during the calculation. The normalization of the acoustic wave is chosen to have the same horizontal effective aperture D within the Bragg cell for different acoustic frequencies. This concerns the diffracted light intensity variation caused by the frequency dependent attenuation coefficient. Thus, the amplitude function of the acoustic wave takes the form of

$$\Gamma(f, \xi) = \frac{1}{\sqrt{D}} e^{-\frac{\alpha(f)\xi}{2}}. \quad (7.33)$$

The relative acoustic power within the aperture of the Bragg cell is calculated by

$$\int_0^D \left| \frac{1}{\sqrt{D}} e^{-\frac{\alpha(f)\xi}{2}} \right|^2 d\xi = \frac{1 - e^{-\alpha(f)D}}{\alpha(f)D}. \quad (7.34)$$

The decaying acoustic wave is then described by the multiplication of (7.29) and (7.33)

$$A_s(\xi, \eta) = \frac{1}{\sqrt{D}} \sqrt{\frac{2}{\pi w_s^2(\xi)}} e^{-\frac{\alpha(f)\xi}{2}} e^{-\frac{\eta^2}{w_s^2(\xi)}}. \quad (7.35)$$

The amplitude distribution of the attenuated and divergent sound wave is depicted in Figure 7-35 as a three-dimensional plot. The axis of ξ and η correspond to the horizontal and vertical crystal directions at the Bragg cell.

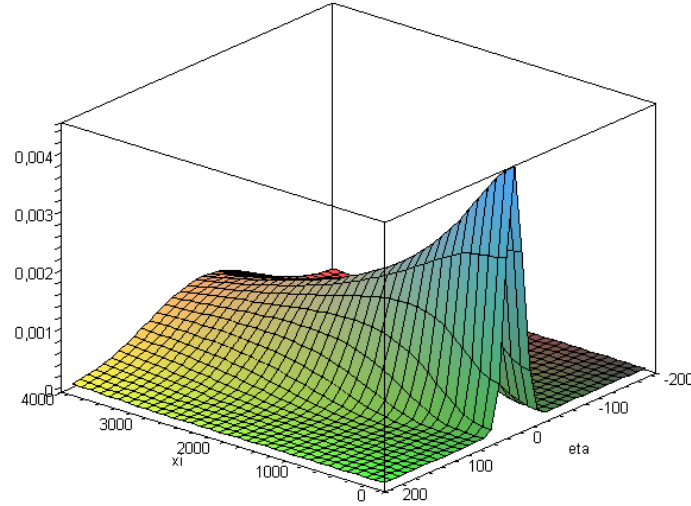


Figure 7-35 Amplitude distribution of the ultrasonic wave at 2.1GHz IF frequency. The waist size is chosen to have approximately the same dimension of beam radius ($200\mu\text{m}$) at the end of the aperture as is experimentally measured (c.f. Section 7.5.3). The useful aperture of the Bragg cell is assumed to be 4mm.

The normalized amplitude of the laser field centred to the ultrasonic wave is given by the definition of Gaussian beams

$$A_L(\xi, \eta) = \sqrt{\frac{2}{\pi w_\xi w_\eta}} e^{-\frac{(\xi-s)^2}{w_\xi^2}} e^{-i(\eta-t)^2 \left(\frac{1}{w_\eta^2} - i \frac{k}{2R_\eta} \right)}, \quad (7.36)$$

where

w_ξ – is the waist of the laser beam (in the horizontal direction),

w_η – is the waist of the laser beam (in the vertical direction),

s – is the distance of the laser beam centre measured from the transducer in the horizontal direction,

t – is the distance of the laser beam centre measured from the centre of the acoustic field (or transducer) in the vertical direction,

R_η – is the radius of curvature of the laser phase front, and

k – is the wavenumber vector of the laser field.

The normalized pupil function $G(\xi, \eta)$ can be calculated as the multiplication of the laser- and the acoustic fields

$$G(\xi, \eta) = A_S(\xi, \eta) A_L(\xi, \eta) = A_R(\xi, \eta) e^{i(\eta-t)^2 \frac{k}{2R_\eta}}, \quad (7.37)$$

where

$$A_R(\xi, \eta) = \left(\frac{2}{\pi} \right)^{3/4} \frac{1}{\sqrt{D}} \frac{1}{\sqrt{w_s(\xi) w_\xi w_\eta}} e^{-\left[\frac{\alpha(f)}{2} \xi + \frac{(\xi-s)^2}{w_\xi^2} \right]} e^{-\left[\frac{\eta^2}{w_s^2(\xi)} + \frac{(\eta-t)^2}{w_\eta^2} \right]}. \quad (7.38)$$

If the laser beam is exactly focused onto the sonic wave, the radius of curvature of the laser phase front is infinity and the pupil function becomes purely real, otherwise, if the active zone is over illuminated this results in a focus position change of the imaging optics behind the Bragg cell. In a practical case, the CCD is always adjusted into the focus, therefore the infinity radius of the phase front used in the calculation is an appropriate consideration.

In the optimized illumination case of the deflector, when the amplitude maximum of the pupil function is in the middle of the useful aperture of the Bragg cell, is shown in Figure 7-36.

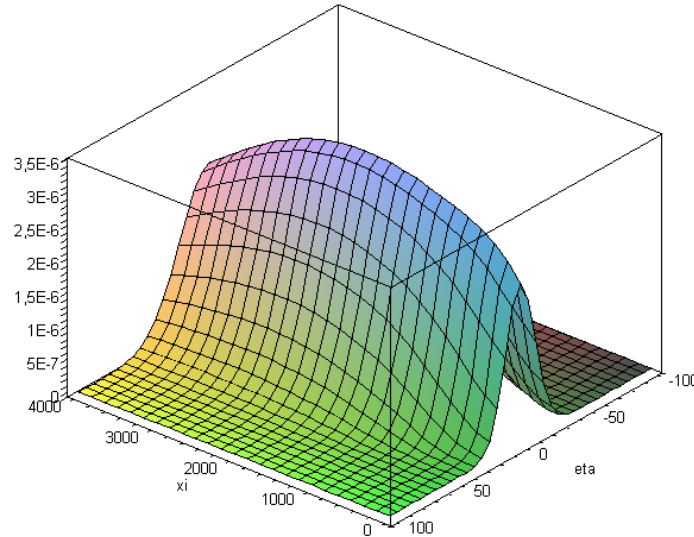


Figure 7-36 Amplitude distribution of the pupil function. For 4mm horizontal aperture size, the amplitude maximum is exactly in the middle of the aperture. This is achieved by shifting the centre of the laser by 3.513mm in the horizontal direction relative to the transducer. The horizontal waist dimension (ξ direction) is 2.786mm.

Substituting the pupil function into the expression of the diffraction integral formula and calculating the intensity of the diffracted light results in

$$I(x, y) = \left| \int_0^D \int_{-\infty}^{+\infty} A_R(\xi, \eta) e^{-ik \left(\frac{x}{F_x} \xi + \frac{y}{F_y} \eta + \frac{(\eta-t)^2}{2R_\eta} \right)} d\xi d\eta \right|^2, \quad (7.39)$$

where the parameters of F_x and F_y denote the effective focal lengths of the scan optics in the horizontal and vertical direction. The variables x and y are the coordinates in the CCD plane. The resulting diffraction pattern corresponds to the intensity distribution observed with a detector that has infinite dimension. To consider the effect caused by the finite dimension of the detector area, the expression of (7.39) must be integrated over the pixel size of the CCD

$$\langle I(x, y) \rangle = \frac{1}{W \cdot H} \int_{x-W/2}^{x+W/2} \int_{y-H/2}^{y+H/2} I(x', y') dx' dy', \quad (7.40)$$

where W is the width and H is the height of a CCD pixel.

7.7.1 Diffraction limit of the focal spot

The complicated complex diffraction integral can not be solved with closed analytic functions, therefore it is numerically computed. The pupil function is mapped within a rectangular aperture that is adequately centred and matched to the active zone of the Bragg cell. Practically, a sampling of 100x100 points of the pupil function provides a detailed diffraction pattern. The result of the diffraction calculation is depicted in Figure 7-37 as a three-dimensional plot of the focal spot.

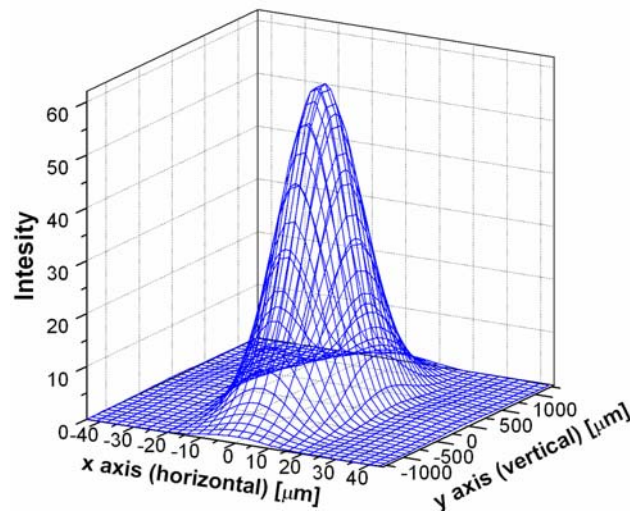


Figure 7-37 Intensity distribution of the focal spot at 2.1GHz IF frequency and 4mm horizontal Bragg aperture size. As a result of diffraction on the acoustic aperture, the side-lobes in the horizontal direction are recognizable.

In order to make the line width in the horizontal and vertical directions visible, the intensity profile is cut through the centre of the image plane. Figure 7-38 shows the spot dimensions measured in resolution bandwidth, fluctuation bandwidth (see Section 7.9) and the FWHM of the Gaussian fit in both directions.

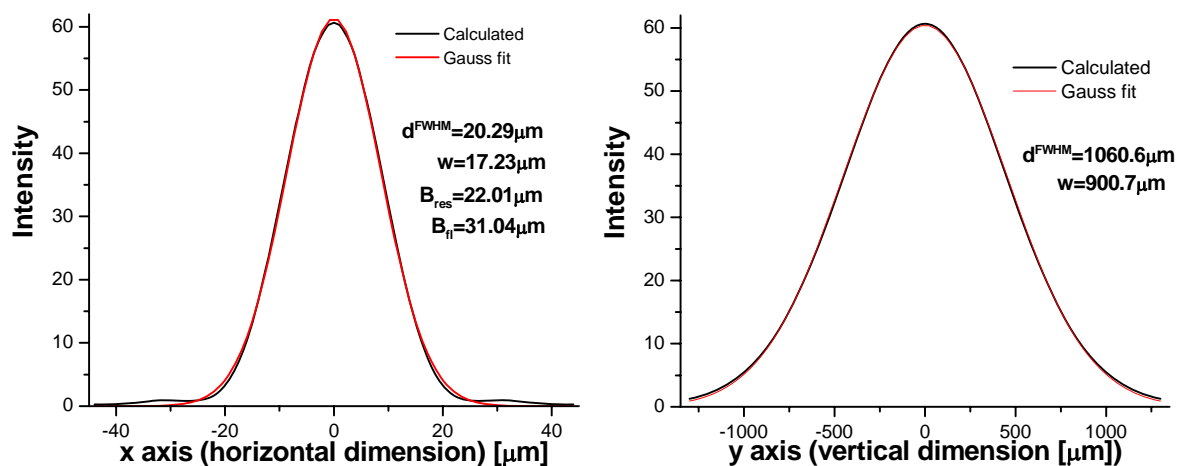


Figure 7-38 Spot dimensions in the horizontal and vertical direction. The vertical spot size is fairly large due to the small aperture at the Bragg cell.

The calculated resolution bandwidth determines the maximum achievable resolution that is limited purely by diffraction on the Bragg aperture (*diffraction limit*). The resolution bandwidth expressed in frequency corresponds to 965kHz. Note that in the model the resolution bandwidth is almost independent of the IF frequency.

The efficiency optimization of the WBO is attained by applying the cylindrical lens behind the scan optics. To model the focusing of the cylindrical lens in the vertical direction, the diffraction calculation must be modified. Due to the one-to-one imaging property of the lens system, this is a simplification of the diffraction integral actually. The vertical intensity distribution at the CCD is calculated from the mirrored illumination function at the Bragg cell. From this reason, there is no integration needed in the vertical direction. Hence, the phase front remains the same as in front of the Bragg cell, but is multiplied by -1. The intensity distribution of the focal spot employing the cylindrical lens is depicted in Figure 7-39.

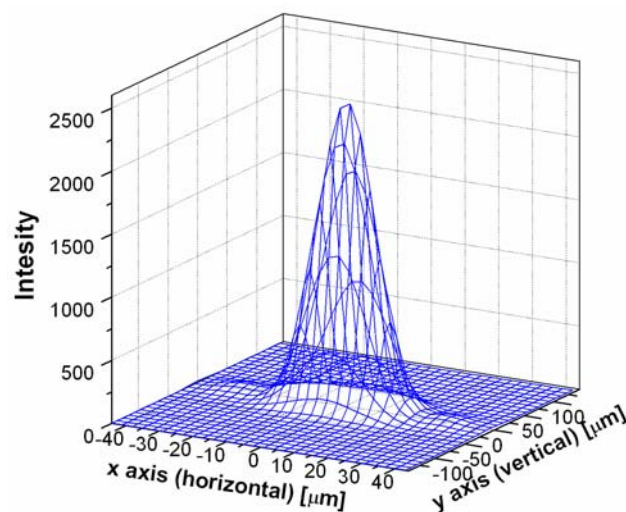


Figure 7-39 Intensity distribution in the focus of the scan optics employing the cylindrical lens. The input frequency is 2.1GHz and the aperture of the Bragg cell is 4mm. The side-lobes in the x direction are well visible due to the focusing of the cylindrical lens. In the vertical direction, from the resolution point of view the diffraction pattern is uninteresting.

The accurate spot dimensions are calculated from the horizontal and vertical cuts through the middle of the image plane, as shown in Figure 7-40.

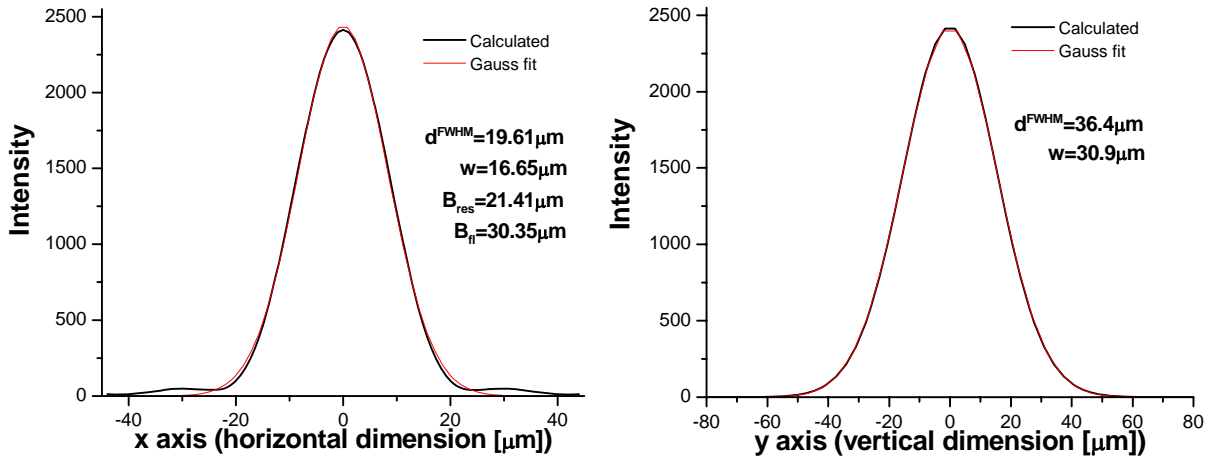


Figure 7-40 Spot dimensions in the horizontal and vertical direction when the cylindrical lens is also applied. The vertical spot size is a factor of about 30 smaller than the case above.

It can be established that using the cylindrical lens has less impact on the resolution, since it does not affect the imaging in the horizontal direction, yet the efficiency increases with a factor of 40 (16dB).

7.7.2 Focal spot quality influenced by lens aberrations

Any optical system contains lens imperfections and assembly errors that degrade the focal spot quality. This means phase front distortions of the laser beam that results in focal spot enlargement and therefore resolution deterioration. In the model of the diffraction analysis used above, lens aberrations can be also incorporated by multiplying the integrand by a polynomial factor that describes the phase front errors. Reasonably, the phase front aberrations are modelled by using Legendre polynomials [11]

$$L_k(x) = \frac{1}{2^n n!} \frac{d^n}{dx^n} (x^2 - 1)^n, \quad (7.41)$$

where $x \in [-1,1]$, $k \in N$ and $L_0 = 1$.

The Legendre polynomials have the advantage that they form a complete set of ortho-normed system and for higher orders than $n > 2$ there is no spherical component present. This property of the Legendre polynomials is very important, because an additional spherical wavefront would change the focus position of the optical system. Thus, the expression of the diffraction integral without averaging through the CCD pixels takes the form of

$$I(x, y) = \left| \int_0^D \int_{-\infty}^{+\infty} A_R(\xi, \eta) e^{-ik\beta(AL_l(\xi) + BL_m(\xi))} e^{-ik\left(\frac{x}{F_x}\xi + \frac{y}{F_y}\eta + \frac{(\eta-t)^2}{2R_\eta}\right)} d\xi d\eta \right|^2, \quad (7.42)$$

where

β – denotes the wavefront distortion in fraction of wavelength,
 $L_l(\xi), L_m(\xi)$ – are different orders of Legendre polynomials, and
 A, B – are weighing factors needed for the linear combination.

The argument of the Legendre polynomial ξ is scaled to the $[-1,1]$ interval. In the first approximation, the aberration error in the vertical direction is uninteresting.

In the diffraction model, the linear combination of only even orders of Legendre polynomials are used, since during the adjustment of the WBO possibly symmetric filter curves are attained. The result of a lens aberration simulation is shown in Figure 7-41, when $\lambda/4$ wavefront error and the averaging of the CCD pixels is considered. During the evaluation, the cylindrical lens is used in the imaging system, otherwise asymmetry is involved in the filter curve through the relative change of the maximum position of the pupil function.

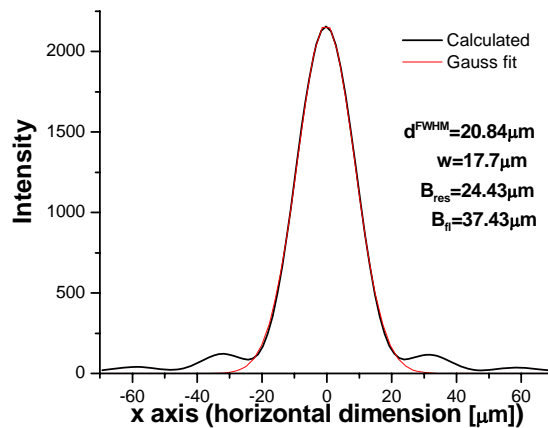


Figure 7-41 Horizontal intensity distribution at the CCD in case of $\lambda/4$ wavefront distortion at 2.1GHz input signal. The increase of the side-lobes results in resolution degradation.

It is striking that the side-lobes increase compared to the idealized case of imaging optics. Due to lens aberration errors, the resolution bandwidth is $24.4\mu\text{m}$, which corresponds to 1.07MHz frequency resolution. This result is well in agreement with the experimentally measured resolution bandwidth of about $<1.1\text{MHz}$ (c.f. Section 10.8).

7.7.3 Simulation of alignment errors

In the real thermal environment, the alignment of the spectrometer changes. The high temperature sensitivity is mainly caused by the laser source unit, as has already been discussed in Section 7.1.3, but mechanical deformations of the WBO housing, module interface plates, and holders due to thermal expansions also contribute to performance changes of the spectrometer. In the laser module, a few hundred nm position change of the laser diode or slight ($<1\text{arc minute}$) bending of the interface plate produce significant beam interdistance variation at the output beams for instance. Consequently, the laser beam does not hit exactly the centre of the acoustic zone of the Bragg cell, resulting in efficiency and resolution degradation of the instrument.

With the diffraction model of the Bragg cell it is possible to simulate alignment errors introduced by horizontal and vertical position changes of the laser beam. These alignment errors between the laser beam and acoustic zone are measured relative to the optimum illumination position. In case of a beam position change in the vertical direction, the resolution bandwidth and efficiency vary as depicted in Figure 7-42. The simulation is performed using a $\lambda/4$ wavefront aberration and without changing the vertical position of the CCD detector.

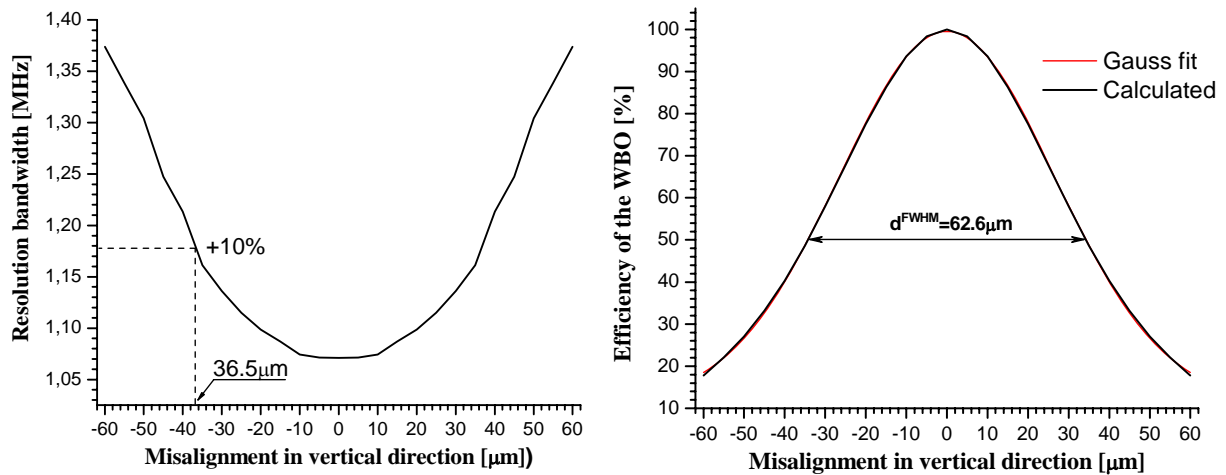


Figure 7-42 Resolution bandwidth and efficiency change due to vertical misalignment of the laser beam relative to the centre of the acoustic zone. About 10% resolution and 50% efficiency degradation can be expected in case of $\pm 35 \mu\text{m}$ vertical shift of the laser beam.

The theoretical results of the efficiency change of the instrument are compared to that of the experimentally observed performance deterioration. In the efficiency optimized and temperature stabilized band of the WBO, the illumination of the Bragg cell is changed in the vertical direction by means of a plane-parallel glass plate in the beam path. The rotation of the glass plate offers fine height adjustment of the laser beam. In order to detect the efficiency variation, the signal of a noise-source is fed into the Bragg-cell, and the averaged counts of all frequency channels are plotted versus relative height change of laser beam. Figure 7-43 shows the measured efficiency degradation in percent relative to the optimum performance.

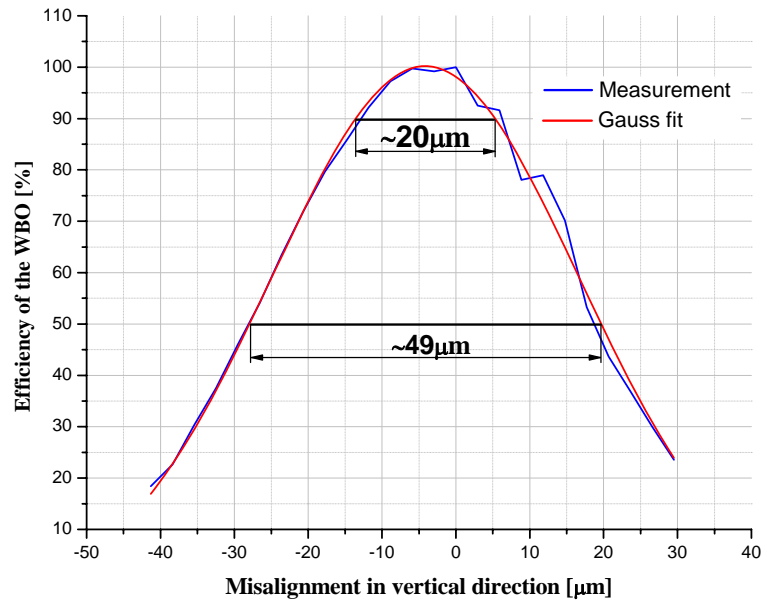


Figure 7-43 Efficiency change of the WBO due to vertical misalignment of the laser beam relative to the centre of the acoustic zone.

The results of the measurement show that $\pm 10\mu\text{m}$ misalignment in height between the Bragg-cell and the laser beam produces approximately 10% efficiency degradation of the spectrometer, and $\pm 25\mu\text{m}$ results in 50% efficiency change. These values are in good agreement with the results of the theoretical calculation.

In the horizontal direction, the alignment error of the laser beam relative to the optimum illumination position of the Bragg cell affects the resolution and the efficiency of the spectrometer.

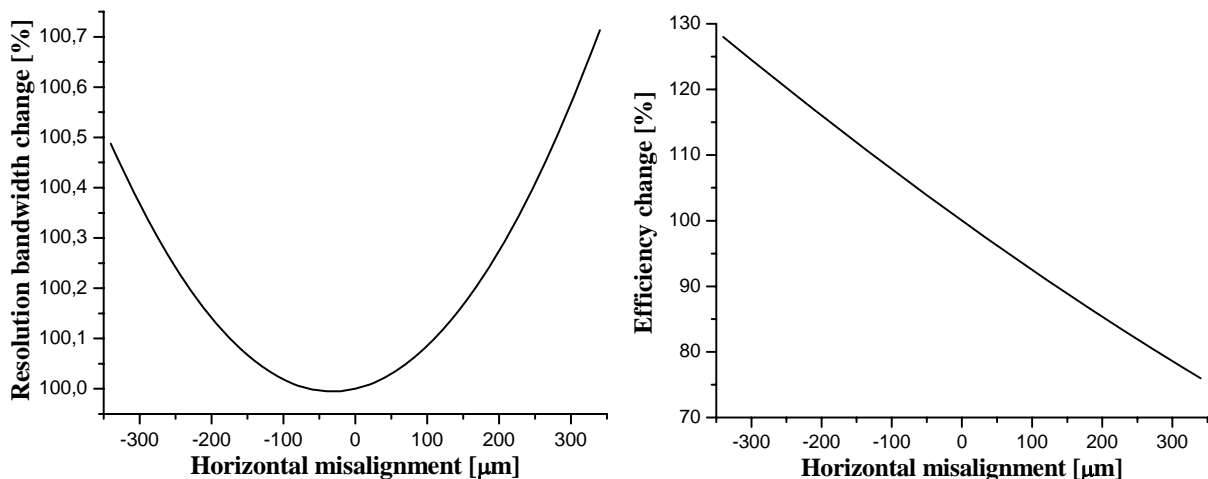


Figure 7-44 Resolution bandwidth and efficiency change of the WBO due to horizontal misalignment of the laser relative to the optimum illumination position. The laser beam does not contain any wavefront aberration, because by shifting the laser the Legendre polynomials introduce asymmetry into the diffraction pattern, as they are defined within the interval of $[-1, 1]$.

This alignment sensitivity is investigated with the diffraction model of the Bragg cell. Figure 7-44 shows the calculated resolution and efficiency variation versus horizontal illumination position of the deflector. A positive shift corresponds to a larger distance between the transducer and the beam centre.

It can be concluded that $\pm 300\mu\text{m}$ horizontal beam position change from the optimum produces $<1\%$ resolution degradation, therefore a few $100\mu\text{m}$ misalignments does not make recognizable change in resolution. At the same time, the efficiency increases if the beam centre moves closer to the transducer. A possible explanation is that the multiplication of a Gaussian beam profile with the attenuation function of the ultrasonic wave results in effectively higher amplitude of the pupil function; thus, the diffracted light intensity is higher. This has been experimentally proven during the alignment procedure of acousto-optical spectrometers. On the other hand, the efficiency decreases drastically if the laser beam shifted away from the transducer.

7.7.4 Simulation of positioning accuracy of the laser diode on the optical axis

The positioning accuracy of the laser diode has already been investigated, however without involving any lens aberration or diffraction effects. Now, it is worth mentioning how the dimension of the focal spot i.e. the resolution varies when the laser position on the optical axis changes. In the diffraction model of the Bragg cell, the collimation change of the laser beam is considered to be radius variation of the phase front at the position of the deflector. Practically, the phase front radius is taken into account by using second order of Legendre polynomials in the phase expression of the diffraction integral, since they represent spherical waves. Figure 7-45 shows the resolution change calculated from the FWHM dimension of the focal spot versus laser position on the optical axis.

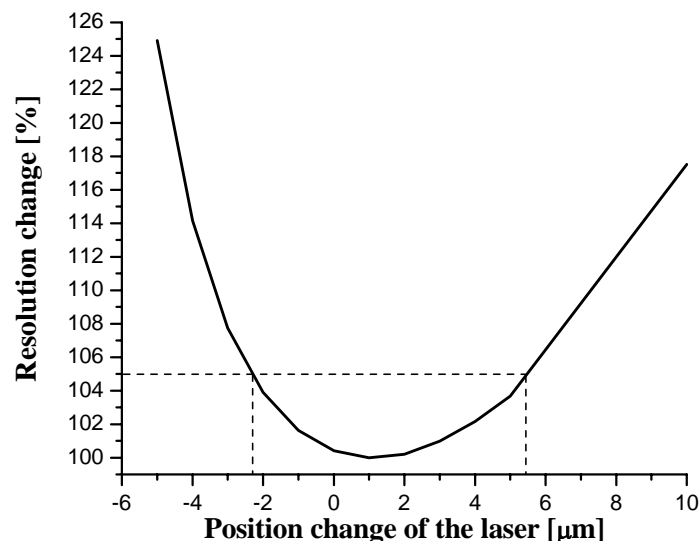


Figure 7-45 Impact of the collimation change on the resolution of the WBO. The laser position change in the positive direction denotes an increased distance between the laser and the collimator. During the calculation a wavefront aberration of about $\lambda/4$ of the laser beam is employed.

It is conspicuous that the smallest focal spot is not at the geometrical focus of the imaging optics, but slightly in front of it. This is because of the different focal length definition between Gaussian and geometrical optics. From the results of the calculation it can be established that $\pm 4\mu\text{m}$ laser position change results in $>5\%$ resolution degradation of the instrument. This value corresponds to about $\pm 400\mu\text{m}$ position change of the CCD or in case of 10% resolution degradation it is about $\pm 600\mu\text{m}$. These achievements are in agreement with the results attained experimentally.

7.8 Scan optics

The deflected laser light must be Fourier transformed in order to get the necessary spectral information from the IF signal. This can be performed by imaging the deflected laser beam with a lens system. The demand for the optical system is that it should provide linear imaging in the deflection angle (the frequency non-linearity of the spectrometer must be defined by the Bragg cell and not by the optics), and the lens system should be diffraction limited in order to guarantee the good resolution and efficiency of the spectrometer. The angle linearity means that the deflected beam angle linearly scales with the image position, which is necessary to produce a linear frequency scale at the image plane. This kind of imaging can be realized by means of scan optics (f - ϑ lens). The necessary focal length of the scan optics is determined by the deflection angle range and resolution provided by the deflector, and the sampling criterion. According to the Nyquist sampling theorem, the resolution information defined by the Bragg cell can be preserved if the number of the sampling intervals is at least twice the number of resolvable spots of the deflector. From the time-bandwidth product, the resolution of the Bragg cell results in 1000 frequency channels i.e. 1MHz . Consequently, the detector should have at least 2000 pixels in order not to lose resolution information. The pixel width of the detector is $13\mu\text{m}$, thus the dimension of the scanning length results in 26mm . The imaging rule of scan optics is defined by

$$f\vartheta = l, \quad (7.43)$$

where f is the focal length, ϑ is half of the scanning angle, and l is half of the scanning length. Substituting the scanning angle of 13.1 degree of the Bragg cell into (7.43), the necessary focal length of the scan optics becomes 113.7mm . In practice, the scan optics with 100mm focal length is proved to be sufficient to guarantee the resolution of the WBO unit.

The diffracted light has larger beam divergence in the vertical direction than in the horizontal, due to the small vertical size of the acoustic zone. Thus, applying the scan optics as a single imaging optics, the focal spot has different dimensions in the vertical and horizontal directions. This means of course a degraded efficiency of the WBO. In addition, the deflected four beams must be imaged onto the CCD, which might not have the same line spacing as the channel distance of the Bragg cell. These effects are compensated by using an additional focusing in the vertical direction. This is performed by means of a cylindrical lens as discussed in Section 6.3.1. With the position and focal length of the cylindrical lens can be adjusted that the laser light is focused in both directions exactly onto the detector area.

7.9 CCD detector

In the WBO, the deflected light is detected by using CCD line detectors. The detector used in the WBO is made by Reticon [68] and has 2048 pixels with the size of $13 \times 26 \mu\text{m}$ (WxH). For the WBO, a custom designed detector array is fabricated, since the commercial detectors are only single line devices. The four lines needed for the spectrometer are cut out from the wafer then the chip is bonded and packaged with respect to space qualification norms. The photo of a qualified CCD array is shown in Figure 7-46.

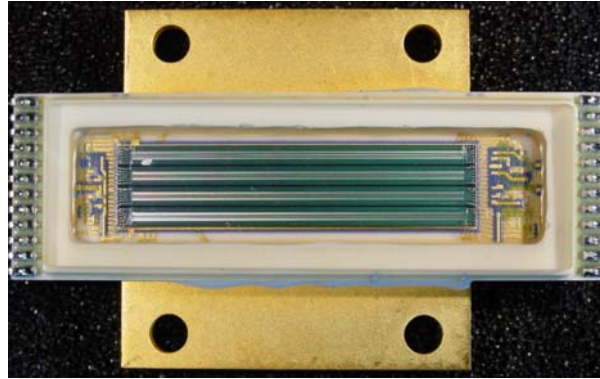


Figure 7-46 The four line hybrid CCD. The bonding and packaging is done by [55]. The heat sink underneath the CCD chip provides good thermal conductivity, mechanical stability, and support for the detector. The glass plate protects the device from mechanical damages, and its wedged surface prevents undesired reflections and interferences from its surface.

The noise performance of the detector is of particular importance for the spectrometer, since it contributes to the noise of the detected signal, and therefore might reduce the S/N ratio of the instrument. The noise contribution of the device within the dynamic range of the CCD (typically 13dB) should remain small compared to the radiometric noise described by the radiometer equation [54]

$$\sigma_R^2 = \frac{\langle S \rangle^2}{B_{fl} \tau}, \quad (7.44)$$

where $\langle S \rangle^2$ is the mean square of the detected signal, τ is the integration time, B_{fl} is the fluctuation bandwidth

$$B_{fl} = \frac{\left[\int_0^{\infty} P(\nu) d\nu \right]^2}{\int_0^{\infty} P^2(\nu) d\nu}, \quad (7.45)$$

and $P(\nu)$ is the channel response (filter curve) of the spectrometer. The fluctuation bandwidth represents the width of an equivalent rectangular filter that transmits the same noise fluctuation as the discussed filter. The channel profile $P(\nu)$ is determined by the diffraction

pattern of the horizontal aperture of the deflector, the finite dimensions of the CCD pixels, and the crosstalk between the neighbouring pixels. The noise contribution of an acousto-optical spectrometer is characterized by the noise dynamic range. This determines the illumination range of the CCD, where the noise contribution to the radiometric noise of the input signal remains below 1dB.

The noise of the spectrometer comprises the detector noise, the noise of the CCD readout electronics, the quantizing noise of the digital electronics, laser power fluctuations, scattered laser light, and laser speckle. These noise contributions can be divided into two types: the *background noise*, which is the eigen noise of the instrument without input signal, and the *shot noise*, which is the noise generated by the photoelectrons in the CCD. The background noise of the spectrometer originates from the thermally produced electrons in the CCD (*dark current*), from the *readout noise* of the electronics, and from the electrons generated by laser speckle and scattered light that is also imaged onto the detector. Statistically, these can be expressed by

$$\sqrt{\sigma_{dark}^2} = \sqrt{n_D + n_R + n_{LS}}, \quad (7.46)$$

where n_D is the number of the dark current electrons, n_R is the number of the readout electrons ($n_D \ll n_R$), and n_{LS} is the number of the light scatter electrons. The shot noise of the instrument comes from the statistical fluctuations of the photoelectrons produced in the CCD. The number of these electrons is dependent on the number of the signal electrons and therefore the illumination level of the detector. The statistical behaviour of the shot noise is determined by

$$\sqrt{\sigma_{shot}^2} = \sqrt{n_S}, \quad (7.47)$$

where n_S is the number of the signal electrons.

In order to keep the noise level of the spectrometer low, not only the high dynamic range of the detector is important but also the number of the maximum photoelectrons n_{FW} (*full well capacity*) of the CCD is decisive. The dynamic range of the detector is defined through

$$R = \frac{n_{FW}}{\sqrt{n_D + n_R}}. \quad (7.48)$$

The total noise contribution of the spectrometer to the radiometric noise (neglecting light scatter and laser speckle) then can be expressed as a function of the detector illumination level [77]

$$\sigma_{tot}^2 = \sigma_{radiometric}^2 \cdot f^2(\alpha) \quad (7.49)$$

$$f(\alpha) = \sqrt{1 + \frac{B_{fl} \delta}{\beta n_{FW} \left(1 - \frac{n_{FW}}{R^2}\right)} \frac{1}{\alpha} + \frac{B_{fl} \delta}{\beta^2 R^2 \left(1 - \frac{n_{FW}}{R^2}\right)^2} \frac{1}{\alpha^2}}, \quad (7.50)$$

where

α – is the relative illumination of the CCD (typically $0.8 \leq \beta \leq 0.9$),
 β – is the relative signal level of the analogue-digital converter ($0 \leq \alpha \leq 1$), and
 δ – is the readout frame time of the CCD (10ms).

With decreasing illumination the noise contribution $f(\alpha)$ of the CCD increase, because there are less photoelectrons generated and the CCD noise becomes dominating besides the radiometric noise (see Figure 7-47).

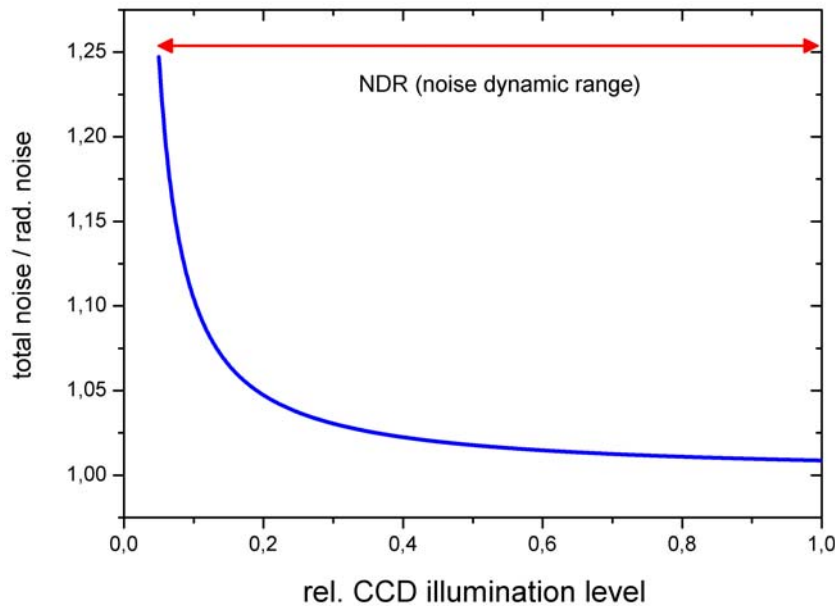


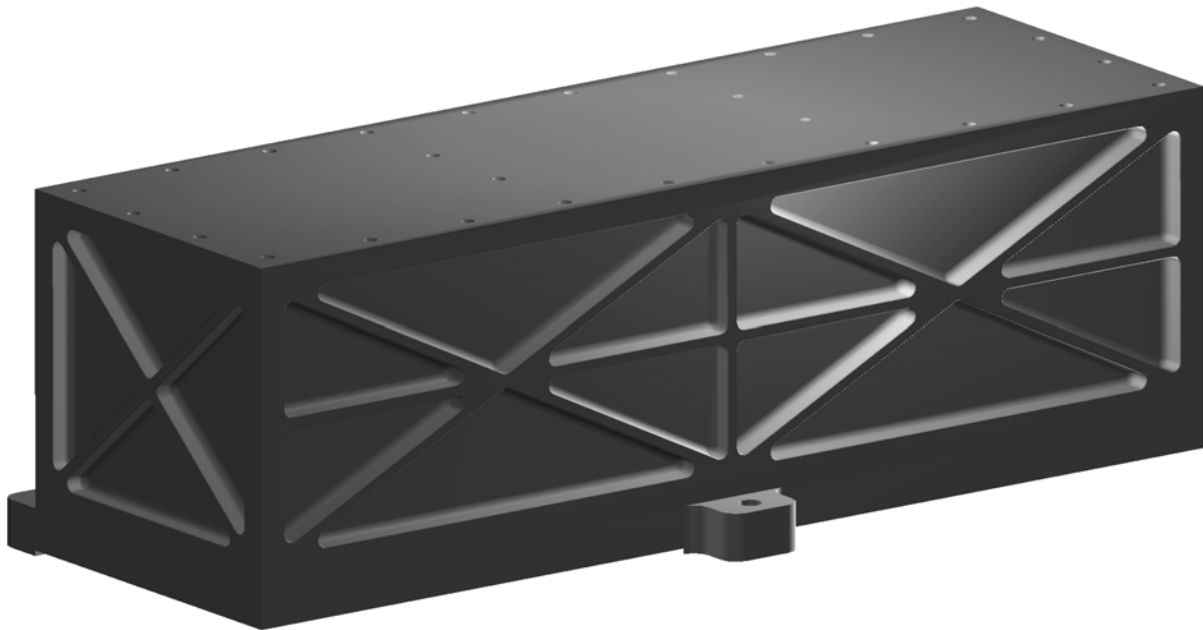
Figure 7-47 Increase of the radiometric noise as a function of relative illumination of the CCD [77]. The 1dB (26%) point of the curve defines the noise dynamic range of the device.

The minimum illumination level of the CCD (approximately 4% at the fluctuation bandwidth of 1.6MHz) determines its noise dynamic range

$$NDR = 10 \cdot \log\left(\frac{1}{\alpha_{\min}}\right) = 14dB. \quad (7.51)$$

The *NDR*, which is dependent on the fluctuation bandwidth of the spectrometer, specifies the dynamic range of the instrument, within observations of radiometric signals can be accomplished. A smaller fluctuation bandwidth results in larger radiometric noise, and therefore the noise contribution of the instrument becomes less, while the *NDR* increases.

8 Mechanical investigations of the WBO Housing



8.1 WBO Housing Deformation Analysis

The stability of the instrument is affected by the mechanical stability of its housing. Due to the relatively long optical path and the small pixel size of the CCD, any alignment instability caused by mechanical or thermal effects might deteriorate the optimal performance of the instrument. These instabilities originate from the combination of the following effects:

- Mechanical stress on the baseplate caused by mounting the WBO box. The WBO housing consists of two main parts: the baseplate, which is the optical bench of the instrument, and the box. Since the optical alignment is done without mounting the WBO box on the baseplate, the alignment change is considerable when screwing these two parts together.
- Integration of the WBO onto the spacecraft service plate. The operating temperature range of the spectrometer is 5-15°C, while the service plate on which the WBO is mounted, is at lower temperature. The about 5 degrees temperature difference between the two units results in a mechanical deformation of the WBO baseplate due to the different thermal expansions.
- Thermal gradient of the spacecraft service plate produced by other instruments. The thermal interface between the spacecraft and WBO guarantees a maximum of a 6-

degree gradient over the whole service plate [41]. This produces a thermal gradient on the WBO optical bench, mechanically deforming it as well.

The alignment of the WBO is done at 15°C stabilized temperature³⁸ in thermal equilibrium. The effects mentioned above may have significant impact on the efficiency, resolution and bandpass ripple of the instrument. From this reason a detailed deformation analysis is carried out for the WBO housing to predict the thermal and mechanical sensitivity of the spectrometer.

During the experiment, the following effects are modelled: the deformation of the WBO baseplate caused by assembling the WBO box, 6-degree temperature gradient generated on the simulated spacecraft service plate, and 6-degree temperature difference between the simulated spacecraft service plate and the WBO baseplate.

8.1.1 Results of the WBO deformation analysis

A comparison of the different thermal cases mentioned above is summarized in Table 1.

| Measurement procedure | Maximum deformation of the WBO baseplate (precision: $\pm 2\mu m$) |
|---|---|
| Assembling the WBO box and baseplate | $14\mu m$ |
| Temperature gradient generated on the dummy service plate (6K) and the WBO baseplate (1K), respectively | $14\mu m$ |
| Constant temperature difference between the dummy service plate and the WBO ($\Delta T=6K$, temp. grad $< 0.1K$) | $9\mu m$ |

Table 8-1 Comparison table of the deformation of the WBO baseplate caused by different mechanical and thermal effects

In worst case, when the deformations are simply added, the resulting maximal deformation is roughly $40\mu m$ over the total length of $400mm$. The $40\mu m$ deformation of the WBO optical bench is a considerable change in the performance of the spectrometer, which is discussed in Section 8.2.

The results of the above measurements led us to the following adjustment strategy of the spectrometer: the height of the CCD is aligned last in order to eliminate the impact of the deformations caused by the assembly of the WBO box and baseplate. Thus, the deformations due to the thermal effects, approximately $25\mu m$, remain a sensitivity constraint on the instrument.

³⁸ The temperature stability is of decisive importance for the spectroscopic stability of the instrument. The Herschel service module guarantees 1K/hour stability for the WBO.

8.2 Impact of the WBO optical bench deformation on the WBO performance

In Section 6.3.2 it was discussed how the focal length of the cylindrical lens affects the optical efficiency of the WBO. Now, having information about the deformation behaviour of the instrument caused by thermal changes, its influence on the optical efficiency can be also investigated. The allowed maximum efficiency variation of the instrument within the operating temperature range is specified to $3dB$.

If we consider that the CCD pixel size is comparable with the image waist dimension, then a vertical shift of the detector, caused by the deformation of the WBO baseplate, decreases the detected light intensity on the CCD. Figure 8-1 shows two different cases of the intensity detection of a $26\mu m$ high CCD pixel. In the upper figure, the CCD pixel is exactly centred on the Gaussian-beam. This situation gives the best optical efficiency of the spectrometer. In the lower figure, the CCD pixel is displaced ($10\mu m$ shift) from the beam centre, which results in efficiency degradation.

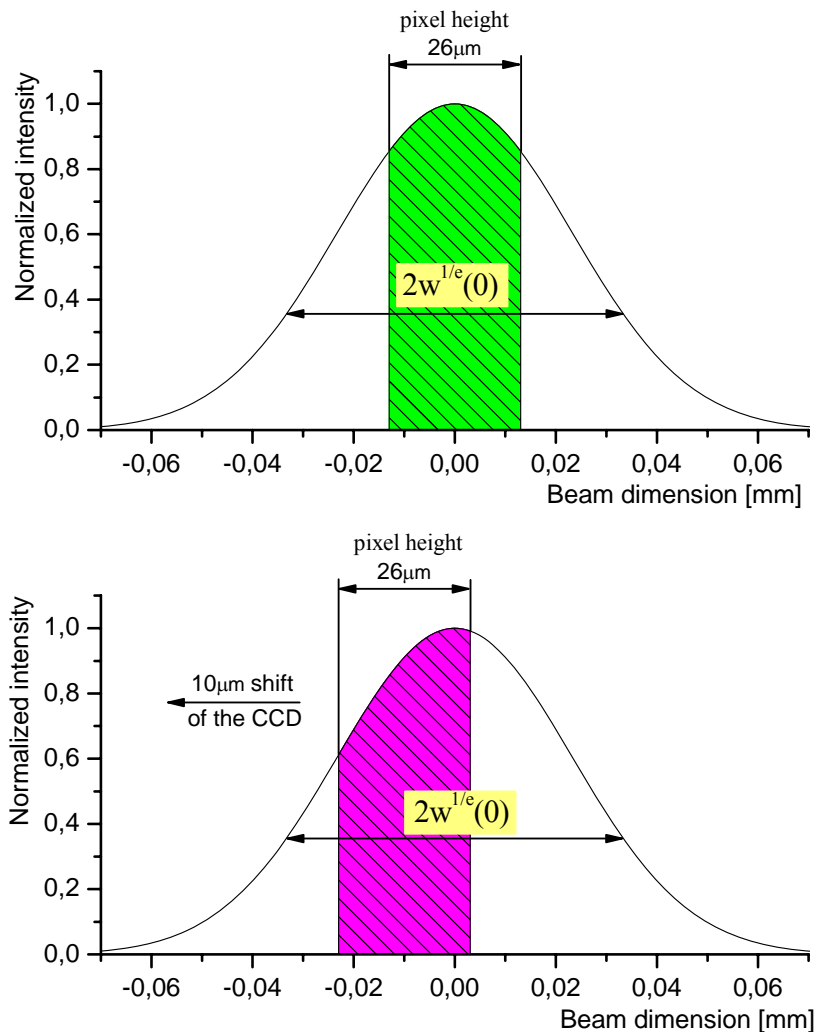


Figure 8-1 Efficiency change of the WBO through the mechanical deformation of its baseplate. The focal length of the cylindrical lens is 100mm, corresponding to a waist of $32.8\mu m$ at the image plane.

The detected intensity is generally given by:

$$I = \frac{1}{w_0 \sqrt{\pi}} \int_a^b e^{-\frac{x^2}{w_0^2}} dx, \quad (8.1)$$

where a and b are the pixel edge positions relative to the optical axis, i.e. the maximum intensity of the Gaussian beam. Figure 8-2 shows the efficiency losses up to $65\mu\text{m}$ displacement of the CCD.

It is also investigated, whether increasing the spot size on the CCD, by means of shorter focal length of the cylindrical lens, improves the positioning sensitivity of the CCD. This simultaneously means reduction of optical efficiency, but the question is whether there is any trade-off. The efficiency change of the spectrometer in case of 80 and 90mm cylindrical lenses is depicted also in Figure 8-2. Note, the array-AOSs built for ground applications so far have 80mm cylindrical lenses. This means an optical efficiency degradation of 4.5dB relative to the 100mm lens, if the CCD is perfectly aligned.

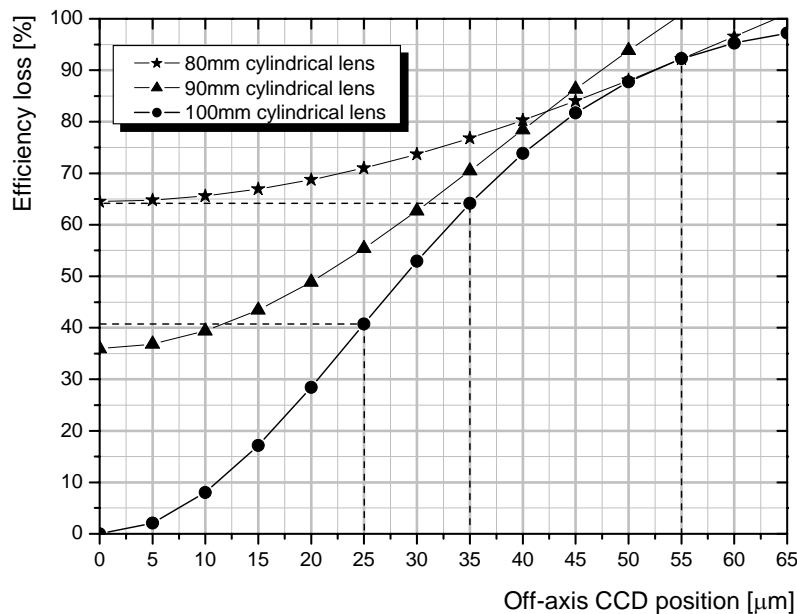


Figure 8-2 Efficiency change versus off-axis position of the CCD pixel applying a 100mm, 90mm, and 80mm cylindrical lens. The intensity distribution of the focal spot is assumed to be Gaussian.

The result of the calculation shows that applying neither an 80 nor a 90mm cylindrical lens improves the positioning sensitivity of the instrument. These lenses introduce larger efficiency decrease than the 100mm lens does at any deformation level. Thus, the decision is taken to apply the 100mm cylindrical lens and have the instrument perform at its maximum efficiency.

8.3 Resonance analysis of the WBO

The Herschel satellite is going to be launched with the Ariane 5 launcher. During the start and transfer to the orbit, the payload must withstand strong vibrations [2]. From this reason, the HIFI WBO has to undergo a detailed resonance analysis. The design of the WBO housing is similar to the SWAS AOS housing, which successfully went through the qualification process [25]. Because of this similarity between the two housings, and in order to spare time and costs of the FEA (Finite Element Analysis), an early resonance test of the WBO housing is accomplished. According to the resonance requirement of the WBO design, the eigenfrequency of the instrument must be above 140Hz [40].

8.3.1 Vibration measurement system

The principle of the resonance frequency search is to vibrate the test object at different frequencies and discover its resonances. The experiment is carried out with the RMS Regulation and Measurement Technique Dynamic Test Systems [70]. The measurement equipment is capable of performing: sine-sweeps; random vibrations; resonance-search; and shock tests. The block diagram of the measurement system is illustrated in Figure 8-3.

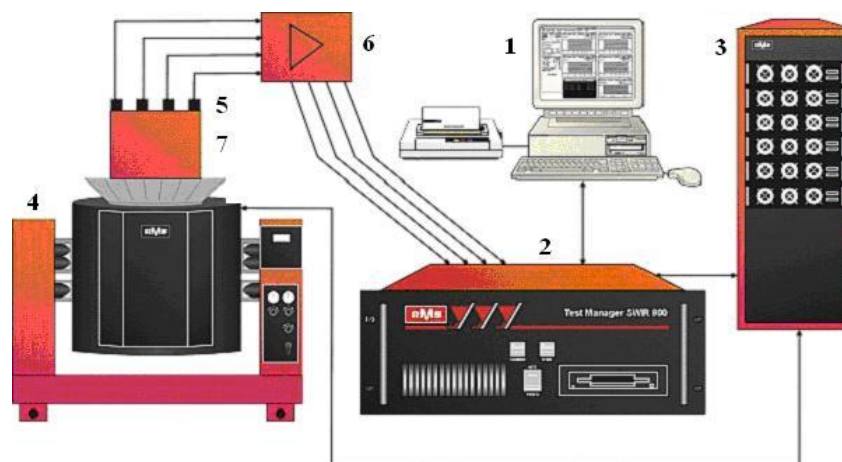


Figure 8-3 Block diagram of the vibrator system [70]. 1. Control PC, 2. Test Manager PC (SWR 900), 3. Performance amplifier (TGA 3005), 4. Vibration exciter (SW 3007), 5. Piezoelectric accelerometer, 6. Preamplifier, 7. Test object

The test object (7) is mounted on the vibration shaker (4), which is controlled by the sine generator (3). The sine generator is commanded by the instrument computer (2) that allows of tuning the exciting frequency and amplitude. The vibration response of the test object is measured by means of piezoelectric accelerometers (5) and their signals are amplified by the preamplifiers (6). Finally, the output signals are analysed by a spectrum analyser card of the instrument PC and printed on the screen of the control computer.

8.3.2 Resonance search of the WBO housing assembled with dummy loads

In order to check the resonance characteristics of the fully assembled spectrometer, a measurement is performed with the WBO housing assembled with physical dummy loads. The loads have the identical mass and interfaces as the real parts of the instrument. The measured resonances are illustrated in Figure 8-4.

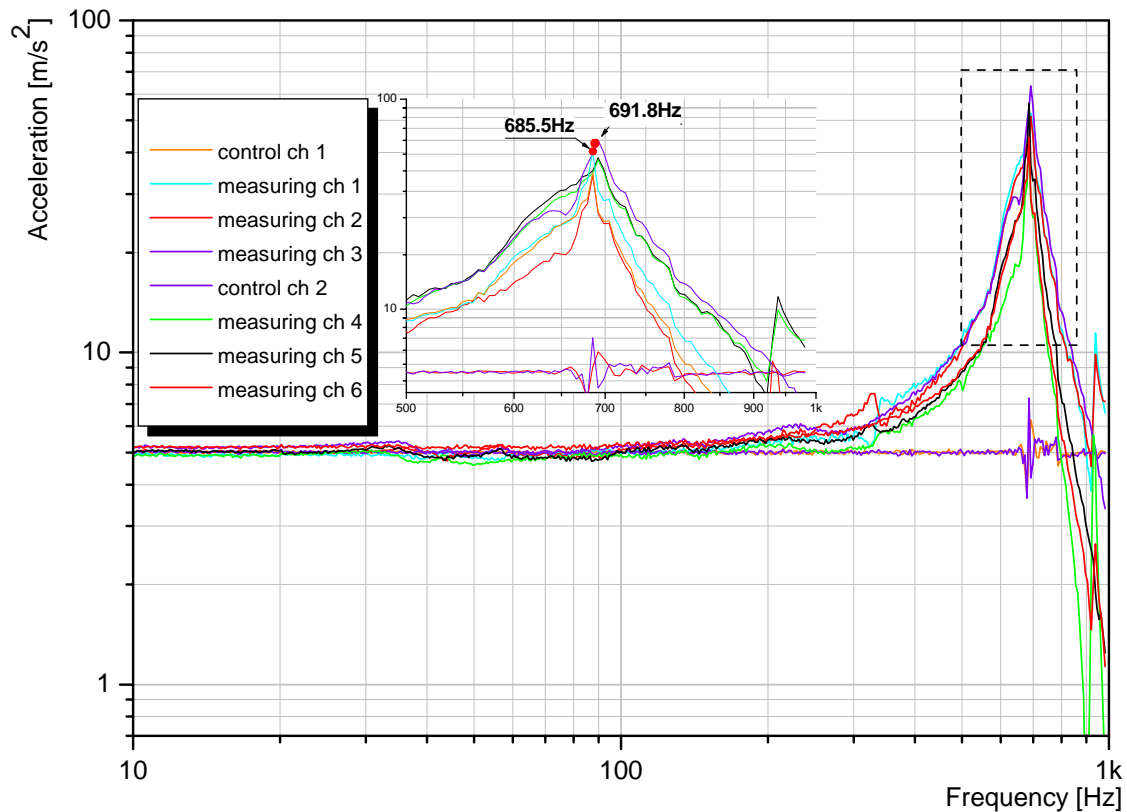


Figure 8-4 Resonance of the WBO box assembled with dummy loads of the modules

The main resonance lies at 686Hz and 692Hz, and the small difference between the measuring channels originates from the different degree of stiffness of the support structure. Below 600Hz, there was not any resonance detected.

During the qualification phase of the WBS, an additional resonance analysis was carried out at DLR³⁹ in Berlin. The vibration facility investigated resonances not only in the z, but in the x, y directions too. The sensors were mounted onto the WBO box [8] and not on the more mechanically stable baseplate, thus the resonance frequencies lie lower than measured above, between 500-550Hz. Nevertheless, both of the measurements show the excellent resonance properties of the instrument at low frequencies. Table 8-2 Summary table of the resonance search measurement summarizes the results of the resonance frequency analysis done with the WBO.

³⁹ Deutsche Luft- und Raumfahrt Agency

| Test object | Resonance frequency [Hz] | |
|--|--------------------------|-------------------|
| WBO baseplate | z axis | 496.6 |
| WBO housing (baseplate mounted with the box) | z axis | 731.1 |
| HIFI WBO | z axis | 685.5 |
| HIFI WBO-QM measured at DLR [7] | x axis | 668 |
| | y axis | 490 ⁴⁰ |
| | z axis | 517 |
| SWAS AOS [25] | z axis | 350 ⁴¹ |
| | x axis | 689 |
| SWAS AOS calculated results [25] | y axis | 572 |
| | z axis | 547 |

Table 8-2 Summary table of the resonance search measurement

It can be concluded that the resonance frequency specification of $\leq 140\text{Hz}$ for the WBO is fully satisfied without any doubt.

⁴⁰ The value does not reflect the eigenfrequencies of the WBO measured on the baseplate, since the sensor was mounted on the mechanically weak sidewall of the WBO box.

⁴¹ During the resonance tests the envelopes of the sidewalls that stiffen the housing were not mounted. This results in the measured relatively low resonance frequency.

9 Laser tests

For the HIFI WBO unit, semiconductor lasers are selected due to their low weight and low power consumption. Among the large variety of laser diodes, there are only a very few that provide the required single mode performance at adequate output power level. The characteristics of the Hitachi made HL7851G multi-quantum well GaAlAs laser diode is excellent. Its single mode behaviour is excellent, and at 785nm wavelength it has sufficient output power (50mW) to drive the 4 Bragg channels with acceptable light power. These laser diodes have very high reliability, which has been demonstrated in several KOSMA AOSs, and they are successfully operating on SWAS and Odin, and they are also used for the SMILES⁴² instrument. During the SWAS program it has been proven that these diodes have good wavelength, optical output power and mode stability, and mode jumps occur only once in the $5\text{-}15^\circ\text{C}$ operating temperature range of the spectrometer [49].

Usually, the output power of a laser diode is regulated by feedback through the monitor diode. However, this kind of regulation plays an important role in the lifetime degradation of the laser. The effect can be explained by the regulating principle of the monitor diode: it maintains a constant output power while with ageing the laser power continuously decreases, therefore the laser current must be continuously increased. This results in an accelerated ageing or even an early failure of the diode. From this reason, in WBO the monitor diode of the laser is only used for monitoring the optical output power.

Other alternatives to stabilize the output laser power are to drive the diode with stabilized current or voltage power supplies. The two different types result in different stability performance of the laser, thus different spectroscopic stability of the instrument.

In Section 9.2 it is shown that applying a stabilized voltage power supply guarantees more stable laser intensity over the 10 degree temperature range, when a serial resistor is connected to the laser. In order to compare the performance differences of a laser attained by using the two different power supplies, the following optical performance experiments were carried out with the laser diodes that are selected from the batch of the HIFI flight lasers:

- optical output power at different laser current versus temperature,
- wavelength variation versus temperature (mode hop behaviour),
- wavelength hysteresis analysis due to thermal drifts, and
- optical output power and wavelength stability at stabilized temperature.

⁴² Submillimeter Limb-Emission Sounder

9.1 Laser power stability attained with constant current supply

The optical output power of the laser diode strongly depends on the laser temperature. This is caused by the temperature dependence of the junction voltage of the laser. Figure 9-1 shows the typical characteristics of the optical output power versus temperature at 100mA stabilized laser drive current (nominal value).

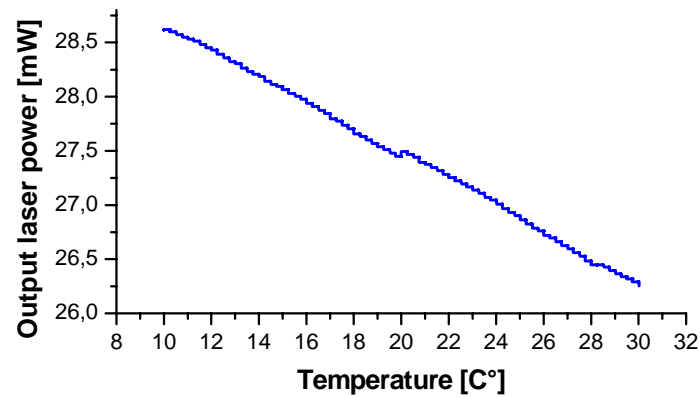


Figure 9-1 Output laser power versus temperature with stabilized current supply

The laser current is stabilized by a commercial laser power supply made by Thorlabs, Inc. (ITC8000) [87], and the temperature of the laser diode is controlled by a water chiller. In order to simulate the real thermal environment of the laser unit on the spacecraft, the temperature of the laser is changed from 10-30°C in 0.25°C steps. This temperature range is calculated considering the following thermal conditions: the thermal operating range of the WBO is provided by the temperature of the SVM plate, which is 5-15°C. But, the laser temperature is expected to be 5.5°C higher than the WBO baseplate (due to the poor thermal conductivity of the titanium laser housing), and 11°C higher than the SVM baseplate (due to the thermal isolation by the stainless steel spherical washers underneath the three feet of the WBO) [81].

The output power versus temperature is essentially linear, besides small power steps caused by mode jumps (cf. Figure 9-5). The average power variation, as a function of the laser drive current, is summarized in Table 9-1.

9.2 Laser power stability attained with constant voltage supply

The strong temperature dependence of the output laser power can be significantly reduced by using a constant voltage power supply and a resistor connected in serial with the laser diode. However, the characteristics of the junction voltage must be known for the optimization, but these can be calculated from the output power measurement taken with the stabilized current power supply as follows. The optical output power (P_{opt}) linearly scales with temperature, consequently, the consumed electrical power (P_e), which is well known from the U-I characteristics of the diode, is also linear

$$P_e(T) = \kappa P_{opt}(T) = \kappa P_{opt}(1 + \gamma T), \quad (9.1)$$

where γ is the slope of the linear optical output function and κ is a power scaling factor according to the electrical power measurement. Electrically, the laser diode can be substituted with a capacitor and resistor connected serially (R_l). The capacitor models the temperature dependence of the junction voltage (U_j), while the resistor, which is assumed as temperature independent one, describes the internal resistance of the laser diode (typically 3.8Ω). From this model and (9.1), the function of the junction voltage versus temperature can be calculated

$$U_j(T) = \frac{P_e(T)}{I} - R_l I = U_j(1 + \alpha T), \quad (9.2)$$

where α denotes the linear thermal coefficient of the junction voltage. The consumed electrical power of the laser diode using the stabilized voltage power supply and the series resistor can be expressed by

$$P_e(T, R_s) = [U_j(T) + I(T)R_l]I(T), \quad (9.3)$$

where the laser current is determined by

$$I(T) = \frac{U_0(R_s) - U_j(T)}{R_s + R_l}. \quad (9.4)$$

The necessary voltage of the power supply (U_0), as a function of the serial resistor, is determined by the required laser light power. But, this can be also expressed by using the results of the laser power measurement performed with the stabilized current power supply at a suitable operating temperature of $20^\circ C$

$$U_0(R_s) = U_j(T = 20) + I_c(R_s + R_l), \quad (9.5)$$

where I_c is the value of the constant current. Substituting (9.4) and (9.5) into (9.3), and considering the power changes that must be minimized ($\frac{\partial P_e(T, R_s)}{\partial T} = 0$) results in the following quadratic function of the serial resistor, R_s

$$I_c R_s^2 + [U_j(T = 20) - 2U_j(T)]R_s - [U_j(T = 20) + I_c R_l]R_l = 0. \quad (9.6)$$

Using the data of a laser diode selected from the batch of the flight diodes, the expression of (9.6) can be solved at $20^\circ C$, the middle of the laser operation temperature range ($15-25^\circ C$). This results in 16.4Ω for the serial resistor. Applying this resistor the power change can be reduced to practically zero, as shown in Figure 9-2. Nevertheless, the value of the series resistor needed for the optical power compensation of the laser is dependent on the laser diode itself.

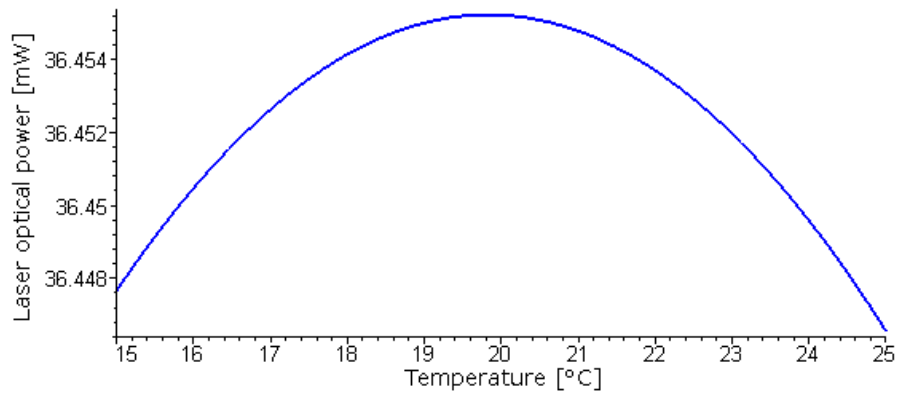


Figure 9-2 Optical output power change of the laser diode. The maximum change of the function within the temperature range of 15-25°C is approximately 7 μ W.

The deviation from this optimized serial resistance value increases the power variation of the laser. In the temperature range of 15-25°C the function of the laser output power versus resistance of the serial resistor is depicted in Figure 9-3.

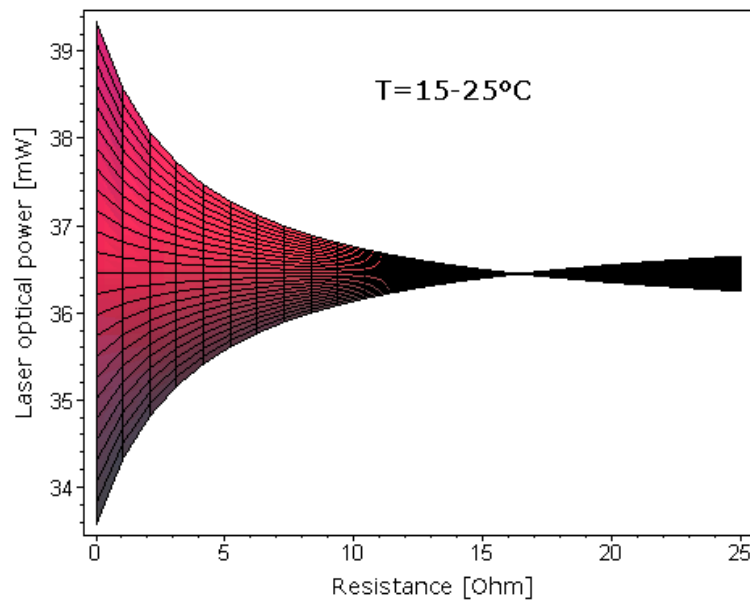


Figure 9-3 Laser output power as a function of serial resistance and temperature

During the SWAS program, good results were reached by means of a 10 Ω serial resistor. Thus, the output power measurement is performed also using the same value of resistance. The voltage of the power supply is adjusted to become approximately the same laser output power level. The measured data are plotted in Figure 9-4.

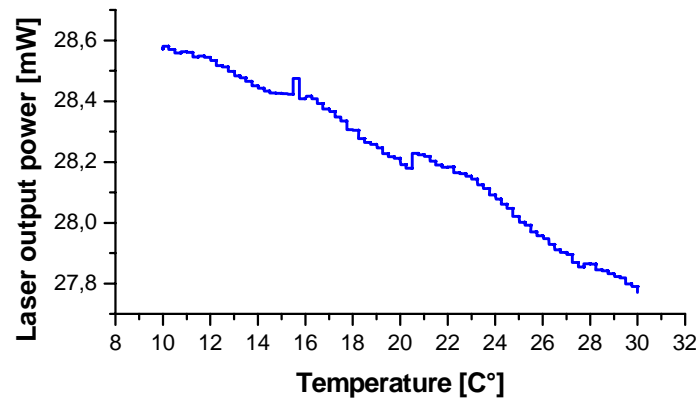


Figure 9-4 Laser output power characteristics versus temperature with stabilized voltage supply applying a 10Ω serial resistor.

The difference between the two laser supplying modes is summarized in Table 9-1.

| Laser drive current [mA] | Output laser power variation with stabilized current supply [mW/K] | stabilized voltage supply [mW/K] |
|--------------------------|--|----------------------------------|
| 100 | 0.12 | 0.041 |

Table 9-1 Comparison table of the power variation of the laser driven with constant current and voltage

It can be concluded that the measured values are well in correspondence with the theoretically predicted results. Using the constant voltage power supply and serial resistor provides better results: the output power variation of the laser is reduced by a factor of 3 at 100mA compared to the constant current supply. Thus, the total power stability of the spectrometer is increased. Moreover, for safety reasons the use of the stabilized voltage supply is also preferred, because a short loss of contact at the laser (for example a bad contact of the laser connector during the assembly phase) does not endanger the functionality of the diode, while in case of the constant current supply the laser voltage increases resulting in an immediate damage of the laser.

9.3 Mode hop characteristics of the laser diode

A characteristic feature of the laser is the temperature and drive current dependence of its wavelength. The wavelength stability plays an important role in the frequency and spectroscopic stability of the spectrometer, because the wavelength change of the laser results in a variation of the Bragg deflection angle, i.e. detected frequency. On the other hand, it causes a focal length change of the optical setup yielding resolution deterioration (see Section 10.14). A typical wavelength characteristic of the Hitachi laser diode applying the constant current power supply is shown in Figure 9-5.

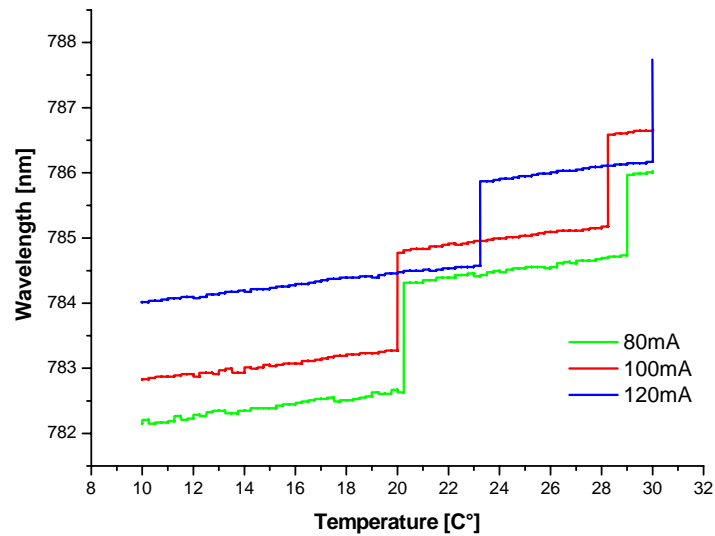


Figure 9-5 Temperature dependence of the wavelength applying the constant current power supply. The wavelength change during a mode jump is in the order of 2nm. The wavelength variation in the mode jump free region at 100mA laser current is 0.042nm/K.

The laser temperature is slowly increased from 10-30°C in 0.25°C steps and the laser wavelength is monitored by means of a grating spectrograph (ETA-SB, wavelength resolution of 0.06nm). In the 15-25°C operating temperature range of the laser diode the wavelength variation is about 2nm and a mode jump occurs only once (the repeatability of the measurement was proven).

The same measurement is accomplished with the constant voltage power supply, in order

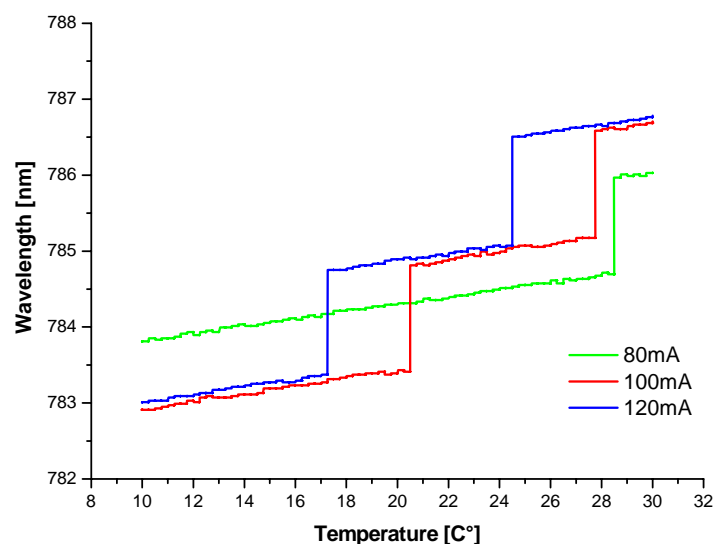


Figure 9-6 Wavelength characteristics of the Hitachi laser diode using a stabilized voltage power supply. In case of a mode hop the wavelength change is typically about 2nm. The average wavelength change in the mode jump free region at 100mA laser current is 0.044nm/K.

to compare the impact of the two different power supplies on the wavelength change. The wavelength versus temperature function is depicted in Figure 9-6.

With the stabilized voltage power supply the mode jumps shift towards lower temperatures with increasing output power, while at lower output power levels (80mA) mode jumps occur less frequently. This is an unusual behaviour and conclusions are very tentative because of low number statistics. In the operating temperature range, the wavelength variation is approximately 4nm (at the 100mA nominal drive current) and mode jumps occur twice.

Principally, the wavelength variation as a function of the laser operating temperature is quite similar for both supply methods, therefore, from the wavelength variation point of view both power supplies are appropriate. Actually, the mode jump property of the laser, i.e. the Bragg deflection angle change, is a tolerable effect. It can be corrected by occasional frequency calibration of the spectrometer.

9.4 Investigation of the wavelength hysteresis

In case of a mode hop, it is important to verify that there is no oscillation between two or more modes, because it immediately results in resolution, frequency stability and frequency calibration degradation of the spectrometer. For other types of laser diodes advertised as single mode lasers (Toshiba, Sharp, etc.), it is well known [48] that during a mode oscillation there are more modes present. These modes compete with each other, which is very undesirable. Such behaviour immediately destroys the resolution of the WBO spectrometer. From this reason, the mode oscillation property of the Hitachi HL7851G laser diodes had to be carefully investigated. During the experiment the laser temperature is slowly increased from 10-30°C then decreased again to 10°C, and every 0.25°C the laser wavelength is monitored by the grating spectrometer. The measurement is performed with the two different supply methods, and Figure 9-7 shows the wavelength of the laser current at 100mA as a function of temperature.

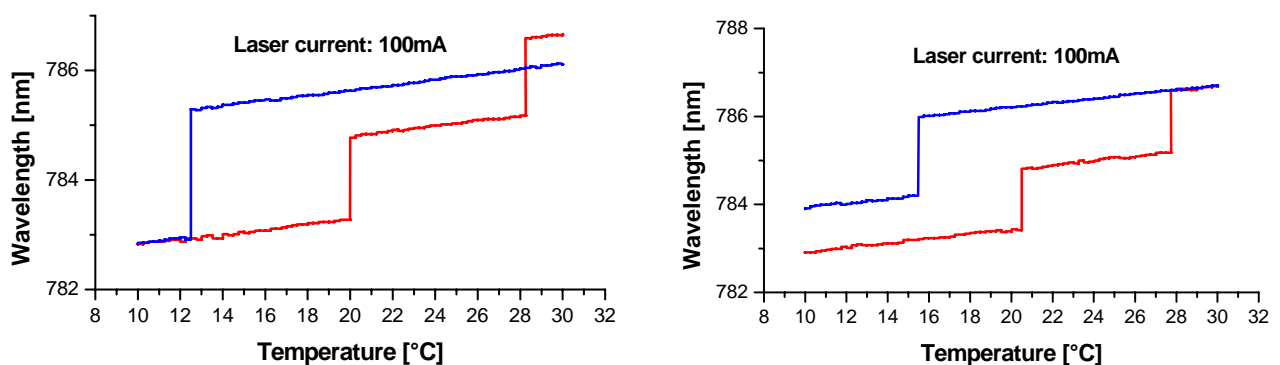


Figure 9-7 Wavelength measurement at increasing and decreasing temperature at different laser powers with constant current (left) and voltage (right) power supplies.

The measurement shows that mode jumps have a large hysteresis in wavelength in both cases, therefore mode oscillations at a given temperature are very improbable.

Since the temperature stability of the SVM is expected to be less than $1K/hour$ and the thermal isolation of the WBO is quite good, the wavelength and power stability of the laser is adequate on the timescale of the astronomical observations. From the required frequency accuracy of $100kHz$, estimates can be made for how frequently a frequency calibration should be done due to the wavelength changes of the laser. The results of the thermal model show that a frequency calibration of the instrument should occur if the temperature change of the SVM is more than $0.2K$. Thus, a realistic frequency of the calibration is expected to be a few times per day.

9.5 Output power and wavelength stability of the laser at stabilized temperature

At stabilized temperatures the laser light intensity and wavelength may vary in different ways depending on the supply methods. Therefore, a measurement was taken in thermal equilibrium, where the laser power and wavelength were monitored over a long time period. Figure 9-8 shows the intensity of the same laser diode driven with two different types of power supplies versus time at $20^{\circ}C$ stabilized operating temperature and approximately at the same $120mA$ laser current.

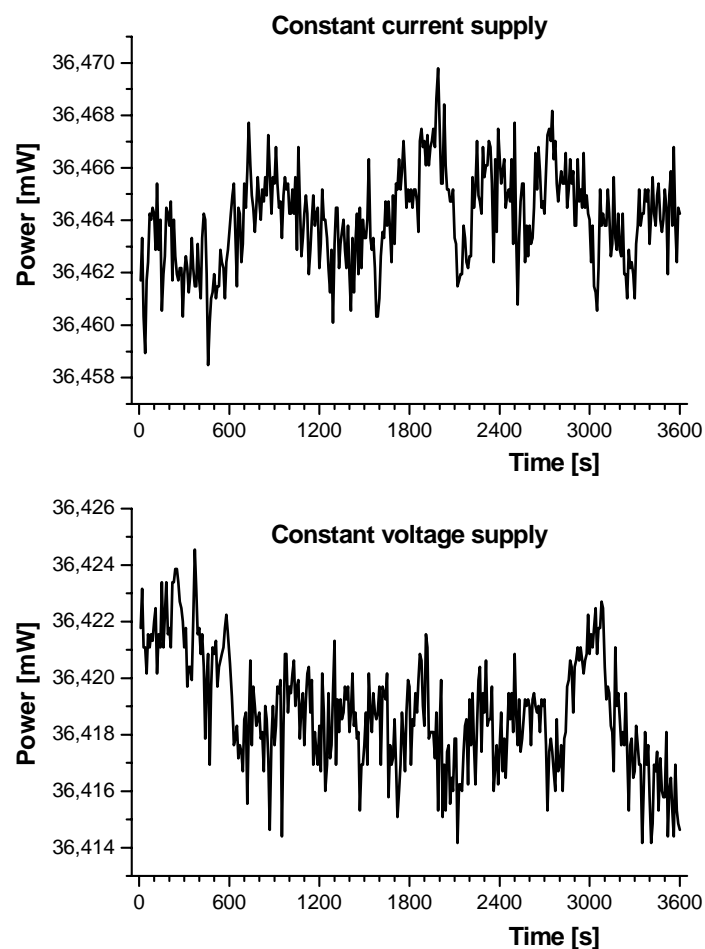


Figure 9-8 Output power stability of the Hitachi laser diode supplied by stabilized current and voltage. In order to guarantee the thermal equilibrium needed for the stability measurement, the laser diode was operated for 1 day before the measurement was taken.

In the measured data, the stability of the measurement system is also included. Performing a relative measurement is not possible, because the stability of the system without signal intensity (dark current) is not reliable. It can be concluded, that within the time scale of one hour, there is no recognizable difference between the two different types of laser supplies; the peak-to-valley power variation is $<10\mu W$ (0.03% of the output power). The measured laser power stability is much better than the power stability of the whole instrument, which is dominated by efficiency changes caused by mechanical deformations. Thus, both power supplies provide appropriate power stability for the instrument.

Within the measurement accuracy (0.06nm), the measured laser wavelengths are constant in both supplying cases: 784,85nm and 784,89nm, respectively.

9.6 Lifetime statistics

In order to guarantee the long-life and safe operation of the WBS during the mission, the laser diodes must undergo a space qualification process. The qualification procedure was done by KOSMA and the following properties of the selected 50 diodes were tested:

- electrical and optical characterization,
- thermal cycling,
- leak and bubble test,
- burn-in, and
- accelerated life time test.

The results of the accelerated life test indicate an average output laser power reduction of 30% at 70°C and 18% at 50°C after 3000hours at the reduced optical power of 40mW [24], [93]. From these data the average lifetime of a laser diode can be approximated by using the statistical law of

$$P_{out}(t) = P_0 e^{-t/\tau}, \quad (9.7)$$

where

- P_{out} – is the output power of the laser after operation time of t ,
- P_0 – is the output power of a new laser, and
- τ – is the average lifetime of the laser.

The average lifetime of the lasers was calculated to be 8411hours (0.96year) at 70°C and 15117 (1.73year) at 50°C. The operation temperature of the laser is about 20°C, therefore the average lifetime is longer than at 50°C, for instance. The relationship between the temperature of the laser diode and the estimated lifetime can be derived by using the Arrhenius formula [67], [26]

$$t = C \cdot e^{\frac{E_a}{k_B T}}, \quad (9.8)$$

where

- E_a – is the activation energy,
- k_B – is the Boltzmann constant ($8.6 \cdot 10^{-5} eV / K$), and

T – is the temperature of the diode in K .

From the ratio of the calculated average lifetimes at known temperatures

$$\frac{t_1}{t_2} = \frac{e^{E_a/k_B T_1}}{e^{E_a/k_B T_2}}, \quad (9.9)$$

the activation energy can be expressed as

$$E_a = \frac{\ln(t_1/t_2)}{\left[\frac{1}{k_B T_1} - \frac{1}{k_B T_2} \right]} = 0.28eV. \quad (9.10)$$

The average lifetime of the lasers at $20^\circ C$ can be determined from the lifetime measured at $50^\circ C$ and from the activation energy by using (9.9). The calculation results in approximately 4.8 years. The probability that one laser diode fails within 2 years of operation is

$$\eta_f(t) = 1 - e^{(-t/\tau)} = 34\%. \quad (9.11)$$

During the mission the two spectrometers are operating simultaneously, thus the probability that one of the WBO fails within 2 years is η_f^2 , about 12%. The probability that the main and redundant lasers in both spectrometers fail is η_f^4 , about 1%, but this is a worst case approximation, because the operation time of the redundant laser is less than 2 years. The lifetime test of the flight lasers clearly shows the WBO has high reliability.

9.7 Laser light feedback from the collimating optics

The power and frequency stability of the laser diode is adversely affected by optical feedback effects, which is mainly coming from reflections of optics behind the laser. To achieve a stable operation of the laser used for HIFI the optical surfaces have to be antireflection coated, especially the surfaces of the collimating optics, and the shape of the lens curvatures must be carefully optimized for minimum feedback. The most important aspects are that the distance between the laser and collimating optics is possibly large and there is no focused reflection from the surfaces of the optics.

The detailed calculation of the laser feedback can be found in Appendix E. In Table 9-2 the feedback level of commercial (made by Melles Griot) and special (developed for the WBO by Galileo Avionica) collimating optics are compared taking into account the elliptical shape of the laser beam. The computation gives details about the reflected power levels if one, two or three reflecting lens surfaces are considered. The feedback power level is calculated in dB , furthermore the reflection coefficient of 0.02 of the antireflection-coated glass is assumed.

| Type of collimating optics | Number of reflecting surfaces of collimating optics | | |
|----------------------------|---|----------|----------|
| | 1 | 2 | 3 |
| Melles Griot | -62.73dB | -62.08dB | -60.70dB |
| Galileo Avionica | -66.52dB | -65.9dB | -64.91dB |

Table 9-2 Comparison table for power feedback of the laser diode in case of two different type of collimating optics in rotational symmetric and elliptical case

The design of the two collimating optics can be seen in Figure 9-9.

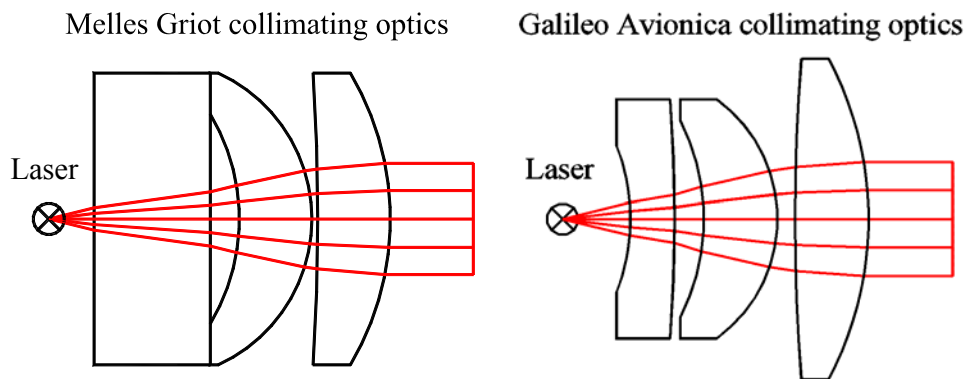


Figure 9-9 Two different types of collimator designs. The Melles Griot optics is a commercial one and the Galileo optics is evaluated for HIFI.

Conspicuously, the first lens in the Melles Griot optics has two plane surfaces, which alone should give better results, but the distance to the laser is much less than in case of the Galileo optics, and there is a focused reflection from the third surface of the Melles Griot optics as well ($R_3=6.95mm$, $d_3=6.56mm$). The Galileo design does not produce any focused reflections at all and the laser-collimator distance is also chosen adequately large. However, the results show that both of the optics are fairly well constructed for low feedback operation. The heritage of the SWAS experience provides us a reliable rule of thumb for the minimum power coupling level of -60dB so both of them guarantee a feedback below this level.

If we consider the glass window of the laser diode in the calculation the power feedback would be -53.5dB with the Galileo optics. The laser glass window is antireflection coated, where 0.02 is assumed for the reflection coefficient. The calculation also shows that in this sense, the collimating optics plays only a minor role in the feedback effect.

10 Performance tests of the WBO

This chapter summarizes the results of the versatile performance tests carried out with the WBS qualification model. These results are direct measure of the opto-mechanical design and adjustment quality. The optical design guarantees the perfect imaging of the signal light intensity onto the detector array performing the demanded efficiency and resolution of the instrument. Further on, the mechanical design of the single components and the housing contributes to the stability feature of the spectrometer. Without a careful adjustment and fixing of the modules the required high performance of the WBS would have not been achieved.

10.1 Zero level of the detector

The even and odd channels of the CCD detector are separately driven. Consequently, they have different offset levels due to the slightly different functioning of the drive electronics. The resulting offsets can be seen in the spectrum, as shown in Figure 10-1.

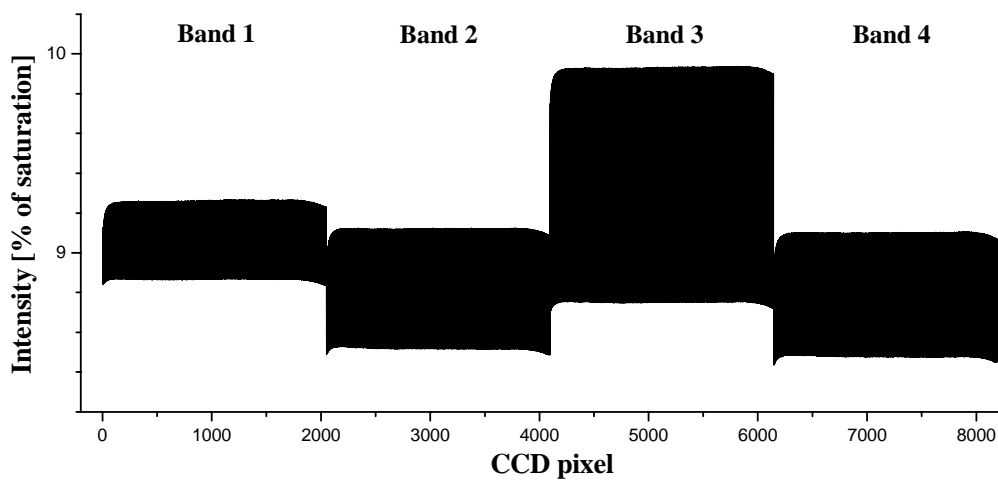


Figure 10-1 Zero level (dark current) of the CCD. The average of 256 scans is plotted over the 4GHz bandwidth.

The average count of the zero levels is approximately 10% of the saturation level. The difference between the dark current level of the even and odd pixels is 2-4 counts (except band 3), which is well within the specified 1% of the saturation level. At band 3, optimisation of the even-odd offset is needed on the analogue circuits of the CCD, as is done during the flight hardware fabrication. In order to reduce differential non-linearity effects of the

analogue-digital converters, a sawtooth-function is applied during the readout of the CCD. The amplitude of the saw is 6% of the saturation level and its period is 256 scans (2560ms).

10.2 Light scatter

Light scatter plays an important role in the stability of the spectrometer, therefore its level must be held as low as possible. In the WBO, the most scattered light is produced in the Bragg cell due to crystal imperfections and reflections from the surfaces of the deflector's mounting, especially on the transducer side. Nevertheless, the polarization switching property of the deflector gives the possibility to use a crossed polarizer in front and behind of the Bragg cell. This reduces the zero order light intensity, and the significantly suppresses the depolarized scattered light.

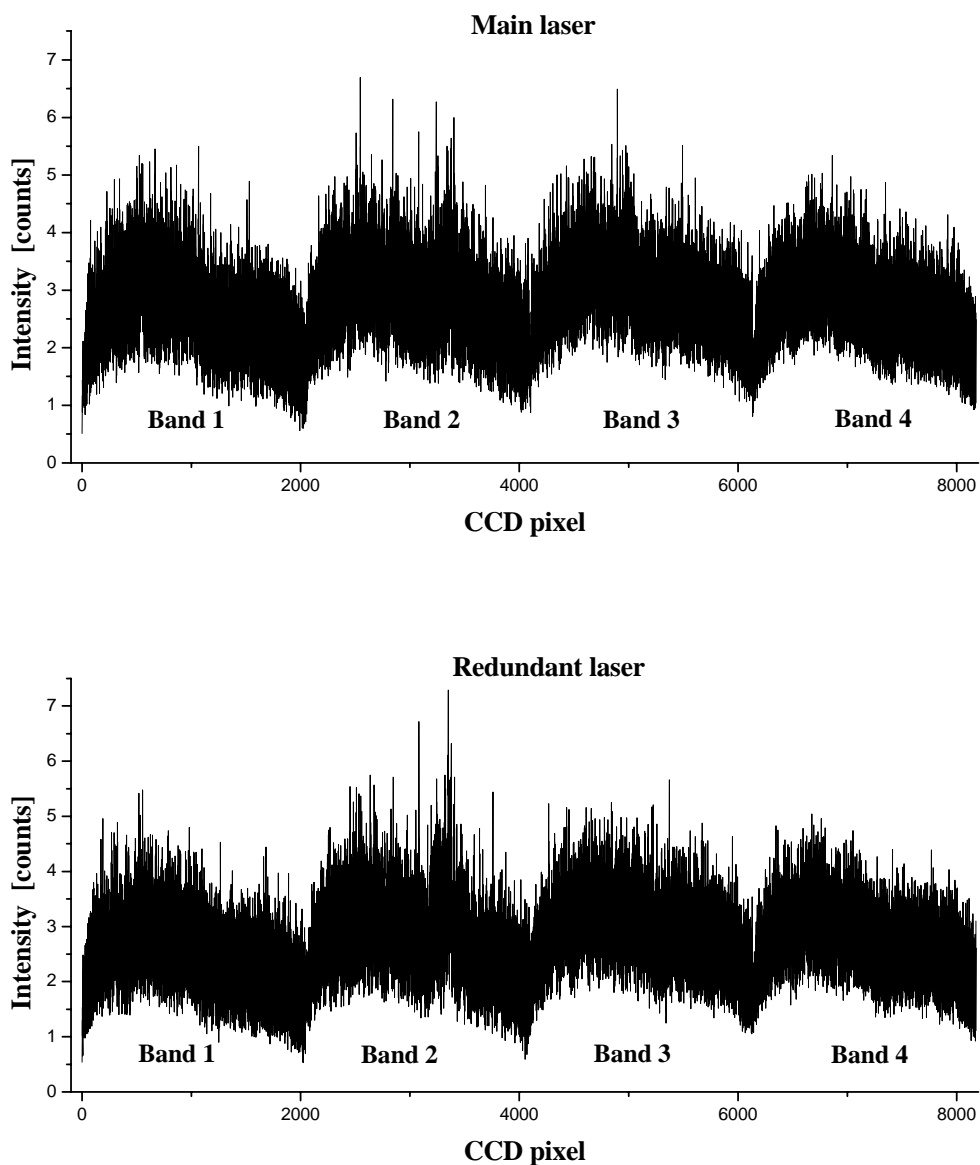


Figure 10-2 Light scatter level of the WBO (single readout) applying the two lasers

The peak light scatter level is smaller than 1% of the saturation level, which meets the specification.

10.3 IF zero level

The zero level of the whole backend system can be characterized by connecting the IF unit to the spectrometer without applying any input signal (zero switch ON) and using the maximum attenuation of the instrument. The measured spectra, depicted in Figure 10-3, correspond to the bandshape of the single bands of the WBO and the IF unit. The IF zero level is well within the allowed maximum noise temperature of the IF unit of 300K.

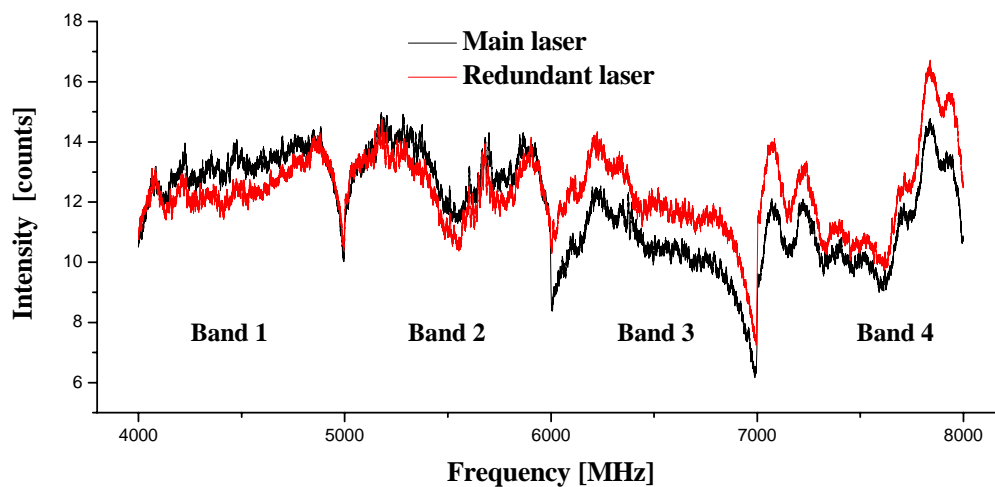


Figure 10-3 IF zero level of the four bands of the WBO. The saturation level is 1024 counts

10.4 Bandpass of the WBO

The frequency bandpass of the WBO sub-bands can be measured either with an external synthesizer, where sharp frequency lines are applied to the input of the WBO in discrete steps (50MHz), or with the internal comb generator of the WBE unit. The advantage of the synthesizer is that symmetric response of the frequency channels (the intensities of the neighbouring pixels are symmetric to the maximum intensity pixel) can be adjusted, which makes it to precisely characterize the bandshape of the instrument. The measurement performed with the main laser is shown in Figure 10-4.

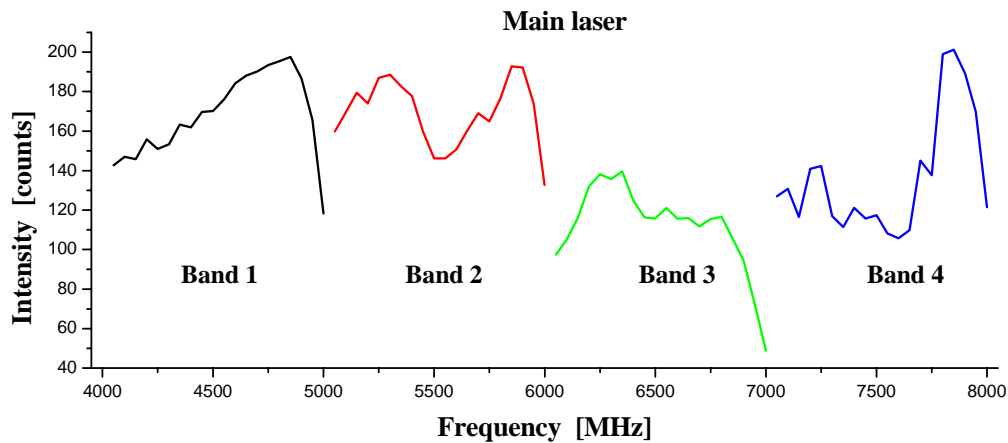


Figure 10-4 Frequency bandshape of the WBO's sub-bands measured with an external synthesizer. The gain variation between the sub-bands is measured to be 1.7dB, slightly worse than specified.

During the adjustment of the spectrometer, the achieved performance of the sub-bands is a compromise of efficiency, resolution, and bandpass ripple between the bands due to the beam tolerances of the laser source unit. For instance, the beam spacing is slightly different from the acoustic zone spacing of the Bragg cell, which results in different illumination of the deflector and therefore different bandshape of the bands. The tolerances of the source unit are rather large in the case of the qualification model; consequently, the required bandpass performance does not meet the specification in all cases. Even the internal sub-band equalizers cannot always improve the bandshape of the WBO channels, since they do not exactly match the bandshape attained with alignment (c.f. summary Table 10-1).

| | Bandpass ripple [dB] | | | |
|------------|----------------------|------------|------------|------------|
| | Sub-band 1 | Sub-band 2 | Sub-band 3 | Sub-band 4 |
| Main laser | 2.2 | 1.7 | 4.6 | 3.2 |

Table 10-1 Bandpass ripple of the WBO sub-bands measured with a synthesizer

The bandpass ripple of the qualification model is within the specified 3dB value; only the bands 3 and 4 are above this limit, but they will be improved during the flight hardware production.

In orbit, the only possibility to check the bandpass of the WBO is to use the internal comb generator. Nevertheless, the measurement accuracy is not as high as achieved with the synthesiser, because the comb lines cannot be shifted to obtain symmetrically illuminated pixels, and therefore the intensity response of the frequency channels results in a smaller value. The bandpass ripple calculated from the maximum counts of the comb lines (see Figure 10-9) is summarized in Table 10-2.

| | Bandpass ripple [dB] | | | |
|-----------------|----------------------|------------|------------|------------|
| | Sub-band 1 | Sub-band 2 | Sub-band 3 | Sub-band 4 |
| Main laser | 1.4 | 1.4 | 2.2 | 2.6 |
| Redundant laser | 1.3 | 1.1 | 2.1 | 3.0 |

Table 10-2 Bandpass ripple of the WBO sub-bands measured with the comb generator

10.5 Power linearity

The total power non-linearity of the spectrometer introduces baseline distortions in the measured spectra. To characterize the linearity of the instrument a noise source is connected to the input of the WBS. The output power level of the noise source is changed by using the attenuators of the WBE, and is measured by an RF power meter that is connected to the RF test port of the noise source. The output of all frequency pixels is averaged then plotted versus output power of the noise source, as seen in Figure 10-5.

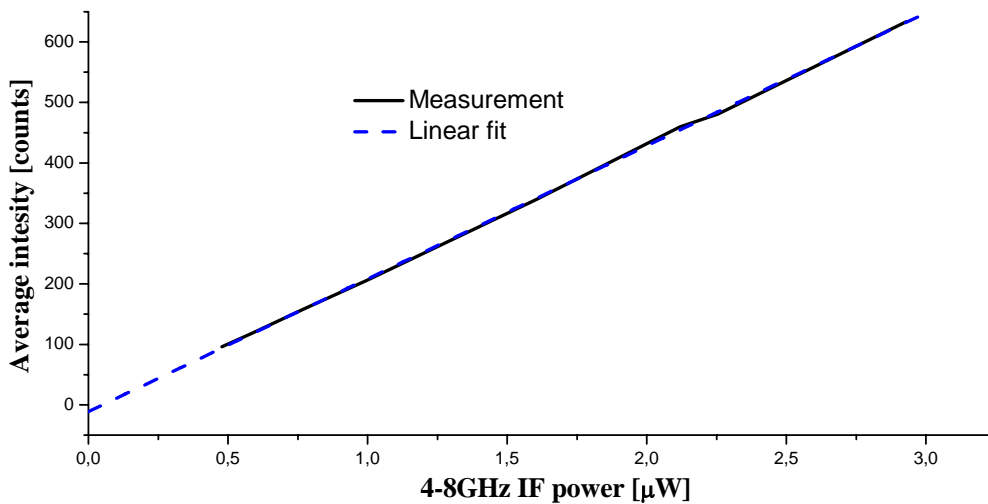


Figure 10-5 Total power linearity of the WBO

The total power non-linearity as a residual plot of the linear fit subtracted from the measured data is depicted in Figure 10-6. The power linearity is given in percentage relative to the saturation level of the instrument.

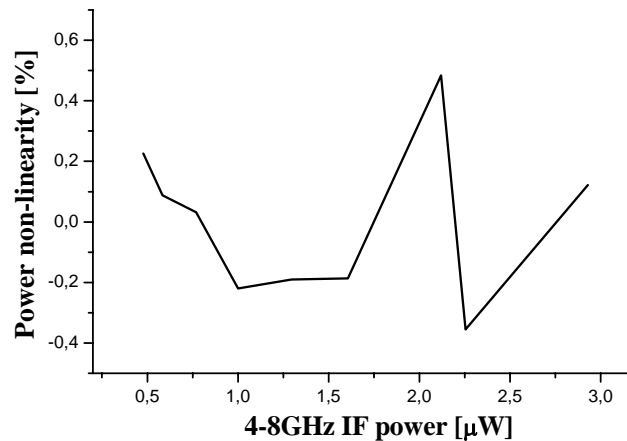


Figure 10-6 Residual plot of the total power non-linearity relative to the saturation level of the CCD

The non-linearity of the instrument scaled to the saturation level of the CCD is in the order of $\pm 0.5\%$, which is well within the specification ($\pm 1\%$). The irregular behaviour at $2\mu W$ IF power is probably caused by the automatic measurement range switch of the power meter.

10.6 Frequency non-linearity

The frequency non-linearity can be calculated using the bandpass measurement done with the synthesizer. From the number of the valid frequency pixels, the frequency range, and the pixel number of the balanced frequency channel, the frequency non-linearity of the spectrometer without frequency calibration can be evaluated. The measured data is shown in Figure 10-7.

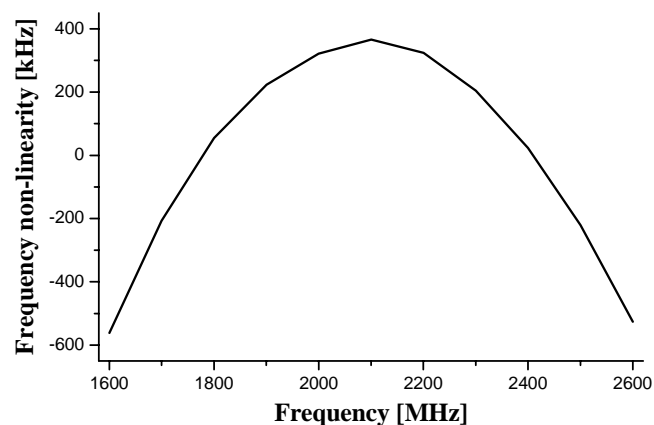


Figure 10-7 Typical frequency non-linearity of a WBO sub-band. The ± 1 pixel corresponds to about ± 0.7 MHz frequency non-linearity.

10.7 Frequency calibration

The frequency calibration of the WBO is performed by means of the comb generator. The spacing of the lines is $100\text{MHz} \pm 0.1\text{MHz}$, which provides a frequency calibration accuracy of

10.8 Frequency resolution

better than $\pm 0.1\text{MHz}$. If a broadband spectrum is needed the data is necessary to be re-sampled (actually this means a few percent resolution loss). The co-added spectrum of the comb measurements are shown in Figure 10-8 and Figure 10-9

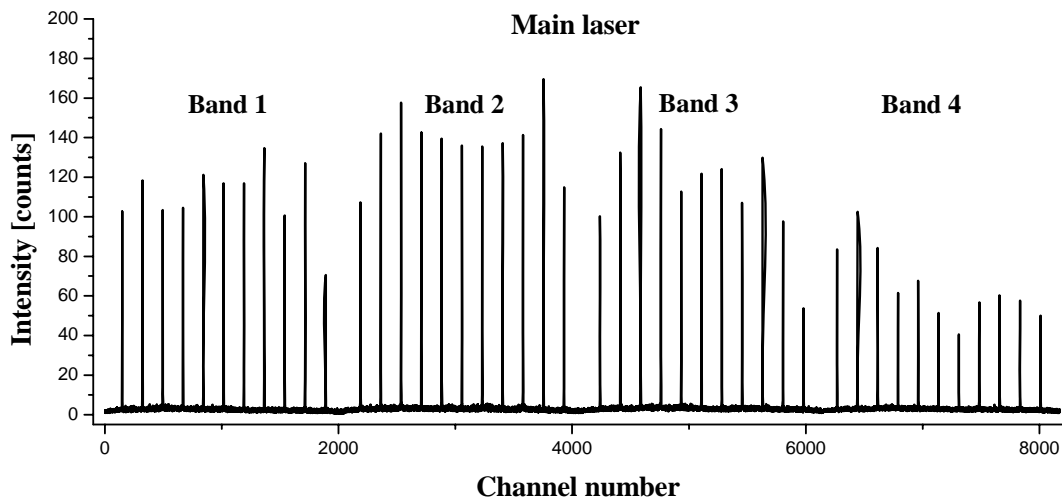


Figure 10-8 Comb signals measured with the main laser

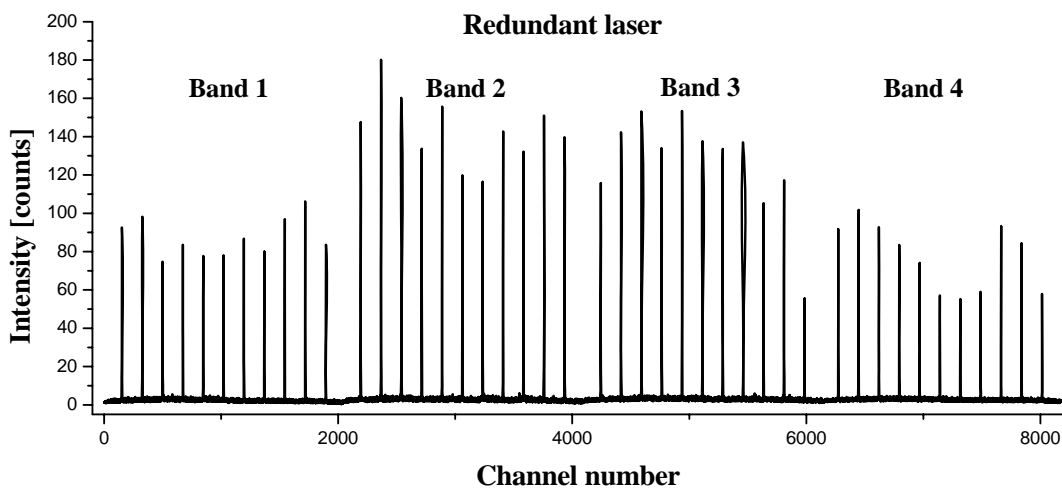


Figure 10-9 Comb signals measured with the redundant laser. In the spectrum, the frequency bandpass of the WBO sub-bands can also be recognized.

The comb lines are also useful to determine in orbit the frequency resolution, line profile, and bandpass of the WBO, as mentioned above.

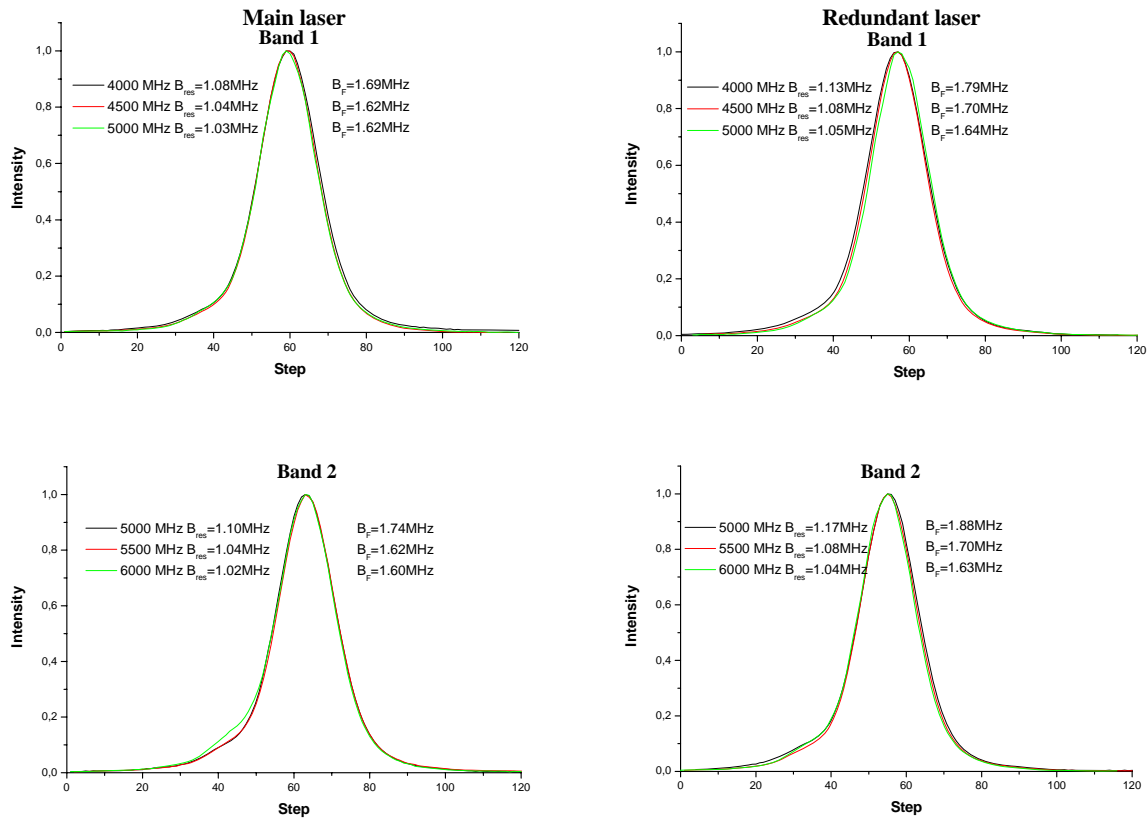
10.8 Frequency resolution

The frequency resolution of the spectrometer is mainly determined by the frequency resolution of the Bragg cell (c.f. Section 4.3), but diffraction and aberration effects, the finite pixel size of the CCD, and the almost Nyquist sampling method also contribute to the

maximum achievable resolution. The response of frequency channel of the instrument is not rectangular (ideal case), but Gaussian at the centre and Lorentzian-like at the wings, due the Gaussian distributed deflected light and lens aberration effects introduced by the optics. A reasonable definition of the frequency resolution of acousto-optical spectrometers is defined by the resolution bandwidth

$$B_{res} = \frac{\int_0^{\infty} P(\nu) d\nu}{P_{max}}, \quad (10.1)$$

where $P(\nu)$ is the response of a frequency channel. The resolution bandwidth expresses the width of an equivalent filter having the same maximum response, which transmits the same average power of white noise. The definition above exactly describes the real frequency resolution of the instrument, as it contains the side-lobes of the filter function of the frequency channels. For the WBO, the filter curves measured at the band ends and in the middle of the band for all four bands are plotted in Figure 10-10.



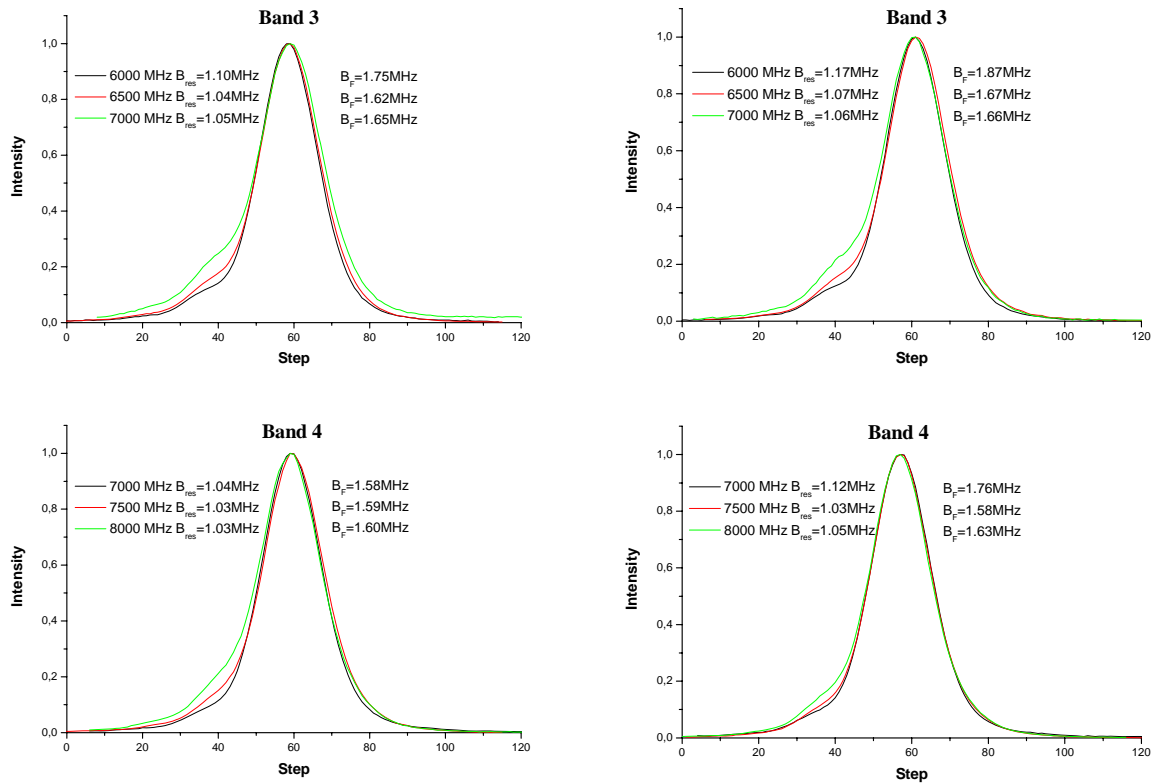


Figure 10-10 Frequency resolution of the WBO sub-bands attained with the main (left) and redundant (right) lasers. The average resolution bandwidth measured with the main laser is 1.05MHz (fluctuation bandwidth is 1.64MHz); while with the redundant laser, it is about 5% worse.

The frequency resolution of the instrument is within the specification of 1.1MHz in all cases with the main laser, and in some cases, it is slightly above with the redundant laser.

In orbit, the frequency resolution can not be verified with the method described above, since there is no synthesizer available onboard the satellite. Thus, the resolution is calculated from the comb measurement using a simple Gaussian fit on the comb lines. The results of the resolution are of course less accurate, but can provide a good comparison database for future performance verification tests done with the instrument. The FWHM dimension of the filter curve is about 10% smaller than the resolution bandwidth. The average frequency resolution over the bands is approximately 1.0MHz.

10.9 Noise performance

10.9.1 Stability

In order to be able to observe weak signals of radio astronomical sources, like interstellar molecular clouds, long integration times are necessary during the measurements. In case of white noise, the radiometric noise decrease according to the radiometer equation with the square root of integration time, and therefore the signal-to-noise ratio increases. The maximum integration time of the spectrometer, when noise contributions of the instrument become dominant, can be determined by the Allan variance method [1]. Actually, for characterization of stabilities of heterodyne receivers equipped with spectrometer backends there are two commonly used methods of computing the Allan variance. The *spectroscopic*

Allan variance, which describes instabilities deviating from common gain variations across the entire band, uses only one or two statistically independent frequency channels. In case of a spectroscopic Allan variance measurement the variance σ_A^2 of the mean value of continuously measured data are plotted versus various integration times t_{int} on double logarithmic scale. To measure only the drifts that are different for the individual frequency channels of the instrument, the variance of difference of two arbitrarily chosen channels S_1 and S_2 is determined [69]

$$\sigma_A^2(t_{int}) = \frac{1}{2} \langle (S_0(i) - \langle S_0(i) \rangle)^2 \rangle, \quad (10.2)$$

where

$$S_0(i) = \left[\frac{1}{\sqrt{2}} \left(\frac{S_1(i)}{\langle S_1 \rangle} - \frac{S_2(i)}{\langle S_2 \rangle} \right) + 1 \right] \frac{\langle S_1 \rangle + \langle S_2 \rangle}{2}. \quad (10.3)$$

The channel distance is chosen adequately large to ensure that their signals are not correlated. However, the result of stability depends on the selection of the two channels, and therefore does not properly characterize the complete instrument.

In order to simulate real astronomical observations, where the detected signals in all channels are equally important, e.g. in frequency surveys of rich emission spectra with hundreds of lines per spectrum, the statistical behaviour of the complete baselines of 1GHz (sub-bands) and 4GHz (co-added broadband) bandwidths of the instrument are investigated. During the baseline measurement the variance of all frequency channels, the *Allan baseline variance*, is computed using different integration times [65]. Since the counts in the measured spectrum strongly depend on the bandpass of the device, a normalization of the baseline statistics is needed. This is realized by the calibration scheme of $(Sig-Ref)/(Ref-Zero)$, where *Sig*, *Ref* and *Zero* denote the signal, reference and zero measurements of a simulated astronomical observation, respectively. The baseline stability measurements of the WBO accomplished at 10% and 50% illumination of the saturation level are depicted in Figure 10-11 and Figure 10-12 respectively. For the simulated astronomical measurement, the signal of a temperature stabilized noise source is applied to the input of the spectrometer.

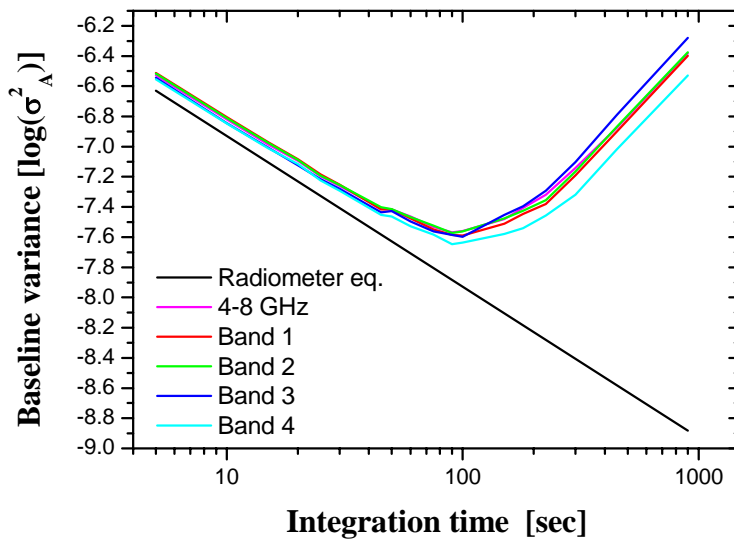


Figure 10-11 Allan baseline stability measurement performed at 10% illumination level. The Allan minimum time is about 100 seconds for all bands.

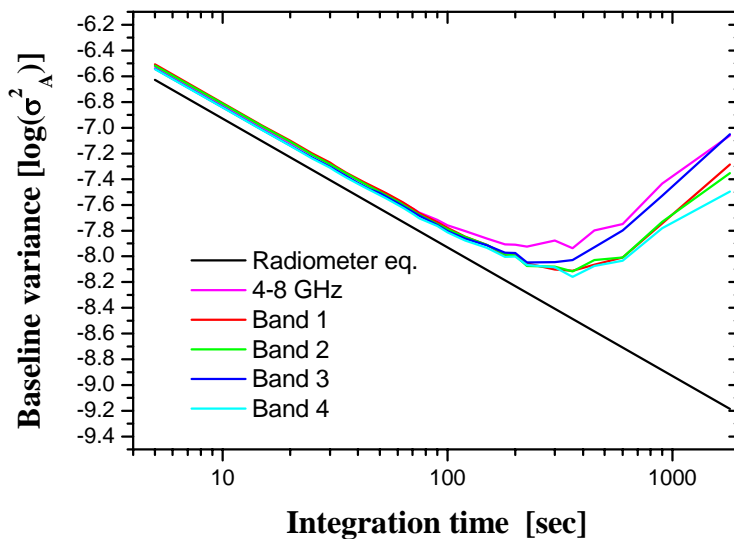


Figure 10-12 Allan baseline analysis done at 50% illumination level. The Allan minimum times of the WBO sub-bands are measured to be approximately 300 seconds. The baseline stability of the total 4 GHz bandwidth is slightly worse than the stability of the single bands.

For pure white noise, the plot of the Allan baseline variance versus time decreases with the slope of -1. Due to increasing drift noises of the spectrometer, the slope increases as well and finally it turns to positive. The minimum of the plot determines the time (*Allan minimum time*), when the white noise becomes equal to the drift noises of the instrument. Hence, the Allan minimum time is a good measure of instrument stabilities. In practice, the integration time during a measurement should be always less than the Alan time in order not to affect the measurement results by drift noises.

In case of lower illumination levels, the noise of the spectrometer becomes dominating and the stability of the instrument decreases. For integration times larger than the Allan minimum time the noise fluctuations corresponds to scattered light dominated noise contribution, which is needed to be improved for the flight models. At larger illumination levels platforming effect is visible in the Allan plot, the Allan minimum time for the total 4GHz bandwidth is smaller than for the sub-bands.

The stability requirement for the instruments of Herschel is very high because of the large mass and slow movement of the telescope. For calibration reasons the telescope is slewed between the signal and reference positions. During this movement the instruments of the receiver system should remain stable. The time needed for switching between the two positions is the dead time of the measurement. With increasing integration time per positions the relative dead time becomes less. One of the most efficient way of observing is using the chop mechanism of the telescope. It provides fast switching between two positions of the sky and therefore results in a small dead time and less stability constraint during an observation [74]. For satellite projects, it is essential to use the observatory in the most efficient way because of the enormous costs of observing time. Thus, the optimization of observing modes is of decisive importance [66].

10.9.2 Noise fluctuation bandwidth – noise dynamic range

The noise fluctuation bandwidth of an acousto-optical spectrometer can be determined from the filter curve measurement (c.f. Eq. 7.45) as well as from the Allan baseline stability measurement. In the Allan plot, considering the range where the slope of the baseline variance is -1, i.e. the radiometer equation exactly describes the behaviour of the radiometric noise, the noise fluctuation bandwidth can be calculated by substituting the measured variance, the integration time of T , and the mean square of the measured signal into

$$B_{fl} = \frac{\langle S(T) \rangle^2}{\sigma_A^2(T) \cdot T}. \quad (10.4)$$

The filter curve measurement and the Allan baseline variance should provide the same value for the fluctuation bandwidth. Nevertheless only in that case if besides radiometric noise there is no additional noise contribution that originates from the instrument. Since the spectrometer produces diverse noises like CCD shot noise, readout noise of the electronics, laser speckle, etc., the fluctuation bandwidth is always slightly different for the two measurement procedures. The theoretically expected difference of fluctuation bandwidth at 50% CCD illumination level is in the order of 2.8%, according to the expressions of (7.49), (7.50), the performance data of the CCD (dark current, full well capacity, etc.), and the average fluctuation bandwidth of 1.65MHz of the filter curve measurements. Figure 10-13 shows a calibrated baseline taken from the Allan baseline stability measurement. The input signal correspond to 50% illumination level of the CCD after 5 seconds integration time, and the noise fluctuation bandwidth related to the 4GHz bandwidth is calculated to be (without linearity correction done per software) 1.68MHz.

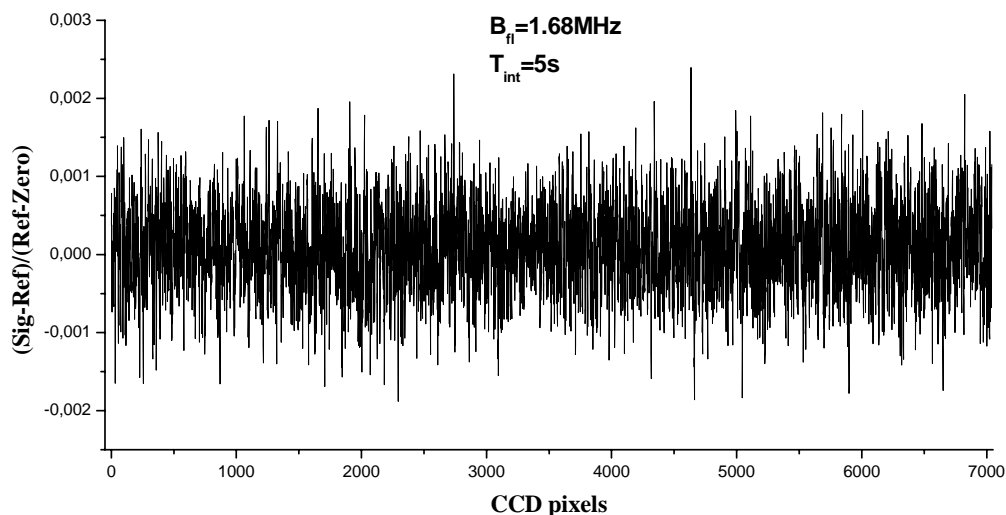


Figure 10-13 Typical baseline after 5 seconds integration time at an average illumination level of 50%. The corresponding noise fluctuation bandwidth is 1.68 MHz.

The measured noise fluctuation bandwidth is larger than the theoretically expected value, which can be explained by the small fluctuation bandwidth calculated from the filter curve measurement. There the large extended “wings” of the filter function are probably not taken into account, i.e. the frequency range of the measurement is set improperly. Nevertheless, the measured noise performance of the instrument is better than specified. The estimated noise dynamic range calculated from the peak-to-peak noise amplitude of a calibrated baseline scan is in the order of $>10\text{dB}$.

10.10 Thermal vacuum performance

The thermal interface of the WBS guarantees the thermal stability of the instrument. The interface temperature changes between $5\text{-}15^\circ\text{C}$, within which the performance of the unit should not change. The thermal environment of the device is simulated in a thermal vacuum chamber. The temperature is changed between 5°C and 15°C in 5 degree steps, and in thermal equilibrium the bandpass of the sub-bands is measured by using an external synthesizer. The bandpass curves applying the main and redundant lasers are plotted Figure 10-14 in and Figure 10-15.

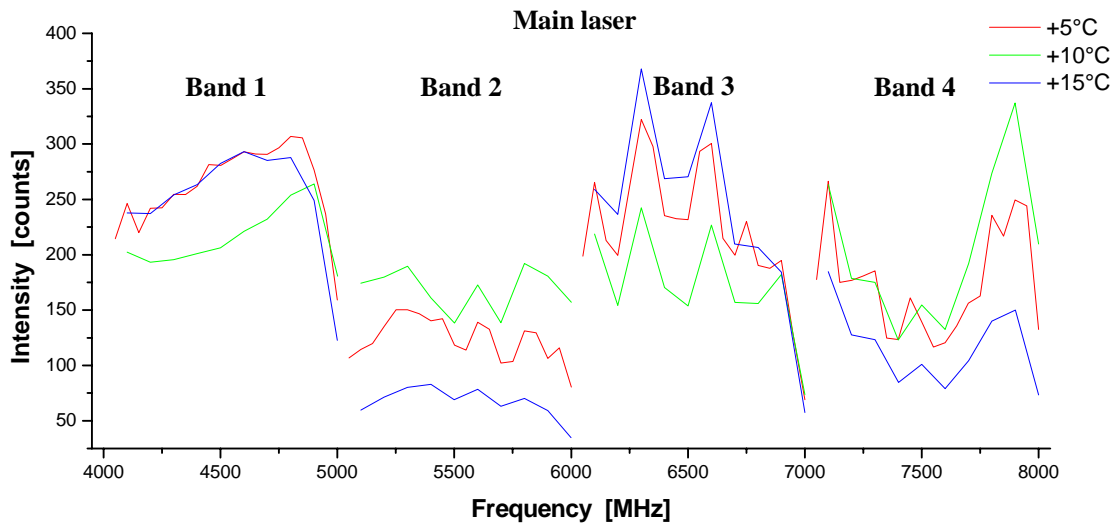


Figure 10-14 Bandpass of the sub-bands measured with the main laser at different temperatures

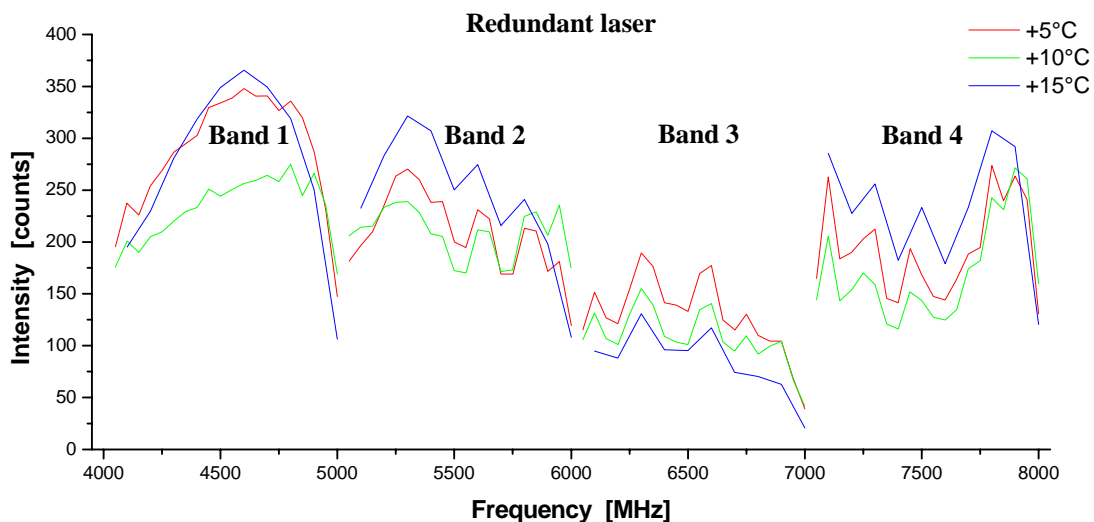


Figure 10-15 Bandpass of the sub-bands measured with the redundant laser at different temperatures

It can be established that in the operation temperature range the bandshape of the sub-bands does not significantly change. The maximum efficiency variation is $3dB$ with the main and $2dB$ with the redundant laser. This is caused by the vertical illumination error of the Bragg cell (errors of beam spacing of the source unit) and the CCD. The optimal operation temperature for all bands (smallest efficiency change) is $10^{\circ}C$ with the main laser and $5^{\circ}C$ with the other.

The bandpass measurement uses the balanced illumination of the CCD pixels. From the measured data the frequency resolution can be also determined by Gauss fitting the lines. This method is of course not as precise as the filter curve measurement, but provides comparable results. The FWHM dimension of the line is approximately 10% smaller than the resolution bandwidth. The measured frequency resolution is shown in Figure 10-16 and Figure 10-17.

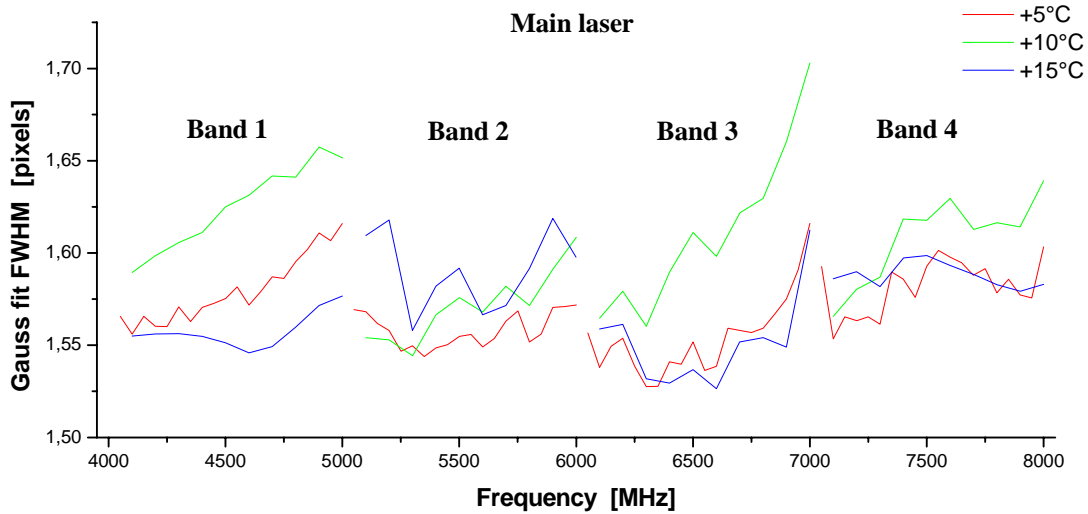


Figure 10-16 Resolution of the sub-bands measured with the main laser at different temperatures

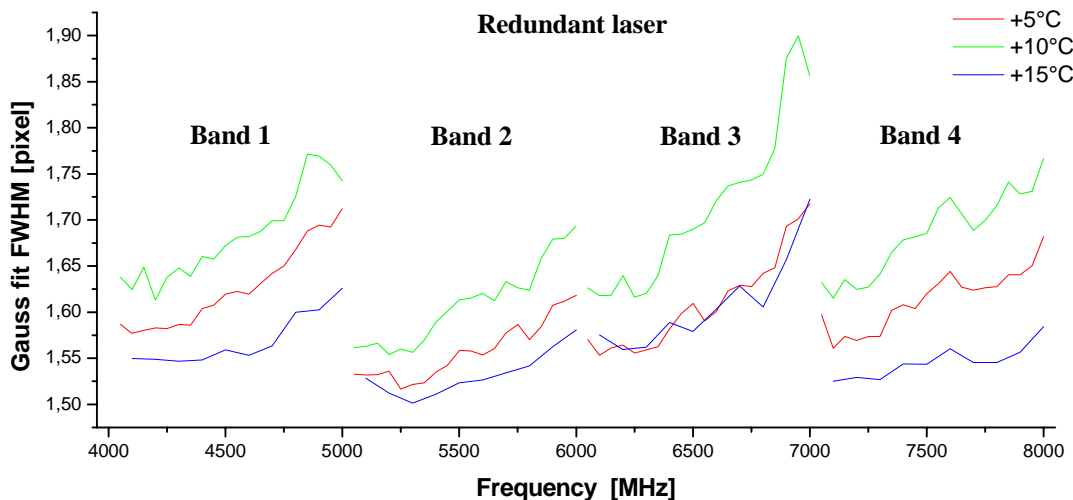


Figure 10-17 Resolution of the sub-bands measured with the redundant laser at different temperatures

The maximum resolution change within the operation temperature range is about 5% in case of the main laser and nearly 10% with the redundant laser. The small change of resolution is attained by the temperature compensated design of the laser housing; moreover, the focus position change of the imaging optics caused by wavelength change of the laser is well compensated by the thermal expansion of the WBO baseplate and laser mounting (see Section 10.14). The irregular behaviour at 10°C can be explained by a mode jump of the laser which corresponds to about 5% resolution degradation.

10.11 Vacuum correction

The alignment of the WBO is performed in air, therefore the focus position of the optical system is located in a different plane in vacuum. Consequently, the focal length change must

be taken into consideration during the adjustment procedure of the instrument. An additional difficulty is that at the source unit, the refractive index change results in not only a different focal length, but accompanies an interdistance change of the four output beams, since the in- and output angles of the beam splitter are also affected.

The refractive index of air at ambient temperature for average humidity at 785nm is $n=1.000276887$. Applying the refractive index difference and using the quasi-optical beam propagation description, the calculated focus position shifts and beam dimension changes at the Bragg cell and at the CCD are summarized in Table 10-3. During the calculation, the waist size attained from the diffraction calculation is used for the horizontal waist dimension at the CCD ($w \approx 18\mu\text{m}$ or $B_{fl} = 1.071\text{MHz} \Leftrightarrow 24.43\mu\text{m}$)

| | |
|--|--------------------|
| Beam interdistance change | $\pm 3\mu\text{m}$ |
| Waist size change at the Bragg cell (horizontal direction) | $-31\mu\text{m}$ |
| Waist size change at the Bragg cell (vertical direction) | $2\mu\text{m}$ |
| Focus shift of the source unit | -1.66mm |

| | |
|---|-------------------|
| Waist size change at the CCD (horizontal direction) | $2.8\mu\text{m}$ |
| Focus shift at CCD (horizontal) | -0.753mm |
| Waist size change at the CCD (vertical direction) | $1.4\mu\text{m}$ |
| Focus shift at the CCD (vertical) | -1.86mm |

Table 10-3 Calculated focal length and beam dimension changes in vacuum compared to the evaluated values in air. The horizontal waist size at the CCD, which defines the resolution of the spectrometer, is degraded by about 15%.

Theoretically, the focal length of the complete optical system in vacuum is shortened by about $750\mu\text{m}$, which makes significant change in the resolution of the instrument. Thus, during the flight hardware alignment performed in air an additional spacer is inserted into the CCD holder, which compensates the focal length variation between air and vacuum. The required thickness of the spacer might differ from the theoretically expected value, because alignment errors of the WBO components result in additional performance degradation, which can be compensated for by the positioning the CCD. After the final adjustment, the spacer is removed. Principally, this action should not change the alignment quality, since every part of the CCD module is tightly pinned together and to the WBO baseplate.

10.12 Vacuum-air performance

The refractive index difference of air and vacuum has impact on the performance of the WBO. In case of the qualification model of the WBO, the performance in vacuum is slightly worse because the instrument is optimized for operation in air. The main intention of the test is to verify the necessary alignment changes needed during the flight model production. The measured frequency bandpass and resolution in vacuum and air are shown in Figure 10-18 – Figure 10-21.

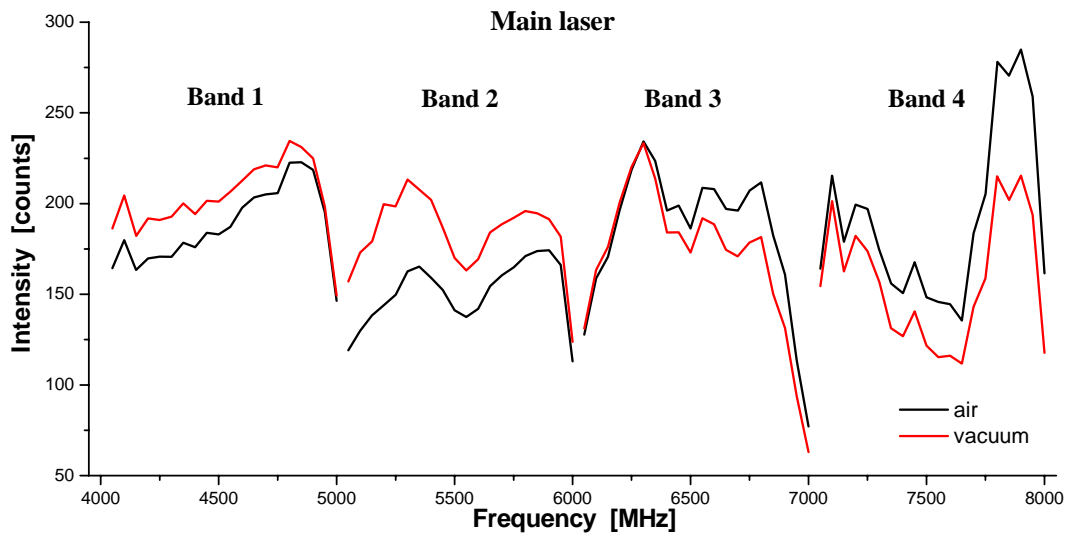


Figure 10-18 Bandpass measured with the main laser in air (black) and vacuum (red)

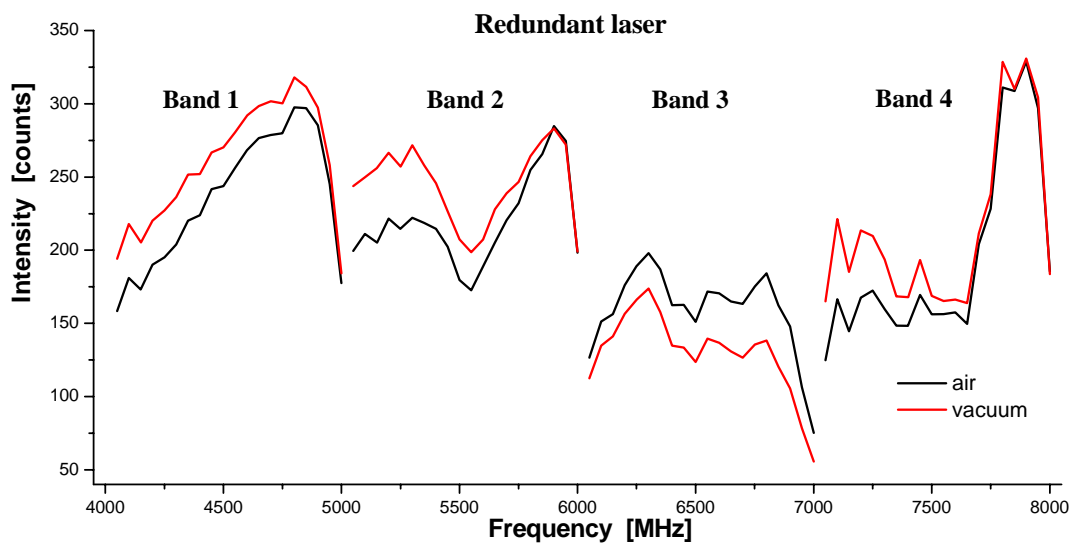


Figure 10-19 Bandpass measured with the redundant laser in air (black) and vacuum (red)

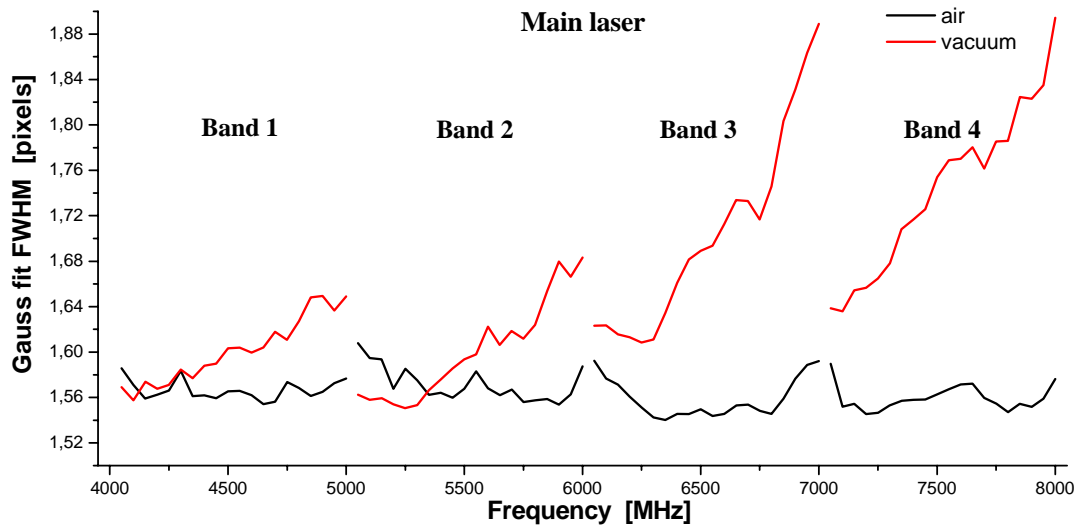


Figure 10-20 Resolution measured with the main laser in air (black) and vacuum (red)

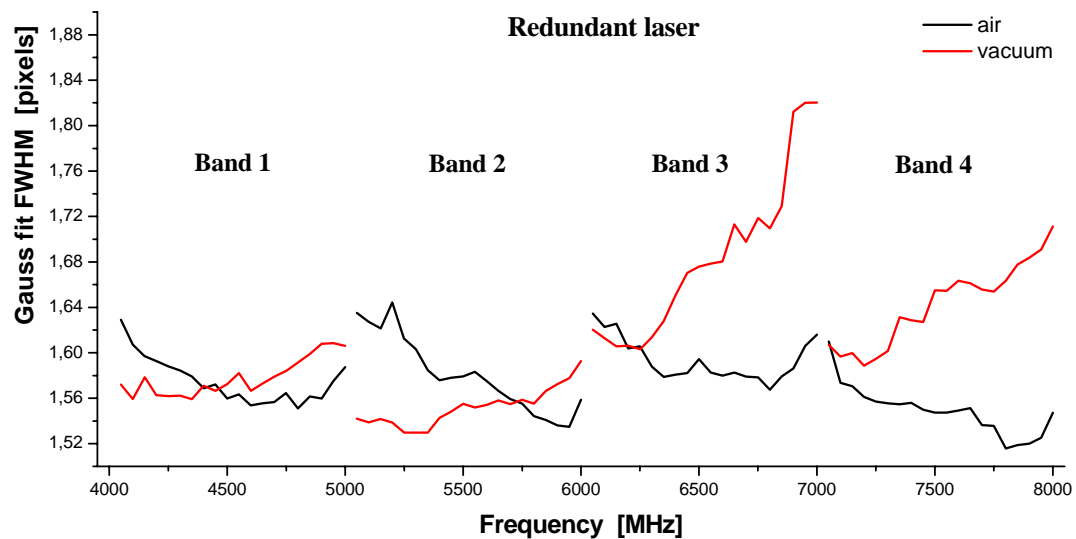


Figure 10-21 Resolution measured with the redundant laser in air (black) and vacuum (red)

The vacuum performance of the instrument shows an average efficiency and resolution degradation of about 10%. This also means the vacuum correction is unavoidable and a shift of the CCD of approximately $500\mu\text{m}$ is appropriate. The difference between the theoretically expected focal length change and the measured value can be explained by the not exactly perfect adjustment of the optical setup.

10.13 Bragg cell heating effect

In case of continuum offset measurements of a galactic centre or calibration of the spectrometer for instance, there are large power changes of the IF signal present at the Bragg cell. The intensity difference of the input signals originates from the different temperatures of the source and reference objects, or the hot and cold loads needed for the power calibration of the instrument. Since the IF signal is absorbed in the Bragg cell, its power effectively heats up the crystal, changing its thermal condition. The small temperature drifts result in small density and refractive index changes in the acoustic material. These effects are also visible in the spectra and therefore contribute to the degradation of the stability of the WBS.

In order to characterize the Bragg cell heating effect and the duration of time until the thermal equilibrium is reached again after calibration, the following measurement was carried out. A white noise-source (4-8GHz) is connected to the temperature-stabilised spectrometer. The output power level of the noise-source is chosen to avoid saturating the spectrometer (Signal level), then the IF power is reduced by 3dB (Reference signal). A sequence of spectra is taken with the WBS just after the power of the noise-source is reduced from the Signal level to the Reference level, applying an integration time of about 4 seconds. After the measurement period of approximately 120 seconds, the spectra are evaluated by using the standard baseline calibration scheme of $\frac{Sig - Ref}{Ref}$, where the last measurement is considered as the reference signal in the calibration formula. The plot of the baseline scans versus frequency at different times after the Signal is turned off is shown in Figure 10-22.

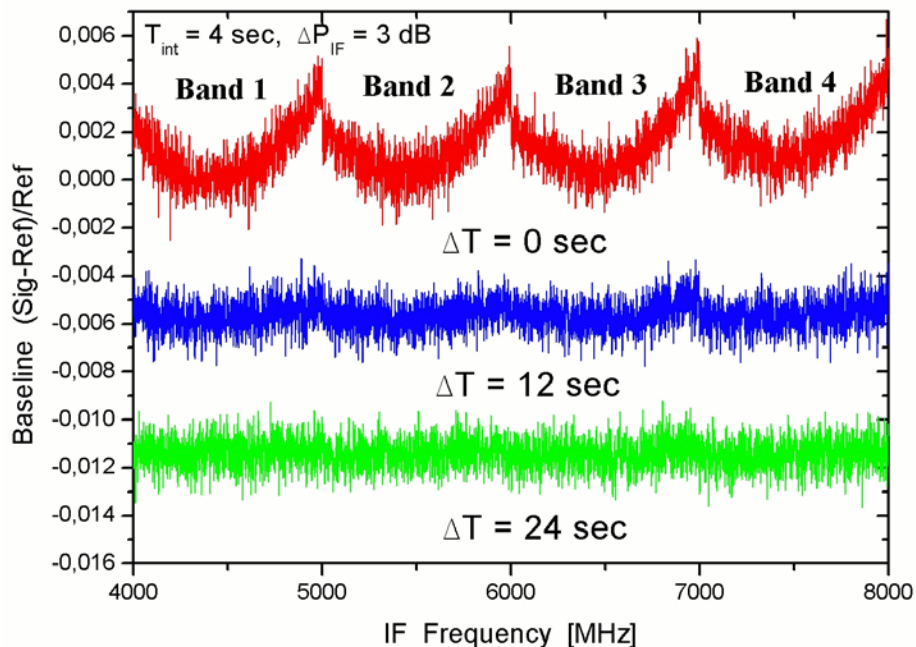


Figure 10-22 Bragg cell heating effect studied with the development model of the WBO. The baseline distortion of the four sub-bands is produced by the IF signal that heats the acoustic crystal due to absorption effects. The power variation of the input signal is 3dB, and the applied integration time is 4 seconds.

The measurement performed with the development model (DM) of the WBO shows a detectable baseline distortion during the first period of integration, and still a recognizable

effect 12 seconds after the Signal is turned off. The strong heating effect of the WBO DM is a direct consequence of the not efficiency optimized design of the instrument. There the spectrometer uses an optical phase grating as beam divider, moreover the laser light deflected from the over-illuminated acoustic zone is not focused in the vertical direction onto the CCD detector. Thus, to attain a detectable signal light intensity, more IF power is needed that results in baseline distortions and stability deterioration. Additional concern is that after a calibration measurement, where the power difference between hot and cold load is in the order of $3dB$, typically a 20 second wait is needed to achieve the thermal equilibrium of the Bragg cell. This unavoidable dead time would be rather undesired for the very limited and costly observation time of the Herschel satellite.

The qualification and flight models of the WBO employ the unique design of the prism beam splitter and the efficiency optimized imaging optics. As a consequence, much less IF power is needed to saturate the instrument. The total efficiency of the flight model is about $2mW$, while in case of the development model it is $>10mW$. Hence, the Bragg cell heating effect measured with the qualification model is significantly smaller and therefore the dead time of the instrument during a calibration or an observation is extensively reduced ($<5s$). It can be also remarked that the dead time after calibration practically can be avoided if the calibration is performed during the slewing of the telescope.

10.14 Resolution performance verification calculation

The resolution of the WBO is influenced by temperature changes. Due to the temperature dependence of the laser wavelength and the thermal expansion of the different mechanical supports, the position of the focus changes, which accompanies resolution degradation.

The collimator lenses, the cylindrical lens in front of the Bragg cell and one lens in the scan optics are made of *SF6G05*, which is highly dispersive optical material. Its *Abbe number* of 25.3 [28] indicates the strong wavelength dependence of the refractive index⁴³. The focus position dependence versus wavelength can be investigated by using the Gaussian ray transformation law. The transformation matrix of the optical system is precisely known from the lens design of the instrument (see Appendix D), thus the transformed horizontal beam radius (only the horizontal focus determines the resolution of the spectrometer) can be expressed as

$$w'(\lambda, z) = w'_0(\lambda) \sqrt{1 + \left(\frac{z}{z'_R(\lambda)} \right)^2}, \quad (10.5)$$

where $w'_0(\lambda)$ is the transformed waist and $z'_R(\lambda)$ is the transformed Rayleigh range. Calculating the focus of the optical system (transformed waist position) at the nominal laser wavelength of $785nm$, the focus shift versus wavelength function can be derived. Table 10-4 shows the horizontal focal length changes relative to $785nm$ (operation wavelength at $25^\circ C$ laser temperature) and its effect on the resolution degradation.

⁴³ As a comparison, BK7G18 has an Abbe number of 63.6

| Laser wavelength [nm] | Focus shift [μm] | Relative spot size enlargement [%] |
|--------------------------|----------------------------------|---------------------------------------|
| 785 | 0 | 0 |
| 784 | -104 | 5.4 |
| 783 | -209 | 20.0 |
| 780 | -526 | 94.1 |

Table 10-4 Relative focus shift and spot size enlargement of the WBO optical system due to wavelength variations.

Fortunately, with decreasing temperature, the laser wavelength also decreases, resulting in a shorter focal length. This is partly compensated by the thermal expansion of the WBO baseplate and the laser supporting structure.

The shrinkage of the baseplate reduces the focus shift, because the CCD detector is moving closer to the optics. The length change of the WBO baseplate due to the linear thermal expansion can be expressed by

$$\Delta l = l_0 \alpha \Delta T, \quad (10.6)$$

where l_0 is the distance between the scan optics and the CCD (160mm), α is the linear thermal expansion coefficient of the aluminium alloy baseplate made of AlMg4.5Mn0.7 ($23.3 \cdot 10^{-6}$ [29]), and ΔT is the temperature range in which the wavelength changes (10-20°C).

On the other hand, with decreasing temperature the distance between the laser and collimating optics is reduced. This results in a divergent laser beam behind the collimator, which increases the focal length of the overall imaging system (10°C corresponds to 100 μm focal length change). Using the results of the mode jump measurements, the focus shifts and their impact on the resolution can be calculated in a similar manner as before. The results are summarized in Table 10-5.

| Laser wavelength [nm] | Focus shift [μm] | Relative spot enlargement [%] |
|--------------------------|----------------------------------|----------------------------------|
| 785 | 0 | 0 |
| 784 | -35 | 0.6 |
| 783 | -71 | 2.5 |
| 780 | -250 | 27.5 |

Table 10-5 Relative focus shift and spot size enlargement of the WBO optical system due to wavelength variations, when the linear thermal expansion of the WBO baseplate and laser support is taken into account.

In the thermal operating range of WBO, the wavelength change is typically in the order of 2nm. The introduced focus position change is almost completely compensated by the thermal expansion of the parts mentioned above in the range of 0-2nm. Note, that the effect can be even more reduced if the adjustment is carried out at the middle of the operating temperature range (15°C at WBO baseplate), as is done at the qualification model of the WBO. In this case the resolution variation becomes symmetric ($\pm 0.6\%$) over the whole range. The

experimentally observed resolution change is slightly larger than the theoretically expected value, because the temperature variation results not only in focal length change, yet accompanies relative beam height changes at the CCD. This influences the efficiency as well as the resolution of the instrument. In addition, within a small temperature range irregular mode jumps of the laser cause step like resolution degradation that cannot be compensated by the smoothly changing thermal expansion of the parts.

Conclusions and Outlook

The acousto-optical technique of signal processing has proven to be a good alternative for space applications. The acousto-optical Wide Bandwidth Spectrometer developed for the Herschel satellite mission is an instrument that provides unprecedented high resolution, large bandwidth, high stability, and exceptionally good efficiency. All of these characteristics are essential for making astronomical observations on space-borne missions. The results of the performance test of the spectrometer carried out after the space qualification procedure have demonstrated that the instrument is highly reliable and meets the strict design specifications. A summary of the specifications and the performance results of the WBS qualification model is given in Table 1.

The special design of the prism-based beam splitter has achieved an unprecedented optical efficiency, which is of crucial importance for processing weak signals. The tight tolerances on the angles and positions of the Bragg cell illuminating beams require that the prisms be manufactured with high precision. Nevertheless, only the sophisticated assembly procedure developed for this work has made it possible to obtain a properly functioning beam splitter. Furthermore, the optical system optimization increases the efficiency of the instrument and allows the maximum resolution. Special care is devoted to achieving high spectroscopic stability, which demands careful mechanical and electrical design. The investigation of the laser diodes demonstrated that they will operate stably and reliably during the mission. In addition, the space-qualified instrument has a compact design and low weight, and it consumes little power.

The results of the theoretical investigation of diffraction at the Bragg cell aperture have shown the maximum attainable frequency resolution. Moreover, the comparison with the experimentally measured values indicates the spectrometer has been perfectly adjusted. The analysis of the laser wavefront aberration unambiguously points out the necessity for the laser beam to be well-collimated to ensure the high resolution of the instrument.

The recent development of array receivers has stimulated a demand for array spectrometers. In principal, acousto-optical signal processing makes it possible to arrange eight or even more channels in a single crystal, radically reducing the complexity of the system and simultaneously improving its reliability. With additional signal processing, these multi-channel spectrometers can be used as either array or hybrid devices, resulting in a large bandwidth (8-10GHz) instrument. The latest experiments based on high density acousto-optical materials like rutile and using currently available short wavelength lasers are promising. The prototype of such a large bandwidth acousto-optical spectrometer is being built at KOSMA [64]. The bandwidth of the instrument is 3GHz, and the frequency resolution is about 1MHz. In addition, spectrometers based on rutile Bragg cells can be constructed as array systems (4, 8, 16 channel) that can be used as hybrid instruments, resulting in ultra-large bandwidth (10-20GHz) array acousto-optical spectrometers.

| Item | Specification | Measurement |
|---|--|--|
| Total Bandwidth | 4000MHz | 4000MHz |
| Frequency Pixel Spacing | $\approx 0.55\text{MHz}$ (Nyquist Sampling) | 0.57MHz |
| Number of Frequency Pixels | 8192 ¹ | 8176 ¹ |
| Pixel Resolution Bandwidth | $\approx 1.1\text{MHz}^2$ | 1.05MHz ³ |
| Pixel Noise Fluctuation Bandwidth | $\approx 1.6\text{MHz}^2$ | 1.68MHz ⁴ |
| Sub-band Gain Variation | < 3dB | < 3dB ³ |
| Allan Variance Minimum Time (at temperature variations <1 K/hour) | $\geq 200\text{s @ 50\%}$ illumination $\geq 100\text{s @ 10\%}$ illumination | $\approx 300\text{s @ 50\%}$ illumination $\approx 100\text{s @ 10\%}$ illumination |
| Comb Generator Spacing (for frequency calibration) | 100MHz | 100 \pm 0.1MHz |
| Frequency Accuracy | $\leq 0.1\text{MHz}$ | < 0.1MHz |
| Frequency Nonlinearity | $\leq \pm 1\text{MHz}$ $\leq \pm 0.1\text{MHz}^5$ | $\pm 0.7\text{MHz}$ < $\pm 0.1\text{MHz}^5$ |
| Power Nonlinearity | $\leq 1\%$ | $\leq 1\%$ |
| Noise Dynamic Range ⁶ | >10dB | >10 ⁷ dB |
| Efficiency | > 97% @ 50% illumination | > 97% @ 50% illumination |
| Spurious Line Signals | < 1% of the saturation level | < 0.5% of the saturation level |
| Crosstalk Between Bands | <30dB | <35dB |
| Weight (WBO) | 7kg | 5.51 kg |
| Power consumption (WBS) | 31.5W | 27W ⁸ |

Table 1 Summary table of the performance data

- 1) ≈ 7450 (spec.) and 7017 (measured) after data processing in the ICC
- 2) After data processing in the ICC
- 3) Average value
- 4) 50% illumination over 4GHz bandwidth
- 5) After resampling
- 6) Input power range with less than 1dB increase of radiometric noise
- 7) Estimated from one scan of the Allan baseline stability measurement
- 8) Only one laser on

The Allan baseline stability measurements clearly show that the stability of the spectrometer is dominated by light scatter of the laser. Despite the application of polarization filters, slit apertures, and spatial filters, there is significant noise contribution from the scattered light and laser speckle. To suppress speckles effectively and thus provide better spectroscopic stability, further theoretical and experimental investigations are needed in this field.

The model that describes the aperture of the Bragg cell in the diffraction calculation can be improved: the dimension of the ultrasound wave can be described more rigorously, and higher diffraction orders of the acoustic wave can also be taken into account. In the theoretical description of diffraction, higher orders of wavefront aberrations could be considered as well, which would allow a more detailed study of the resolution bandwidth function. As the alignment procedure of the instrument demonstrated, the correction of diverse wavefront errors is possible. Thus, a detailed theoretical analysis of this phenomenon should be explored.

Appendix A

Acousto-optic materials

| | Index of Refraction for Optical Mode | Acoustic Mode and Velocity (10^5 cm/sec) | Figure of Merit, M_2 (10^{-18} s ³ /g) | Acoustic Attenuation at 500 MHz (dB/ μ sec) | |
|--------------------------------------|--------------------------------------|---|--|---|------|
| $\lambda = 633$ nm | | | | | |
| Fused silica (SiO ₂) | 1.46- \perp | longitudinal | 5.96 | 1.56 | 1.8 |
| Dense flint glass (SF-59) | 1.95- \square | long. | 3.26 | 19 | |
| LiNbO ₃ | 2.20- \square | long. [100] | 6.57 | 7.0 | 0.03 |
| | | shear [100] | 3.60 | 13.0 | |
| TeO ₂ | 2.27- \perp | long. [001] | 4.26 | 34.5 | 1.6 |
| | 2.27- \square | shear [110] | 0.617 | 793 | 73 |
| TiO ₂ ⁴⁴ | 2.7312- \square | long. [100] | N.A. | N.A. | N.A. |
| | 3.0588- \perp | shear [100] | N.A. | N.A. | N.A. |
| GaP | 3.31- \square | long. [110] | 6.32 | 44.6 | 0.6 |
| | 3.31-arb. | shear [100] | 4.13 | 24.1 | |
| TiO ₂ | 2.58-[010] | long. [100] | 8.03 | 3.9 | 0.11 |
| PbMoO ₄ | 2.39- \perp | long. [001] | 3.66 | 36.1 | 1.4 |
| | 2.26- \square | | | 36.3 | |
| H ₂ O | 1.33-arb. | long. | 1.5 | 126 | 90 |
| $\lambda = 1150$ nm | | | | | |
| As ₂ S ₃ glass | 2.46- \square | long. | 2.6 | 347 | 1.7 |
| Tl ₃ AsS ₄ | 2.63- \square | long. [001] | 2.15 | 510 | 0.3 |
| $\lambda = 10600$ nm | | | | | |
| Ge | 4.00- \square | long. [111] | 5.50 | 840 | 1.4 |
| | 4.00-arb. | shear [100] | 4.13 | 290 | 0.7 |
| Te | 4.80- \square | long. [100] | 2.2 | 4400 | 6 |

Table A-1 Acousto-optic materials and properties at room temperature [31], [21], [22], [90], [18], [84], [6].

The figure of merit (M_2) varies with wavelength and temperature, since the refractive index and density of the material are also functions of such (see. Eq. (4.17)). The symbols of \square and \perp indicate the optical polarization directions with respect to acoustic-wave propagation direction.

⁴⁴ Measured at 488nm wavelength by [4].

Appendix B

Normalization of Gaussian beams in cylindrical coordinate system.

The intensity of a Gaussian beam in cylindrical coordinate system is defined by

$$\iint |\tilde{E}(r, \varphi, z)|^2 r dr d\varphi = 1. \quad (\text{B.1})$$

The normalization factor, N can be calculated by the following integral

$$N^2 \int_0^{2\pi} d\varphi \int_0^{\infty} r e^{-\frac{2r^2}{w^2}} dr = 2\pi N^2 \int_0^{\infty} r e^{-\frac{2r^2}{w^2}} dr = \frac{\pi w^2}{2} N^2 = 1, \quad (\text{B.2})$$

thus $N = \sqrt{\frac{2}{\pi w^2}}$. The amplitude of the Gaussian distributed electromagnetic field is then expressed by

$$\tilde{E}(r, \varphi, z) = \sqrt{\frac{2}{\pi w^2(z)}} e^{-i\left(kz + \Phi_0(z) + \frac{k}{2} \frac{r^2}{R(z)}\right) - \frac{r^2}{w^2(z)}}. \quad (\text{B.3})$$

Normalization of Gaussian beams in Descartes coordinate system.

The intensity normalization in rectangular coordinate system is given by

$$N_x^2 N_y^2 \int_{-\infty}^{\infty} e^{-\frac{2x^2}{w_x^2}} dx \int_{-\infty}^{\infty} e^{-\frac{2y^2}{w_y^2}} dy = 1. \quad (\text{B.4})$$

The evaluation of the integral results in

$$N_x^2 N_y^2 \frac{\sqrt{2\pi} w_x}{2} \frac{\sqrt{2\pi} w_y}{2} = 1, \quad (\text{B.5})$$

which determines the normalization factors of

$$N_x = \sqrt{\frac{\sqrt{2}}{\sqrt{\pi} w_x}}, N_y = \sqrt{\frac{\sqrt{2}}{\sqrt{\pi} w_y}}, \text{ and } N = N_x N_y = \sqrt{\frac{2}{\pi w_x w_y}}. \quad (\text{B.6})$$

The normalized amplitude of the electromagnetic field then yields

$$\tilde{E}(x, y, z) = \sqrt{\frac{2}{\pi w_x(z) w_y(z)}} e^{-i\left(kz + \frac{\Phi_x^0(z)}{2} + \frac{\Phi_y^0(z)}{2} + \frac{k}{2} \frac{x^2}{R_x(z)} + \frac{k}{2} \frac{y^2}{R_y(z)}\right) - \frac{x^2}{w_x^2(z)} - \frac{y^2}{w_y^2(z)}}. \quad (\text{B.7})$$

Appendix C

Dimensions of Gaussian beams

The amplitude distribution of a Gaussian beam is given by:

$$E(x) = E_0 e^{-\frac{x^2}{w_0^2}}, \quad (\text{C.1})$$

where w_0 is the beam waist and E_0 is the normalized amplitude ($\int_{-\infty}^{+\infty} |E(x)|^2 dx = 1$). The intensity is the square of the amplitude that is measured by a detector

$$I(x) = I_0 e^{-\frac{2x^2}{w_0^2}}. \quad (\text{C.2})$$

The function of the normalized Gaussian intensity is depicted in Figure C-1.

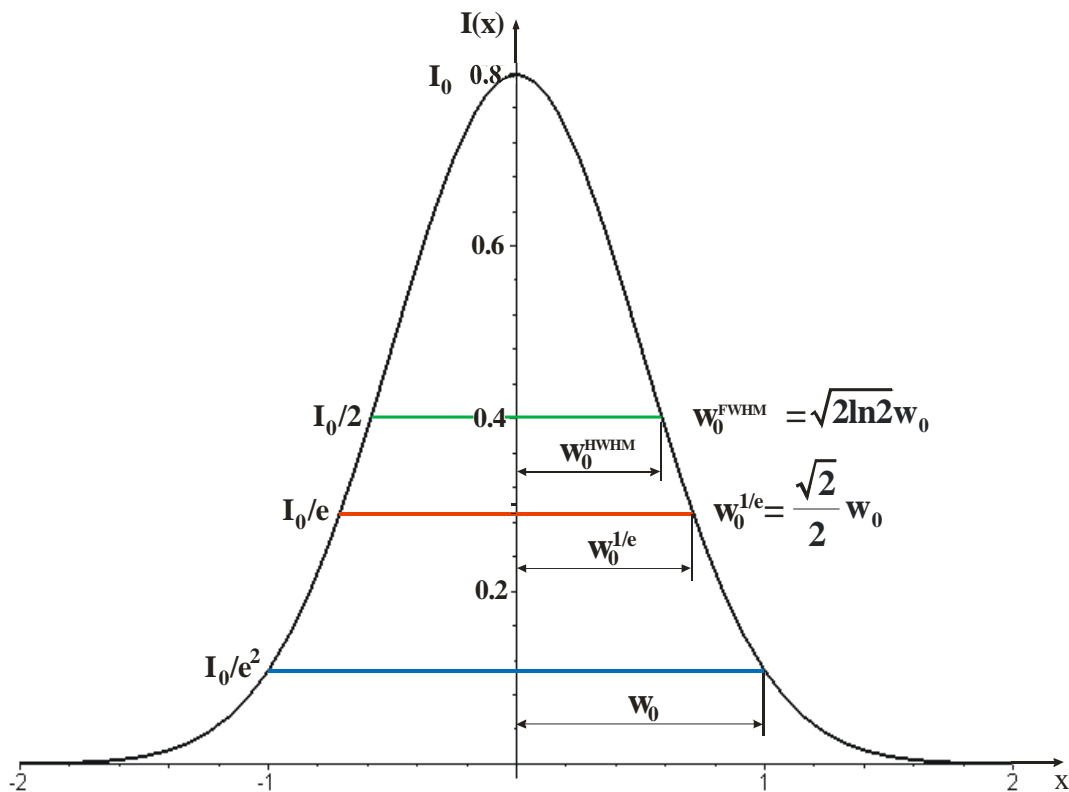


Figure C-1 Normalized Gaussian function

The natural dimension of a Gaussian beam is defined by the waist (beam radius, $x=w_0$), where the amplitude falls to $1/e$ of the maximum amplitude (E_0) or the intensity falls to $1/e^2$ of the maximum intensity

$$E_0 e^{-\frac{w_0^2}{w_0^2}} = \frac{E_0}{e}. \quad (\text{C.3})$$

In practice, the dimension of a Gaussian beam is often given with the Full Width at Half Maximum (*FWHM*) intensity contour. This means a beam diameter where the intensity is half of the maximum intensity

$$\frac{I_0}{2} = I_0 e^{-2\frac{(2x)^2}{(2w_0)^2}}. \quad (\text{C.4})$$

At this position the beam diameter (full width) can be expressed with the Gaussian waist

$$2x = w_0^{FWHM} = \sqrt{2 \ln 2} w_0. \quad (\text{C.5})$$

Appendix D

Lens prescription data of the laser source unit

(Designed by [27])

System Aperture: Object Space NA = 0.238752

SURFACE DATA SUMMARY

| Surface | Type | Comment | Radius | Thickness | Glass | Diameter |
|---------|----------|--------------------|----------|-----------|--------|-------------|
| OBJ | STANDARD | Laser diode | Infinity | 0.0021026 | | 0 |
| STO | PARAX_XY | Hitachi HL7851 G | | 0.005148 | | 0.0010339 |
| 2 | STANDARD | | Infinity | 2.294926 | | 0.003565297 |
| 3 | STANDARD | Collimation optics | -6.93 | 1.5 | SF6G05 | 5 |
| 4 | STANDARD | F=8mm | -57.6 | 1 | | 8.2 |
| 5 | STANDARD | | -7.52 | 2.5 | SF6G05 | 6.652 |
| 6 | STANDARD | | -5.1 | .59 | | 8.2 |
| 7 | STANDARD | | 69.22 | 2.5 | SF6G05 | 11 |
| 8 | STANDARD | | -11.82 | 6.293 | | 11 |
| 9 | TOROIDAL | Cyl. lens 148mm | 116.5 | 3 | SF6G05 | 3.896 |
| 10 | STANDARD | | Infinity | 100.121 | | 3.896 |
| 11 | COORDBRK | | | 0 | | |
| 12 | NONSEQCO | Beam splitter | Infinity | 0 | | 4.259 |
| 13 | STANDARD | | Infinity | 0 | | 20 |
| 14 | STANDARD | Polfilter | Infinity | 0.5 | BK7 | 6.15 |
| 15 | STANDARD | | Infinity | 29.39283 | | 6.15 |
| IMA | STANDARD | Focal Plane | | | | 10 |

INDEX OF REFRACTION DATA

| Glass | Temp | Pres | 785nm |
|--------|-------|------|------------|
| SF6G05 | 20.00 | 1.00 | 1.78903345 |
| BK7 | 20.00 | 1.00 | 1.51107956 |

THERMAL COEFFICIENT OF EXPANSION DATA

| Glass | TCE *10E-6 |
|--------|------------|
| SF6G05 | 7.8 |
| BK7 | 7.1 |

Appendix E

Laser light feedback calculation

For rough estimates, it is sufficient to investigate the reflection from the first surface of the collimator, but in order to have a more appropriate description, reflections from the first three surfaces are also considered. The simple optical system, that describes the effect in case of one reflecting surface, can be modelled as shown in Figure E-1.

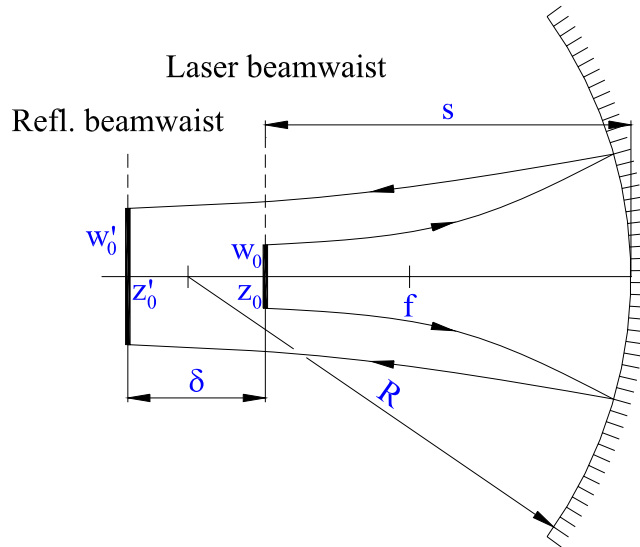


Figure E-1 Laser light feedback from the first surface of the collimating optics

The imaging law of a simple spherical mirror is given by [9]

$$\frac{1}{s} + \frac{1}{s + \delta} = -\frac{2}{R}, \quad (\text{E.1})$$

where s is the object distance i.e. the position of the diode, $s + \delta$ is the image distance referring to the position of the transformed beam waist, and R is the radius of the sphere. If $R < 0$ then it is about a collecting mirror, otherwise it is a scattering one. For positioning the laser diode, there are two possible cases depending on the object distances. If $s < R/2$ then the object lies between the focus and the mirror and the image is virtual. In this case, the imaging law takes the form of

$$\frac{1}{k} = \frac{2}{R} - \frac{1}{t} < 0. \quad (\text{E.2})$$

In the other case if $s > R/2$, the image is real and equation (8.12) describes the imaging properly. The paraxial beam transformation matrix of the laser beam, that describes the laser light propagation from the laser chip to the spherical mirror then the reflected light on the same way back to laser, can be expressed by \mathbf{T}

$$\mathbf{T} = \begin{bmatrix} 1 & s \\ 0 & 1 \end{bmatrix} \cdot \begin{bmatrix} 1 & 0 \\ -\frac{2}{R} & 1 \end{bmatrix} \cdot \begin{bmatrix} 1 & s \\ 0 & 1 \end{bmatrix} = \begin{bmatrix} 1 - \frac{2s}{R} & 2s \left(1 - \frac{s}{R}\right) \\ -\frac{2}{R} & 1 - \frac{2s}{R} \end{bmatrix}. \quad (\text{E.3})$$

In this case, only one reflecting lens surface is taken into consideration. The constant of s represents the distance between the laser and the collimator i.e. the spherical mirror.

Substituting the components of the transformation matrix into the expression of (6.5), the transformed beam parameter can be calculated. Considering only the waist transformation, the real part of the complex beam parameter represents the distance between the object and image beam waist.

$$\Re\{\tilde{q}'(z)\} = \left(s - \frac{2}{R}\right) \left(1 - \frac{1}{\left(\frac{2z_R}{R}\right)^2 + \left(1 - \frac{2s}{R}\right)^2}\right). \quad (\text{E.4})$$

The imaginary part of the beam parameter describes the transformed confocal distance that can be expressed as

$$\Im\{\tilde{q}'(z)\} = z'_R = \frac{z_R}{\left(\frac{2z_R}{R}\right)^2 + \left(1 - \frac{2s}{R}\right)^2}, \quad (\text{E.5})$$

from which we can determine the required $1/e$ contour of amplitude of the transformed beam waist by applying eq. (6.4)

$$w'(\delta) = \frac{w_0}{\sqrt{\left(\frac{2z_R}{R}\right)^2 + \left(1 - \frac{2s}{R}\right)^2}}. \quad (\text{E.6})$$

Now having the exact description of the laser beam propagation, the laser coupling caused by the collimator can be derived.

The feedback phenomena can be described by evaluating the overlap integral of the initial laser- and from the optics reflected electromagnetic field at the location of the laser. In principally the laser diodes always have astigmatism, which is in the order of a few microns [92]. This will result an asymmetric beam intensity distribution in the beam cross section. For the appropriate simulation of the laser beam propagation, it is necessary to have the non-symmetrical description of the electromagnetic field. Thus, the normalized laser electromagnetic field in *Descartes*-coordinate system is given by

$$\tilde{E}_L(x, y, z) = \sqrt{\frac{2}{\pi w_x(z) w_y(z)}} e^{-i \left(kz + \frac{\Phi_x^0(z)}{2} + \frac{\Phi_y^0(z)}{2} + \frac{k x^2}{2 R_x(z)} + \frac{k y^2}{2 R_y(z)} \right) - \frac{x^2}{w_x^2(z)} - \frac{y^2}{w_y^2(z)}}, \quad (\text{E.7})$$

where the laser waist size $w_{x,y}(z)$, according to the Gaussian quasioptical beam propagation description, can be expressed as

$$w_{x,y}^2(z) = w_{0x,y}^2 \left[1 + \left(\frac{z}{z_{Rx,y}} \right)^2 \right]. \quad (\text{E.8})$$

The beam waist radius is given by

$$R_{x,y}(z) = z + \frac{z_{Rx,y}^2}{z}, \quad (\text{E.9})$$

and the *Guoy*-phase shift

$$\Phi_{0x,y}(z) = \arctg\left(\frac{z}{z_{Rx,y}}\right). \quad (\text{E.10})$$

In a manner similar to the laser beam, the reflected beam can be written as

$$\tilde{E}_R(x, y, z') = \sqrt{\frac{2}{\pi w_x(z') w_y(z')}} e^{-i \left(kz' + \frac{\Phi_x^0(z')}{2} + \frac{\Phi_y^0(z')}{2} + \frac{k}{2} \frac{x^2}{R_x(z')} + \frac{k}{2} \frac{y^2}{R_y(z')} \right)} \frac{x^2}{w_x^2(z')} \frac{y^2}{w_y^2(z')}. \quad (\text{E.11})$$

The field of the Gaussian functions forms a complete, ortho-normed system; therefore, the reflected beam can be expanded with the linear combination of its eigenfunctions

$$\tilde{E}_R = a_0 \tilde{E}_L^{(0,0)}(x, y, z_0) + a_1 \tilde{E}_L^{(1,0)}(x, y, z_0) + a_2 \tilde{E}_L^{(0,1)}(x, y, z_0) + \dots, \quad (\text{E.12})$$

where $\tilde{E}_L^{(0,0)}(x, y, z_0)$ is the TEM_{00} modus of the laser electromagnetic field in the $z = 0$ position, $\tilde{E}_L^{(1,0)}(x, y, z_0)$ is the TEM_{10} , etc. The laser diode has excellent single mode performance so that it is sufficient to use the first term approximation. The coupling coefficient \tilde{a}_0 can then be calculated with the overlap integral of the complex conjugated incident- and reflected electromagnetic fields

$$\tilde{a}_0 = \int_{-\infty-\infty}^{+\infty+\infty} \tilde{E}_L^{*(0,0)}(x, y, 0) \tilde{E}_R^{(0,0)}(x, y, -\delta) dx dy. \quad (\text{E.13})$$

where we used the $\delta = z - z' = z_{0x} - z'_{0x} \cong z_{0y} - z'_{0y}$ parameterisation during the coordinate transformation. The magnitude of δ represents the distance between the image and the incident laser beam waist, which is considered to be equal for the horizontal and vertical directions. Substituting the electromagnetic field components into the expression of the coupling coefficient as well as using the following parameterization

$$\beta = -k\delta - \frac{\Phi_x^0(\delta)}{2} - \frac{\Phi_y^0(\delta)}{2}, \quad (\text{E.14})$$

$$\tilde{\alpha} = \frac{8}{\pi} \frac{1}{\sqrt{w'_x(\delta)w'_y(\delta)}} \frac{1}{\sqrt{w_x(0)w_y(0)}} e^{-i\beta}, \quad (\text{E.15})$$

$$\xi_x = \frac{1}{w_x^2(0)} + \frac{1}{w_x^2(\delta)}, \quad (\text{E.16})$$

$$\xi_y = \frac{1}{w_y^2(0)} + \frac{1}{w_y^2(\delta)}, \quad (\text{E.17})$$

$$\eta_x = \frac{k}{2R'_x(\delta)}, \quad (\text{E.18})$$

$$\eta_y = \frac{k}{2R'_y(\delta)}, \quad (\text{E.19})$$

the integral expression of (E.13) can be written in the form of

$$\tilde{a}_0 = \tilde{\alpha} \int_{-\infty}^{+\infty} e^{-x^2(\xi_x+i\eta_x)} dx \int_{-\infty}^{+\infty} e^{-y^2(\xi_y+i\eta_y)} dy. \quad (\text{E.20})$$

These types of integrals can be solved by means of the Γ -functions [11]

$$\int_0^{\infty} e^{-x^2(\xi_x+i\eta_x)} dx = \frac{\Gamma(1/2)}{2\sqrt{\xi_x+i\eta_x}} = \frac{\sqrt{\pi}}{2\sqrt{\xi_x+i\eta_x}}. \quad (\text{E.21})$$

Gathering all the expressions into the formula and separating the equations for x and y components the coupling coefficient can be expressed with the following expression

$$\tilde{a}_0 = \tilde{a}_{0x} \tilde{a}_{0y}, \quad (\text{E.22})$$

$$\tilde{a}_{0x} = \sqrt{2} e^{-\frac{i\beta}{2}} \frac{\sqrt{\frac{w'_x(\delta)}{w_x(0)}}}{\sqrt{1 + \frac{w_x^2(\delta)}{w_x^2(0)} + i \frac{\delta}{z'_{Rx}}}}, \quad (\text{E.23})$$

$$\tilde{a}_{0y} = \sqrt{2} e^{-\frac{i\beta}{2}} \frac{\sqrt{\frac{w'_y(\delta)}{w_y(0)}}}{\sqrt{1 + \frac{w_y^2(\delta)}{w_y^2(0)} + i \frac{\delta}{z'_{Ry}}}}. \quad (\text{E.24})$$

The coupling coefficient as a function of the distance of the two waists has a maximum if δ is equal to zero. This would mean that the width of the transformed waist is equal to the initial beam waist, so the beam is reflected into the laser itself. In this case the first surface of the collimator would act for the laser diode as a low reflecting, focusing mirror. This would of course endanger its stability.

Since the intensity is the most commonly used characterizing parameter of the laser light, it is important to determine the power coupling, which is the product of the absolute squares of the amplitudes of the coupling coefficients

$$\alpha = |a_{0x}|^2 |a_{0y}|^2 = \frac{2 \frac{w'_x(\delta)}{w_x(0)}}{\sqrt{\left(1 + \frac{w_x'^2(\delta)}{w_x^2(0)}\right)^2 + \left(\frac{\delta}{z'_{Rx}}\right)^2}} \frac{2 \frac{w'_y(\delta)}{w_y(0)}}{\sqrt{\left(1 + \frac{w_y'^2(\delta)}{w_y^2(0)}\right)^2 + \left(\frac{\delta}{z'_{Ry}}\right)^2}}. \quad (\text{E.25})$$

In case of arbitrary number of reflecting surfaces the reflected laser power, that the laser itself perceives, can now generally be written as

$$P_{coupled} = P_0 r \left[\alpha_0 + (1-r)\alpha_1 + (1-r)^2\alpha_2 + \dots + (1-r)^i\alpha_i + \dots \right], \quad (\text{E.26})$$

P_0 – is the laser power,

r – is the reflection coefficient of the antireflexion coated glass, and

$\alpha_0, \alpha_1, \alpha_i$ – are the power coupling coefficients concerning the lens surfaces.

The following example shows how the third order transformation matrix looks like if we consider the third lens surface as reflecting. Otherwise, the coupling calculation remains the same as described above.

$$\mathbf{T} = \begin{bmatrix} A & B \\ C & D \end{bmatrix} = \begin{bmatrix} 1 & s_1 \\ 0 & 1 \end{bmatrix} \cdot \begin{bmatrix} 1 & 0 \\ \frac{n_1 - n_2}{-n_1 R_1} & \frac{n_2}{n_1} \end{bmatrix} \cdot \begin{bmatrix} 1 & s_2 \\ 0 & 1 \end{bmatrix} \cdot \begin{bmatrix} 1 & 0 \\ \frac{n_2 - n_1}{-n_2 R_2} & \frac{n_1}{n_2} \end{bmatrix} \cdot \begin{bmatrix} 1 & s_3 \\ 0 & 1 \end{bmatrix} \cdot \begin{bmatrix} 1 & 0 \\ -\frac{2}{R_3} & 1 \end{bmatrix} \cdot \begin{bmatrix} 1 & s_3 \\ 0 & 1 \end{bmatrix} \cdot \begin{bmatrix} 1 & 0 \\ \frac{n_1 - n_2}{n_1 R_2} & \frac{n_2}{n_1} \end{bmatrix} \cdot \begin{bmatrix} 1 & s_2 \\ 0 & 1 \end{bmatrix} \cdot \begin{bmatrix} 1 & 0 \\ \frac{n_2 - n_1}{n_2 R_1} & \frac{n_1}{n_2} \end{bmatrix} \cdot \begin{bmatrix} 1 & s_1 \\ 0 & 1 \end{bmatrix}.$$

The distances between the diode and the surfaces are s_1, s_2 , and s_3 , the radii of curvatures are R_1, R_2, R_3 as shown in Figure E-2. The air and the glass material have a refractive index of n_1 and n_2 respectively.

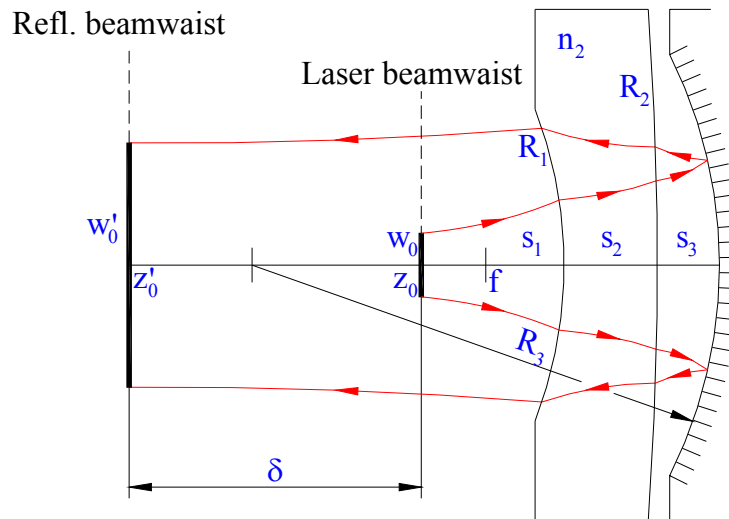


Figure E-2 Laser light feedback from the third surface of the collimating optics

References

1. Allan, D. W., “*Statistics of atomic frequency standards*”, Proc. IEEE, Vol. 54, pp.221-230, 1969.
2. Arianespace, Inc., Ariane 5 User’s Manual
http://www.arianespace.com/site/documents/ariane5_man_index.html, 2004.
3. ASTRIUM, “*Herschel Telescope Optical Design Justification*”, 8/4/2002
HER.NT.183.T.ASTR
4. BAE Systems Advanced Technology Centre, Acousto-optical devices, UK
5. Bagshaw, J. M., Lowe, S. E., Willats, T. F., “*Performance of Anisotropic Lithium Niobate Bragg Cells*”, IEEE Colloquium, Physics and device applications of acoustic waves, London, 1987.
6. Blistanov, A. A., Bondarenko, V. S., Perelomova, N. V., Strizhevskaja, F. N., Chkalova, V. V., Shaskolskaia, M. P., “*Acoustic Crystals*“, Moscow, Izdatel'stvo Nauka, pp. 632, 1982.
7. Boogaerts, W., “*Wide Band Optics O-Box / QM Properties Horizontal*”, HIFI Document Database at MPAE in Lindau, “*WBO/QM Properties Report*”, HIFI-MPAE-RP-OQ010-001_D_-.pdf, 2004.
8. Boogaerts, W., Steinmetz, E., Boerner, P., “*Vibration Test Procedure WBS/QM*”,
<http://www.linmpi.mpg.de/english/projekte/hifi/docDB/hifibin/DocList.cgi>, “HIFI-MPAE-PR-SQ010-003_1_b.pdf”, 2004.
9. Born, M., and Wolf, E., “*Principles of Optics*”, 6th Edition Cambridge U. Press, New York, 1980.
10. Bragg cell technical data sheet provided by BAE Systems
11. Bronstein, I. N., Semendjajew, K. A., „*Taschenbuch der Mathematik*“, Harry Deutsch, Thun und Frankfurt/Main, 1989.
12. Canabal, J. R., Hechler, M., “*Orbital Aspects of the SOHO Mission Design*”, Proceedings of the AAS/NASA International Symposium, Greenbelt, MD, (A90-43486 19-13), pp. 347-357, 1989.
13. Chang, I. C., Lee, S., “*Efficient wideband acousto-optic cells*”, Proc. IEEE Ultrasonics Symp., IEEE No. 83CH 1947-1, pp. 427, 1983.
14. Chang, I.C., „*Acousto-optic Devices and Applications*”, IEEE Transactions on Sonics and Ultrasonics, Vol. SU-23, No 1, p2 onwards, January 1976.
15. Churchwell, E., Winnewisser, G., Walmsley, C. M., ”*Molecular observations of a possible proto-solar nebula in a dark cloud in Taurus*“, Astronomy and Astrophysics, vol. 67, no. 1, pp 139-147, June 1978.
16. Cobos, J., Hechler, M., “*FIRST/PLANCK Mission Analysis: Transfer to Lissajous Orbit Using the Stable Manifold*”, MAS WP 412, ESOC December 1998.
17. Cooper, B.F.C, “*Correlators with 2-bit Quantization*”, Australian Journal of Physics, No.23., 1970.
18. Coquin, G. A., Pinnow, D. A., Warner, A. W., “*Physical properties of lead molybdate relevant to acousto-optic device applications*”, J Appl. Phys., 42, 2162, 1971.

19. Das, P. K., DeCusatis, C. M., “*Acousto-Optic Signal Processing: Fundamentals & Applications*”, Artech House, Inc., Norwood, 1991.
20. Debye, P., Sears, F. W., “*On the Scattering of Light by Supersonic Waves*”, Proc. Nat. Academy of Science, Vol. 18, pp. 409-414, 1932.
21. Dixon, R. W., “*Acoustic Diffraction of Light in Anisotropic Media*“, IEEE J., Quantum Electron., QA-3, 85., 1967.
22. Dixon, R. W., “*Photoelastic properties of selected materials and their relevance for applications to acoustic light modulators and scanners*“, J Appl. Phys., 38, 5149, 1967.
23. Emrich, A., “*Autocorrelation spectrometers for space borne (sub)mm spectroscopy*”, ESA Symposium, held 15-17 April 1997 in Grenoble, France, ESA SP-401, pp. 361-364, 1997.
24. Franke, B., “*The Qualification Procedure for the Laser Diodes of the WBS*”, HIFI Document Database at MPAe in Lindau, HIFI Technical Report, HIFI-KOSM-RP-LA100-001_2_a, 2003.
25. Frerick, J., “*Vibration Test Results of the SWAS-AOS-EM Optical Unit*”, March 1993.
26. Fukuda, Mitsuo, “*Reliability and degradation of semiconductor lasers and LEDs*”, Artech House, Inc., Norwood, MA, 1991.
27. Galileo Avionica, Florence Italy: <http://www.galileoavionica.it/>
28. Glass catalogue of Zemax (ray tracing software), <http://www.zemax.com>
29. Gleich GmbH Metallplatten-Service, Technical information site of G.AI[®]C250: http://www.gleich.de/produkte/galc250_td.php
30. Goldsmith, P. F., “*Quasioptical Systems, Gaussian Beam Quasioptical Propagation and Applications*” IEEE Press, Chapter 2, 1998.
31. Gupta, M. C., “*Handbook of Photonics*”, CRC Press, New York, 1997.
32. Güsten, R., Camara, I., Hartogh, P., Hübers, H.-W., Graf, U., Jacobs, K., Kasemann, C., Röser, H.-P., Schieder, R., Schnieder, G., Siebertz, O., Stutzki, J., Villanueva, G., Wagner, A., van der Wal, P., and Wunsch, A., “*GREAT: The German Receiver for Astronomy at Terahertz Frequencies*”, in: Proc. SPIE, vol. 4857, pp. 56–61, Bellingham, USA, 2003. <http://www.linmpi.mpg.de/english/projekte/sofia/great-cts/index.html>
33. Gysel, U., “*Signale der Nachrichtentechnik*“, Frequenzversetzte Übertragung - Modulation, <http://home.zhwin.ch/~gys/SNTf/Modulationf/Modulation.pdf>, 2003.
34. Hechler, M., “*FIRST/Planck Consolidated Report on Mission Analysis*”, ESA Directorate of Technical and Operational Support, Ground System Engineering Department, FP-MA-RP-0010-TOS/GMA, December 1999.
35. Hechler, M., “*GAIA/FIRST Mission Analysis: ARIANE and the Orbits around L2*”, MAS WP 393, ESOC February 1997.
36. Hechler, M., Cobos, J., “*FIRST Mission Analysis: Transfers to Small Lissajous Orbits around L2*”, MAS WP 398, ESOC July 1997.
37. Hechler, M., Cobos, J., “*FIRST/PLANCK and GAIA Mission Analysis: Launch Windows with Eclipse Avoidance Manoeuvres*”, MAS WP 402, ESOC December 1997.
38. Hecht, D. L., “*Multifrequency Acousto Optic Diffraction*”, IEEE Trans Sonics and Ultrasonics, SU24, 1, pp. 7-18, 1977.
39. Herman, R. M., Pardo, J. and Wiggins, T. A., “*Diffraction and focusing of Gaussian*

- beams,” Appl. Opt. 24, pp. 1346-1353, 1985.
40. Herschel/Planck Project Team, “*Herschel/Planck Instrument Interface Document, IID Part A*”, Herschel Documentation Server at SRON, the Netherlands, <http://www.sron.nl/divisions/lea/hifi/>, SCI-PT-IIDA-04624, 2004.
 41. Herschel/Planck Project Team, “*Herschel/Planck Instrument Interface Document, Part B, Instrument HIFI*”, Herschel Documentation Server at SRON, the Netherlands, <http://www.sron.nl/divisions/lea/hifi/>, SCI-PT-IIDB/HIFI-02125, 2004.
 42. Hitachi data sheet, laser diode *HL7851G*. Technical report, 1991.
 43. Horn, J., “*Development of an array acousto-optical spectrometer*”, Dissertation, Universität zu Köln, 1997.
 44. Hunsperger, R. G., “*Integrated Optics: Theory and Technology*”, 2nd Ed. Springer Verlag, New York, 1984.
 45. Institute of Astronomy ETH Zürich, *ARGOS Statement of Work*, http://www.astro.phys.ethz.ch/instrument/argos/argos_nf.html
 46. JENOPTIK Laser, Optik, Systeme GmbH, <http://www.jenoptik-los.de/>
 47. Kent, L. W.J. “*Herschel Bragg Cells Progress Report*”, HIFI Document Database at MPAA in Lindau, HIFI Technical Report , HIFI-BAE-RP-BA104-001_1_-, 2003.
 48. Klumb, M., “*Aufbau und Qualifikation eines weltraumtauglichen akusto-optischen Spektrometers*”, Dissertation, University of Cologne, 1995.
 49. Klumb, M., “*Aufbau und Qualifikation eines Weltraumtauglichen Spectrometers*”, Dissertation, Universität zu Köln, 1992.
 50. Klumb, M., Frerick, J., Tolls, V., Schieder, R., Winnewisser, G., “*The SWAS Acousto-Optical Spectrometer*“, Proc. of SPIE Infrared and Spaceborne Remote Sensing II., ed. M. Scholl, Volume 2268, pp. 305-315, 1994.
 51. Knauf, W., “*Begründer der Radioastronomie Grote Reber Silent Key*“, Funkamateure, 52, pp. 460, 2003.
 52. Kramer, C., “*Calibration of the beam*”, HIFI calibration review, Groningen, HIFI-ICC Documentation Server, internal page, <https://www.lra.ens.fr/hifi-icc/>, 2003.
 53. Kramer, C., “*Spatial response, Contribution to the framework document of the FIFI/Herschel Calibration group*”, HIFI-ICC Documentation Server, internal page, <https://www.lra.ens.fr/hifi-icc/>, 2003.
 54. Kraus, J.D., „*Radio Astronomy*“, Cygnus Quasar Books, Second Edition, 1986.
 55. LEWICKI microelectronic GmbH, Germany, <http://www.lewicki-gmbh.de/>
 56. Lischka, H., “*Untersuchung des Auflösungsvermögens eines Akusto-Optischen Spektrometers*”, Master’s Thesis, Universität zu Köln, 1990.
 57. Magdich, L. N., Molchanov, V. Ya., “*Acousto-optic Devices and their Applications*”, Gordon and Breach Science Publishers, 1989.
 58. Mahajan, V. N., “*Optical Imaging and Aberrations,*” Part 1 Ray Geometrical Optics, SPIE Optical Engineering Press, Chapter 1, Gaussian Optics, pp. 77-81, 1998.
 59. Manual of the “*Small Beam Share Interferometer*”, TOPTICA Photonics AG, Martinsried, Germany (former name TuiOptics GmbH), <http://www.toptica.de>
 60. Manual of the Coherent CCD Camera (LaserCam III type)

61. Mauersberger, R., „*IRAM 30-m Telescope System Summary*“, http://iram.fr/IRAMES/telescope/telescopeSummary/telescope_summary.html
62. Melles Griot online catalogue: *Collimating and focusing lenses for visible and near IR diode lasers*, Type 06 GLC 002, <http://shop.mellesgriot.com/products/optics>
63. Möckel, C., „*Breitbandiger akusto-optischer Korrelator*“, Dissertation, Universität zu Köln, 1999.
64. Olbrich, M., „*Ultra Large Bandwidth Acousto-Optical Spectrometers Using Rutile*“, PhD Thesis, Universität zu Köln, in prep.
65. Ossenkopf, V., „*A unified Allan variance computation scheme*“, SRON Technical note, HIFI-ICC Documentation Server (internal page, <https://www.lra.ens.fr/hifi-icc/>), 2003.
66. Ossenkopf, V., „*HIFI Observing Modes Document*“, HIFI-ICC Documentation Server (internal page, <https://www.lra.ens.fr/hifi-icc/>), ICC/2002-001 V0.41, 2002.
67. Ott, M., „*Capabilities and Reliability of LEDs and Laser Diodes*“, NASA Goddard Space Flight Center, ISBN: 301-286-0127, 1997.
68. Perkin Elmer, Inc., (formerly EG&G Reticon), <http://www.perkinelmer.com/>
69. Rau, G., Schieder, R., Vowinkel, B., „*Characterization and Measurement of Radiometer Stability*“, Proc. 14th European Microwave Conf., Liege, Belgium, 248-253, 1984.
70. RMS Systems Co., Ltd, <http://www.rms-testsystems.de/de/produkte/schwinganlagen/swr1200/swr1200.html>
71. Salech, B. E. A., Teich M. C., „*Fundamentals of Photonics*“, John Wiley & Sons, Inc., USA, 1991.
72. Sapriel, J., „*Acousto-Optics*“, John Wiley & Sons Ltd., Chichester, 1979.
73. Schieder, R., „*About the required alignment accuracy of the Laser Source Module*“, HIFI technical correspondence, June 2003.
74. Schieder, R., Kramer, C., „*About the use of Allan Variance measurements*“, A&A 373, 746, 2001.
75. Schieder, R., Siebertz, O., Gal, C., Olbrich, M., Schlöder, F., Bieber, R., Schmülling, F., Tolls, V., Horn, J., „*Toward Very Large Bandwidth with Acousto-Optical Spectrometers*“, Proc. SPIE Int. Soc. Opt. Eng., Volume 4855, pp. 290-300, 2003.
76. Schieder, R., Siebertz, O., Schloeder, F., Gal, C., Stutzki, J., Hartogh, P., Natale, V. „*Wideband spectrometer for HIFI-FIRST*“, Proc. SPIE Int. Soc. Opt. Eng. Volume 4013, 313, 2000.
77. Schlöder, F., „*Untersuchung der Eigenschaften von CCD-Zeilensensoren*“ Diploma Thesis, Universität zu Köln, 1997.
78. Shibayama, Y., Kattaoka, K., „*Optics for modulating multiple beams using an asymmetric multilevel phase grating and a multichannel acousto-optic modulator*“, Appl. Opt., Vol. 36 (No. 4), pp. 853-861, 1997.
79. Siebertz, O., „*Akusto-optisches Spektrometer mit variabler Auflösung*“, Dissertation, Universität zu Köln, 1998.

80. Siebertz, O., “*WBS design description*”, HIFI Document Database at MPAe in Lindau, HIFI technical documentation, HIFI-KOSM-SP-SA100-002, 2003.
81. Siebertz, O., “*WBS QM Functional and Performance Test Report*”, HIFI Document Database at MPAe in Lindau, HIFI technical documentation, HIFI-KOSM-RP-SQ210-001, 2004.
82. Siebertz, O., Natale, V., Gal, C., “*Optics for HIFI, Specification*” HIFI technical documentation, AOS Group, Universität zu Köln, 2003.
83. Siegman, A. E., “*Lasers*,” University Science Books, Chapter 15. Ray optics and ray matrices, pp. 595-596, 1986.
84. Singh, N. B., Todd, D. J., “*Growth and Characterization of Acousto-optical Materials*”, Trans Tech Publications, Switzerland, 1990.
85. Smith, T. M., Korpel, A., “*Measurement of Light-Sound Interaction Efficiencies in Solids*”, IEEE J. Quantum Electronics, Vol. QE-1, pp. 283-284, 1965.
86. Snell, R. L., Howe, J. E., Ashby, M. L. N., Bergin, E. A., Chin, G., Erickson, N. R., Goldsmith, P. F., Harwit, M., Kleiner, S. C., Koch, D. G., Neufeld, D. A., Patten, B. M., Plume, R., Schieder, R., Stauffer, J. R., Tolls, V., Wang, Z., Winnewisser, G., Zhang, Y. F., and Melnick, G. J., “*Submillimeter Wave Astronomy Satellite Observations of Extended Water Emission in Orion*“, Astrophysical J., Volume 539, Nr. 2, Part 2, 2000.
87. Thorlabs, Inc., TEC module documentation, <http://www.thorlabs.com/Thorcat/7500/7542-D02.pdf>
88. Tielens, A.G.G.M, Helmich, F.P., “*Science User Requirements Document*”, Herschel Documentation Server at SRON, the Netherlands, <http://www.sron.nl/divisions/lea/hifi/SRON-G/HIFI/SP/2000-001>, 2000.
89. Uchida, N., Niizeki, N., “*Acoustooptic deflection materials and techniques*”, Proc. IEEE, Vol. 61, No. 8, pp. 1073-1092, 1973.
90. Uchida, N., Ohmachi, Y., “*Elastic and Photoelastic properties of TeO₂ single crystal*”, J Appl. Phys., 42, 4692, 1969.
91. Universität zu Köln, DADA homepage, <http://www.ph1.uni-koeln.de/dada>
92. University of Cologne, I. Physics Institut, AOS-Group, “*AOS Manual II*”, 1998.
93. van den Berge, G.A.A., “*Reliability estimation of Hitachi HL7851G laser diode*”, HIFI technical note, SRON-U/HIFI/TN/2003-008., 2003.
94. Walker, S. J., Jahns, J., “*Array generation with multilevel phase gratings*”, J. Opt. Soc. Am. A, Vol. 7, No.8, pp.1509-1513, 1990.
95. Whyborn, N.D., Aarts, H., Beintema, D.A., van Leeuwen, W., “*Instrument Design Description & Justification*”, Herschel Document Database at SRON, the Netherlands, SRON-G/HIFI/RP/2000-001, 2003.

Acknowledgement

I would like to thank everybody who was involved in the successful achievement of this work. Especially, I would like to thank

Mr. Prof. Dr. Gisbert Winnewisser who generously offered me the possibility to work for his institute in the very interesting HIFI satellite project. During my stay in Germany his personality and friendship were unceasingly conducive to the success of finding my feet.

Mr. Prof. Dr. Rudolf Schieder who paid much attention to this work. The success of this thesis was guaranteed by his tremendous theoretical as well as experimental support. During the countless discussions, his exceptional good ideas helped to answer diverse problems that seemed to be ridiculous to solve.

Mr. Prof. Dr. János Hajdu for helping so much at the very beginning and who send me on my way of promotion.

Mr. Dr. Oliver Siebertz the chef of the AOS crew for the excellent cooperative work, the marvellous experimental achievement in practice, the support in solving different theoretical themes, as well as for solving the hundreds of technical problems that always kept the development of the WBS instrument exciting, and for the very pleasant atmosphere.

The AOS crew with Mr. Dr. Frank Schmülling, Mr. Michael Olbrich, Ms. Bettina Franke, for their important support, and Mr. Frank Schlöder for the sophisticated software developments used for several measurements.

Mr. Martin Hirschhorn, Dr. Carsten Kramer, and Dr. Nikolaus Volgenau for reading and correcting this thesis.

The fine mechanics workshop under the leading of Mr. Mathias Mondt for the fast and precise fabrication of mechanical components, and for the outstanding technical advises needed for the successful design of the WBO.

My wife Annamária, my sons Gergő and Krisztián as well as my parents and my brothers for their interests, patience, and personal support during the years of my promotion.

This work has been financed by the German Aerospace Center (DLR) within the satellite project of “Entwicklung eines raumfahrttauglichen akusto-optischen Spectrometers für das Heterodyninstrument “HIFI” auf der ESA cornerstone mission Herschel“.

Erklärung

Ich versichere, dass ich die von mir vorgelegte Dissertation selbständig angefertigt, die benutzten Quellen und Hilfsmittel vollständig angegeben und die Stellen der Arbeit - einschließlich Tabellen, Karten und Abbildungen -, die anderen Werken im Wortlaut oder dem Sinn nach entnommen sind, in jedem Einzelfall als Entlehnung kenntlich gemacht habe; dass diese Dissertation noch keiner anderen Fakultät oder Universität zur Prüfung vorgelegen hat; dass sie - abgesehen von unten angegebenen Teilpublikationen - noch nicht veröffentlicht worden ist sowie, dass ich eine solche Veröffentlichung vor Abschluß des Promotionsverfahrens nicht vornehmen werde.

Die Bestimmungen dieser Promotionsordnung sind mir bekannt. Die von mir vorgelegte Dissertation ist von Herrn Prof. Dr. R. Schieder betreut worden.

Csaba Gál

Teilpublikationen

R. Schieder, O. Siebertz, F. Schloeder, C. Gal, J. Stutzki, P. Hartogh, V. Natale, “*Wideband spectrometer for HIFI-FIRST*”, Proc. SPIE Int. Soc. Opt. Eng., Volume 4013, pp. 313-324, 2000.

R. Schieder, O. Siebertz, C. Gal, M. Olbrich, F. Schlöder, R. Bieber, F. Schmülling, V. Tolls, J. Horn, “*Toward Very Large Bandwidth with Acousto-Optical Spectrometers*”, Proc. SPIE Int. Soc. Opt. Eng., Volume 4855, pp. 290-300, 2003.

O. Siebertz, R. Schieder, C. Gal, M. Olbrich, P. Hartogh; “*Acousto-Optical spectrometers for THz heterodyne instruments*”, Proc. SPIE 4857, 56, 2003.

O. Siebertz, C. Honigh, T. Tils, C. Gal, M. Olbrich, R. Bieber, F. Schmuelling, R. Schieder, “*The effect of standing waves in the LO path of a heterodyne receiver*”, in prep., 2005.

Curriculum Vitae

Csaba Gál

Birth of date: 22 July 1973
Birth of place: Bonyhád (Hungary)
Nationality: Hungarian
Marital status: married

Education

6/1999-5/2005 PhD student at the I. Physics Institute of the University of Cologne. Thesis: “Development of a Wide Bandwidth Array Acousto-Optical Spectrometer for the Herschel Satellite Mission”.

9/1992-10/1997 Technical University of Budapest, Faculty of Natural and Social Sciences, engineering physicist. Diploma thesis: “Theoretical and experimental research of laser light scattering on macroscopic particles” at the Technical University of Budapest, Atomic Physics Department, Surface Optical Laboratory.

9/1987-6/1991 Certificate of final examination in the Secondary School Monor.

Work experience

6/1999-12/2005 Science associate at the I. Physics Institute of the University of Cologne. Technical manager of the Wide Bandwidth Spectrometer in the Herschel project.

5/1998-6/1999 Developing engineer at the Phillips Mediagnost Ltd. Medical and Diagnostics Company. Development and construction of parts of an X-ray apparatus with the help of computer aided design tools.

5/1996-10/1997 Department of Atomic Physics of the Technical University, construction of an experimental gas flow meter, experiences in electronics and signal processing.

Lebenslauf

Csaba Gál

Geburtsdatum: 22 Juli 1973
Geburtsort: Bonyhád (Ungarn)
Staatsangehörigkeit: ungarisch
Familienstand: verheiratet

Schule

9/1987-6/1991 Allgemeine Hochschulreife Gymnasium Monor
9/1979-6/1987 Grundschule

Studium

9/1992-10/1997 Physikstudium an der Technischen Universität Budapest Diplomarbeit mit dem Thema: "Theoretische und experimentelle Untersuchung der Lichtstreuung makroskopischer Teilchen"

Promotion

6/1999-5/2005 Universität zu Köln, I. Physikalisches Institut
Thema: "Entwicklung eines raumfahrttauglichen akusto-optischen Spectrometers für das Satellitenprojekt Herschel"

Berufliche Erfahrung

6/1999-12/2005 Wissenschaftlicher Mitarbeiter am I. Physikalischen Institut der Universität zu Köln
5/1998-6/1999 Phillips Mediagnost GmbH für Medizinische und Diagnostische Geräte, technischer Entwicklungsingenieur
5/1996-10/1997 Diplomarbeit an der Technischen Universität Budapest, Atomphysik Institut